Ultrahigh Vacuum Studies of the Kinetics and Reaction Mechanisms of Ozone with Surface-Bound Fullerenes

Erin Durke Davis

Dissertation submitted to the faculty of the
Virginia Polytechnic Institute and State University
In partial fulfillment of the requirements for the degree of

DOCTOR OF PHILOSOPHY
In
Chemistry

John R. Morris, Chair
Karen J. Brewer
Gary L. Long
Diego Troya
Sungsool Wi

October 10, 2011
Blacksburg, Virginia

Keywords: C_{60}, ozone, fullerenes, ultrahigh vaccum, endohedrals, ozonolysis

Copyright 2011, Erin D. Davis

Ultrahigh Vacuum Studies of the Kinetics and Reaction Mechanisms of Ozone with Surface-Bound Fullerenes

Erin Durke Davis

(ABSTRACT)

Acquiring in depth knowledge of the ozone oxidation of surface-bound fullerenes advances the understanding of fullerene fate in the environment, as well as the reactivity of ozone with carbonaceous nanomaterials. Recent ultrahigh vacuum studies of the reaction of gas-phase ozone with surface-bound fullerenes have made it possible to observe the formation and subsequent thermal decomposition of the primary ozonide (PO). As the use of nanomaterials, such as C_{60}, continues to increase, the exposure of these molecules to humans and the environment is of growing concern, especially if they can be chemically altered by common pollutants. These experiments are made possible by combining ultrahigh vacuum surface analysis techniques with precision dosing using an O_3 gas source. The experimental setup also provides the capability of monitoring surface-bound reactants and products *in situ* with reflection-absorption IR spectroscopy, while gas-phase products are detected with a mass spectrometer. Our results indicate that ozone adds across a 6/6 bond on the C_{60} cage, forming an unstable intermediate, the primary ozonide. The observed initial reaction probability for the PO is $\gamma = 4.1 \times 10^{-3}$. Energies of activation for the formation and decomposition of the PO were obtained via temperature-dependent studies. After formation, the primary ozonide thermally decomposes into the Criegee Intermediate which can rearrange or, upon further exposure to ozone, react with another ozone molecule to form a variety of products such as carbonyls, anhydrides, esters, ethers, and ketenes. Larger fullerenes (C_{70}, C_{76}, C_{78}, and C_{84}) were also exposed to gas-phase ozone, in order to observe the reaction rate for ozonolysis and to propose an initial mechanism for ozone exposure. The results indicate that the structure of the fullerenes has little to no impact on the rate of oxidation via ozone. Lastly, Terbium endohedral were exposed to ozone, in an effort to determine whether ozone was capable of oxidizing both the outer fullerene cage, as well as the Tb atom sequestered inside. The preliminary XPS data suggests ozone oxidizes both within an hour of continuous exposure. Understanding this atmospherically-relevant reaction from both a mechanistic and kinetic standpoint will help predict the environmental fate of fullerenes and their oxides.

For Mom

Acknowledgments

This achievement was nothing short of a group effort. Without the support of my family, friends, and colleagues, this never would have been possible. First, I'd like to thank my husband, Eric. Your constant encouragement, support, and appreciation have made me a better scientist and, more importantly, a better person. I would not be who I am today without you, and for that, I am forever grateful. I would also like to thank my mom, dad, and brother. Mom – to this day, you continue to push me, expect nothing but the best from me, and always remind me to never give up on my goals. Dad – your support and understanding has been endless. Thank you for always providing some much needed perspective. Bryce – you always make me smile. Everyday I'm thankful for such an amazing brother, but as I've aged, I'm even more appreciative of our friendship.

To my fellow Morris group members: "Fair warning! During graduate school, you may meet heavy resistance!" The quest for my degree has been nothing short of a momentous challenge, but I can honestly say, I would not have made it to the end without each and every one of you. Larry – thank you for teaching me all you could. I enjoyed my graduate research immensely, and that is largely in part to you. Leslie, Jessica, and Will – thank you for engaging discussions, challenging questions, and a little bit of fun on the side. I'm so glad that we went through this experience together and I wish you all the best of luck in the future. Alec, Monica, and Yafen – my ozone team! I, literally, would not have been able to make it through without you! Your help was invaluable and I hope you all enjoyed working together as much as I did. I'd also like to thank Josh Uzarski, Amanda Bolger, Dimitar Panayotov, Tommy Rockhold, Wesley Gordon, and Steve Burrows.

My research would not have been possible without the help of Tom Wertalik, the most talented glass blower I know; an important person to know when you work with ozone! Thank you to Dave Simmons and Darrell Link from the Engineering machine shop for all those last minute parts. I'd also like to thank Josh Layfield and Tim Fuhrer for their help with numerous calculations. A big thank you to my committee for all your help and advice over the last few years.

Finally, I am forever grateful to my advisor, John Morris. John – your support, patience, and understanding throughout my years in your group made all the difference. I thank you for helping me become the scientist I am today. I can honestly say, I am more passionate about, not only chemistry, but learning and teaching than I have ever been. As difficult as this journey was, it only makes it that much more rewarding now that I've reached the end. Thank you for holding your students to such high standards and always pushing me forward.

Table of Contents

List of Figures

List of Tables

Index of Acronyms

UHV	Ultra-high vaccum
RAIRS	Reflection-absorption infrared spectroscopy
MS	Mass spectrometry
TPD	Temperature-programmed desorption
XPS	X-ray photoelectron spectroscopy
STM	Scanning tunneling microscopy
CNTs	Carbon nanotubes
MWNTs	Multi-walled nanotubes
FBGCs	Foreign body giant cells
NMR	Nuclear Magnetic Resonance
IPR	Isolated Pentagon Rule
GC	Gas chromatography
SAMs	Self-assembled monolayers
AFM	Atomic force microscopy
SEM	Scanning electron microscopy
AES	Auger electron spectroscopy
TOF-SIMS	Time-of-flight secondary ion mass spectrometry
FT-IR	Fourier transform-infrared
AM1	Austin Model 1
PO	Primary Ozonide
CI	Criegee Intermediate

DFT	Density Functional Theory
ESC	Electronic Structure Calculations
MFP	Mean Free Path
UHP	Ultra-high purity
PID	Proportional Integral Derivative
CE	Crucible Evaporator
CAD	Capillary Array Doser
IRD	Infrared detector
IMFP	Inelastic mean free path
QCM	Quartz crystal microbalance
MCT	Mercury cadmium telluride
XRD	X-ray powder diffraction

Chapter 1

Introduction and Motivation

Thesis Statement

The objective of this research is to develop a fundamental understanding of the mechanism and kinetics of the gas-surface reaction between gas-phase ozone and surface-bound fullerenes. Once the primary knowledge of the system is obtained, factors such as fullerene structure or functionalization will be considered to determine the impact on the overall mechanism and kinetics.

1.1 Background

Understanding gas-surface interactions is essential to comprehending the chemistry occurring in the atmosphere. Hydrocarbons, many containing double bonds, are a prevalent species in both the stratosphere and the troposphere. Natural alkenes are a notably reactive component of the atmosphere, as well. Some studies report that natural alkenes can affect the circulation of ozone throughout the atmosphere.[1] Other studies have shown that the reaction of NO_2, another prominent atmospheric pollutant, with olefins in the atmosphere produces a variety of hazardous materials.[2] In an attempt to understand the gas-surface reactions between oxidizing gases and fullerenes (a very olefinic family of molecules) the research will focus on three objectives:

1. Determine a full mechanism for the oxidation of C_{60} – the most common fullerene
2. Create a kinetic model for the oxidation of C_{60}
3. Determine the effect of fullerene structure (i.e. cage size) on the oxidation

The experiments will be performed in an ultrahigh vacuum system (UHV), using reflection-absorption infrared spectroscopy (RAIRS), mass spectroscopy (MS), temperature programmed desorption (TPD), and x-ray photoelectron spectroscopy (XPS) as the analysis techniques. Utilizing a UHV system and surface analysis techniques will provide important data that will be essential to developing a complete understanding of the gas-surface reaction mechanisms.

1.1.1 Carbon Nanomaterials in the Troposphere

With nanotechnology producing increasing quantities of nanomaterials every year and pollution continuing to add harmful molecules into the environment, it is important to investigate the outcome of nanomaterial/pollutant reactions, and whether the resulting products will be harmful to humans and the environment. The fate of carbonaceous nanomaterials in the troposphere is an area of study without an abundance of knowledge. Nanomaterials, themselves, have been intensely investigated since the eruption of nanotechnology. Nanotechnology was born in the early 1980s, in response to the dawning of cluster science and the creation of the scanning tunneling microscope (STM). In general, nanotechnology is the study of the ability to control the size of matter on an atomic and molecular scale. This field typically deals with matter ranging in size between 1 nm to 100 nm, in at least one dimension. Within this diverse area of study, much focus has encompassed nanomaterials that have nanoscale morphological features. The nanoscale features impart unique properties on the materials; in other words, the nanoscale structure can affect the behavior of the material in many systems.

Carbonaceous nanomaterials include molecules such as carbon nanotubes, nanohorns, nano-onions and, of course, fullerenes. Carbon nanomaterials are used in a variety of research areas: field emission displays,[3] advanced acoustic devices,[4] biomedical applications,[5] and various types of coatings.[6] With their broad range of applications, carbon nanomaterials are being

produced by the tons every year.[7] Scientists have recently begun to study the environmental and health implications of the final nanomaterial products being produced. Researchers are considering what happens to these molecules when they enter the air, water, and soil, as well as their impact on animals and humans upon exposure. Several studies in 2008 have likened inhalation effects of carbon nanotubes (CNTs) to that of asbestos.[8] Asbestos particles' needle-like fiber shape allows them to lodge in the mesothelial lining of the lungs which causes inflammation and eventually mesothelioma, a rare type of cancer. Since carbon nanotubes have a similar shape, see Figure 1.1, concern was raised that these nanomaterials may have the same effect on the mesothelium. In the study performed by Poland *et al.*, CNTs, specifically multi-

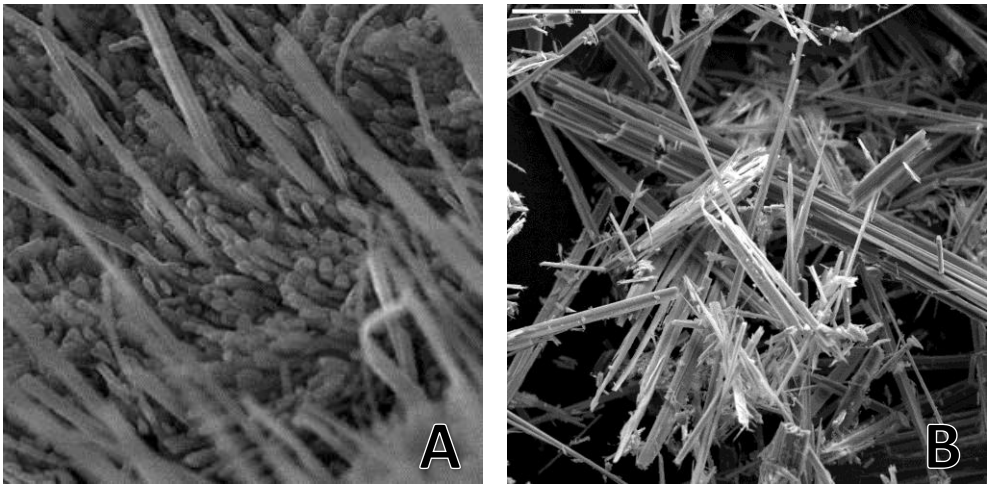

Figure 1.1: (A) SEM image of carbon nanotubes (Reproduced in courtesy of Prof. Xinwei Wang at Iowa State University), (B) SEM image of asbestos particles (Credit: U.S. Geological Survey).

walled nanotubes (MWNTs), were injected into the peritoneal cavity of mice to assess the effect of these molecules on the mesothelial lining. They observed that the long MWNTs (> ~20μm) caused inflammation, foreign-body giant cells (FBGCs), and granulomas which were qualitatively and quantitatively comparable to the response caused by long asbestos.[8a] A similar study was carried out by Jun Kanno and colleagues at the Tokyo Metropolitan Institute of Public Health, also in 2008. These researchers used the same MWNTs as Poland, injected them into the

abdominal cavity of mice; however, an important difference between the two studies was the type of mice used for testing. In Kanno's study she tested p53+/- heterozygous mice – a common genetically engineered mouse that rapidly develops malignant mesothelioma following repeated exposure to asbestos fibers. Upon exposing the p53 mice to MWNTs, 88% developed mesothelioma tumors, while only 79% of the mice developed tumors upon exposure to crocidolite, a particularly potent form of asbestos.[9] Along with the potential health risks, CNTs effects on the environment are also of concern. CNTs chemical and physical properties make them one of the most widely manufactured and commercialized nanomaterials. Often, it is because of these very properties that the nanotubes are deliberately modified, structurally manipulated, or even incidentally altered by natural environmental processes once they enter the air, water, and soil. Scientists have yet to fully understand how CNTs interact with toxic contaminants and pollutants or how they move through environmental media. CNTs are just one of the many types of carbonaceous nanomaterials, all of which are not completely well understood in terms of their health implications and environmental fate. To better understand these popular molecules and how they will influence the earth as a whole, fundamental studies must be performed. Information obtained from these studies can be used to improve models, applications, and current processes. The data could also help predict how these molecules may react in more complicated scenarios, e.g. in the body, in polluted waterways, and in the atmosphere.

In terms of complicated scenarios, the atmosphere is one of the most complex systems on the planet, specifically the troposphere. The troposphere, shown in Figure 1.2, is the lowest layer of the earth's atmosphere, and also the smallest, only extending 7.5 miles above the ground. This small layer contains ~ 75% of the total mass of the atmosphere, as well as 99% of the aerosols

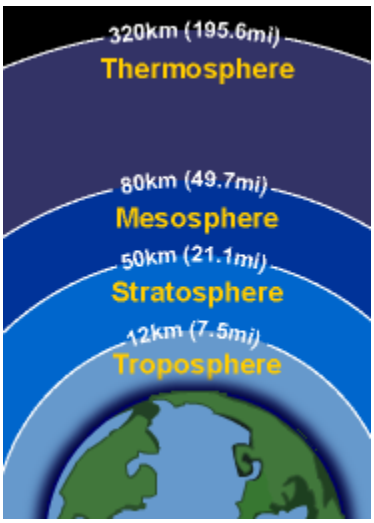

Figure 1.2: Diagram of the four separate layers of the earth's atmosphere.

and water vapor. Besides water and aerosol particles, the troposphere is home to many other molecules, a growing number of them pollutants. Known as a secondary pollutant, ozone is also one of the most important oxidizers in the atmosphere. It is known to react readily with aerosol particles and other organic species in the air.[10] Ozone is especially reactive with species containing unsaturated sites, or double bonds. Many carbonaceous nanomaterials are comprised of fused hexagonal and pentagonal rings, containing numerous reactive sites for ozone to attack. Researchers have begun to investigate how ozone reacts with these nanomaterials in the gas, aqueous and even solid phases,[11] but the gas-surface interface has yet to be explored. With respect to the atmosphere, gas-surface chemistry is an extremely relevant system to study. There are many surfaces in the atmosphere, from aerosols and dust particles, to the faces of buildings, cars, and even vegetation. In the atmosphere, the most likely way molecules will interact with these surfaces will be through gas-surface collisions. The chemistry of this particular type of interaction can vary greatly from that seen in other systems, like the solution phase for example. In solution-phase chemistry, solvation and solvent effects can have a significant impact on the reactions. When reactions are observed at the gas-surface interface, solvation is no longer a factor. Instead, other factors must be considered, such as the possible effects of restricted geometries and the competition between rates of desorption and rates of reaction. Even if a reaction is well understood in the solution phase, it

must be reconsidered at the gas-surface interface because the chemistry could be completely different.

Fullerenes are grouped with CNTs as some of the most widely studied and utilized carbon nanomaterials in the industry. While the bulk of fullerene production comes from man-made sources, fullerenes are also present naturally in the environment as a result of volcanic eruptions, forest fires, and the combustion of carbon-based materials. These unique cage molecules have even been discovered in space.

In the present studies, the focus is the reaction between surface-bound fullerenes and gas-phase ozone. The goal is to obtain a detailed mechanistic picture as well as a comprehensive kinetic model for this atmospherically prominent system. The rest of this chapter is dedicated to the properties of these two molecules as well as a discussion of important literature pertaining to this reaction.

1.1.2 Fullerenes

1.1.2.1 The History of Fullerenes

The structure of the regular truncated icosahedron has been known since the 1500s. A sketch, supposedly drawn by Leonardo da Vinci, of the truncated icosahedron exists in the 1509 publication, "De Divina Proportione".[12] Another representation of this unique structure was drawn by Renaissance painter, Albrecht Dürer. His depiction could reproduce the cage structure by folding up a sheet of cardboard along the hexagons and pentagons, see Figure 1.3.[13] Even though intellectual thinkers had envisioned this structure for hundreds of years, fullerenes, specifically C_{60}, weren't actually discovered until 1985 by scientists at Rice University.[14] The experiments, performed by Kroto et al., were originally aimed at determining the mechanisms by

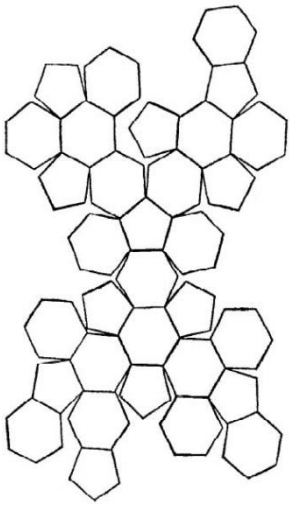

Figure 1.3: A. Dürer's illustration of truncated icosahedron.

which long-chain carbon molecules are formed in interstellar space. Upon detecting a stable cluster of 60 carbon atoms, the researchers concluded the most likely structure to be a truncated icosahedron. Twenty five years later, fullerenes are defined as any molecule that is entirely composed of carbon atoms, in the form of a hollow sphere, ellipsoid, or tube.

1.1.2.2 Fullerene Structure

Fullerenes, an allotropic form of carbon, can exist in different shapes; spheres, ellipsoids, and tubes, although the tubes are known as carbon nanotubes. Fullerenes generally refer to the family of cage molecules, of which C_{60} is the most well-known. Fullerenes are similar in structure to graphite, the major difference being the pentagonal rings included in the fullerene structure. Looking again at Figure 1.3, notice the gaps of space surrounding the pentagons and hexagons when C_{60} is shown in a planar orientation. Observing the molecule in this manner helps show, first that the pentagons impart curvature upon the structure, and second, that these five-membered rings are required to close the cage. Buckminsterfullerene, also known as C_{60}, is the most prominent fullerene in

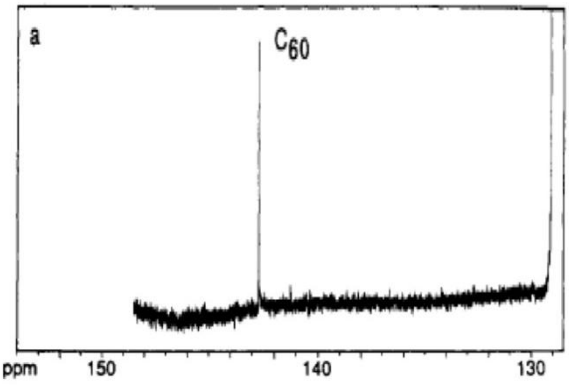

Figure 1.4: ^{13}C NMR of gas-phase C_{60}.[15] Reprinted with permission from Kroto *et al. Chem. Rev*. 1991, *91*, 1213-1235. Copyright 1991 American Chemical Society.

existence. Its 60 carbon atoms are equivalent and form a truncated icosahedron structure. The equality of the carbon atoms has been confirmed with ^{13}C NMR, shown in Figure 1.4.[15] Fullerenes are comprised of fused hexagonal and pentagonal rings. The inclusion of the pentagonal rings is essential to close the cage structure of these molecules. While the exact pathway for the formation of fullerenes is still up for debate (graphene-to-fullerene transformation, pentagon road or Limacon model, ring stacking, or the fullerene road), it is known that the presence of pentagons within the cage structure is what adds curvature and eventually allows the cage to close. Using Euler's theorem for the properties of polyhedra,

$$f + v = e + 2 \tag{1.1}$$

where f, v, and e are the number of faces, vertices, and edges,[13] one reaches the conclusion that for fullerenes, which only contain hexagons and pentagons, the molecules must contain 12 pentagonal rings within its cage structure. Applying Euler's theorem to various sizes of fullerene molecules, one also sees that the number of hexagonal rings is completely arbitrary. It then follows that theoretically the smallest fullerene, based on Euler's theorem, is C_{20}. C_{20} would be a dodecahedron, consisting only of 12 pentagons and no hexagons. In the dodecahedron, the pentagon rings are fused together, a configuration that brings up the issue of stability. The inclusion of the pentagon rings induces curvature, but it also imparts a certain degree of strain upon the cage. Therefore, the more pentagons, and more importantly, the more pentagons sharing edges with one another, the greater the strain inherent in the molecule. Another important requirement for the formation and stability of these cage molecules is that the structure conforms to the Isolated Pentagon Rule (IPR). The Isolated Pentagon Rule states that for a fullerene molecule to be thermodynamically stable, the 12 pentagon rings must be surrounded on all sides by hexagons, therefore isolating them from other pentagons. The IPR can be used to predict

which fullerenes are most likely to occur naturally as well as which fullerenes can be expected using man-made methods of production.

The easiest fullerene to manufacture is C_{60}. It is the fullerene produced in the greatest abundance, regardless of the type of method, whether it is man-made or natural formation. As stated earlier, C_{60} is composed of 60 equivalent carbon atoms arranged in pentagons and hexagons. Each carbon atom is trigonally bonded to three other carbon atoms with a sp^2 bonding configuration. However, since these bonds exist on a curved surface, there is some sp^3 (tetrahedral) character mixed in with the trigonal bonds. In general, though, all of C_{60}'s carbon atoms are referred to as having sp^2 hybridization. While the carbon atoms may all be fundamentally the same, C_{60} does have two different types of bonds. The two bond types are commonly denoted as 5/6 bonds and 6/6 bonds. The 5/6 bond is an edge between a pentagon ring and a hexagon ring. The 6/6 bond is an edge between two hexagons. Though the bonds differ only by 0.06Å (5/6 bond = 1.46 Å, 6/6 bond = 1.40 Å), the shorter bond is designated a double bond. This means that the C_{60} cage has essentially 30 double bonds. The unique structure of this family of molecules gives rise to their equally unique chemical properties.

1.1.2.3 Fullerene Properties

Fullerenes have a distinctive and varied range of chemical properties, which is what makes them so popular in so many different fields of study. While only a few of these properties will be discussed in detail in this document, there are many more, such as optical properties, transport and thermal properties, superconductivity, and magnetic resonance. The aromaticity of fullerenes is actually not as one might have expected. Using C_{60} as an example, with so many double bonds on the molecule's surface, one might expect the molecule to possess "superaromaticity". Superaromaticity, a result of aromaticity that is spread over a number of

fused or conjugated rings, is not seen in the C_{60} molecule. The electrons of this molecule do not delocalize over the entire cage. The reason the electrons do not delocalize in C_{60}, or other fullerene molecules, is because of the curvature of the molecule, a result of the included pentagons. The pentagons are comprised of single bonds, which prevent the movement of the electrons and hold the double bonds in certain positions or locations (i.e. along the edges of two hexagon rings). The electron localization helps to stabilize the molecule, but does not make it entirely unreactive. In fact, because of the large number of reaction sites on one cage (C_{60} has 30 reaction sites or double bonds) there are many possible chemical combinations. Figure 1.5 shows many of the different chemical reactions which can be used to functionalize fullerene molecules.[16] By functionalizing these molecules, or attaching new chemical groups to the surface, the researcher has the ability to alter the chemical and physical properties of the fullerenes. Functionalization can also occur by adding atoms or molecules inside the fullerene cage. Internal modification of the fullerene cage is known as endofunctionalization. The most common type of fullerene reaction is an electrophilic addition. Electrophilic addition occurs at the 6/6 bonds, which reduces angle strain and changes the sp^2 hybridization to a sp^3 configuration. Often times, by adding molecules to the outside or inside of the fullerene, the overall stability of the cage is improved. The cycloaddition reaction of fullerenes results in a four-, five-, or six-membered ring fused to the outside of the fullerene cage. One side of the ring is part of the cage structure. The attachment is generally across a 6/6 bond, or reaction site, and the produced ring connects two pentagon rings to one another.

Keeping the electrophilic and cycloaddition reactions in mind, it is important to point out that ozone is an electrophile known to react with double bonds through cycloaddition. The result of ozone's addition to a double bond is a five-membered ring known as the primary ozonide.

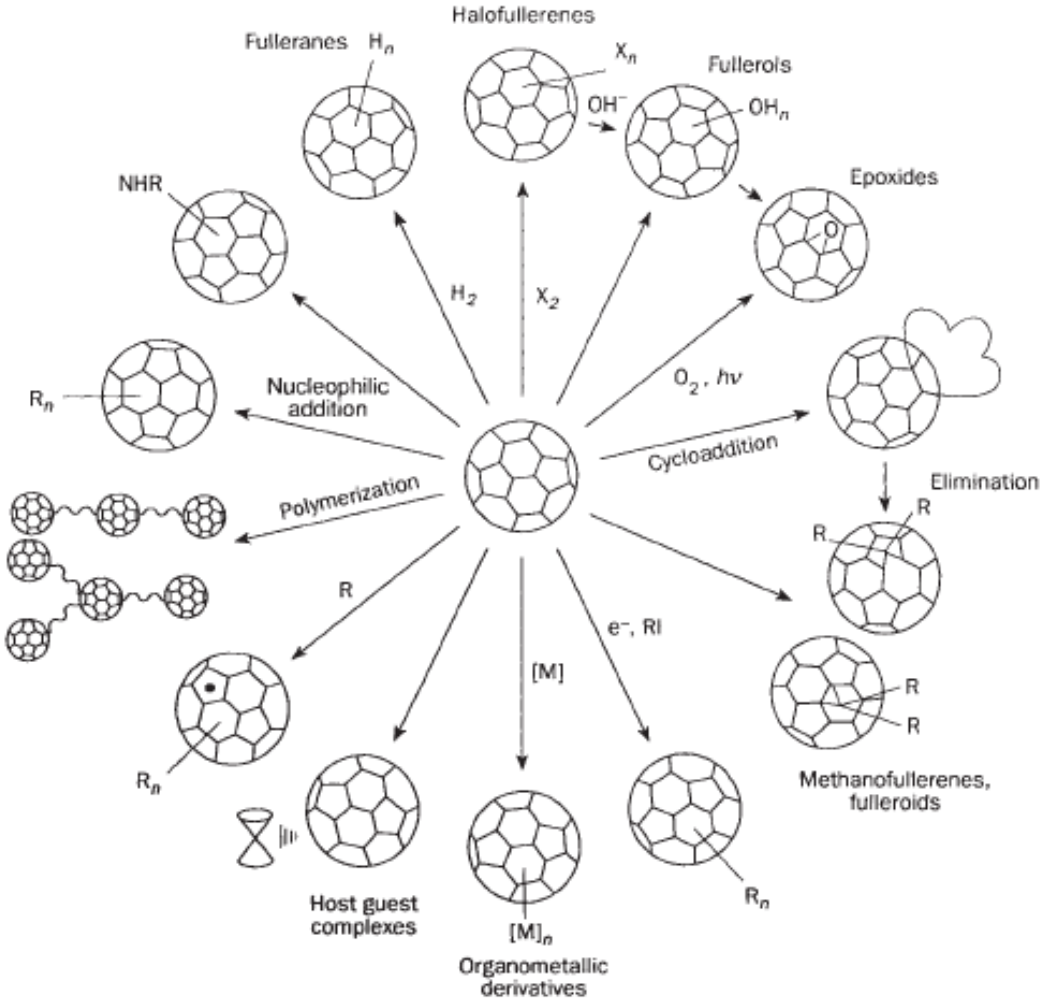

Figure 1.5: A summary of the many different types of reactions fullerenes can undergo along with the resulting products.[16] Reproduced from Taylor *et al. Nature* 1993, *363,* 685-693.

1.1.3 Ozone

1.1.3.1 Ozone's History

For centuries, man has been detecting ozone, even if only by smell. Homer mentions the smell of lightning and thunder in both *The Illiad* and *The Odyssey*, *"*When beneath the blast of father Zeus an oak falleth uprooted, and a dread reek of brimstone ariseth therefrom,—then verily courage no longer possesseth him that looketh thereon. . ." (The Odyssey) and, "Zeus thundered and hurled his bolt upon the ship, and she quivered from stem to stern, smitten by the bolt of Zeus, and was filled with sulphurous smoke." (The Illiad) In 1785 a Dutch scientist by the name of Martin van Marum noted what he classified as an "electrical odor" while passing an electrical spark through diatomic oxygen.[17] Regardless of these earlier observations of ozone, the discovery of this molecule would be credited to Christian Friedrich Schönbein in 1840. Schönbein had been studying the electrolysis of water when he noticed a new odor in his laboratory. The new odor indicated a new product in his reaction. He named the new product "ozone", derived from the greek word "*ozein*", meaning "to smell".[17] Quickly after its official discovery, the study and production of ozone grew rapidly, with the development of the first industrial generator in 1857 by Ernst Werner von Siemens.[17] But it would not be until fifteen years later that the actual structure of ozone was determined by Jacques-Louis Soret.[18]

1.1.3.2 Ozone's Properties

Ozone is an extremely reactive allotrope of oxygen consisting of three oxygen atoms. It is less stable than O_2, another allotrope of oxygen. The molecule has four resonance structures, shown in Figure 1.6. The bond lengths in the ozone molecule are 1.278Å, with a bond angle of ~116°. In any given resonance structure, the middle oxygen atom always has at least one lone

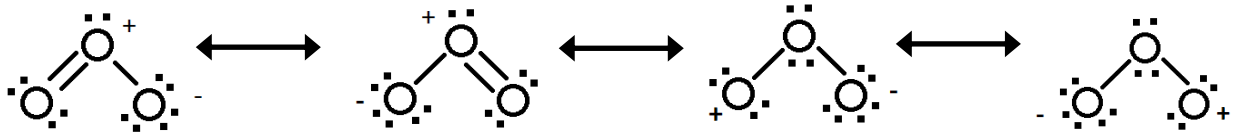

Figure 1.6: Depiction of the four separate resonance structures of ozone.

pair on it giving it sp^2 hybridization, as well as making the molecule bent.[19] Ozone's unstable structure makes it challenging to work with. At room temperature, it is a slightly pale blue gas, but if the temperature is lowered to ~ -112°C, ozone becomes a liquid with a dark blue color. Upon further cooling, below -193°C, ozone becomes a dark violet-black solid. When working with ozone in the liquid or gas-phase forms it is important to pay close attention to the temperature because at high enough concentrations these substances will readily detonate![20] Ozone also reacts violently with organics, so care should be given to the introduction of organic material to pure ozone.

Ozone is found naturally in small concentrations in the stratosphere, the upper layer of the Earth's atmosphere. Ozone is also found in the troposphere, the lowest layer of the atmosphere, where it is a powerful oxidizer and a lung damaging substance. It exists in this layer as a man-made product. Ozone is a result of air pollution from such things as automobile exhaust and industrial emissions. The ozone in the stratosphere is often termed "good" ozone, while the amount existing in the troposphere is referred to as "bad" ozone. In the stratosphere, ozone helps protect Earth from harmful ultraviolet radiation. In the troposphere, where the molecule is considered a pollutant, it can react with aerosols, the surfaces of buildings, plants, and human/animal lungs. Understanding how this highly oxidizing atmospheric pollutant reacts with species present in the air is a particular motivation for this research.

1.1.3.3 Reactions of Ozone and Organics

The reaction of ozone with olefins has been studied in great detail. A highly unstable initial ozone-olefin adduct was first identified in 1959 by Criegee and Schröder. The ozone-olefin adduct, now commonly known as the "primary ozonide" was presumed to decompose in two different ways. In the solution phase, one reaction pathway produces ketones and/or aldehydes and hydrogen peroxide. The other decomposition pathway yields an aldehyde, or ketone, and the carbonyl oxide zwitterion.[21] When the primary ozonide splits into an aldehyde and the carbonyl oxide zwitterion, the products can react separately or together. If the products react with one another, the Criegee ozonide is formed.[22] The carbonyl oxide zwitterion can also react with water to form hydroxy hydroperoxide. Hydroxy hydroperoxide, a species that is metastable in aqueous solutions, hydrolyzes to hydrogen peroxide and an aldehyde. In a study

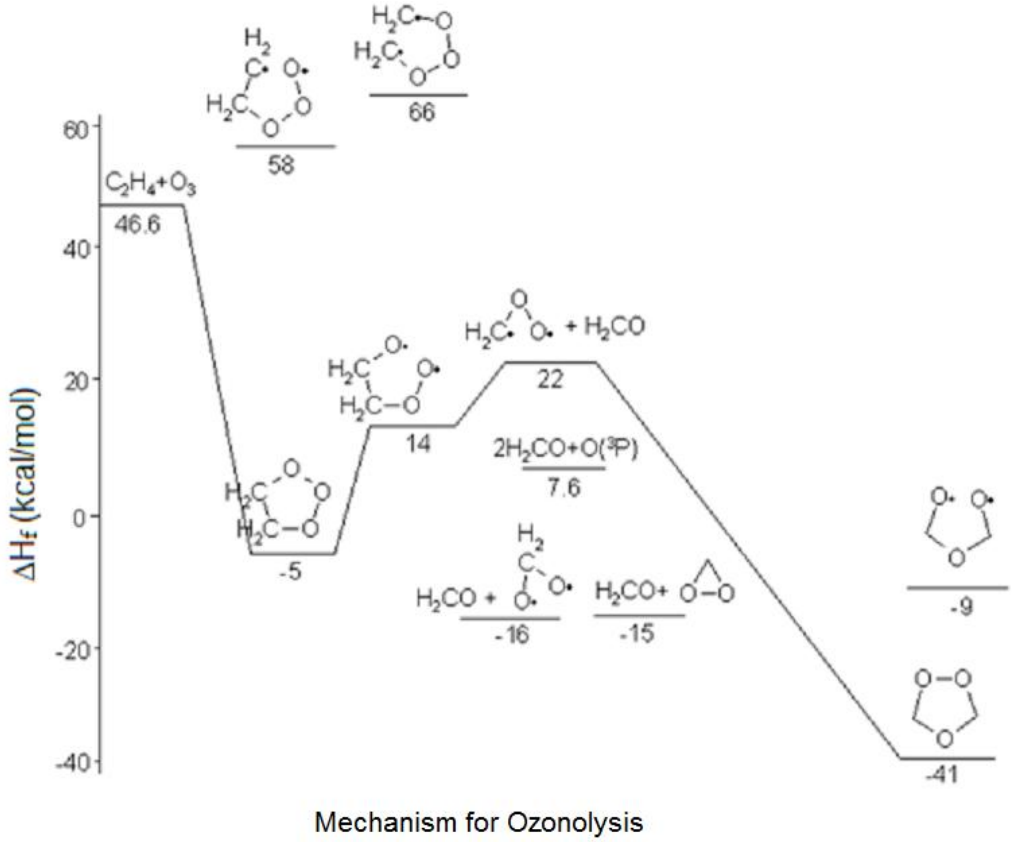

Figure 1.7: Energy diagram for the Primary Ozonide – modified from Wadt Study.[24] Adapted with permission from Wadt *et al. JACS* 1975, *97(11)*, 3004-3021. Copyright 1975 American Chemical Society.

performed by Pryor *et al.*, the rate at which the carbonyl oxide zwitterion reacts with water is significantly faster than the rate at which it would react with an aldehyde.[22] Several other studies support Pryor's conclusion, having utilized aprotic solvents; the studies identified the Criegee ozonide as the major product.[21, 23] The energy diagram in Figure 1.7 shows the heats of formation for the primary ozonide and various intermediates as well as the Criegee ozonide, as presented in a study performed by Wadt and Goddard.[24] The diagram indicates that, when the primary ozonide is formed, there is a measurable energy barrier that must be overcome to allow for the formation of the Criegee ozonide.

Gas phase reactions, rather than condensed phase reactions, are undoubtedly the dominant reactions in the atmosphere. Ozone is an indirect product of the photochemical decomposition of nitrogen dioxide in air; it reacts in the atmosphere with various hydrocarbons and other pollutants to produce smog, eye irritants, and plant toxicants.[25] The first gas phase ozonolysis was performed by Schönbein in 1868.[26] Since then, numerous studies have been performed that focus on this system. Wadia *et al.* report the mechanism shown in Figure 1.8 as a summary of the O_3-alkene reactions in the gas and solution phases.[27] In the gas phase, the Criegee zwitterion is referred to as the Criegee intermediate, its corresponding diradical, $H_2\dot{C}OO\cdot$. Diradicals are known to contain an excess of internal energy which prompts internal rearrangement, usually resulting in decomposition.[28] It is apparent from Figure 1.8 that more reaction pathways are possible for the Criegee intermediate in the gas phase.

With more reaction pathways available in the gas phase, studying ozone's course (i.e. decomposition, reaction, intermediate and product formation) through a reaction becomes more challenging. A 1995 study performed by Atkinson *et al.* observed the products of the gas-phase reactions of ozone with alkenes.[29] The experiments were carried out under atmospheric

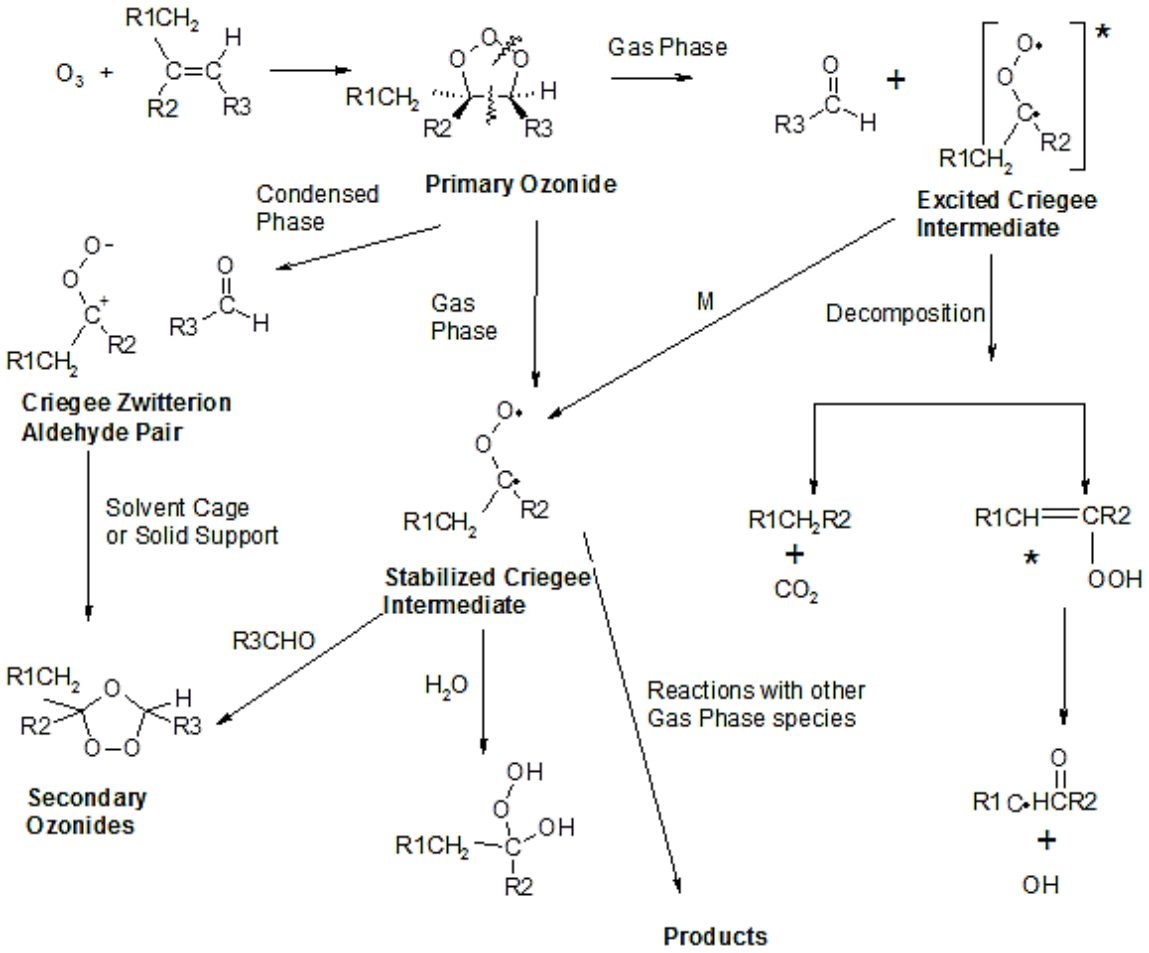

Figure 1.8: Summary of O_3-alkene reactions in the gas and solution phases – modified from Wadia Study.[27] Adapted with permission from Wadia *et al. Langmuir* 2000, *16,* 9321-9330. Copyright 2000 American Chemical Society.

conditions. OH radical scavengers, cyclohexane and *n*-octane were utilized. Radical scavengers are beneficial because OH radicals produced in alkene-ozone reactions continue to react with alkenes, complicating the determination of the products created from the ozone reaction. The results of the investigation were quantified by gas chromatography (GC) and FTIR absorption spectroscopy. GC analyses indicated the presence of cyclohexanone and cyclohexanol from all the alkene species reacted with ozone. Cyclohexanone and cyclohexanol are both products resulting from the interaction of cyclohexane with an OH radical. The researchers also detected the existence of two carbonyl species formed from the reaction of ozone with alkenes. All alkene species used in the study produced two carbonyls. The sum of the yields for the two carbonyls

are approximately equal to unity.[29] Atkinson et al. attribute the formation of products to the reactions shown in Figure 1.9.

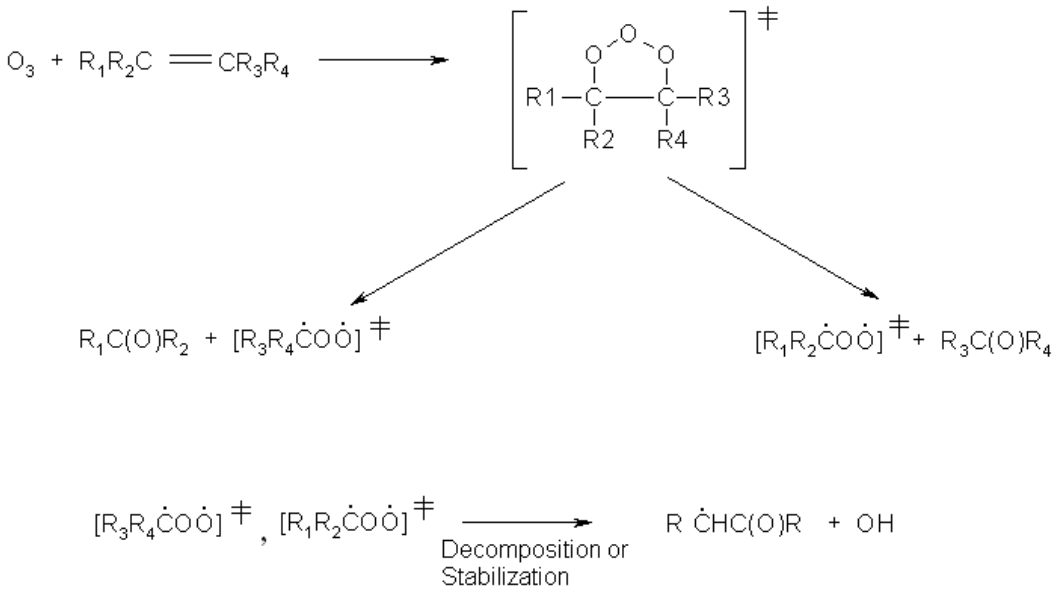

Figure 1.9: Formation of Carbonyls and Products – modified from Atkinson study.[29] Adapted with permission from Atkinson *et al. ES& T* 1995, *29(7),* 1860-1866. Copyright 1995 American Chemical Society.

In another report, by Feltham *et al.*, the researchers attempted to identify secondary ozonides from the gas phase reactions of ozone and numerous alkenes. The researchers also monitored the reaction products, in an effort to obtain a better understanding of the mechanisms of ozonolysis.[30] One alkene focused on in the study was ethene. The researchers mixed O_3/O_2 and ethene/argon for one hour, then deposited the mixture onto a CsI window for IR analysis. The spectrum taken after mixing the gases contained a number of bands not observed in spectra for either starting materials.[30] To determine which bands were due to ozonides, the condensate was subjected to broad-band UV-vis photolysis. Ozonides are known to decompose with photolysis; therefore any peaks due to an ozonide species would be expected to decrease. Figure 1.10 shows the IR spectrum of the ethene/ozone mixture before and after 20 minutes of broad-band UV-vis

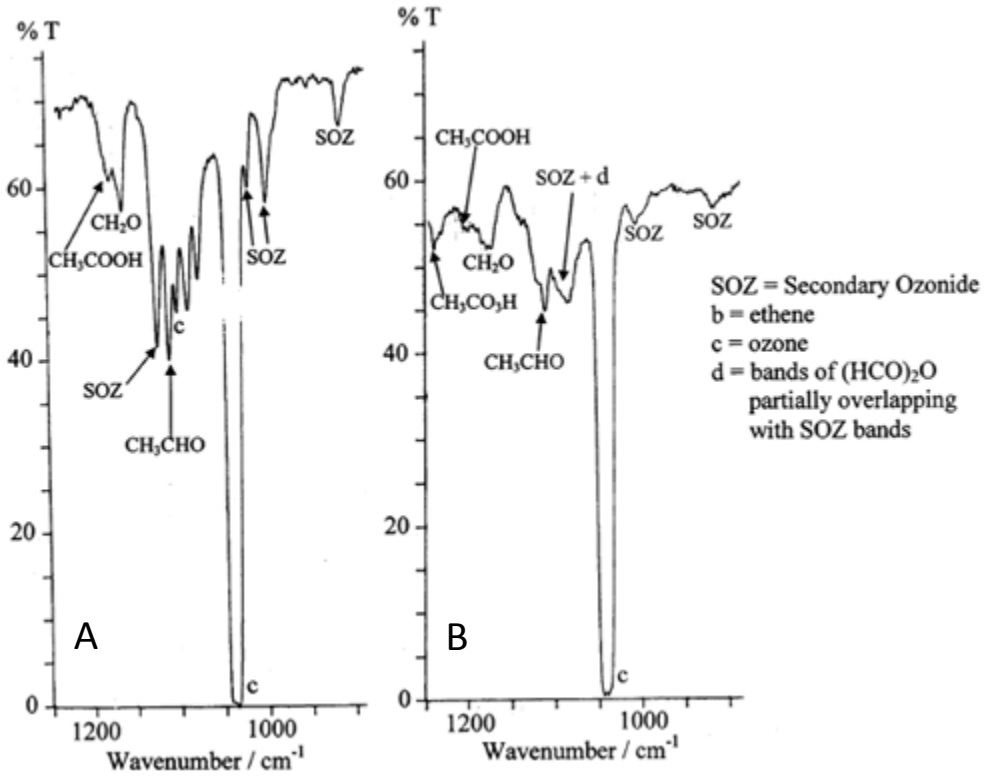

Figure 1.10: The region 1250-900 cm^{-1} of the transmission IR spectrum of a matrix initially containing products of the gas phase reaction of ethene and ozone: (a) after mixtures of ethene (1%) in argon and ozone (5%) in oxygen had been allowed to mix for 1 hr. and the resulting mixture deposited onto a CsI window held at 12 K; (b) after the condensate had been subjected to 20 min. broad-band UV-vis photolysis.[30] Reprinted from *ES&T, 56,* Reactions of alkenes with ozone in the gas phase: a matrix-isolation study of secondary ozonides and carbonyl-containing products, 2605-2616, Copyright 2000, with permission from Elsevier.

photolysis. Upon comparing the two spectra, the bands assigned to the secondary ozonide had decreased noticeably. Further analysis of the products of the ozone-ethene reaction showed the duration of mixing time affected the amount of formaldehyde versus acetaldehyde. Formaldehyde, the primary product, is dominated by acetaldehyde, the secondary product, after longer periods of mixing. The researchers concluded the results show an increased importance of secondary reactions at longer reaction times.[30]

1.1.3.4 Reactions of Ozone with Organics at the Gas-Surface Interface

While little work has been done on gas-surface reactions with ozone, compared to the amount of literature available on gas and condensed phase reactions, gas-surface research may display an entirely different type of reaction chemistry. The modeling of surface reactions is important, and relevant to the chemistry occurring in the troposphere. To conduct gas-surface experiments, many research groups have begun to utilize self-assembled monolayers (SAMs). Fiegland *et al.* investigated the reaction of ozone with undec-10-ene-1-thiol SAMs on Au using reflection-absorption infrared spectroscopy (RAIRS).[31] The experiments were carried out in an ultra-high vacuum system (UHV). Figure 1.11 shows the IR spectrum of the undec-10-ene-1-thiol SAM before and after ozone exposure. The spectra show that the peaks due to the double bond are gone after exposure to ozone; also, three new peaks are present. The peaks shown at 1821 and 1750 cm^{-1} are attributed to the in-phase and out-of-phase stretching of an interchain carboxylic anhydride group.[32] The peak at 1040 cm^{-1} is assigned to a C–O stretch. Fiegland presents time- resolved data suggesting the formation of a carboxylic acid intermediate. With increasing exposure, the acid intermediate becomes a carboxylic anhydride group. The mechanism assigned to the reaction includes the formation of the primary ozonide,

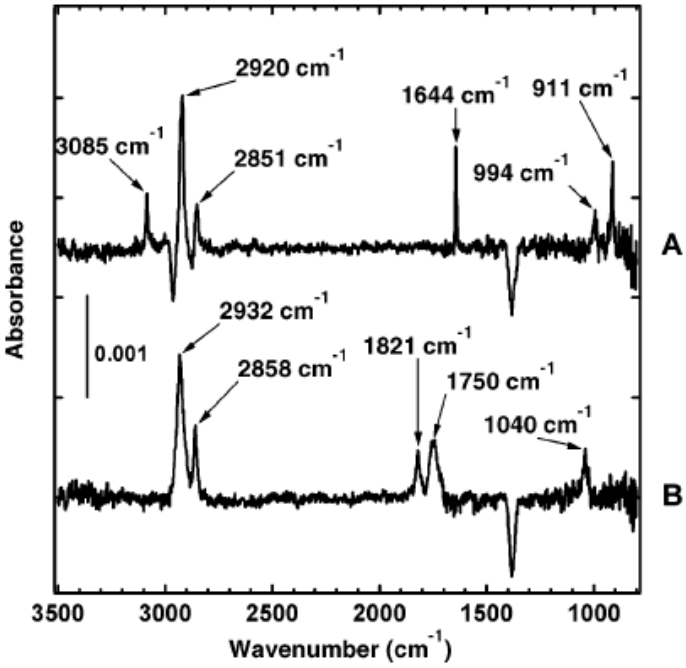

Figure 1.11: IR spectrum of C=C terminated SAM on Au: (A) before exposure to ozone; (B) after exposure to ~1000L of ozone.[31] Reprinted with permission from Fiegland *et al*. *Langmuir*, 2005, *21*, 2660-2661. Copyright 2005 American Chemical Society.

which decomposes to a diradical intermediate. The diradical intermediate rearranges to form the carboxylic acid group. Upon elimination of water, the anhydride remains.[31, 33]

Examining ozone reactions at atmospheric pressures is just as important for developing a complete understanding of the molecule's reactivity, as carrying out studies in a vacuum environment. McIntire and Finlayson-Pitts performed a study using vinyl-terminated 3- and 8-carbon SAMs on silicon substrates, reacted with ~1ppm gaseous O_3. The group reported the first observation of large organic aggregates on the surface. The experiments were carried out in a Teflon reaction chamber at room temperature and utilized atomic force microscopy (AFM), scanning electron microscopy (SEM), Auger electron spectroscopy (AES), and time-of-flight secondary ion mass spectrometry (TOF-SIMS) to study the surface composition and morphology after ozone exposure.[33] Results showed that ozone oxidation of the vinyl-terminated SAMs created surface organic aggregates. While no accurate determination has been made, the group hypothesizes the aggregates may be composed of organic polymers. The possibility of small organic oxidation products nucleating and growing into the aggregates is also mentioned; however, the idea is not as seriously considered. A nucleation mechanism would be expected to create spherical "droplets" on the surface of the substrate, rather than the porous material observed by the researchers. Figure 1.12 shows the possible reactions pathways which may lead to the formation of the surface aggregates. It is well known that the decomposition of the Criegee Intermediate can produce OH radicals[34], which may commence polymerization. McIntire *et al.* assert the data gives evidence for an unrecognized mechanism for the oxidation of alkene SAMs on silica surfaces.[33] They also state that the presence of water could possibly increase the formation of aggregates, but upon experiment the opposite effect was observed. Other work has promoted the idea that ozone oxidation may convert a hydrophobic coating to a hydrophilic

one,[35] but McIntire *et al.* find no difference in water uptake before and after the ozone oxidation of both the C3 and the C8 vinyl-terminated SAMs.[33] The study is important because it reveals a new pathway for the behavior of organics in the atmosphere. The data suggests that vinyl-terminated SAMs may be readily oxidized in environments where even trace amounts of ozone are present.

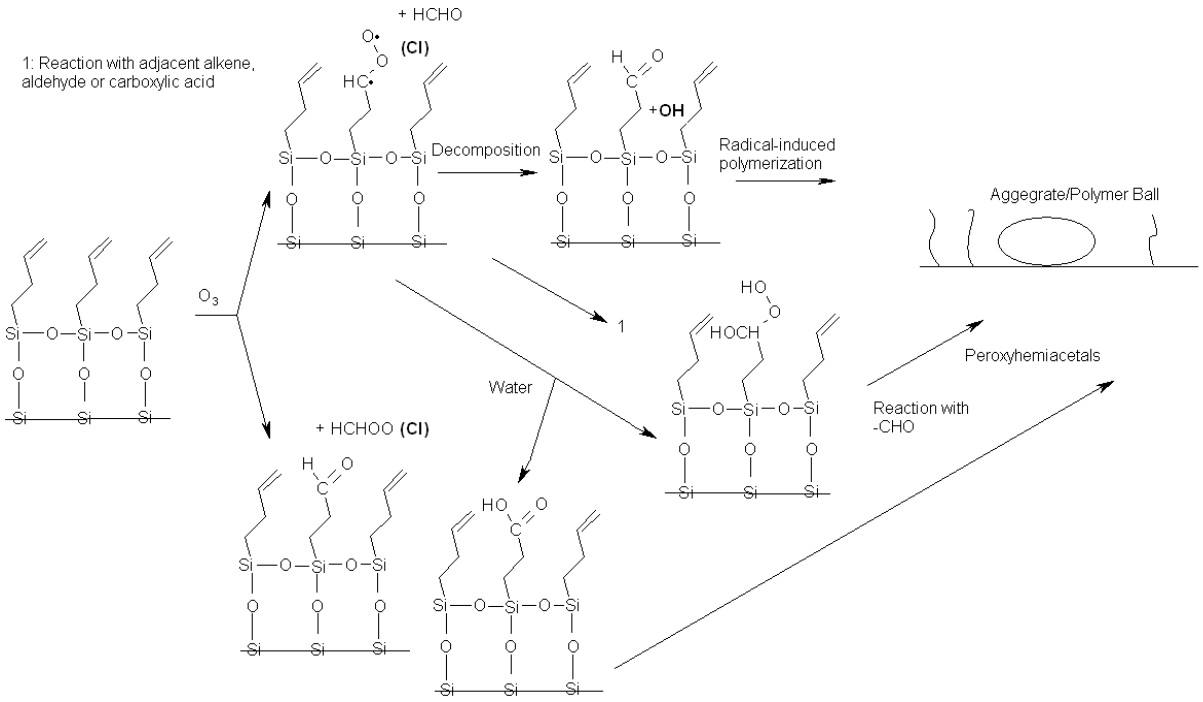

Figure 1.12: Overall scheme for ozone oxidation of unsaturated SAMs on a silica surface. For simplicity, the excited and stabilized Criegee intermediates (CI) have not been shown separately.[33] Reproduced by permission of the PCCP Owner Societies. http://pubs.rsc.org/en/content/articlelanding/2005/cp/b508147e

1.2 Reactivity of Ozone with C_{60}

Current literature indicates that organic material with even one unsaturated site is readily oxidized by ozone. C_{60} has essentially 30 unsaturated sites and therefore, is expected to be at least as reactive towards this important pollutant.

1.2.1 Reactions of Ozone with C_{60} in Solution

The most significant amount of research on the ozonolysis of C_{60} has been performed in the solution phase. While C_{60} is not soluble in aqueous solutions, without forming nC_{60}, a large aggregate of C_{60} molecules, it is readily soluble in many non-polar solvent such as toluene, carbon disulfide, and methylene chloride. In 2000, a study was performed by Heymann *et al*. on the ozonolysis of C_{60} in toluene solutions. The C_{60}/toluene solutions were mildly ozonated by bubbling a mixture of O_2/O_3 through them. After ozonation, the samples were run through an HPLC with a cooled column to slow down the reaction, in hopes of observing any intermediates.[36] Ozone is hypothesized to react with C_{60} in much the same way it reacts with other alkenes, i.e. through the formation of the primary ozonide.[36] In this study, Heymann reported the detection and isolation

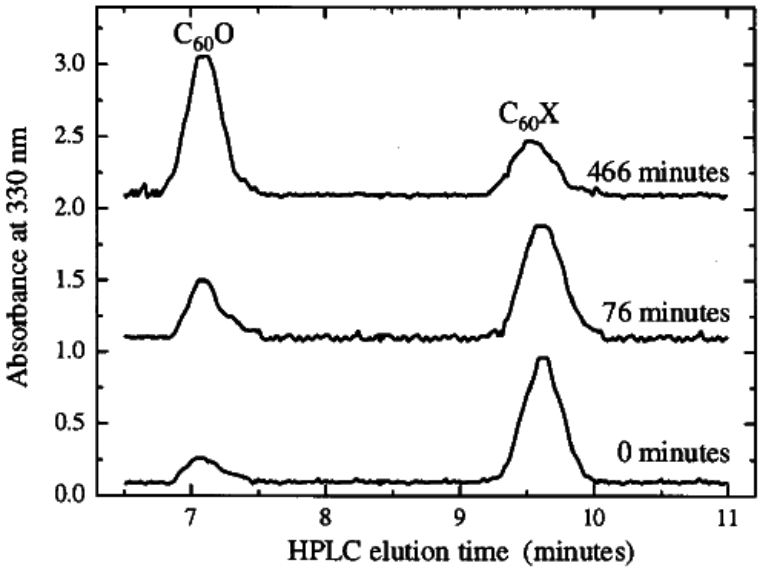

Figure 1.13: HPLC chromatograms of three samples taken from an ozonated C_{60}/toluene solution. The times indicated on the chromatograms are the amount of time the solution had been exposed to ozone.[36] Reprinted with permission from Heymann *et al. Journal of the American Chemical Society* 2000, *122(46)*, 11473-11479. Copyright 2000 American Chemical Society.

of an unstable intermediate resulting from the exposure of ozone to C_{60} solutions. In Figure 1.13, Heymann has shown three separate samples taken from an ozonated C_{60}/toluene solution. The solution was held at a temperature of 0.4°C while being exposed to ozone. Figure 1.13 indicates the amount of time each sample solution was exposed to ozone. At 0 minutes of ozone exposure, the peak denoted $C_{60}X$ is significantly larger than the peak for the epoxide product, $C_{60}O$. However, as time progresses it is obvious that the $C_{60}X$ peak represents an intermediate species, one that is converting to the epoxide product. The authors also report the production of molecular oxygen during the reaction. The $C_{60}X$ species is assigned to the primary ozonide of C_{60}, $C_{60}O_3$. Figure 1.14 shows the proposed mechanism for the oxygenation of fullerenes, where O_3 adds across a 6/6 bond forming a five-membered ring which includes two of C_{60}'s carbon atoms in this unstable intermediate. The ring quickly decomposes to the epoxide and releases O_2. This study provides the first evidence for support of the theory that ozone should react with fullerenes in the same manner as with alkenes. Another study carried out by Cataldo and Heymann that same year, focuses on the extensive oxidation of C_{60} and C_{70} solutions upon exposure to ozone. The fullerenes were dissolved in toluene and methylene chloride, and then exposed to an ozonized stream of oxygen (~ 1% ozone by weight).[11f] The researchers utilized FT-IR

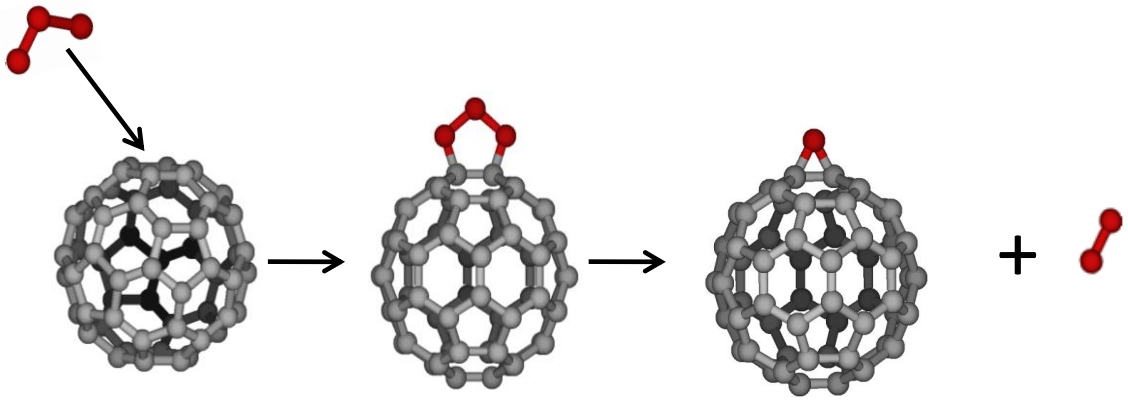

Figure 1.14: Proposed mechanism for the initial reaction of O_3 and C_{60}.

spectroscopy in this study to observe the frequency changes associated with ozonolysis. Figure 1.15 shows transmittance spectra from three separate C_{60} solution samples. It is important to point out several peaks present in spectrum A, that spectrum being most closely comparable to data presented later in Chapter 4 of this document. Extensive oxidation of the fullerenes in solution is evidenced by the carbonyl region in spectrum A. The peaks at 1740 and 1780 cm^{-1} are representative of, not only carbonyl functional groups but, anhydride groups -C(=O)-O-C(=O)-.[11f] Cataldo also states that the strong bands at 1200 and 1090 cm^{-1} can be assigned to ether groups and ozonide species. It is important to note that Cataldo and Heymann do not provide justification for their assignment of the peak at 1090 cm^{-1} to the primary ozonide of C_{60}. They go on to discuss the formation of an "ozopolymer" after extensive exposure to ozone. The ozopolymer supposedly forms as a result of rearrangement constraints of the cage molecule. In a typical ozonolysis experiment, once the primary ozonide decomposes to the Criegee intermediate and a carbonyl species, these two can recombine to form the secondary ozonide, see Figure 1.16. However, for a

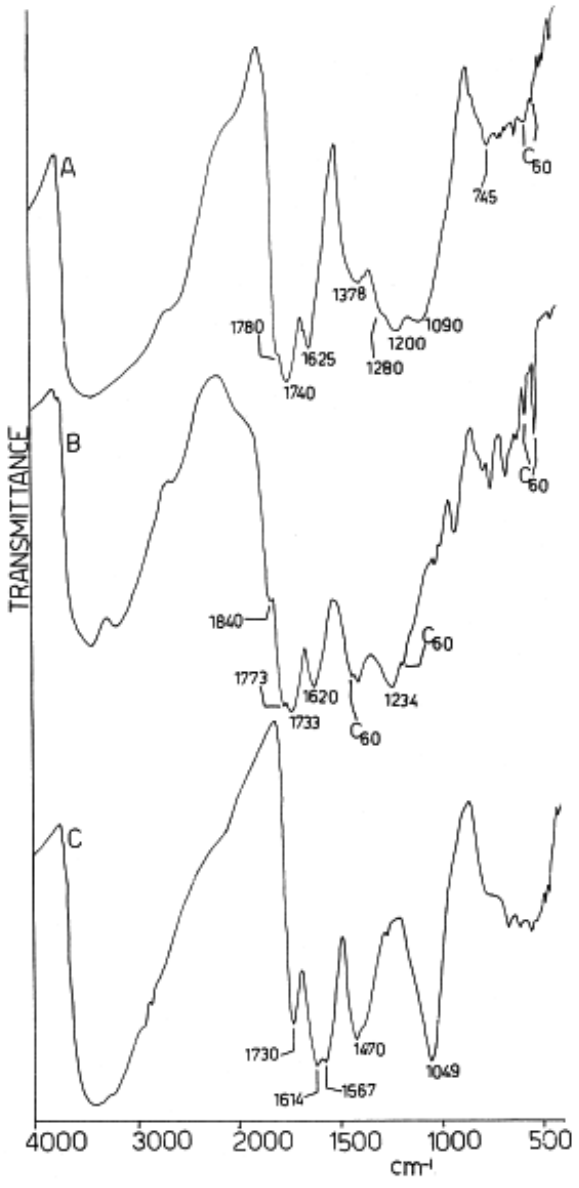

Figure 1.15: FT-IR spectra of ozonated C_{60} solutions. (A) C_{60} ozopolymer formed from the ozonolysis of a C_{60}/CH_2Cl_2 solution. (B) C_{60} ozopolymer heated to 300°C under N_2. (C) C_{60} ozopolymer treated with aqueous KI solution.[11f] Reprinted from *Polymer Degradation and Stability, 70(2)*, 237-243, Copyright 2000, with permission from Elsevier.

secondary ozonide to be formed on the fullerene cage, one oxygen atom must be incorporated into the actual cage structure.[11f] During the initial stages of ozonolysis, a C_{60} secondary ozonide would cause excessive strain on the cage, and therefore its formation is extremely unlikely. However, as the fullerenes undergo extensive oxidation, ozone creates holes in the molecules and breaks down the closed cage structure. It is possible that secondary ozonides can form among the ruptured sections of the fullerenes; which most likely flatten out, resembling a corannulene or graphite-like structure. An alternative to the formation of the secondary ozonide, is the possibly of the Criegee intermediate reacting with another 6/6 bond on a neighboring fullerene cage. This pathway, shown below in Figure 1.16, suggests the formation of intermolecular anhydride linkages, as well as potential formation of intermolecular secondary ozonides.

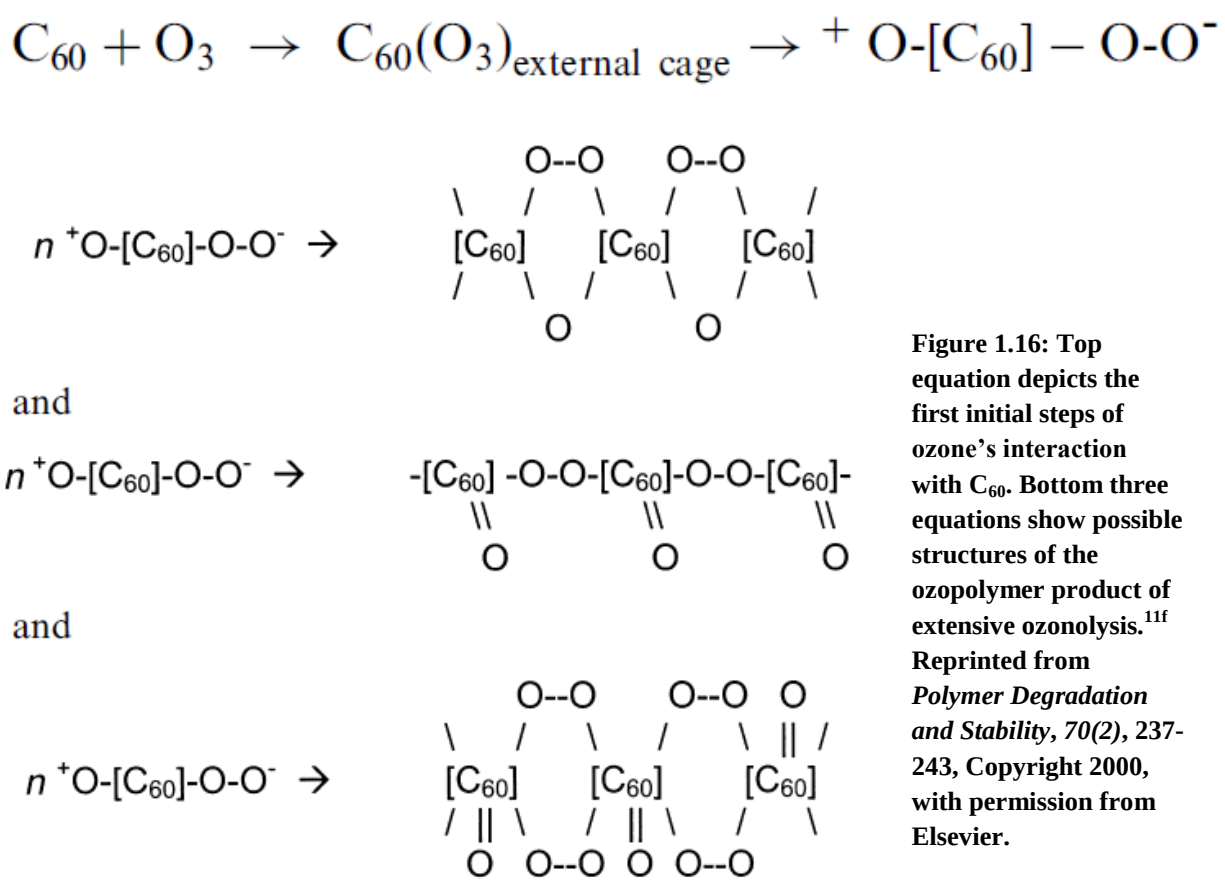

Figure 1.16: Top equation depicts the first initial steps of ozone's interaction with C_{60}. Bottom three equations show possible structures of the ozopolymer product of extensive ozonolysis.[11f] Reprinted from *Polymer Degradation and Stability, 70(2),* 237-243, Copyright 2000, with permission from Elsevier.

Intermolecular bonding may lead to the formation of the species Cataldo and Heymann have labeled the ozopolymer, as shown in Figure 1.16. Two years later, Cataldo released another publication discussing the ozonolysis of C_{60} in CCl_4. Using FT-IR spectroscopy again; he reports the presence of IR peaks similar to those seen in the previous study.[11a] There is still no explanation for why specific peaks are assigned to the ozonide species. The ozopolymer is also observed in a CCl_4 solution, showing that the formation of this oxidation product is independent of the solvent used.

1.2.2 Reactions of Ozone with C_{60} in the Solid Phase

The exposure of ozone to solid C_{60} is the most comparable data to the research presented later in this document. However, there is very little ozonolysis work on these types of samples. In 2007, Cataldo produced a paper on the reaction between solid C_{60} and C_{70} with ozone. The results were very similar to what he observed in the solution phase. Large peaks in the carbonyl region supported the formation of carbonyl species and anhydride linkages.[11c, d] Cataldo also reports kinetic values for the ozonolysis of solid C_{60}. He determined that the reaction follows pseudo first order kinetics with $k_{C60} = 2.0 \times 10^{-4}$ s^{-1} and reported a value for the activation energy of 84.9 kJ/mol for the decomposition of the primary ozonide of C_{60}. Cataldo also noticed that after ~1000 s the reaction slows down. He theorizes that this slowing down of the reaction is most likely due to a decrease in available reaction sites.[11c, d] Based on his experiment, the ozone only reacted with the molecules on the outer surface, and once all of the available sites have been consumed by ozone, the rest of the sample was unavailable for further oxidation.

1.2.3 Computational Studies of Reactions of Ozone with C_{60}

The use of computational studies to support experimental data is an invaluable tool for chemists and many other researchers. A handful of computational studies have been carried out

on the reaction of C_{60} with ozone. Later, calculations performed in the course of these studies will be presented in support of the experimental research. Probably one of the very first theoretical studies of C_{60} and O_3 was done in 2000, by a group at Nankai University in China. The group, led by Xuezhuang Zhao, used semiempirical molecular orbital calculations to determine the most likely approach and bonding position of O_3 on the C_{60} cage. They wanted to develop theoretical support for the assumption that ozone would attack the 6/6 bonds on the fullerene molecule.[37] Using the Austin Model 1 (AM1) method these researchers were able to show that the 6/6 adduct is thermodynamically preferred over the 6/5 adduct. Their work also demonstrated that the 6/6 adduct was also favored kinetically.[37] The results included a calculation of the activation energy (84.1 kJ/mol) for the addition of ozone to the fullerene cage, as well. Figure 1.17 shows the mechanism they developed based on their computational results.[37] The mechanism not only has ozone adding across a double bond (6/6 bond) to form the five-membered primary ozonide (PO) ring, but also shows the PO decomposing into the Criegee intermediate and a carbonyl species. From there the Criegee intermediate can rearrange in two ways, either forming the epoxide product ($C_{60}O$), or a diketone species. Zhao's results also support pathway 1 (P1) as the more favorable route, concluding that the epoxide product is the most likely outcome. In more recent years (2008), density functional theory (DFT) studies have been performed on the ozone/C_{60} system. Sabirov *et al.* approached

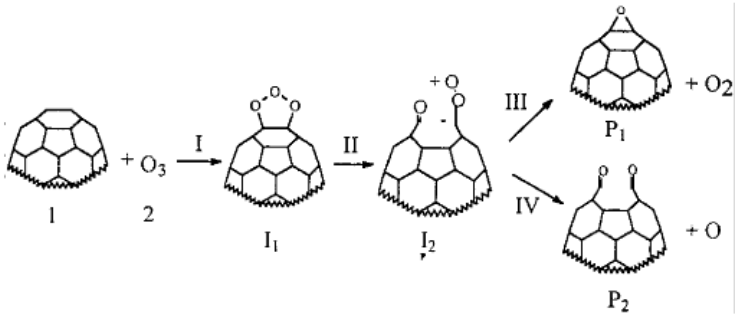

Figure 1.17: The mechanism for the initial reaction of ozone and C_{60}.[37] Reprinted with permission from Shang *et al. JPC A* 2000, *104(9)*, 1915-1919. Copyright 2000 American Chemical Society.

this problem with DFT (a method that is more efficient at describing polar molecules and products of their addition) and reported similar findings to Zhao.[38]

The literature reviewed above has led researchers studying fullerenes to the conclusion that ozone reacts with C_{60} via ozone addition across one of the 6/6 bonds. Experimental results supported by prediction from computational methods indicate that the most likely product of this reaction is the epoxide species, $C_{60}O$. Investigations of extensive ozone exposure have detected the presence of a product labeled as an "ozopolymer". The ozopolymer is found to be soluble in water and methanol, solvents in which fullerenes do not dissolve. Preliminary kinetics have been recorded for solution phase and solid phase studies. Until this time, there have not been any reports on the reaction of gas-phase ozone and surface-bound C_{60}. Presented herein is the most detailed picture available of the mechanism for the C_{60}/O_3 reaction at the gas-surface interface, as well as preliminary kinetics.

1.3 Ultra High Vacuum Experiments

The research presented in the remainder of this document was performed in order to achieve the following goals:

1. Determine a mechanism for the oxidation of C_{60} – the most common fullerene.
2. Create a kinetic model for the oxidation of C_{60}.
3. Determine the effect of fullerene structure (i.e. cage size) on the oxidation.

The current research has been able to determine that ozone readily oxidizes C_{60}. It is known that ozone adds across the 6/6 bonds of the fullerene cage to form the primary ozonide. The most likely product of the decomposition of the primary ozonide is $C_{60}O$, an epoxide species. While some of the literature does report the observance of peaks due to the primary ozonide,[11a, 11d, 11f]

there is not conclusive evidence of its existence, or that of the Criegee Intermediate of C_{60}. With the experimental approach described in Chapter 2, these studies have the potential to, not only enable observation of the primary ozonide, but also its decomposition, as well as the formation of the Criegee Intermediate. Another advantage of these experiments is the isolation of these two molecules from any other reactants. By using an ultra-high vacuum (UHV) chamber, with base pressures in the 10^{-9} Torr range, there is confidence that the only species involved in the reactions are surface-bound fullerenes and gas-phase ozone. Since the chamber is equipped with a reflection-absorption infrared spectrometer (RAIRS), the entire reaction process can be watched in real time. The mass spectrometer can be used to detect gas-phase products and perform temperature-programmed desorption (TPD) analyses. The x-ray photoelectron spectrometer (XPS) provides the capability of performing elemental analyses on samples before and after ozone exposure. Finally, since the manipulator is fitted with a button heater and a liquid nitrogen reservoir, kinetic studies can be undertaken to determine activation energies for the species involved in the reaction. This setup will allow for the development of a mechanistic picture of this reaction system in addition to kinetics of the gas-surface interface reaction. This information will help create models and advance understanding of the way fullerenes interact with molecules in the environment.

1.4 Summary

The chemistry of carbonaceous nanomaterials is an important field of study as these materials are continuously utilized in new ways. In order to understand the consequences of the increased presence of these molecules in the environment, studies must be performed to determine their products, mechanisms of reaction, and kinetics.

This research focused on the reaction of a particular type of carbonaceous nanomaterial, fullerenes, with an important atmospheric pollutant, ozone. The fullerenes C_{60}, C_{70}, C_{76}, C_{78}, and C_{84} were deposited on an Au surface and exposed to gas-phase ozone. To focus strictly on the ozone oxidation of fullerenes, the sample were prepared and oxidized in an UHV chamber, eliminating any reactions due to other atmospheric species. Terbium endohedrals (a Tb atom inside a C_{84} cage) were also exposed to ozone. The hypothesis was ozone would rupture the cage via oxidation, expose the internal Tb, oxidize the Tb, and finally release the oxidized lanthanide in the gas-phase. All experiments were monitored with RAIRS, XPS, and MS to fully characterize the sample and reaction.

Chapter 2

Instrumental Modifications and Experimental Approach

2.1 Vacuum Considerations

The goal of this research was to develop a fundamental understanding of the gas-surface reaction between fullerenes and ozone. In order to achieve this goal, the study monitored the reaction of only these two specific species. The approach to this problem was to work in an ultra-high vacuum (UHV) environment. The UHV setup allowed the sample surface to be studied with minimal exposure to unwanted adsorbates. In other words, once the fullerene surface was formed and placed in the vacuum chamber, it experienced negligible recontamination. The degree of vacuum reached by the UHV chamber increases the amount of time the surface remains clean. For example, if the goal is to observe a reaction at atmospheric pressure, assuming a sticking probability of one (S=1), the surface would only remain clean for ~ 10^{-9} s, before it is covered with a monolayer of atmospheric gases. At pressures in the 10^{-3} Torr range, pressures typically achieved using a mechanical pump; a monolayer of coverage would be obtained after 10^{-3} s. A pressure of 10^{-6} Torr allows one second before monolayer formation is complete, and finally at UHV pressures (~10^{-10} Torr) the experimenter has 10^{4} s (or ~3 hrs) before a full monolayer sticks to the surface. It is obvious that the lower the pressure, the longer the sample will stay clean, helping to ensure that the only species reacting with the gas of interest are those present on the surface.

The pressures that characterize UHV are typically 10^{-9} Torr and below. At pressures within this range, the mean free path (MFP) of a molecule, defined as the average distance a molecule travels between collisions with other molecules, is maximized. To help extend the

MFP, UHV chambers should contain minimal amounts of water and other trace gases, providing the cleanest environment possible for fundamental studies.

Finally, the last important aspect of the UHV chamber is the analysis techniques that can be employed. Systems such as reflection-absorption infrared spectroscopy (RAIRS), x-ray photoelectron spectroscopy (XPS), and mass spectrometry (MS) are best operated in a vacuum environment and were essential to these unique studies.

The ultra-high vacuum chamber utilized in these experiments was designed and built by my predecessor.[1] The chamber was created with the objective of performing in depth studies at the gas-surface interface. This experimental setup allows for extensive surface characterization, precision dosing, and *in situ* monitoring of reactions.[39]

2.2 Experimental Approach

The following section describes the experimental procedure from start to finish in full detail. To perform an ozone exposure of fullerene films deposited in vacuum, the first task required is preparation of gas-phase ozone.

2.2.1 Ozone Generation, Purification, and Storage

Warning: Ozone is a VERY TOXIC, DANGEROUSLY REACTIVE, OXIDIZING gas![40]

Special precautions should be made when working with this chemical!

The generation of ozone ($[O_3]_g$ > 75%) for this project was achieved by using a commercial ozone generator (Ozone Solutions, model: SR-32). The generator uses a corona discharge and produces ~2.0% ozone from a 10 L/min flow of research grade oxygen (Airgas Specialty Gases).

In order to work with high concentrations of ozone on a regular basis, the ability to create and store large quantities for extended periods of time was required. Ozone has a very short lifetime at room temperature, and as a result, the production and storage were carried out at temperatures well below 25°C. At a temperature of -112°C, ozone becomes a dark blue liquid, and at -193°C a violet-black solid is formed.[40] In all three phases, (solid, liquid and gas) ozone is capable of detonation. In order to improve the stability of the produced ozone, a trapping and storage method that utilized high surface area silica gel (Sigma-Aldrich, grade 03, >8 mesh) was implemented.[41] The silica gel was placed inside a custom-made, all-glass trap, as illustrated in Figure 2.1.[39] The silica gel was sandwiched between two coarse sintered-glass frits,[42] shown in Figure 2.1 as gray disks. The frits were necessary during pressurization of the apparatus, or experiments requiring large amounts of gas flow as they prevented the silica gel from leaving the trap and migrating/blocking narrow parts of the apparatus. The entire ozone apparatus was comprised of either glass or Teflon tubing. Only these two materials were utilized because of ozone's catalytic decomposition on metal surfaces. A full depiction of the ozone apparatus, which was designed and built by L.R. Fiegland, is shown in figure 2.2.[39]

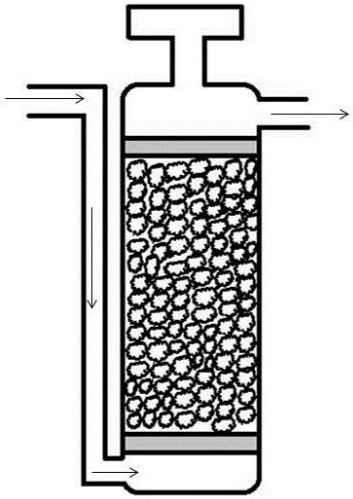

Figure 2.1: Drawing of the custom, all-glass ozone trap.

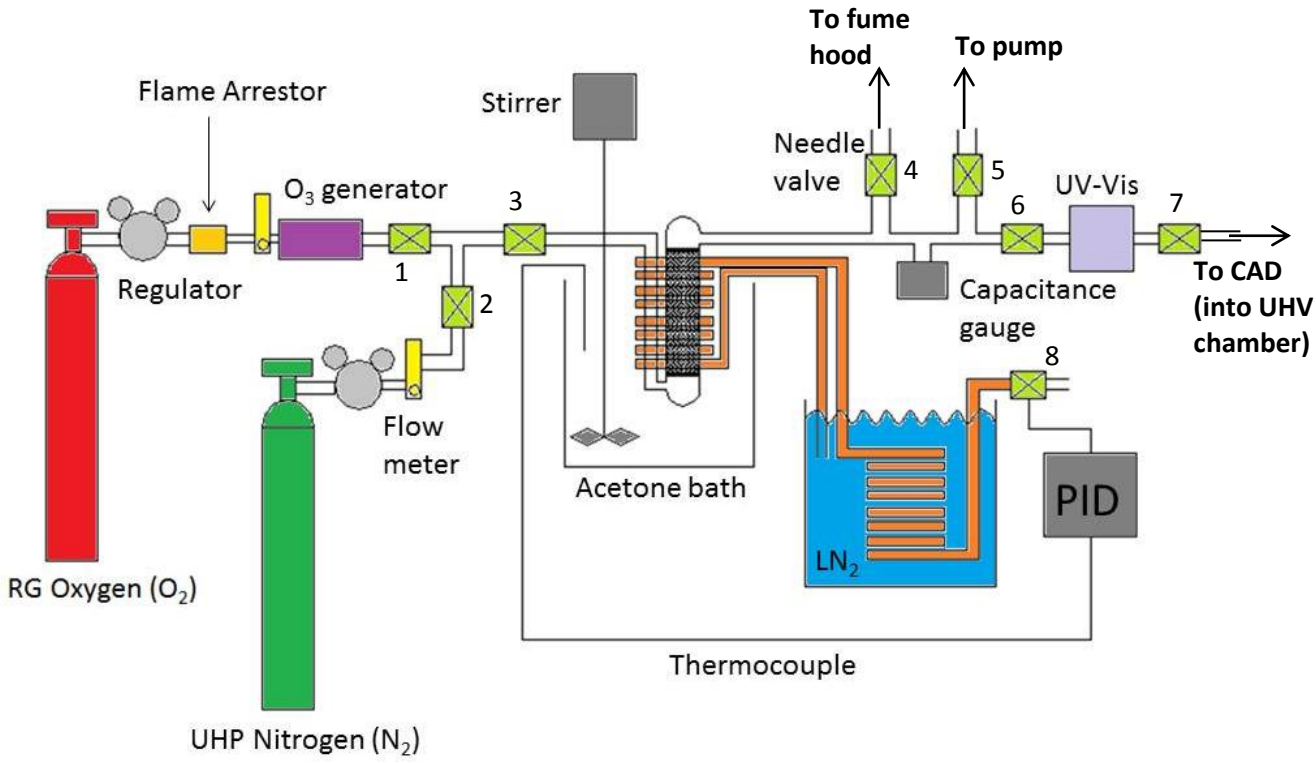

Figure 2.2: A schematic of the ozone trapping and storage apparatus. Objects with the same coloring are identical, unless otherwise noted. Reproduced from the dissertation of L. R. Fiegland.[39]

An important component of the system was the specific type of valve used. Swagelok® stainless steel Bellows-Sealed Valves (model: SS-4H) were employed at all junctions within the apparatus. The advantage of the bellows-sealed valves (also referred to as needle valves) was the lack of a sealing o-ring, which was advantageous because ozone is highly reactive, especially with materials such as rubber. In the past, ¼ turn valves from Swagelok® were used; valves that contain rubber o-rings. After minimal exposure to high concentrations of ozone the valves were extremely difficult to open and close; an undesirable condition when working with explosive chemicals.

The procedure for trapping ozone is as follows: First, the entire apparatus was evacuated to pressures below 2 Torr, using a mechanical pump (opening valve 5 and closing valves 1, 2, 4, and 6). With the system open to the pump, the trap was baked out overnight (at ~150°C) to remove any water and other contaminants from the silica gel. After bake out, the apparatus was

pressurized to ~700 Torr using UHP N_2, by closing valve 5 and opening valve 2. After pressurization to ~700 Torr, valve 4 was opened to vent the system to the fume hood. The system was pressurized to values close to atmosphere before opening valve 4 to ensure there was no backstreaming and therefore preventing any recontamination of the silica gel. The pressure of the apparatus was monitored using a compact capacitance gauge (Pfeiffer Vacuum, Inc., model: CMR 261). The capacitance gauge was utilized because it accurately reports pressures from ~1000 Torr to values in the 10^{-3} Torr range.

Next, the ozone trap was inserted into a coil of copper tubing, and then a Dewar was placed around the ozone trap and coils. At this point, it was imperative that the Dewar surrounding the ozone trap was filled with enough dry ice and acetone to maintain a constant temperature of -80°C. The temperature of the bath was monitored with a K-type thermocouple. The copper coils surrounding the trap were connected to a solenoid valve from ASCO Valve, Inc. (model: 8210LT). Both the solenoid valve and the thermocouple were wired to a proportional-integral-derivative (PID) controller (Omega Engineering, model: CN-2041). Once a positive flow of N_2 was achieved through the system into the fume hood, and the ozone trap temperature was at -80°C, oxygen was flowed through the system by opening valve 1, and the nitrogen was closed (closed valve 2). The final step was to turn on the ozone generator. Depending upon the desired amount of ozone, trapping was performed for as little as 1 hour, or as long as 12 hours.

Once trapping was complete and the ozone was needed, the newly trapped gas was purified and warmed up. The first step in purifying the ozone was to shut off the generator and start flowing UHP N_2 through the system, by opening valve 2. As soon as the N_2 flow was started, the oxygen tank was closed (closed valve 1). UHP N_2 was flowed through the system for

10 minutes to remove any atomic or molecular oxygen that lingered in the trap. After flushing the system with N_2, the valves to the fume hood (valve 4) and the nitrogen tank (valve 2) were closed, and the valve to the mechanical pump was opened (valve 5).

It is important to mention that while mechanical pumps were utilized in these ozone experiments, every precaution was taken to prevent any interaction between the ozone gas and the oil of the mechanical pump, a potentially explosive combination. First, the mechanical pumps were filled with Fomblin® oil. Fomblin® oil is inert vacuum pump oil specially designed for use in high oxygen or corrosive environments. Second, a foreline trap was placed on the mechanical pump. A foreline trap helps prevent oil vapor from backstreaming along the foreline. The insert in the foreline trap was a copper wool filter, which was very advantageous as ozone is known to readily break down on copper surfaces. Therefore, any ozone that might have made it to the foreline trap was likely broken down before it entered the pump. The final and most important precaution for pumping large quantities of high concentrations of ozone was to place a liquid nitrogen trap in-line before the mechanical pump. A liquid nitrogen trap is used to trap volatile materials, preventing them from entering the mechanical pump, and it can also trap oil vapors from the pump to prevent them from entering a chamber. The liquid nitrogen trap, in this system, was where the majority of the ozone was first trapped, to be pumped away in a more controlled manner. With all of the precautions in mind, the mechanical pump may be used to evacuate the headspace of the apparatus after trapping.

Once the ozone apparatus was flushed with nitrogen and pumped out with the mechanical pump, the ozone was warmed to start desorbing it from the silica gel. To warm up the ozone, the dry ice was removed from the Dewar; this required removing the entire Dewar from the ozone trap. *THIS IS THE MOST DANGEROUS STEP IN THE ENTIRE PROCEDURE!* When the

Dewar was removed from the trap the source of stabilization for the trap was gone and if the trap warmed up too much the ozone could have spontaneously detonated. To prevent detonation, a PID controller was used. The PID controller, in this instance, was used to control the temperature of the trap. A set point was entered in the controller (here the set point was -55°C) and if the temperature measured by the thermocouple read warmer than the set point, the PID would open the solenoid valve (valve 8) and flow nitrogen through the copper coils. The copper tubing possesses two sections of coils, the first set rests inside a large metal container filled with liquid nitrogen, and the second were wrapped around the ozone trap. After valve 8 opens, the nitrogen gas flows through the liquid nitrogen cooled coils then around the trap coils. As long as the PID measured a temperature above the set point the solenoid valve (valve 8), the valve stayed open; liquid nitrogen cooled $N_2(g)$ was constantly flowed around the trap, until the temperature was $\leq$ the set point. Once the set point temperature was reached the solenoid valve closed, cutting off the flow of nitrogen. With the use of the PID controller and the liquid nitrogen cooling system, the Dewar was safely removed and the dry ice discarded.

After the dry ice was removed from the acetone bath, the Dewar was replaced around the ozone trap and filled with room temperature acetone. Before the room temperature acetone was added, a stirrer inside the Dewar was turned on to help quickly equilibrate the bath temperature. The room temperature acetone raised the overall temperature of the trap to -55°C, the temperature at which ozone desorbs from silica gel. The system was continuously pumped on while the trap was filled with acetone, but as soon as the set point temperature was reached, the valve 5 was closed to isolate the mechanical pump. This last step ensured a minimal amount of ozone was removed from the trapped volume. Acetone was added until the solvent level reached the height of the silica gel inside the trap. By carefully controlling the temperature of the trap, the

experimenter can vary flux of ozone into the chamber. When the trap was full of acetone and an equilibrium temperature of -55°C was reached, the ozone was ready to be introduced into the chamber.

2.2.2 Sample Preparation

All fullerene films were deposited onto polycrystalline Au slides. The slides, purchased from EMF Corportion, were 1" x 1" x 0.062", with a glass substrate, a Chromium adhesion layer, and a coating of 1000Å of gold. To prepare the slides for vacuum introduction, they were cleaned in Piranha solution (70% concentrated sulfuric acid, 30% hydrogen peroxide (30%)) for 45 minutes to remove adsorbed organics from the surface. After the slide was removed from the Piranha solution, it was rinsed thoroughly with deionized water and then dried completely with UHP N_2. Once dry, the sample was placed on the sample holder, see Figure 2.3. The sample is attached to the sample holder with two screw mounted tabs. The tabs can be tightened to secure the sample in place for transfer and experimentation. After the sample is placed onto the sample holder, it is attached to the transfer arm, via the transfer key, inside the load lock. Before the load lock is

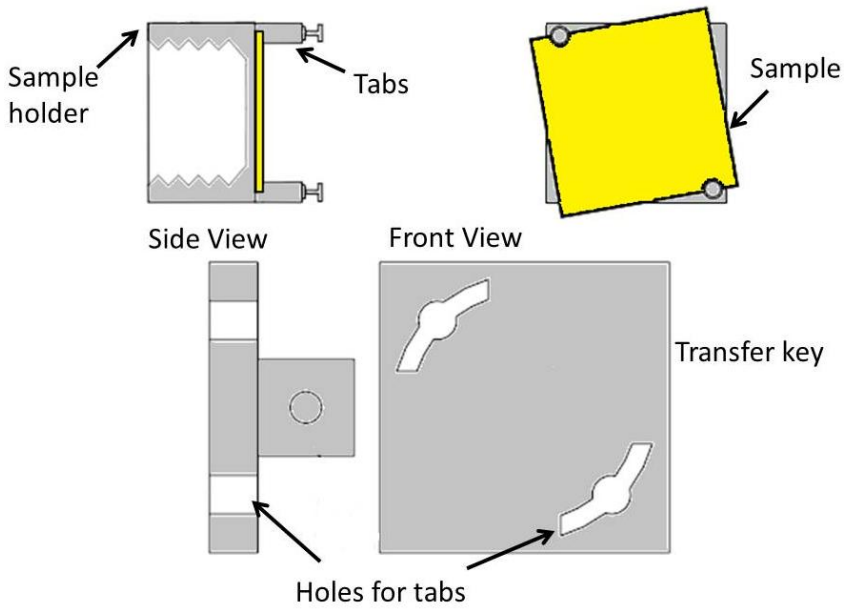

Figure 2.3: A drawing of the sample holder. The image on the top left is a side view of the sample holder and shows the screw tabs as well as the threads used to attach the sample holder to the sample mount on the manipulator. Modified from the dissertation of L. R. Fiegland.[39]

pumped back down for sample introduction, the crucible evaporator, used to deposited fullerenes in vacuum, is loaded with new fullerene powder.

The objective of this research is to study the fundamental reaction between gas-phase ozone and surface-bound fullerenes. In order to achieve this goal, the ability to deposit fullerenes in a vacuum environment was required. If films can be made in vacuum, the likelihood of contaminants on the surface significantly decreases. The instrument used to make the vapor-deposited fullerene films is a crucible style evaporator from McAllister Technical Services (model: EVAP-B). The crucible evaporator (CE), shown in Figure 2.4, is equipped with a water-cooled jacket and has attachments for a thermocouple and power supply. The CE mounts on a 2 ¾" conflat flange, allowing the instrument to be installed on an available flange on the load lock chamber. The crucible, itself, is made of 98% Al_2O_3, and is situated within the filament block, which can be easily removed to replace or change the evaporative material (www.mcallister.com). Therefore, before each experiment, more fullerene powder was added to the crucible to ensure an adequate film was deposited onto the surface for investigation.

Figure 2.4: Crucible Style Evaporator used for the high vacuum deposition of fullerene films.

Once the crucible was loaded, the load lock was evacuated for sample introduction. When the pressure was low enough ($\leq 3 \times 10^{-7}$ Torr), the Au slide was transferred immediately into the main chamber and attached to the sample mount on the end of the manipulator, see Figure 2.5. The sample mount has several capabilities; with a resistive heater nestled inside the

mount and a liquid nitrogen reservoir attached to the back, experiments can be performed over a wide range of temperatures. The temperature can be monitored during heating and cooling as well, with the thermocouple attached to the sample mount.

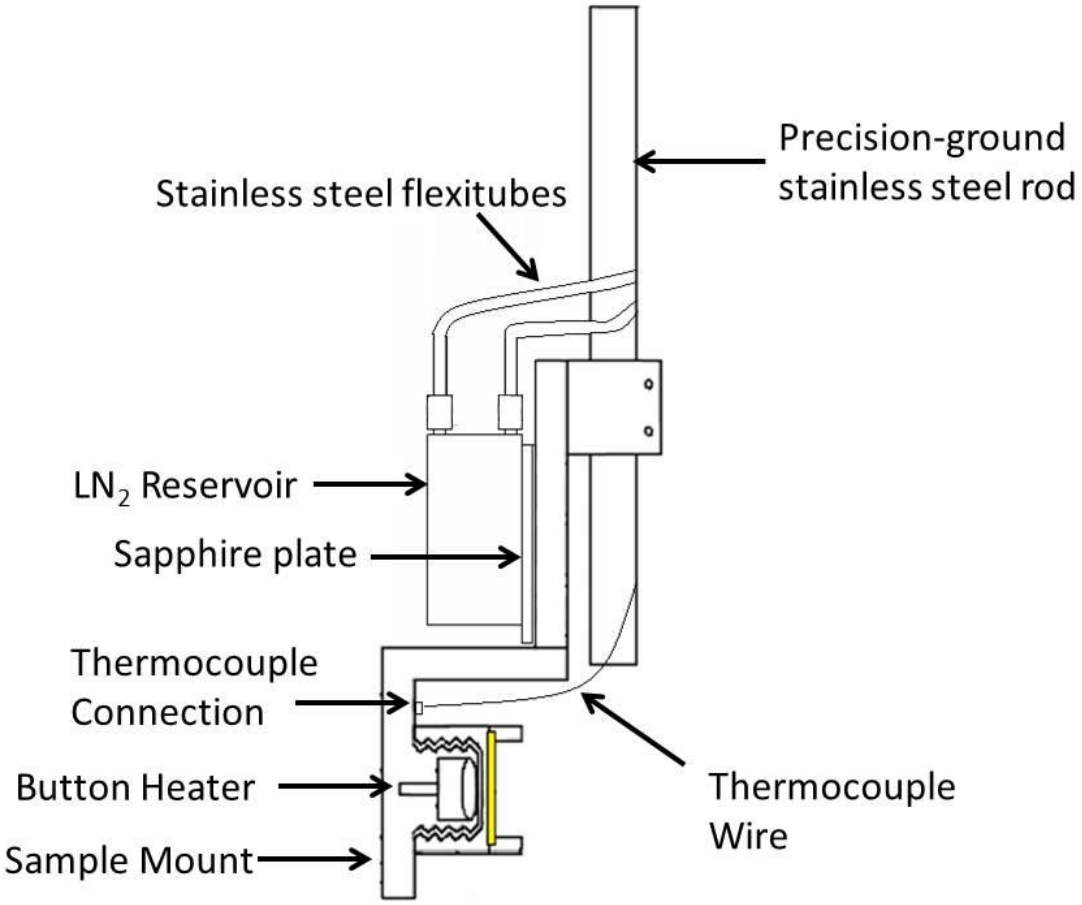

Figure 2.5: A drawing of the sample mount configuration. The sample mount is equipped with a button heater and a LN_2 reservoir. The heater and reservoir allow the sample temperature to be varied over a significant range (77 – 800 K). Modified from the dissertation of L. R. Fiegland.[39]

The sample was transferred immediately into the main chamber for additional cleaning with gas-phase ozone. Even though Piranha solution was used to clean the Au slide initially, any exposure to atmosphere resulted in the readsorption of contaminants, such as hydrocarbons. To further ensure a minimum amount of contaminants were present on the surface, ozone was used to clean the Au slide for an hour inside the main vacuum chamber. As soon as the ozone cleaning

was complete the surface was transferred back into the load lock to deposit the fullerene of choice.

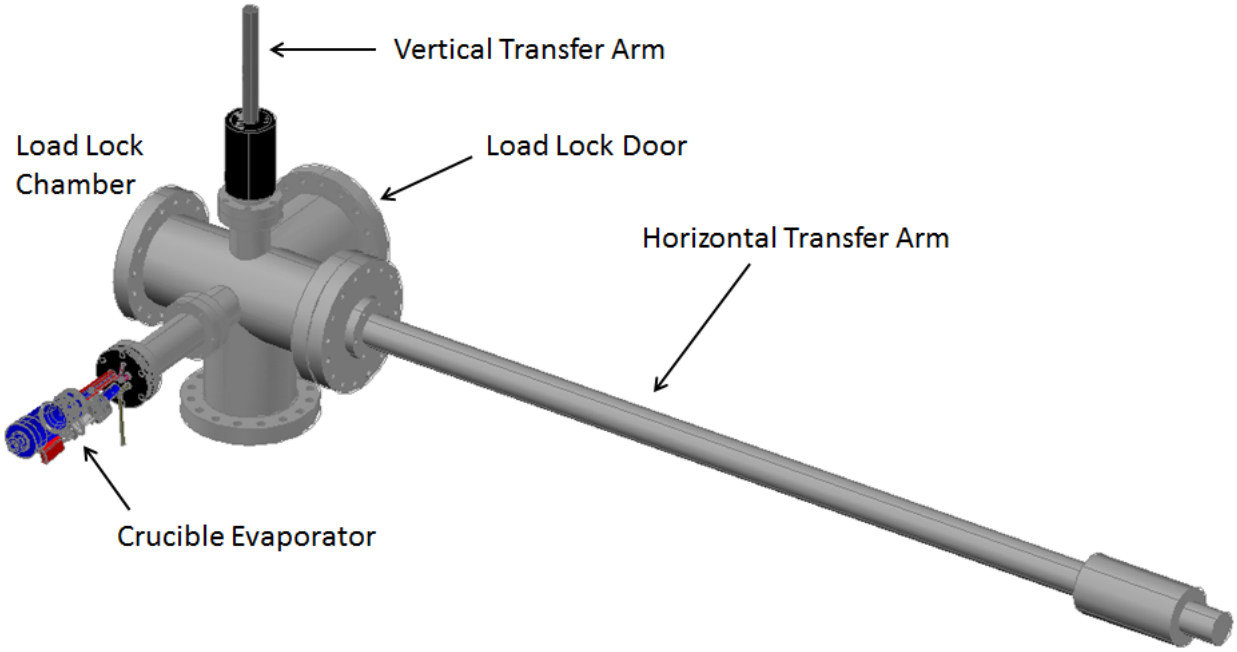

Figure 2.6: A drawing of the load lock/deposition chamber. The addition of the vertical transfer arm and the crucible evaporator allow for *in vacu* fullerene deposition.

The load lock doubled as the fullerene deposition chamber once the CE was attached. Another linear translator was installed on the load lock, this one at a 90° angle to the CE, see Figure 2.6. The inclusion of the second transfer arm allowed for fullerene samples to be made entirely in vacuum. Once the Au slide was returned to the load lock chamber, it was transferred from the horizontal transfer arm onto the vertical one. The vertical transfer arm is able to rotate 360°, so the slide was positioned directly in front of the CE. The power supply and water chiller attached to the CE were then turned on and the voltage and current were ramped over approximately 30-45 minutes. The specifics of the deposition (voltage, current, time, and temperature) vary depending upon the fullerene being deposited. C_{60}, for example, took ~35 minutes to deposit, with the maximum voltage and current being 4V and 4 Amps. When the

deposition was complete the sample was transferred back onto the horizontal transfer arm and then transferred into the main chamber for the exposure experiment.

2.2.3 Main Chamber and Analytical Instrumentation

The characterization and ozone exposures were performed in a 304L stainless steel ultra-high vacuum chamber. The main analysis chamber was a 23 L dome with numerous ports to accommodate the variety of instruments utilized in these studies. When the sample was introduced into the main chamber after deposition, it was, again, attached to the sample mount at the end of the manipulator, shown in Figure 2.5. The manipulator was bolted to the flange directly on top of the main chamber (McAllister Technical Services, model: MA1002). This component allowed for precise alignment of the sample in the x, y, and z planes, and was necessary for the rapid transfer of samples and accurate positioning for RAIRS, dosing

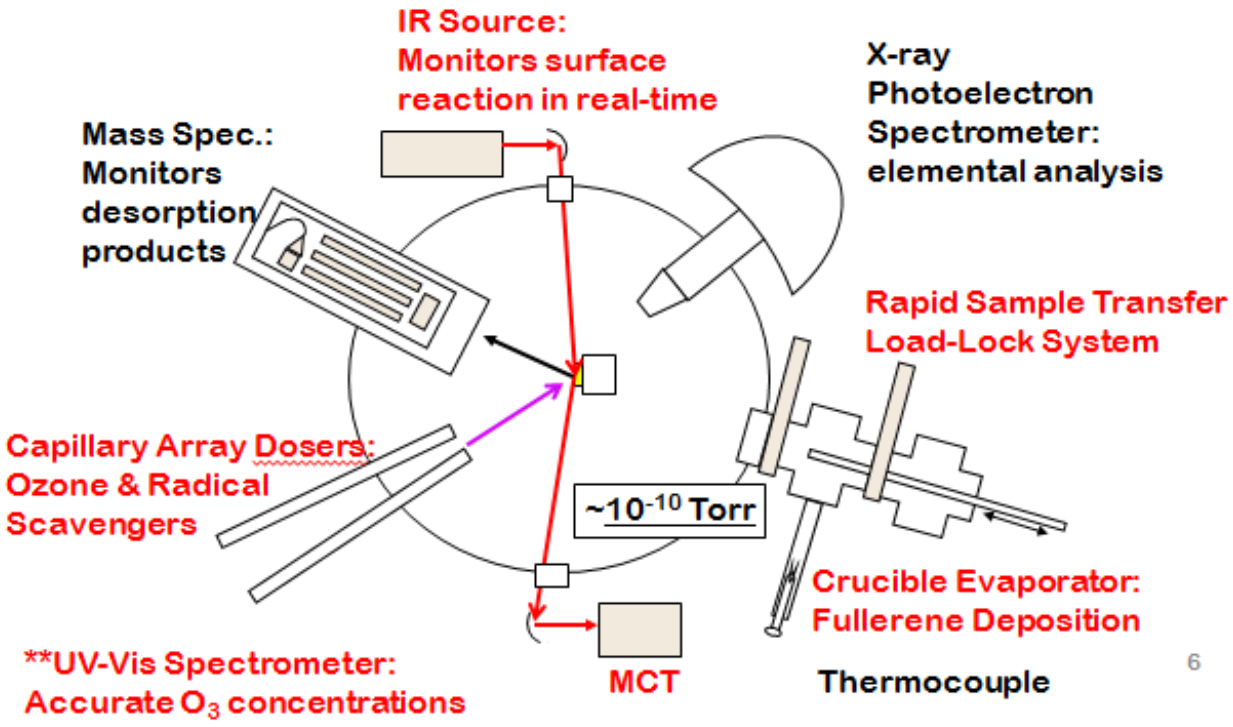

Figure 2.7: A basic schematic of the UHV chamber. Items highlighted in red were utilized in every experiment discussed in this document.

experiments, XPS, and MS.

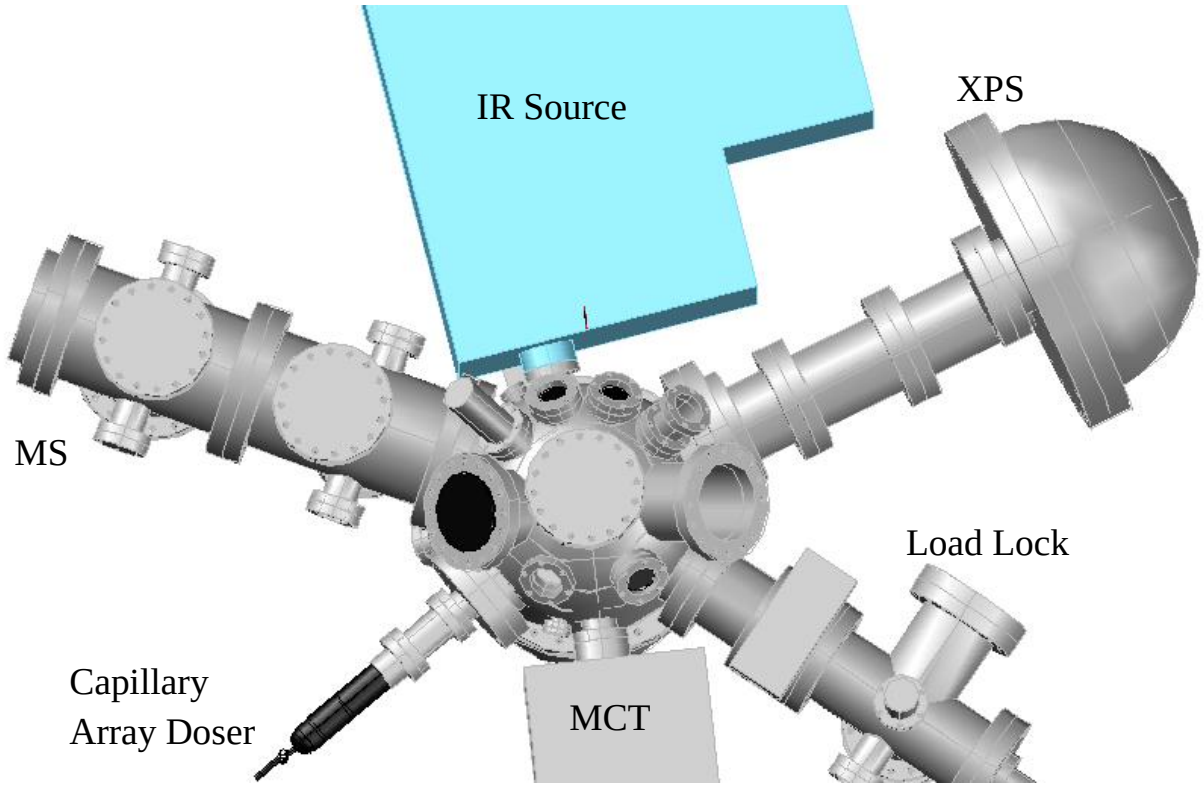

Figure 2.8: An AutoCAD drawing of the main components of the UHV chamber.

The schematic shown in Figure 2.7 highlights the components and instruments specific to these experiments; while Figure 2.8 shows an AutoCAD drawing depicting a more realistic image of the chamber. After the sample was attached to the sample mount, it was aligned for reflection-absorption infrared spectroscopy (RAIRS). RAIRS was the main technique of analysis used in these experiments. As a specialized type of infrared spectroscopy, specifically utilized to observe the chemistry of surfaces, it was ideal for the experiments performed in these studies. The technique is non-destructive, permitting further analysis of samples once the initial experiment was complete and also allowed sampling of the entire surface; from molecules laying exactly at the gas-surface interface to those in contact with the gold. RAIRS can be performed in

real-time, so the reaction can be monitored as it progresses. As with other forms of spectroscopy, every chemical functionality has a specific absorbance in the RAIR spectrum but, unlike traditional IR, RAIRS can also give information about the orientation and chemical environment of the molecules on the surface.[43] For all of these reasons, RAIRS was employed to develop a mechanistic and kinetic picture of the ozone oxidation of surface-bound fullerenes.

Reflection-absorption infrared spectroscopy has many similarities to traditional FT-IR spectroscopy. RAIRS utilizes a spectrometer equipped with a Michelson interferometer, allowing the experimenter to observe all the frequencies of the desired infrared region at one point in time.

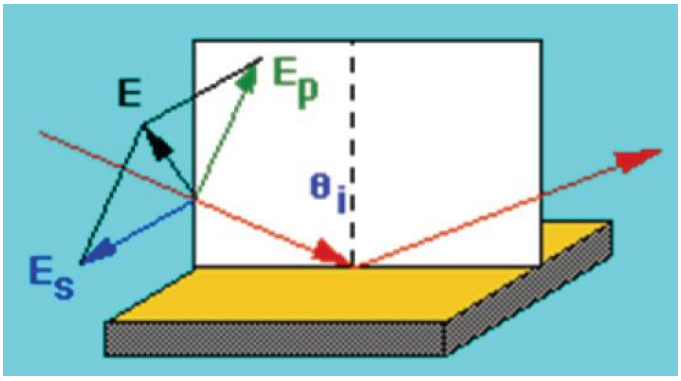

Figure 2.9: A schematic depicting the two components of the electric field of light: E_S and E_P.

The output of the interferometer is an interferogram, which is acquired in the time domain, then Fourier-transformed into the frequency domain. After transformation, the end result is a spectrum which plots absorbance vs. wavenumber (cm^{-1}). The most important difference between RAIRS and traditional IR techniques is that which is implied in its name: the exploitation of reflection.

The act of reflecting light off of a surface, instead of transmitting it through, imparts certain rules upon the interpretation of the data.[43a] First of all, the electric field of light is made of up two components (shown in Figure 2.9): an S-component (E_S) and a P-component (E_P). The S-component of light is perpendicular to the plane of incidence (shown as the white rectangle in Figure 2.9) and parallel to the surface. The P-component is parallel to the plane of incidence. When light is reflected off a surface it undergoes a phase change. There are two things that

determine the magnitude of the phase change upon reflection: 1) the angle of incidence, and 2) the polarization of the incident light. Figure 2.10 shows the degree of phase change upon reflection of the S- and P-components of light as a function of the incident angle of the light.[43a]

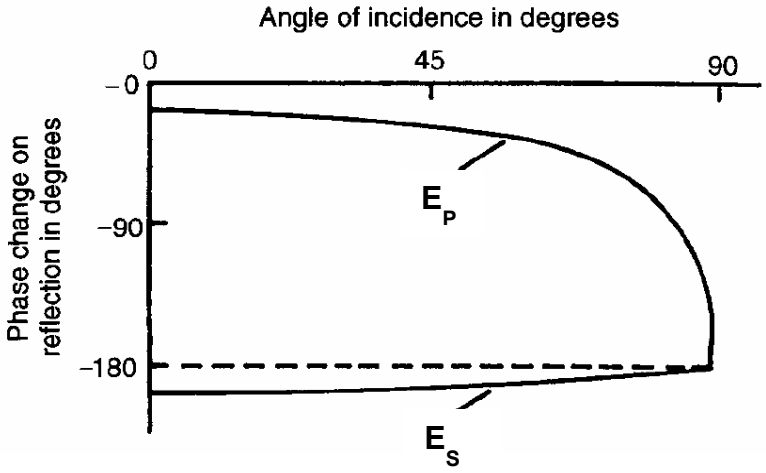

Figure 2.10: The degree of phase change of light as a function of the incident angle of the light. Figure acquired from the study done by Greenler *et al.* in 1966.[43a]

Figure 2.10 shows that upon reflection the S-component of light will undergo a phase shift of approximately 180° at all angles of incidence. If the S-component experiences a phase change of 180° it will be essentially cancelled out due to destructive interference. The P-component, however, experiences the opposite effect. At higher angles of incidence, the phase change for the P-component increases until it too undergoes a 180° change. The important fact to take away from Figure 2.10 is that there is a specific angle of incidence that induces a phase change of ~90° for the P-component of light. With a phase change of 90° the P-component of light will interfere constructively with itself, thereby intensifying. Understanding what happens to light upon reflection is an important part of grasping the RAIRS technique, however, the most essential concept to comprehend is the probability of a transition (T) for a molecule on the surface. Equation 2.1 expresses the

$$T \ \alpha \ \left|\vec{\mu}\cdot\vec{E}\right|^2 = |\boldsymbol{\mu}|^2 |\boldsymbol{E}|^2 \cos^2\Theta \qquad (2.1)$$

probability for a transition as it depends on the angle between the transition dipole moment and the incident light. Just like in traditional IR spectroscopy, RAIRS uses infrared radiation to excite

molecular vibrations. Equation 2.1 refers to the probability of a transition from the ground state of a particular vibration to its excited state. The most likely situation for this transition to occur in is when the transition dipole moment (μ) of the molecule is perpendicular to the surface, and so aligned with the P-polarized light (E). Using equation 2.1, theta (Θ) is the angle between μ and E; if the transition dipole moment of a molecule is exactly perpendicular to the surface, $\Theta = 0$ therefore $\cos^2\Theta = 1$. When $\Theta = 0$, the probability of transition is most favorable and so this molecule will be observable with RAIRS. If $\Theta = 90°$ therefore $\cos^2\Theta = 0$, in this instance, the transition dipole moment is parallel to the surface and the molecule is not observable via RAIRS. This rule, a consequence of the molecule's orientation upon the surface, is known as the surface selection rule. The surface selection rule is what allows experimenters to determine surface characteristics like the degree of order of a surface and molecules' particular orientation. One RAIR spectrum can reveal an overwhelming magnitude of information about a surface.

The IR spectrometer utilized in these studies was a Bruker IFS 66v/S model. The source of infrared radiation in the spectrometer was a SiC globar. The first mirror the IR light reflected from was a gold coated parabolic mirror (focal length 180 mm), see Figure 2.11. The reflected light was focused through a slit (0.9 x 4 mm) on a rotatable aperture wheel. The slit aperture

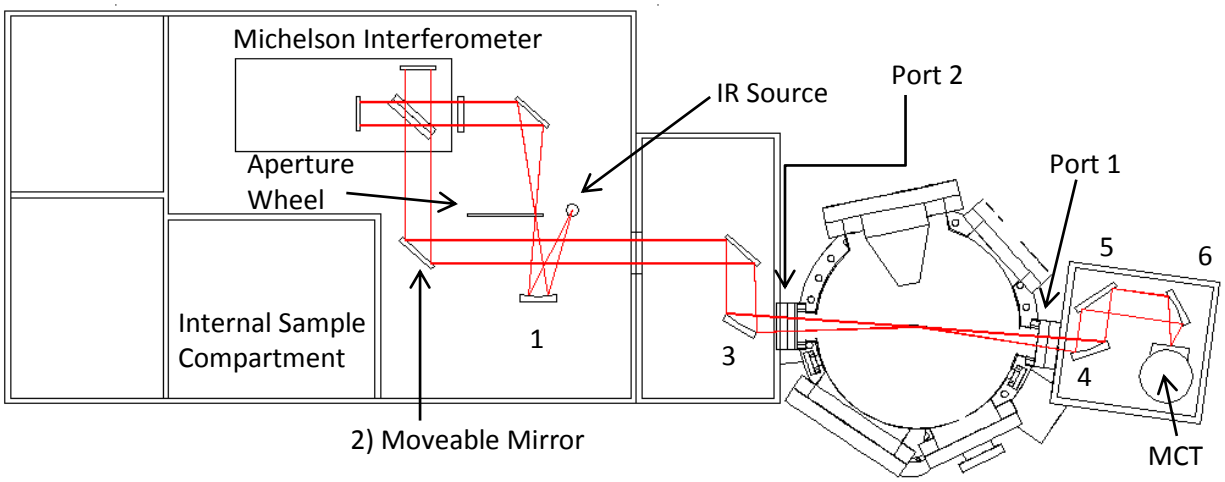

Figure 2.11: A simple schematic of the IR path through the spectrometer, optic boxes, chamber, and detector box.

was the most favorable opening for the Au slide samples because it maximized the spot size on the sample surface (i.e. the largest amplitudes are observed when using the slit aperture). After passing through the aperture wheel the IR beam entered the Michelson interferometer. Upon exiting the interferometer the beam was either directed into an internal sample compartment or an external sample compartment by way of a moveable mirror (2). The typical setup was to direct the beam into the external sample compartment, which contained a parabolic mirror (3) with a focal length of 250 mm. This parabolic mirror focused the light through the KBr window attached to port 2 on the main chamber. Once focused through the KBr window the IR beam hit the sample surface in the middle of the UHV chamber. The optimum incident angle for the IR beam was ~86°. The beam reflected off the surface and exited the UHV chamber via another KBr window, attached to port 1, and then entered the IR detector (IRD) box. Inside the IRD box there were three mirrors: a parabolic mirror (f = 250 mm) (4), a flat mirror (5), and another parabolic mirror (f = 43 mm) (6). These three mirrors focused the beam into a mid-range (750-4000 cm^{-1}) mercury cadmium telluride (MCT) detector. The settings used for the spectra presented herein were as follows: 1) each spectrum was an average of 100 scans collected over a 90 second time period, 2) resolution was set at 2 cm^{-1}, 3) the scanner velocity was set at 20.0 kHz.

The UHV chamber was designed with the intention of employing several different analytical techniques simultaneously. When the sample was positioned for RAIRS, it was also correctly positioned for dosing with the gas(es) of interest and monitoring gas-phase reactants/products with the Extrel Mass Spectrometer. The chamber possesses two gas dosers, one was used explicitly for ozone, the other was used for a variety of other gases, such as NH_3, D_2O, and CO.

The ozone doser, also known as the capillary array doser (CAD), was designed by L. R. Fiegland.[39] His design was based on studies by Zhukov *et al.*[44] and John T. Yates Jr.[41] For a thorough description of the capillary array doser (CAD), shown in Figure 2.12, please see L. R. Fiegland's dissertation.[39]

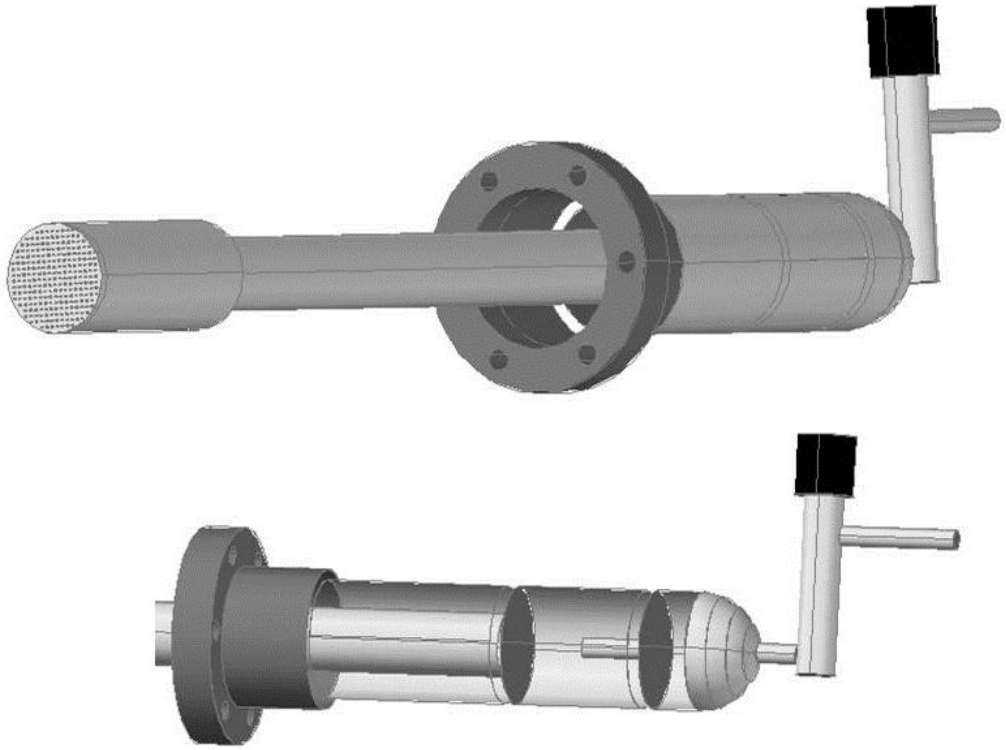

Figure 2.12: The top image shows the entire CAD with an emphasis on the vacuum side of the doser, while the bottom image shows the detail inside the atmospheric side of the doser. The small tube represents the Pyrex capillary.

The ozone exposure of surface-bound fullerenes required a slight modification of the CAD. The inner diameter of the Pyrex capillary was increased from 0.08 mm to 0.50 mm. This increase was carried out to decrease the amount of time needed to oxidize a surface, i.e. provide a higher flux of ozone molecules upon the sample surface.

The other doser included in the experimental setup was a stainless steel doser, designed and built in the process of these studies. The second doser was used for product confirmation

experiments, but also allows co-dosing or humidity impact studies. The doser was comprised entirely of stainless steel and all connections were VCR. The 7" focal length (from the knife edge of the conflat flange to the sample surface) aimed the gas directly at the sample, without obstructing any of the instrumentation or the CAD.

One of the goals of this research is to develop a full mechanistic picture for the reaction between gas-phase ozone and surface-bound C_{60}. To achieve this goal, the ability to not only monitor the surface-bound products, but also to detect any gas-phase products that may result from the interaction was necessary. Along with the possibility of detecting gas-phase products, a sensitive mass spectrometer would allow for Temperature Programmed Desorption (TPD) studies. TPD is a widely used surface analysis technique that involves heating a sample enough to desorb any surface species. While the sample is being heated, the researcher simultaneously detects any residual gases using a mass spectrometer. There are two methods of thermal evaporation, one being flash desorption, and the other known as TPD. In these experiments, the TPD technique was utilized. The method consists of raising the temperature of the sample more slowly than flash desorption (between 15 seconds to a couple of minutes, as opposed to ~0.5 seconds). When the temperature rises, surface species will gather enough energy to escape from the surface. The result of the species desorbing is a rise in pressure for specific masses. Each chemical species will desorb from particular surfaces at their own unique temperatures (i.e. specific energies). The last statement means that measuring the temperature where a certain mass' pressure peaks, can tell us something about the binding energy for that species on that particular surface. With TPD experiments being the main function of the mass spectrometer, a MS system that would be extremely sensitive to the low quantities of chemicals used (monolayer and submonolayer amounts) was employed. Extrel mass spectrometers are capable of detecting

partial pressures of ~10^{-16} mbar with the added ability to monitor an unlimited number of masses. To accommodate the Extrel MS (ABB Extrel, model: MEXM 1000), a detector chamber was designed in house, built by Kurt J. Lesker Company, and attached to the main chamber on flange 6, see Figure 2.1. The detector chamber is a doubly-differentially pumped chamber, with the second differential stage housing the actual quadrupole mass spectrometer. Differential pumping is required for the use of the mass spectrometer during dosing experiments because the pressures at which dosing was performed were much higher than allowed by the internal set points of the mass spectrometer. Differential pumping is achieved by placing apertures between chambers to significantly reduce the gas load between chambers, or pumps. The aperture between the main chamber and the first differential stage is 4.3 mm in diameter, and the aperture between the first and second differential stages is 4.7 mm in diameter. This particular Extrel model has a mass range of 2-1000 amu, and an impressive 1 amu resolution. A large, 220 L s^{-1}, ion pump (Varian Vacuum Products, model: 912-7014) is used to pump down the second differential stage, while a 180 L s^{-1} turbomolecular pump (Pfeiffer Vacuum, model: TMU 200M P) evacuates the first differential stage. The turbomolecular pump is backed by a scroll pump from ULVAC KIKO, Inc. (model: DIS-250). The pressure in the second differential stage of the detector chamber is monitored using a compact cold cathode gauge from Pfeiffer Vacuum, Inc. (model: IKR 270).

Another surface sensitive technique employed in the experiments was X-ray Photoelectron Spectroscopy (XPS). XPS allows for elemental analysis of the surface before, during, and after ozone exposures. An elemental analysis of the surface will not only inform researchers what species are on the surface, but also what kind of bonding environments in which the molecules exist. XPS, also known as Electron Spectroscopy for Chemical Analysis (ESCA), was developed in the mid-1960s by K. Seigbahn and his research group.[45] The

technique utilizes Einstein's Photoelectric Effect. The photoelectric effect says that electromagnetic radiation falling upon a surface can cause the ejection of electrons from the surface. The ejection of these electrons occurs because energy contained within the incident light is absorbed by the electrons in the surface. The absorption of energy gives the electrons sufficient energy to escape the bulk of the surface, and the escaping electrons are known as photoelectrons. The key concept is the fact that the photoelectrons must *escape* from the bulk. In a solid material the atoms are densely packed. For an ejecting electron, the deeper the atom exists within the bulk the more difficult it will be for that electron to escape the material; a result of the

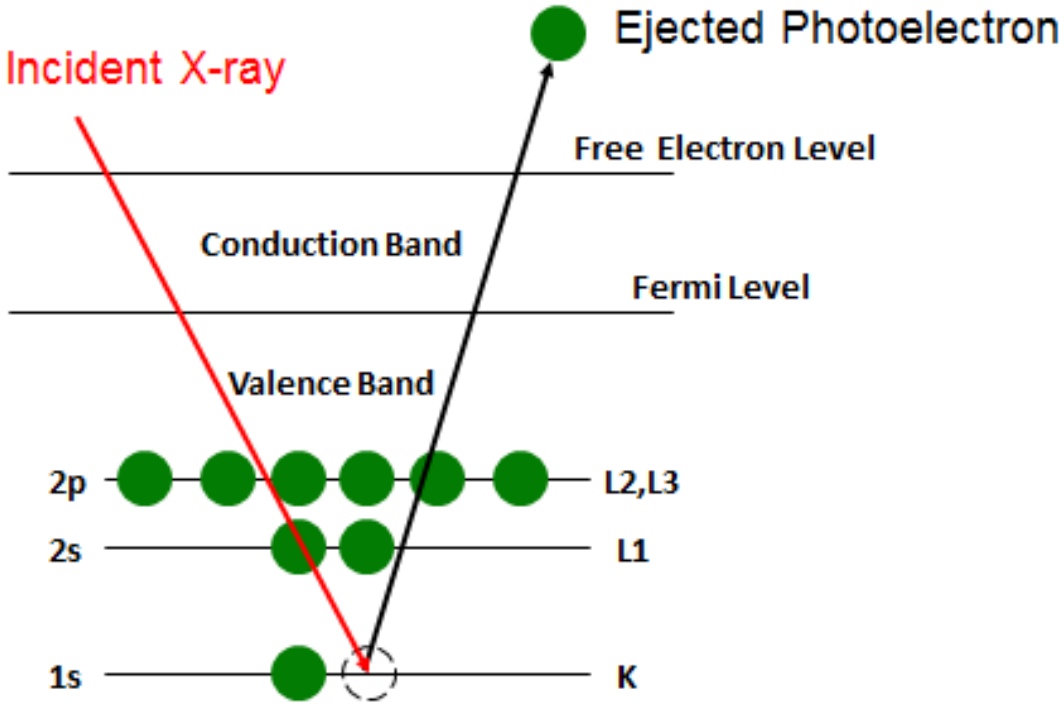

Figure 2.13: A depiction of the ejection of a core level electron after illumination with x-rays. The energy of the ejected photoelectron is directly related to the core level from which it was removed.

Inelastic Mean Free Path (IMFP). The IMFP is a measure of the average distance travelled by an electron through a solid before it is inelastically scattered. It is logical that the deeper the atom is situated within the material the smaller the inelastic mean free path. Atoms located at the surface

of the bulk have the largest IMFPs. It is because of this inherent quality that XPS is known as a "surface" technique. In an effort to lengthen the IMFP of every sample, XPS is performed in high vacuum environments. The high vacuum environments not only remove molecules from the air, which could deflect ejected photoelectrons from their path to the detector, but it also helps to keep contaminants from adsorbing to the surface of the sample, increasing the IMFP of the atoms at the surface of the bulk. The ejected photoelectrons are actually from the core levels of the atoms in the material. Figure 2.13 shows the one electron process that takes place during an XPS experiment, as opposed to the two-electron process of Auger Electron Spectroscopy (AES). In XPS, a photoelectron is expelled upon irradiation of the sample with x-rays. The energy range of the x-rays is between 200-2000 eV; x-rays within this eV range will impart enough energy on the surface to eject core level electrons. The x-rays are generated through processes known as *Bremsstrahlung radiation* and *X-ray fluorescence*.[46] While the details of these two processes will be spared in this particular document, the most important fact about x-rays and XPS is that the resulting spectrum is completely characteristic of the x-ray source anode material. The two most commonly used x-ray sources are magnesium (Mg, $h\nu$ = 1253.6 eV) and aluminum (Al, $h\nu$ = 1486.6 eV). Regardless of the source used, it is possible to determine both the kinetic energy of the ejected photoelectron, as well as its binding energy. Equation 2.2 relates the binding energy (E_B) to the energy of the incident radiation ($h\nu$), the kinetic energy of the photoelectrons (E_K), and the work function of the spectrometer (φ).

$$E_B = h\nu - E_K - \varphi \qquad (2.2)$$

The work function of the XPS spectrometer is the minimum amount of energy needed to remove an electron from the bulk of a solid to a point immediately outside the solid surface. The value of the work function is dependent upon the material being studied. It is for this reason that the work

function should be recalibrated every time an XPS experiment is performed. In these experiments, the work function was calibrated with the Au 4*f* peak, which should be positioned at approximately 83.8 eV. Gold is a perfect peak for calibration, for these purposes, because of the sheer amount of solid unoxidized Au present on the sample slide. The unoxidized quality is relevant because XPS is capable of revealing not only the elements present in the surface, but also details about their bonding environment. For instance, later in this text, the significant C 1*s* peak due to the fullerenes on the surface will be discussed, as well as the effect of ozone oxidation on the peak because of the C-O and C=O bonds present on the surface. The bonding situation of the elements affects their oxidation state; these changes in the oxidation state can be detected using the XPS.

In these studies, two different XPS instruments were employed. The first instrument was installed on the UHV chamber. The UHV XPS, purchased from SPECS, was equipped with a dual-anode (Mg and Al) x-ray source (model: XR-50). The source was typically operated at 250 W (12.5 kV and 20 mA). To detect the photoelectrons, a 16.5" hemispherical energy analyzer (model: Phoibos 100), with a single channel electron multiplier, was used. The second instrument was located *ex situ*, in the Surface Science lab in the Chemistry Department at Virginia Tech. The instrument was made by Perkin Elmer (model: PHI-5600 ESCA) and included both Mg and Al anodes.

2.2.4 Reactant Calibration

The determination of kinetics for a reactive system requires knowledge of the concentration of the reactants. According to collision theory, molecules must collide in order to react, so increasing the concentration of reactants will directly affect the number of collisions

and therefore the rate of the reaction. The concentrations of both reactants involved in these studies were measured to accurately calculate the rates of reaction.

The concentration of gas-phase ozone was measured prior to entering the CAD and chamber using a UV-Vis Spectrometer. Two Teflon valves must be opened to introduce ozone into the main chamber. Between these two Teflon valves was the UV-Vis spectrometer (StellerNet, Inc., model: EPP200C with deuterium light source). Ozone was monitored at 254 nm and the measured absorbance value was used to calculate the flux of ozone above the surface. The other variables needed to correctly determine flux were the backing pressure of ozone (measured in the ozone apparatus with the capacitance gauge), the conductance of the capillary array doser (1.60 cm^3 s^{-1}), the path length of the UV-Vis flow cell (1 cm), and the extinction coefficient of ozone (3036 L/mol·cm). With all the values, Beer's Law (Equation 2.3) was used to calculate the ozone concentration every 90 seconds throughout the entire exposure.

$$A = \varepsilon b C \tag{2.3}$$

Where A is the absorbance measured with the UV-Vis, ε is the extinction coefficient, b is the path length of the flow cell, and C is the concentration.

In order to know the surface coverage of fullerenes at the start of an experiment a calibration curve for film thickness was created. To develop the calibration curve, a Bell Jar Evaporator (BJE) equipped with a Quartz Crystal Microbalance (QCM) was employed. The BJE is a thermal evaporator that uses an electric resistance heater to melt the deposition material, raising its vapor pressure into a useful range. This type of evaporator is a vacuum evaporator, functioning in the 10^{-6} – 10^{-7} Torr range. A vacuum environment is necessary so the vaporized material can be transferred to the surface with a decreased chance of interaction with other gas-

phase particles. The lower the vacuum of the evaporator, the cleaner the deposited film. The BJE used to create the calibration curve is owned by the Physics Department of Virginia Tech; who purchased it from Ladd Research. While the BJE's method of vapor deposition is almost identical to the *in situ* method using the CE, the advantage of the BJE is its inline QCM. A QCM is an instrument that measures the change in mass per unit area by measuring the change in the resonance frequency of a quartz crystal. Quartz is one of a number of crystals that experiences the piezoelectric effect – that being the internal generation of an electric field resulting from an applied mechanical force. In these experiments, the Au-coated quartz crystal has a specific resonance frequency when there is nothing deposited on the Au slide. After deposition the resonance frequency is altered. This change in frequency corresponds to a change in mass (i.e. corresponds to the mass deposited on the surface of the Au slide). The mass deposited on the slide can be determined from the change in frequency using the Sauerbrey equation, Equation 2.4.

$$\Delta f = \frac{-2\Delta m f_0^2}{A\sqrt{\rho_q \mu_q}} = -\frac{2 f_0^2}{A\sqrt{\rho_q \mu_q}} \Delta m \qquad (2.4)$$

The Sauerbrey equation was developed in 1959 by G. Sauerbrey specifically for the purpose of determining the mass deposited on a piezoelectric crystal. The equation relates the change in frequency (Δf) to the resonant frequency (f_0), the area of the crystal (A), the density of the quartz (ρ_q), the shear modulus of the quartz (μ_q), and of course the change in mass (Δm). Sauerbrey was able to derive the equation by treating the mass deposited as an extension of the quartz crystal. With use of the QCM, which was calibrated for C_{60}, and the knowledge of C_{60} packing dimensions (C_{60} centroid-centroid distance = 10.08 nm,[47] distance between C_{60} layers = 0.33 nm[48]), the thickness of the deposited fullerene films was determined. The surfaces, with known

film thicknesses, were then transferred into the UHV chamber and scanned with RAIRS. By integrating the fullerene IR modes, specific film thicknesses were associated with certain IR intensities, creating a calibration curve. The procedure helps give validity to the measured kinetic rates for the ozone oxidation of fullerene surfaces.

2.2.5 Electronic Structure Calculations

While a kinetic picture of the system of interest was one of the desired goals, it was also important to gather a detailed description of the actual mechanisms of these reactions. To further support the mechanistic data Density Functional Theory (DFT) calculations were carried out on not only the fullerenes, but also several oxidized species of fullerenes. DFT is a quantum mechanical modeling method that can be used to study many different qualities of a molecule. For these purposes, DFT was used as a support for IR peak assignments.

2.3 Summary

Since the end goal is to understand the reaction between gas-phase ozone and surface-bound fullerenes on a very fundamental level, specific techniques for analysis were employed. The analysis is not only important for the actual reaction, but also for the characterization of the gas of interest, and the surface before and after exposure. To develop an accurate picture of the system, it is important to know the state of the surface before and after exposure to ozone. The UHV chamber, equipped with the aforementioned instruments, provides the capability to accurately characterize the ozone and the fullerene surfaces, as well as ensure they remain uncompromised before, during, and after exposure.

Chapter 3

Vibrational Spectra of Surface-Bound Fullerenes: C_{60}, C_{70}, C_{76}, C_{78}, C_{84}

3.1 Introduction

A molecule's infrared spectrum is analogous to a person's fingerprint and, for identification purposes, can be utilized in the same way. Different molecules have their own specific energies, or vibrational frequencies. Infrared spectroscopy (IR) can be employed to measure the vibrational frequencies. IR can even be used to determine the phase (solid, liquid, or gas) of the material under study. By observing the particular combination of frequencies, as well as their peak shape, a great deal of information can be gained. In this chapter, the vibrational spectra of surface-bound fullerenes were analyzed in order to characterize these molecules on a polycrystalline Au surface.

Infrared spectroscopy has been used to study fullerenes since their initial discovery in 1985. While numerous reports exist in the literature, describing the IR spectra for fullerenes in the gas, solution, and even a few on the solid phase, there is very little work detailing the infrared spectra of fullerenes on surfaces. Wang *et al*. performed a study of vapor-deposited solid C_{60} films (4 μm thick) in 1993 and found 102 observable IR frequencies.[49] Besides the four first-order-allowed modes, at 526.6, 575.8, 1182.9, and 1428.2 cm^{-1}, at least 98 additional peaks were present. They assigned the extra lines to combination modes and isotopically induced modes. A later study by Lyon and Andrews, focused on the IR spectra of C_{60} in argon, deposited onto a CsI window.[50] They reported the four main IR peaks of C_{60} at 529.6, 579.0, 1184.5, and 1432.1 cm^{-1}. A simple change in surface formation technique results in a shift in the peak frequencies and the additional peaks seen in the Wang study are a functional of the C_{60} film thickness.

C_{70} has also been studied in depth via experiment and calculations. Based on the reports, there appears to be less variation in the peak positions, regardless of gas, solution, or solid sample under study.[51] However, the C_{70} film has yet to be well characterized. It is likely that additional modes will be observed, similar to C_{60}, due to the intermolecular interactions of the film.

As the fullerenes increase in size, the extent of knowledge decreases, simply because there are fewer investigations of the larger C_n molecules. The only study reporting an IR spectrum of C_{76} in toluene was performed in 1991 by Etti *et al.* A number of peaks were observed, a result of lower symmetry, with the strongest ones at 660, 747, 1035, 1127, and 1434 cm^{-1}. [52] In 1996, two different isomers of C_{78} in toluene were characterized with Raman and IR. Each isomer possessed its own unique spectrum. [53] Finally, C_{84} was studied in 1997, displaying a very complex spectrum, which led the authors to conclude that individual isomers could not be distinguished by way of IR spectroscopy. [54] It is clear from a review of the existing literature that a detailed characterization of surface-bound fullerenes is needed. This study aimed to fill this gap in knowledge with a detailed study of C_{60}, C_{70}, C_{76}, C_{78}, and C_{84} deposited on an Au surface.

The goal of Chapter 3's research was to create a detailed characterization of C_n molecules on a surface by analyzing their vibrational spectra. Comparison of the IR data to Electronic Structure Calculations helped support the observations and conclusions. The information presented herein will help to explain how the spectra of these molecules change as they increase in size.

3.2 Experimental Details

3.2.1 Materials

All chemicals were used as received without further purification unless otherwise noted. Fullerenes (C_{60}, C_{70}, C_{76}, C_{78}, and C_{84}) were purchased from Bucky USA. Research grade ultrahigh purity nitrogen and liquid nitrogen were purchased from Airgas Specialty Gases. Polycrystalline gold substrates were received from Evaporated Metal Films.

3.2.2 Formation of C_n Surfaces

Fullerenes were deposited on polycrystalline gold slides. The slides were purchased from Evaporated Metal Films, Inc. They are made by first depositing a 50 Å thick layer of chromium onto a glass slide, then depositing ~1000 Å of Au. The dimensions of the slides are 1" x 1" x 0.062". To clean the Au slides before introduction into the UHV chamber, they are submersed in a solution of 70% sulfuric acid and 30% hydrogen peroxide (30%), also known as piranha solution, for ~45 minutes. *Warning: Piranha solution is an oxidizing agent which reacts violently with organics! Extreme caution should be taken when using this solution!* The piranha solution was used to remove the majority of the hydrocarbons which adsorb to the surface from exposure to air. Once the Au slide was removed from the piranha, it was rinsed thoroughly with deionized water (Millipore Purification Systems, 18.2 MΩ), and then dried completely with UHP nitrogen. After drying, the slide was placed into the UHV chamber. Immediately after the Au slide was placed into the load lock chamber, the crucible evaporator was detached from the load lock, any remaining fullerene from the previous experiment was taken out, the crucible was cleaned, and then new fullerene powder was placed in the crucible. After transferring into the UHV main chamber, the Au slide was then cleaned with ozone for one hour. Ozone was used to

remove any remaining hydrocarbons from the surface before fullerene deposition. Two advantages of cleaning the surface with gas-phase ozone in UHV were: 1) the actual removal of the hydrocarbons was monitored using RAIRS and 2) the surface remained clean until deposition because the fullerenes were also deposited in vacuum. After one hour of ozone cleaning, a spectrum of the freshly cleaned Au slide was recorded with the IR. The spectrum was saved to be used later as a background. The Au slide was transferred into the load lock to deposit the fullerene of choice. As stated in Chapter 2, the voltage and current required to deposit fullerenes on the Au slide varied depending upon the fullerene. For C_{60} and C_{70}, total time for film deposition was 35 minutes, with the maximum voltage and current of 4.5 V and 4.5 A. The maximum temperature during C_{70} deposition was 772 K. C_{76} deposition required 5 V and 5 A, resulting in a maximum deposition temperature of 984 K. C_{78} and C_{84} deposition lasted 45 minutes, was achieved with 7 V and 7 A, and reached a maximum temperature of 1299 K.

3.2.3 RAIRS Data Acquistion

The infrared spectra of surface-bound fullerenes were collected with a Bruker IFS 66v/S spectrometer. The spectrometer is equipped with a SiC globar source, which produces an IR beam. The IR beam is focused onto the Au surface in the middle of the UHV chamber at an incident angle of ~86° relative to the surface normal. The detector used with the Bruker spectrometer is a mid-range MCT detector (750 - 4000 cm^{-1}), that requires cooling with liquid nitrogen. Every spectrum shown in this dissertation was produced by the co-addition of 100 scans acquired over 90 seconds. The resolution was set at 2 cm^{-1} and the scanner velocity was held at 20 kHz.

3.2.4 Electronic Structure Calculations

Electronic structure calculations were performed on each fullerene molecule, in its unoxidized form. The calculations are an important addition to the experimental data because they were used to help assign the numerous peaks that were observed in the IR spectra. The modeling method used was density functional theory (DFT). Specifically, the exchange-correlation hybrid functional B3LYP with a small 3-21G* basis. This particular method has been employed by other researchers and found to predict the geometry and electronic structure of fullerenes with unusual success.[55]

3.3 Results

3.3.1 Surface-Bound C_{60}

The C_{60} films were characterized immediately after formation. Figure 3.1 shows the RAIR spectrum of a C_{60} film deposited in high vacuum. The spectrum is absorbance versus wavenumber (cm^{-1}). The spectrum recorded for the unoxidized C_{60} surface contains a considerable amount of information about the fullerene film. First of all, while gas-phase C_{60} possesses 174 intramolecular vibrational modes, only four of those modes are IR active: 527, 577, 1182, and 1428 cm^{-1}.[49] Each IR active mode corresponds to an F_{1u} symmetry mode.[49] In Figure 3.1, only two of the modes for the isolated gas-phase C_{60} are observed. The reason all four are not present is a limitation of the detector employed; the MCT's observable range is from 750 to 4000 cm^{-1}. Regardless of the fact that C_{60} only has four IR active modes, every other peak in the spectrum can be assigned to a mode of the C_{60} fullerene cage. Most of the peaks are identified as second-order combination modes, while the remaining few are due to isotopically-

induced modes.[49] Specifically, two IR active modes (1182 and 1428 cm^{-1}), 4 isotopically-induced modes, and ~60 combination modes were observed in the spectrum.

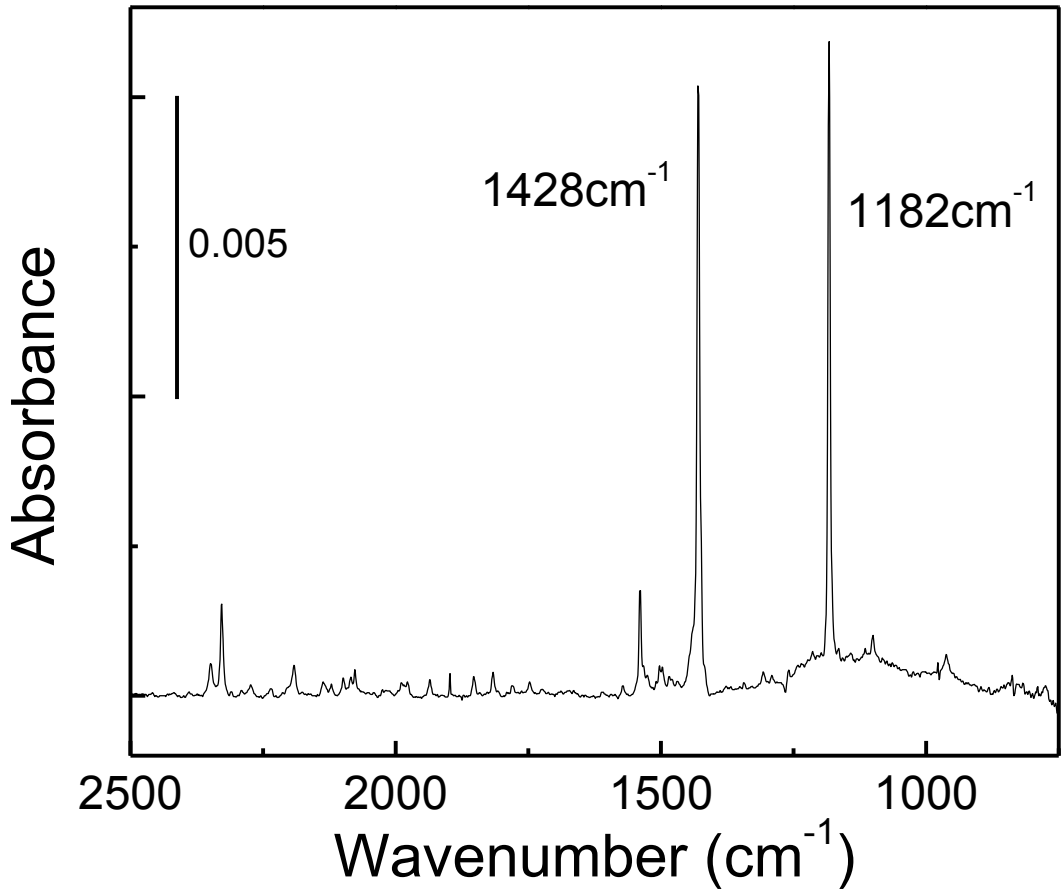

Figure 3.1: RAIR spectrum of a C_{60} film deposited on Au slide in high vacuum. The two intense peaks are IR active modes, while the rest of the peaks can assigned to combination, isotopically-induced, and higher order IR modes.

A table with all observed frequencies and their corresponding assignments can be found in the Appendix – Section 8.2.

The peaks in the spectrum have very narrow line widths. This characteristic reveals important information about the film. In the early 1990s, researchers used several different techniques, like nuclear magnetic resonance (NMR) spectroscopy, x-ray powder diffraction (XRD), and Raman spectroscopy, to show that C_{60} molecules rapidly rotate and move within the film.[56] The reorientation time was calculated to be 9.1 picoseconds at room temperature.[56b] At

temperatures below 260 K, the motion transitions from a free rotation to a jump rotation, or "ratchet motion". The narrowness of the peaks is therefore due in part to vibration-rotation coupling of the individual freely rotating molecule.[57] This also means that, while it is known that the C_{60} molecules strongly physisorb to the Au surface, there are minimal solid-state intermolecular interactions within the C_{60} film.

The final, and most important, feature of the spectrum of the unoxidized C_{60} film is the height of the two peaks assigned to the IR active modes of C_{60} (1182 and 1428 cm^{-1}). The height of these peaks is directly proportional to the film thickness, and therefore number of C_{60} molecules present on the surface. These peaks are used later in Chapter 4 to create a calibration curve, in order to reasonably determine surface coverage, a necessity for the kinetic measurements.

X-ray photoelectron spectroscopy (XPS) was used to confirm and support the RAIRS data. Since XPS is a quantitative spectroscopic technique capable of detecting as little as 0.1 At% (atomic percent) of an element, it is an ideal method to verify the process by which C_{60} surfaces are formed. XPS was used to follow each step of the procedure and ensure the end result was indeed a surface covered with unoxidized C_{60} molecules. The binding energy values of each

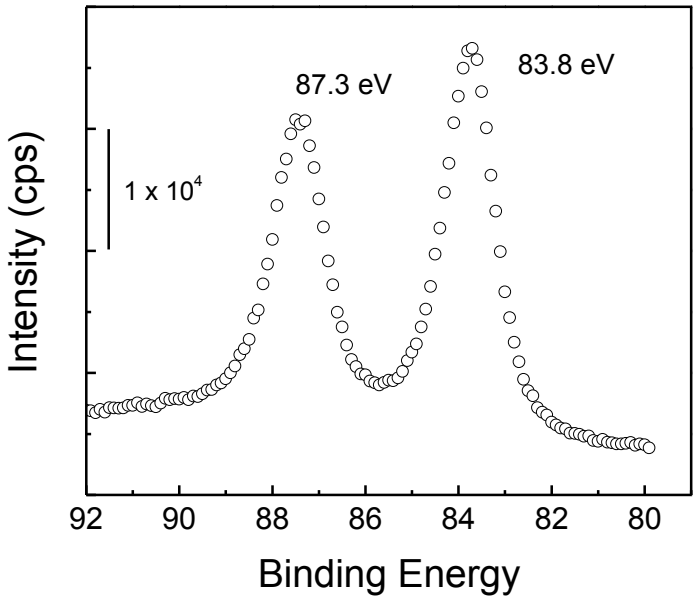

Figure 3.2: XPS data of the Au $4f_{7/2}$ and Au $4f_{5/2}$ peaks. The Au $4f_{5/2}$ peak was used to adjust the work function thereby calibrating the rest of the elemental regions observed.

observed data region were calibrated using the Au $4f_{5/2}$ peak centered at 83.8 eV, shown in Figure 3.2. The position of the Au $4f_{5/2}$ peak can be adjusted by changing the value of the spectrometer's work function, a variable that shifts depending upon the material under investigation. The Au slide, before fullerene film deposition, was monitored with XPS before ozone cleaning, after ozone cleaning, and finally, after C_{60} deposition.

Figure 3.3 shows the C 1s region and the O 1s region of the Au slide before any ozone cleaning. The graph on the left contains the data from the C 1s region, and depicts a peak centered at 284 eV. The presence of this peak indicates the existence of carbon species,

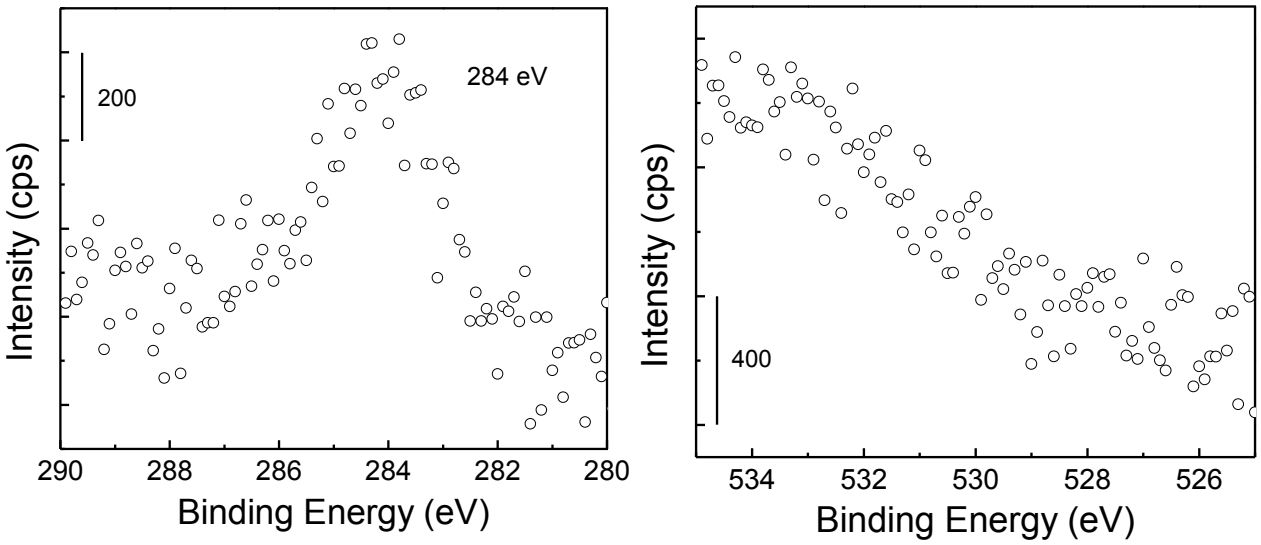

Figure 3.3: XPS data of the C 1s region (left) and the O 1s region (right) of an Au slide removed from piranha solution and introduced into the main chamber. The data indicates the presence of adsorbed hydrocarbons on the surface.

specifically –C-C–, on the surface of the Au slide. The most likely source of these species is from atmospheric hydrocarbons that have physisorbed to the surface during sample transfer from the piranha solution into the chamber. The graph on the right represents the O 1s region. It is clear from this graph that, before ozone cleaning, there are no oxygen species on the surface, within the signal to noise.

Figure 3.4 shows the C 1s region and O 1s region after cleaning the Au surface for one hour with ozone. Again, the C 1s region is shown in the graph on the left and the O 1s region is

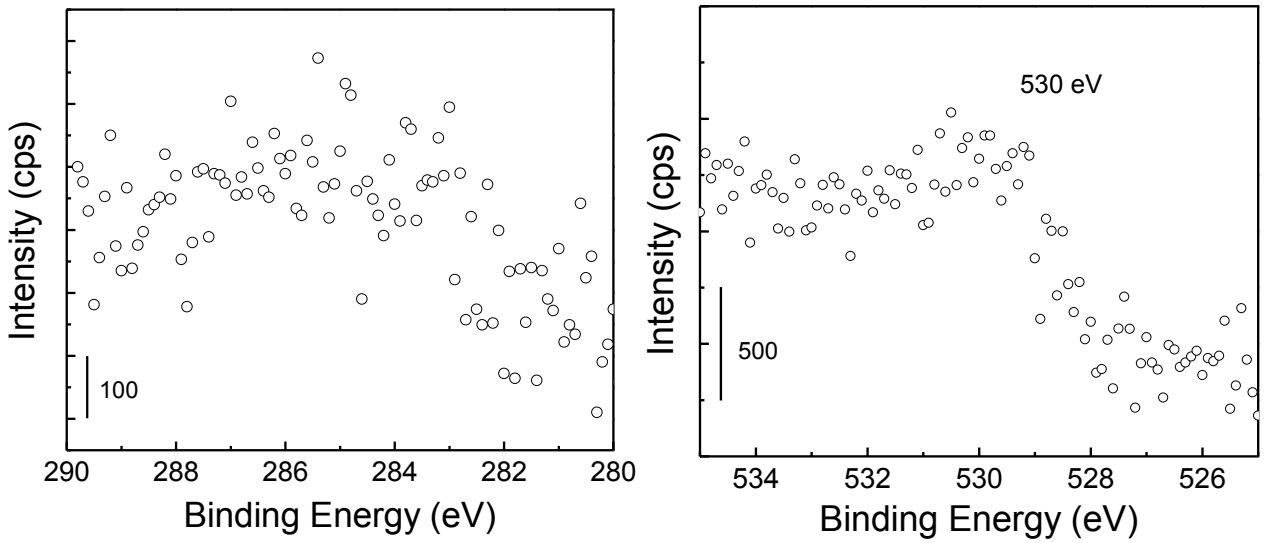

Figure 3.4: XPS data of the Au slide after cleaning with ozone for one hour. The peak previously seen in the C 1s region is gone and a small peak in the O 1s region is most likely due to gold oxide species.

portrayed in the graph on the right. When C 1s data collected after ozone cleaning is compared to that collected before, the conclusion can be drawn that ozone has removed the majority of the adsorbed hydrocarbons, leaving the surface free of significant organics and other contaminants and ready for fullerene deposition. The O 1s region appears to have a small peak after the ozone cleaning, which is most likely due to a negligible amount of oxidized gold.[58]

The final figure in this section, Figure 3.5, shows the C 1s and O 1s regions after C_{60} has been deposited in high vacuum. The C 1s clearly shows a prominent peak centered around 284.2 eV, with no shoulders or neighboring peaks. This peak represents the C_{60} film that has been deposited on the surface of the Au slide. The lack of shoulders or neighboring peaks at higher binding energies means there is only one oxidation state of carbon present within the film. The observed oxidation state is characteristic of –C-C– bonding, which would be expected in the

XPS data of C_{60} molecules. There is no indication of carbon-oxygen bonds within the data, signifying an unoxidized fullerene film.

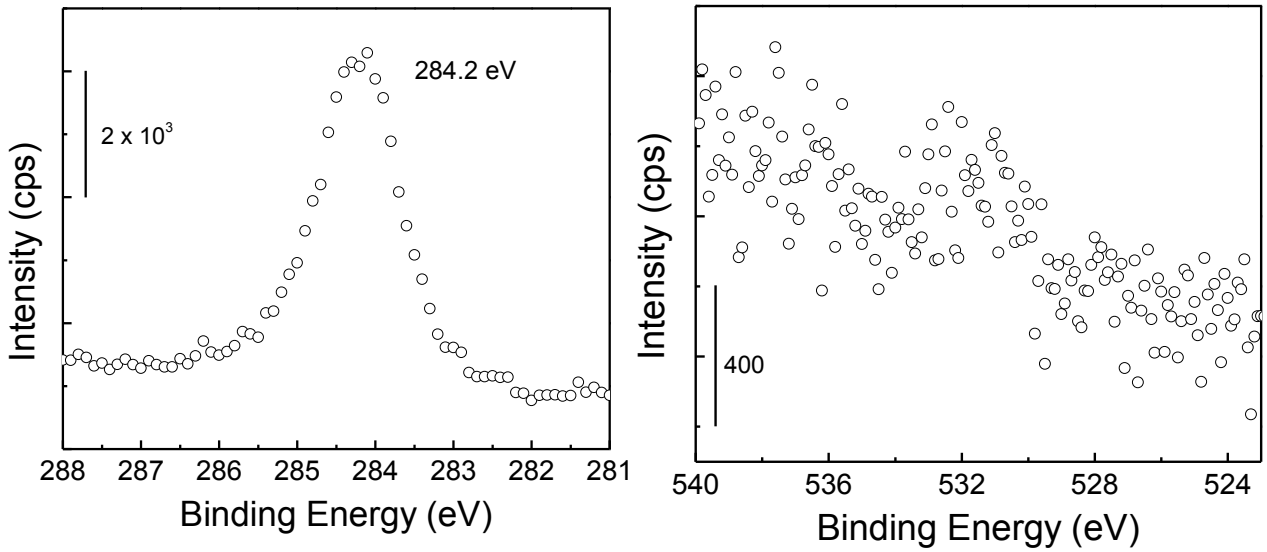

Figure 3.5: XPS data of a C_{60} film deposited on an ozone-cleaned Au slide. The peak centered at 284.2 eV represents the C-C bonds of the fullerene molecules and the lack of a detectable oxygen species implies an unoxidized film is present on the surface.

The Extrel mass spectrometer was used to further characterize the C_{60} film present on the surface. The adsorption of multiple layers upon any surface is a common occurrence when vapor-deposition is employed as a technique for making thin films. Temperature-programmed desorption (TPD) experiments can be utilized to characterize the thin film.

After the C_{60} film was deposited on an ozone-cleaned Au slide, the surface was heated to 500°C, to drive the fullerenes from the surface. Two masses were monitored with the mass spectrometer: 720 amu – the molecular weight of C_{60}, and 360 amu – the major crack detected for C_{60}. In this TPD experiment, the temperature of the sample was increased by stepping up the current on a power supply attached to the surface heater. The current was not set above 5.5 amperes because of limitations of the button heater. Figure 3.6 shows the TPD profile for C_{60}, recorded at a mass of 360 amu. The TPD graph on the left shows the entire experiment. There are two obvious peaks present, the first appears at 154°C and the second at 230°C. The first peak

is most likely due to an incomplete monolayer existing directly at the gas-surface interface. The second and most intense peak is assigned to the bulk of the C_{60} film and perhaps implies that the majority of the film possesses similar binding energies.

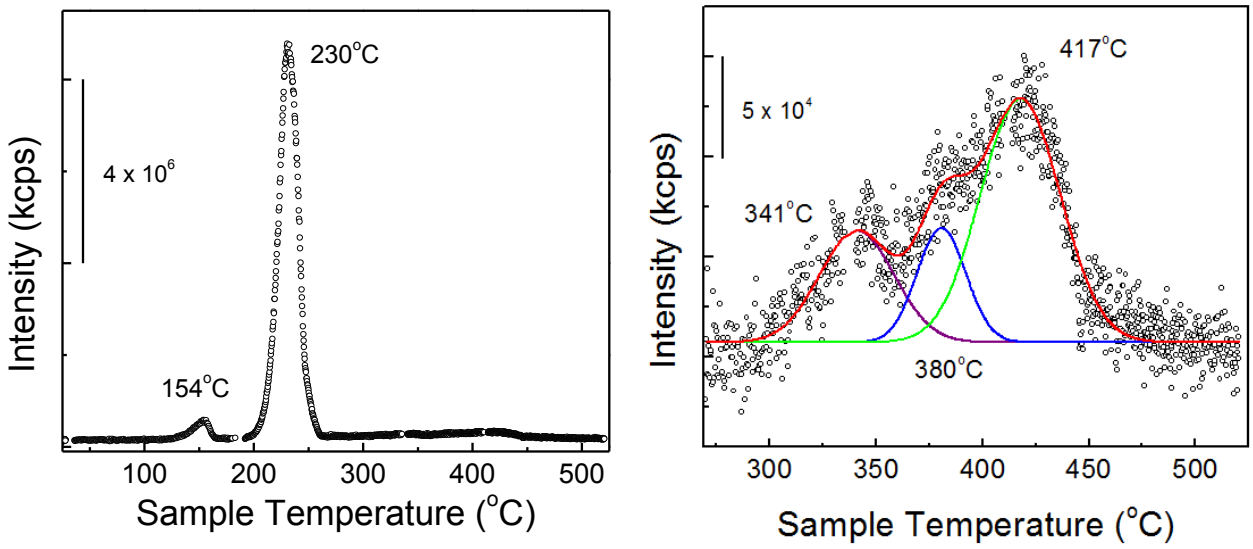

Figure 3.6: TPD data recorded at m/z 360. The graph on the left displays the entire TPD experiment. The graph on the right shows the three small peaks, assigned to the final monolayers on the Au slide.

The graph on the right, in Figure 3.6, is an expanded view of the high temperature region of the experimental data. At this point in the experiment, the rate at which the temperature was increasing had slowed significantly, a function of this particular ramping method. If the temperature ramp had been held constant the resolution of these three peaks would be greatly improved. The three peaks in the graph on the right have been assigned to the final layers of C_{60} on the Au surface. While a quantitative conclusion cannot be determined from this single experiment, it gives a general idea of the basic binding energies of the monolayers within the C_{60} films deposited on the Au slides.

Gaussian 09[59] was used to perform electronic structure calculations on the C_{60} molecule. The program used B3LYP 3-21G*, a density functional theory (DFT) method, to optimize the

geometry of the molecule and then complete a frequency analysis. The resulting frequencies were compared to the experimental ones obtained with the RAIR spectrometer. It is important to point out that the calculations are run on a single C_{60} molecule and those results are compared to measurements of a C_{60} film. Figure 3.7 shows the calculated frequencies, represented by red lines, overlaid on the experimentally acquired C_{60} IR spectrum. While there seem to be several similarities in peak position, the main interest is the prediction of C_{60}'s IR active modes. Ensuring the unoxidized cage can be accurately modeled will give validity to the calculations run on the C_{60} molecules with oxygen species added to the cage.

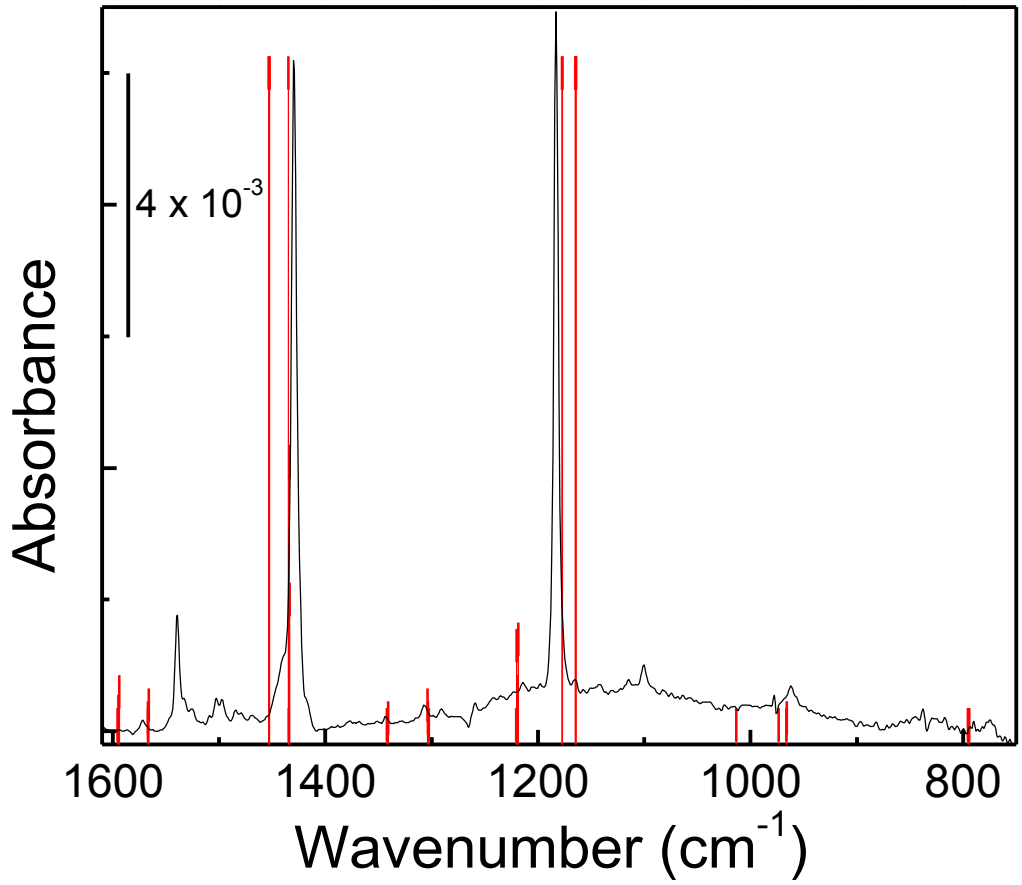

Figure 3.7: A RAIR spectrum of an unoxidized C_{60} film (shown in black). The red lines represent the calculated frequencies of a C_{60} molecule. Calculations were performed using B3LYP/3-21G*.

3.3.2 Surface-Bound C_{70}

The C_{70} films were characterized immediately after deposition. Figure 3.8 shows the RAIR spectrum of a C_{70} film deposited in high vacuum. The spectrum is a plot of IR absorbance versus wavenumber (cm^{-1}). Based on the IR data collected with this instrument and the current information available in the literature,[11d, 11f, 38, 60] the presence of a film of C_{70} fullerene molecules on the Au slide was confirmed. C_{70} follows C_{60}, ranking as the second most stable fullerene in existence. This slightly larger fullerene has D_{5h} symmetry and resembles an elliptical or "rugby ball" shape. The difference in structure between C_{60} and C_{70} is created by the addition of 10 carbon atoms located along the molecule's equator. C_{70} can be thought of as a band of hexagons capped with halves of a C_{60} molecule. The C_{70} cage possesses 5 types of inequivalent carbon atoms, unlike C_{60} where all the carbon atoms are identical. The addition of the 10 carbon atoms makes C_{70}'s long axis (pole to pole) ~ 2 nm in length, while the short axis is almost the same as C_{60}'s cross-sectional diameter. C_{70} experiences 122 intramolecular vibrational modes, with 31 of those modes IR-active.[61] Because the symmetry of C_{70} is lower than that of C_{60}, there should be more observable IR-active modes. The most intense IR-active modes detected in this work appear at 794, 1134, and 1431 cm^{-1}. Each of these peaks corresponds to an

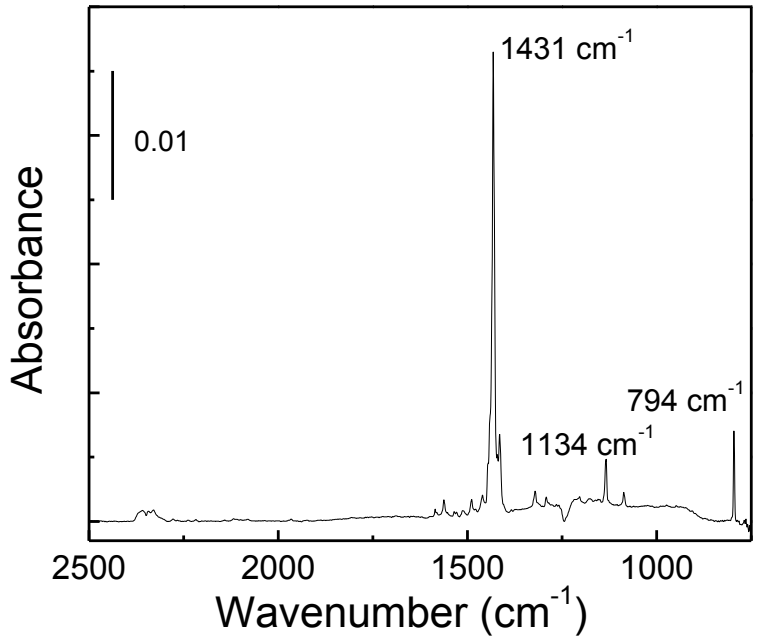

Figure 3.8: A RAIR spectrum of an unoxidized film of C_{70} on an Au slide. The peaks at 794, 1134, and 1431 cm^{-1} are characteristic of the C_{70} molecule.

E'_1 symmetry mode.[51b-d] Every other peak in the spectrum can also be assigned to the C_{70} cage, see Table 3.1. As with C_{60}, the charge transfer from the Au surface to the C_{70} cage makes some of the Raman-active modes visible in the IR spectrum.[50] The low intensity peaks seen in Figure 3.8 are attributed to the C_{70} film (i.e. intermolecular interactions) and have been observed in other experimental results.[61] A number of studies have shown that, like C_{60}, the C_{70} molecules undergo constant reorientation and molecular motion within solid films.[62] Cheng and Klein used molecular dynamics simulations to study the structure and orientational ordering of solid C_{70}. They found that under ambient conditions the C_{70} molecules rotate around the long axis and as the temperature rises (> 300 K) the molecules begin to tumble (rotating about the short axis).[62a] After Cheng and Klein's study, several other researchers used ^{13}C NMR to observe the anisotropic rotation of the C_{70} molecules.[62b, 63] Motion of the C_{70} molecules within the films is evidenced by the narrow bands observed in the IR spectra and indicates that the C_{70} molecules experience little intermolecular interaction within the unoxidized film. Because of the minimal interactions between cages, and the constant rotation of the molecules, the spectrum resembles one recorded for gas-phase C_{70}, as opposed to a solid film. This characteristic is particularly advantageous for the computational work, which was performed on the isolated gas-phase molecule.

Similar to existing reports of C_{70}, not all the IR active modes were observed in the experimental data.[61, 64] One of the main reasons all are not reported here is because of the limitations of the MCT detector. The detector used in these studies has an observational range of 4000-750 cm^{-1}. At least six intense IR active modes are located between 750-450 cm^{-1}.[61]

Table 3.1: C_{70} peaks observed in this work, with the corresponding symmetry modes. These peaks are compared to the existing literature values.

Peak (cm^{-1}) – this work	Literature Value (cm^{-1})[51a, b]	Symmetry Mode
795	795 – IR	E'_1
993	980 – Raman (calc.)	E'_2
1086	1086 – IR	A''_2
1133	1134 – IR	E'_1
1164	1165 – Raman	A'_1
1182	1182 – Raman	E'_2 , E''_1
1204	1203 – Raman (calc.)	E'_2
1222	1227 – Raman	E'_2 , E''_1
1251	1252 – IR	E'_1
1291	1292 – IR	A''_2
1321	1321 – IR	E'_1
1415	1414 – IR	E'_1
1431	1430 – IR	E'_1
1460	1460 – IR	A''_2
1488	1493 – Raman	E''_1
1511	1515 - Raman	E''_1 , E'_2
1535	1540 – Raman (calc.)	E''_1
1561	1562 - IR	E'_1
1585	1585 – Raman (calc.)	A'_1

In order to support the assignments for the frequencies observed in the experimental data, electronic structure calculations were performed on a C_{70} molecule. Previous computational studies have attempted to calculate frequencies for solid C_{70}, however, the results deviate significantly from those observed experimentally.[61, 64-65] Shinohara *et al*. used MNDO and PM3 methods to calculate the infrared absorption intensity of a C_{70} molecule. The methods produced molecular vibration frequencies that differed from the experimental values by 100-200 cm^{-1}.[64] More recently, Zandler and D'Souza found that the B3LYP functional with a 3-21G* basis set is much more appropriate for generating accurate frequency values.[55] The calculations included herein, executed with the same method as Zandler and D'Souza, have produced values within 10 wavenumbers from the experimentally observed IR peaks. In addition, similar intensities were predicted, see Figure 3.9. Most importantly, both ESC and IR data support the theory that the C_{70} molecules are rotating freely in the solid film. The narrow character of the IR peaks indicates that there is little interaction between fullerenes within the solid film. If the molecules did interact, the peaks observed in the spectra would be broad. Also, because of the strong agreement between experimental and calculated values, the calculations also support fullerenes within the

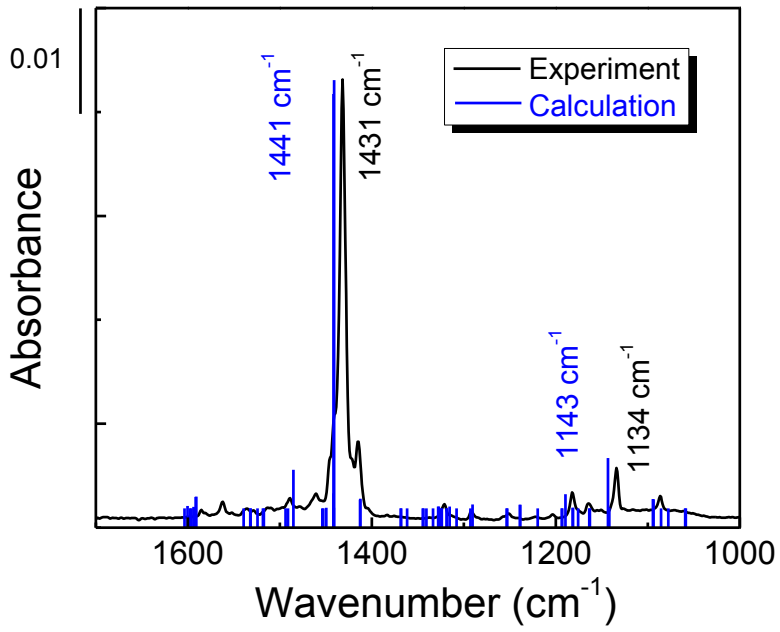

Figure 3.9: Comparison of an experimentally obtained spectrum of C_{70} (black trace) with calculated frequencies (blue lines).

film experiencing gas-phase motions. The calculations were performed on a single C_{70} molecule, expected to produce frequencies similar to those observable for gas-phase species. A rapidly rotating molecule, even within a solid film, would be expected to produce a gas-phase IR spectrum. The data showed that both the C_{60} and C_{70} molecules experienced significant rotation within the solid film.

Table 3.2: Comparison of experimentally observed and calculated frequencies for the C_{70} molecule.

Expt. Peak (cm^{-1}) – this work	Calc. Peak (cm^{-1}) – this work
795	**779**
993	**999**
1086	**1094**
1133	**1143**
1164	**1162**
1182	**1189**
1204	**1193**
1222	**1239**
1251	**1252**
1291	**1290**
1321	**1323**
1415	**1412**
1431	**1441**
1460	**1453**
1488	**1485**
1511	**1518**
1535	**1531**
1561	**1539**
1585	**1590**

3.3.3 Surface-Bound C_{76}

Although the C_{70} films provided well-resolved high resolution IR spectra, the coverage for the C_{76} film appeared to be much lower than any other system studied. Like the other surfaces made, the C_{76} film was characterized immediately after formation. Figure 3.10 shows the RAIR spectrum of a C_{76} film deposited in high vacuum. The spectrum is a plot of absorbance versus wavenumber (cm^{-1}). The spectrum recorded for the unoxidized C_{76} surface possesses less intense peaks than those observed for vapor-deposited C_{60} and C_{70}. For reasons, which have remained undetermined, formation of the C_{76} film was not as simple as the other depositions. While the data implies that C_{76} molecules were deposited onto the Au slide, it is unclear as to why the peak intensities for this particular fullerene film were significantly less than every other fullerene studied. The observed peaks at 1363, 1440, and 1517 cm^{-1} correspond with existing literature data (1371, 1441, and 1513 cm^{-1} – solid phase study).[66] Lack of intense peaks in the spectra is most likely a result of low surface coverage. A possible explanation for the difficulty in film production is the existence of contaminates within the C_{76} powder. Shown in Figure 3.10, a broad peak appears in the carbonyl region, potentially indicative of some oxidized C_{76}. To further understand this system and

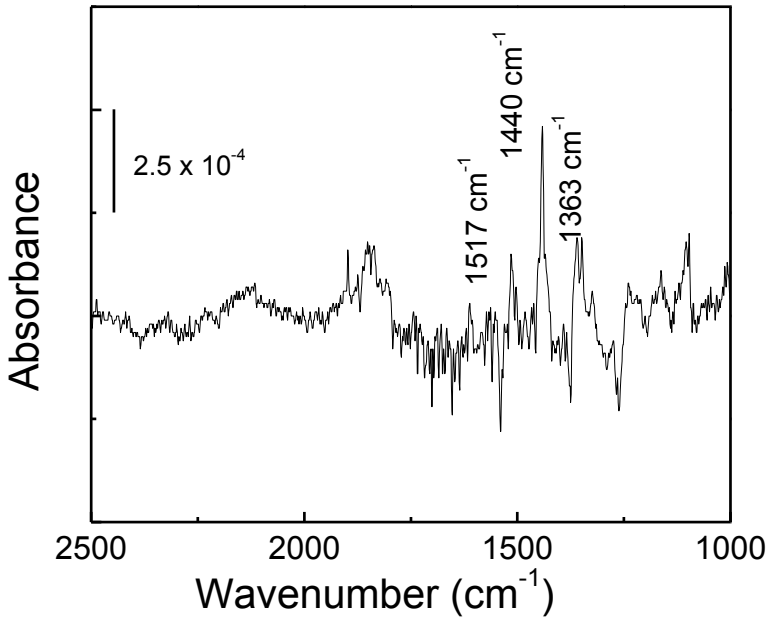

Figure 3.10: RAIR spectrum of C_{76} film on Au surface. Peaks at 1363, 1440, and 1517 cm^{-1} are characteristic of C_{76} molecule.

properly characterize the deposited films, NMR should have been performed on the starting powder used for deposition. The C_{76} powder, obtained from Bucky USA, was received and marked as > 99.9% pure, however, this should have been confirmed. Further experiments, such as XPS or TPD, could have been performed to detect the presence of impurities.

Regardless of the poor IR spectrum collected for C_{76}, the main peaks for the C_{76} film can still be correlated with frequencies from the electronic structure calculations at the B3LYP/3-21G* level. Figure 3.11 shows the experimentally observed peaks at 1363, 1440, and 1517 cm^{-1} and their corresponding calculated peaks at 1393, 1445, and 1534 cm^{-1}. The spectrum also agrees quite well with that collected by Michel *et al*. in 1994.[66]

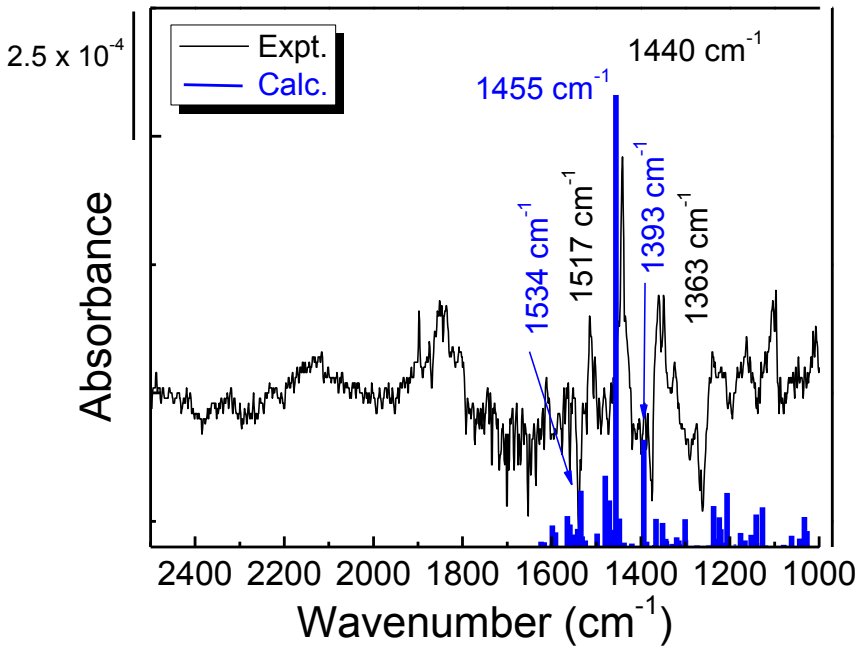

Figure 3.11: RAIR spectrum collected for a C_{76} film made in high vacuum (black trace), compared with calculated frequencies (blue lines).

3.3.4 Surface-Bound C_{78}

The C_{76} fullerene was difficult not only to deposit, but also to observe and study, while the C_{78} molecule, larger by only two carbon atoms, was easily observable. Figure 3.12 shows the RAIR spectrum of a C_{78} film deposited in high vacuum. The spectrum is a plot of IR intensity versus Wavenumber (cm^{-1}). The spectrum recorded for the unoxidized C_{78} looks very different than the ones observed earlier for smaller fullerenes. The most obvious contrast is the peak shape. In spectra of the smaller fullerenes (e.g. C_{60} and C_{70}) the peaks are very narrow and sharp. In the C_{78} spectrum, the peaks are very broad, most likely encompassing several peaks within one intense absorbance band. There are several plausible reasons for this change in the spectrum. One possible explanation for the different peak shape is the existence of multiple C_{78} isomers within the film.

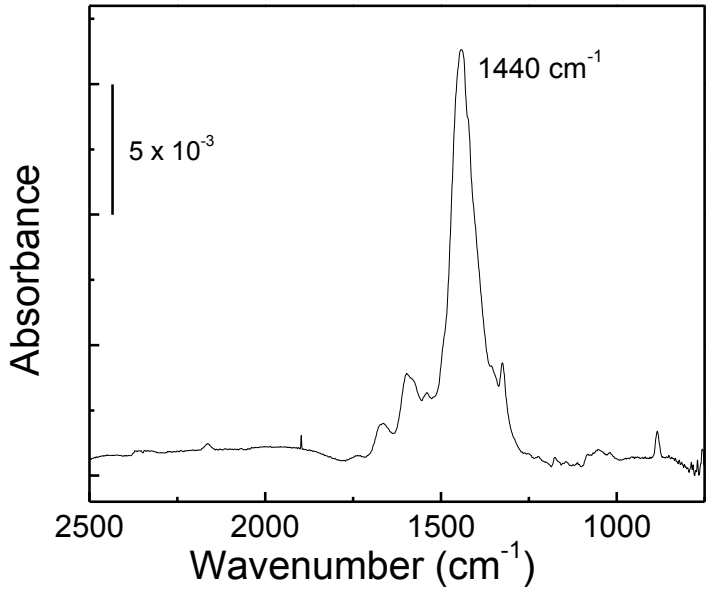

Figure 3.12: A RAIR spectrum of a C_{78} film deposited in high vacuum. The intense peak at 1440 cm^{-1} is characteristic of C_{78} molecule.

As the fullerene cages increase in size, the number of possible structural isomers increases as well. For example, C_{70} has only one isomer, C_{76} has two, and C_{78} has 5. The isomers differ in the location of the pentagon rings within the cage structure.[67] Current literature shows that each isomer possesses its own, unique IR spectrum.[53] With the possibility of several different isomers existing within the film, it is likely that the resulting IR spectrum would be a

combination of the individual isomers' IR spectra. Regardless of the isomers present, the most intense peak in the spectrum, at 1440 cm^{-1}, appears in all reported C_{78} isomer spectra. Another reason for the absence of well-defined narrow peaks is the position of the fullerenes on the surface. Many studies have shown that C_{70} molecules can exist in two orientations on the surface: laying down or standing up.[62a, 68] It is likely that the C_{78} molecules are randomly oriented, leading to broader peaks. The C_{78} molecule may have more than two surface orientations, which could also explain the peak shape in the spectra. Additionally, as the fullerene molecules increase in size the likelihood of their rotation within the film also decreases.[69] The loss of molecular rotation within the film makes the molecule's orientation a factor in the resulting peak shape. Different orientations will result in transition dipole moments in various positions, some well aligned, therefore absorbing intensely, and others poorly aligned, but still observable, leading to weak absorbance. The combination of a variety of alignments for a particular transition dipole moment will broad the peak associated with that mode. The final explanation for the peak characteristics is the continuation of Stone-Wales transformations, after deposition is complete. The Stone-Wales, or pyracylene, transformation (SWT) is a 90° bond rotation within the plane of a sp^2-carbon network. The SWT allows pentagons and hexagons to migrate over a fullerene cage surface.[70] Hawkins *et al*. found that C_{76} and C_{84} are configurationally stable up to 600-700 °C; however, at higher temperatures the pyracylene units readily rearrange, migrating pentagons in order to equilibrate the cage.[71] Since the higher fullerenes had to be deposited at temperatures above 600 °C, it is a valid assumption that there were some SWTs within the fullerene film. Even after deposition is complete the transformations will continue for some time as the surface cools to temperatures below 600-700 °C. With all of

these potential explanations for the broad peaks in the spectrum, it was even more necessary to perform calculations.

Since C_{78} has 5 different isomers, calculations on the two of the isomeric structures (C_{2v}, D_3) were completed in an effort to characterize the films and support the IR assignments. Figure 3.13 overlays the experimental IR data with two calculated spectra. The experimental spectrum shows broad peaks in the 1350 – 1700 cm^{-1} region. The computational results also produce a number of peaks in this region for both the C_{2v} and D_3 isomers. The calculations do show several larger peaks around 1200 cm^{-1} that are not observed in the experimental spectrum. Steric restrictions imposed upon the individual molecules, hindering them from experiencing all of the possible molecular vibrations, may result in fewer observed IR peaks. It is also possible that the surface contained more of a different isomer, perhaps the C_{2v}'. Regardless of the particular isomers present within the fullerene film, the absence of expected vibrational modes is an unexplained phenomenon which has been seen in experiments of C_{76}, C_{78}, and C_{84}.[53-54, 66]

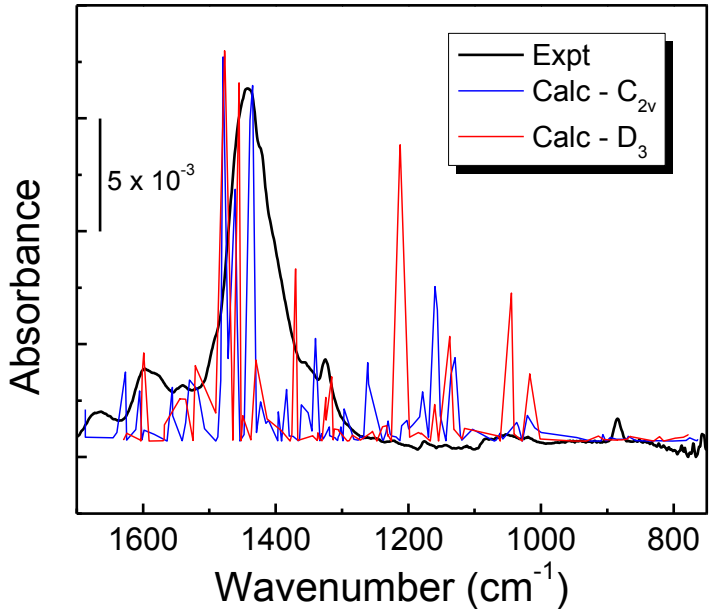

Figure 3.13: RAIR spectrum of C_{78} film deposited on an Au surface (black trace). Calculated spectra of the C_{2v} isomer (blue trace) and the D_3 isomer of C_{78} are overlaid on the experimental spectrum for comparison.

The vibrational spectra of larger fullerenes (C_n) are expected to become more complex as the size of the molecules increase. The C_{60} and C_{70} molecules possess only a few IR active

modes as a result of their high symmetry. In fact, out of the 174 intramolecular vibrations that C_{60} possesses, only 4 are IR-active. C_{70} is only slightly less symmetric, with 31 of its 122 vibration modes IR-active. Unlike C_{60} and C_{70}, spectra of the larger fullerenes have been recorded in numerous instances and always display fewer frequencies than group theory predicts. Michel *et al.* collected IR spectra of purified C_{76} in 1994, and among the 165 expected modes, only 39 were observed. The researchers attributed the absence of predicted peaks to some centrosymmetric characteristic of the molecule. They did acknowledge the fact that C_{76} has no center of symmetry but suggest that because of its near spherical shape, the molecule may still experience this phenomenon.[66] Another study, performed by Benz *et al.*, of C_{78}, which possesses five structural isomers, reported 59 observable peaks out of as many as 173 predicted frequencies.[53] Benz cites the experiments by Michel *et al.* and gives no explanation as to why the C_{78} fullerene has so few peaks in the IR spectrum. He goes on to discuss the broadening of the IR peaks at higher wavenumbers and ascribes the trend to interactions between the vibrational mode fundamentals and multiple-quantum dark states. The study does not discuss this theory in detail, but suggests that further research must be done to determine the relationship between the density of states and the resulting line widths.[53] Finally, Avent *et al.* carried out an IR study of the minor isomers of C_{84}, a fullerene with 24 different structural isomers. The 1997 study was the first to publish an experimental IR spectrum of this larger fullerene. Avent found that even MNDO theory was unable to adequately predict an IR spectrum for C_{84}.[54]

3.3.5 Surface-Bound C_{84}

The C_{84} film was characterized immediately after formation. Figure 3.14 shows the RAIR spectrum of a C_{84} film deposited in high vacuum. The spectrum is a plot of IR absorbance versus Wavenumber (cm^{-1}). Similar in peak shape to the spectrum of C_{78}, the C_{84} film also displays broad peaks. The likelihood that different isomers are contributing to the IR spectrum is even more probable with a C_{84} film because this large fullerene has 24 isomers. Another explanation for the lack of narrow peaks is the hindrance of molecular rotation within the C_{84} film. An STM study performed by Li *et al.* reports the high-resolution imaging of C_{84} molecules on cleaved GaAs(110).[69] The researchers concluded that they are able to image the large fullerene because its decreased symmetry and stronger van der Waals surface interactions lead to steric hindrance of rotation. The inability of C_{84} to rotate freely within the film, as its smaller counterparts do, could explain the difference in peak shape. In Figure 3.14, the main band of the C_{84} film appears at 1342 cm^{-1}, a position that is in agreement with the existing literature.[54]

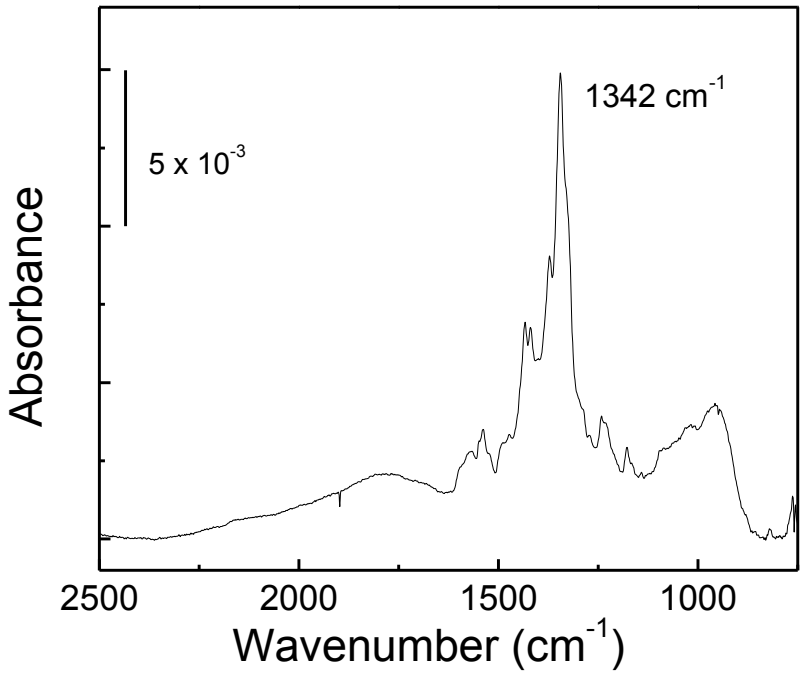

Figure 3.14: RAIR spectrum of a C_{84} film deposited on an Au slide. The intense band at 1342 cm^{-1} is indicative of a C_{84} film.

IR frequency analyses were performed on the D_2 and D_{2d} isomers of C_{84} using B3LYP/3-21G*; the resulting spectra are shown in Figure 3.15. The most intense peak in the D_{2d} spectrum does not line up with the major peak in the experimental spectrum. As with C_{78}, the presence of multiple isomers within the film (each with their own distinct IR spectrum) can account for the difference between calculated spectra and those experimentally observed. This fact is even more prominent with C_{84} because this larger fullerene possesses 24 different isomers. As stated earlier, the individual C_{84} molecules, when within a film, are hindered from rotating freely.[69] The steric hindrance of the molecules would have an effect on the resulting IR spectra. The calculations were performed on an individual C_{84} molecule, so the resulting spectrum will be most comparable with a gas-phase IR spectrum. This may be another reason for the poor agreement between calculated spectra and the experimental data collected.

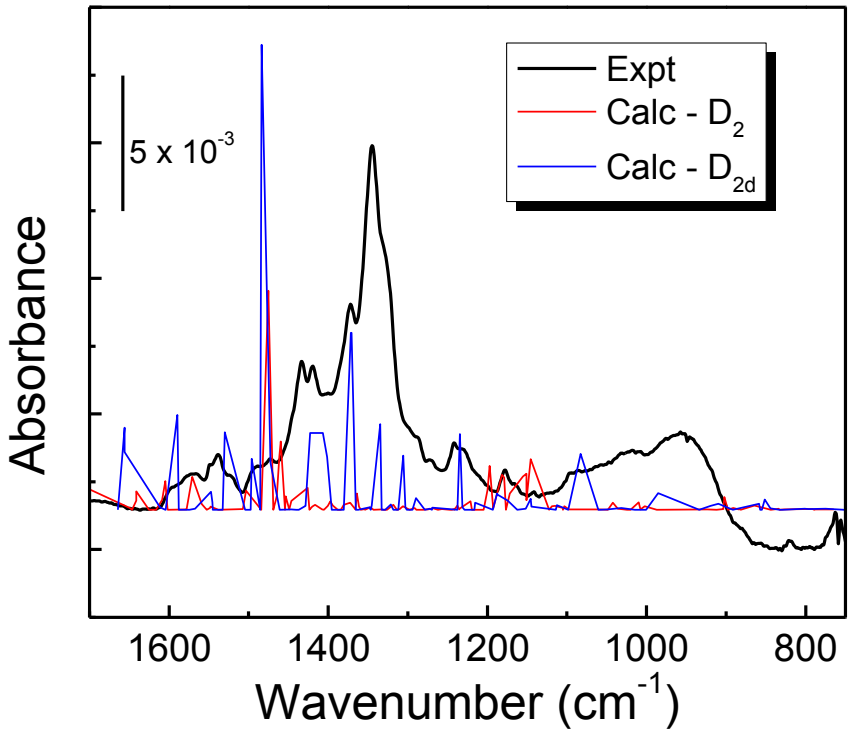

Figure 3.15: The black trace represents the experimentally-obtained RAIR spectrum of a C_{84} film deposited in high vacuum. The blue trace is the calculated IR spectrum for the D_{2d} isomer of C_{84} and the red trace belongs to the D_2 isomer of C_{84}.

3.4 Summary

Surface-bound fullerenes, C_{60}, C_{70}, C_{76}, C_{78}, and C_{84} were characterized with reflection-absorption infrared spectroscopy and density functional theory calculations. While some literature does exist reporting the IR frequencies for each of these molecules, in most cases, it was recorded for gas or solution phase samples. IR frequencies can shift based on the nature of the sample, therefore it was necessary to characterize each of these molecules as films on Au surfaces. The IR spectra for C_{60} and C_{70} agreed well with current reports and the calculations produced similar frequencies and intensities. For the three larger fullerenes, while there are some similarities between the experimental and computational data, and existing studies, more research is required to definitively assign the IR spectra.

With the fullerene films characterized, the next goal was to expose the surfaces to ozone and determine how the molecules were affected. RAIRS and DFT were utilized again, along with MS and XPS.

Chapter 4

The Reaction of Ozone with Surface-Bound C_{60}: Mechanism and Kinetics

4.1 Introduction

The overall state of the environment, including the fertility of the soil, the cleanliness of the water, and the breathability of the air is affected by many factors. The fact is, everything that occurs on this planet (e.g. volcanic eruptions, chemical reactions on stratospheric ice crystals), and some events – off the planet (e.g. solar flares), has an effect on the environment. Admittedly, some factors impact the planet more than others; regardless, before the environmental effect can be properly characterized, fundamental information must be acquired. In this instance, the influential reaction is that between ozone, a significant pollutant, and fullerenes, unique molecules with many uses and applications. It must be determined whether or not the ozone oxidation of fullerenes alters the molecules in such a way that they begin to interact with the environment in a different, more harmful manner. In their unoxidized form, fullerenes are hydrophobic and do not have any known negative effects for humans and animals. Upon oxidation, however, the molecules may become hydrophilic, allowing them to be easily transported through water, soil, air, and the human body.

The research presented in this chapter was conducted in an effort to address two of the three main experimental goals of this work. First, the goal was to determine a mechanism for the oxidation of C_{60}. Second, the intention was to gain initial insight of the oxidation of C_{60}.

4.1.1 C_{60} Surfaces

Fullerenes have been used in a number of fields, such as organometallic chemistry,[72] superconductor development,[73] medicine,[74] and surface science.[75] As discussed in

Chapter 1, there are numerous sizes of fullerenes, each possessing unique properties. Films of C_{60}, in particular, are used to make organic field effect transistors,[76] anodes for lithium secondary batteries,[77] and thin-film solar cells,[78] just to name a few applications. Since these molecules are used in a wide variety of scientific studies, it is important to understand and sufficiently characterize the structure and properties of fullerene films.

Researchers began studying the properties of C_{60} films on various metal surfaces shortly after the molecule was discovered in 1985.[79] Only five years after the discovery of C_{60}, members of the IBM Research Division in San Jose, California obtained Scanning Tunneling Microscopy (STM) images of C_{60} clusters on an Au(111) crystal.[80] The fullerenes were sublimed onto a piece of gold foil, and then transferred to the Au crystal by placing the fullerene-coated foil 3 cm away from the crystal and flash heating the foil to 800°C. The STM images revealed roughly spherical features on the surface. The features formed mobile hexagonal arrays with an intercluster spacing of 11.0 Å.[80] The ability to form films of C_{60} molecules on a metal surface opened the door for further investigation into the properties of these organic thin films. Studies showed that films of C_{60} could be used to create transistors because of their significant charge carrier mobility.[81] They can also be super solid lubricants as a result of the film's ability to reduce friction and adhesion.[82] Numerous groups went on to study C_{60} films on a variety of different metal surfaces,[79] each metal surface having its own effect on the fullerene film. For the purposes of this document, the following section will only focus on the studies of C_{60} films on Au surfaces.

Solid C_{60}, although considered a van der Waals solid,[83] experiences some interactions with Au surfaces upon the formation of thin films.[79] A study performed by Ohno *et al.* focused on the interaction of C_{60} with a few different metal surfaces, including Au. The results showed that, regardless of the variation in work-functions, the C_{60} energy levels aligned to the Fermi

level for *all* of the metals investigated.[84] C_{60}'s unique ability to mix the lowest unoccupied molecular orbital (LUMO) with states of the metal substrate explains why charge transfer from the Au surface to the fullerene cages can be observed. Another study by Hunt *et al*. quantifies the charge transfer from the Au surface to be ~ (1±1) electrons per cage. This significant charge transfer results in a strong binding of fullerenes to the Au surface; a value for the binding energy of approximately 1.3 to 2.6 eV has been measured and determined by a number of experimental and theoretical studies.[79d] So even with no chemical bonding present, the manner in which fullerenes associate and situate themselves on a surface is dependent upon the specific surface.

Extensive experiments have been performed to determine the structure of C_{60} films on Au surfaces,[79b, 84-85] which turns out to be a very complex topic. Studies show that when C_{60} is deposited on a gold surface, whether by vapor deposition, sublimation, or drop-casting techniques, the fullerene monolayer begins to form at step edges, Au atom vacancy islands, and other defects in the Au surface.[79b, 85b, 86] Fullerene nucleation at these types of sites first forms short chains of molecules that grow into small compact C_{60} islands. As deposition continues, the islands grow into domains; the domains enlarge and eventually grow together, imparting characteristics within the film like point defects, domain boundaries, and surface faceting. Research shows that there are at least 3 different lattice packings observable in C_{60} monolayers on Au(111). The most common structures of the C_{60} films on Au are $2\sqrt{3}$ x $2\sqrt{3}R30°$ and 7 x7 $R0°$. The $2\sqrt{3}$ x $2\sqrt{3}R30°$ structure is considered the ground state arrangement. Understanding the structure and configuration of C_{60} films is important, but a more relevant consideration for the included studies is the stability of the C_{60} films, especially in a vacuum environment.

4.1.2 Fullerene Surface Stability

The ability to make a stable, reproducible fullerene surface is imperative to these studies. Previous research provides a detailed picture of fullerene films on a variety of different metals, especially gold. A valuable observation of the structural studies of fullerene films is the

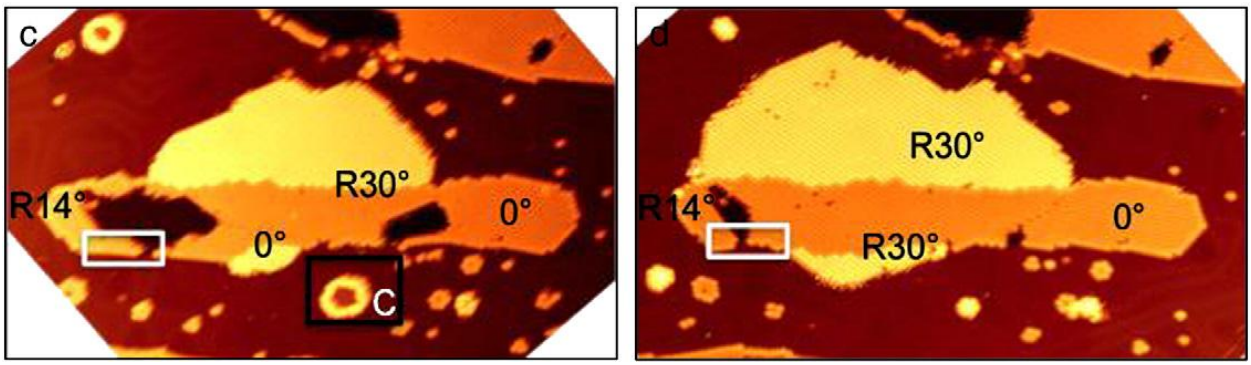

Figure 4.1: STM images of C_{60} grown on a Au(111) surface. The image on the left shows the surface after 0.175 ML of C_{60} have been deposited. The image on the right shows the same surface, without further deposition, 10 hours later.[85b] Reprinted from *Surface Science, 604,* 1310-1314, Copyright 2010, with permission from Elsevier.

significant mobility of the fullerenes on the Au surface. Figure 4.1 shows two STM images from a study performed by Tang *et al*.[85b] The images were obtained from the same area of one sample. The only difference between the two images is the amount of time that elapsed between image collection. The image on the left shows 0.175 monolayers (ML) of C_{60} on the Au. The image on the right is the same sample shown on the left, only after 10 hours in a room temperature, UHV environment.[85b] Since there were no additional fullerenes added to the surface in the time between imaging, it is apparent that the C_{60} molecules diffused from other sites on the surface. This same study also observed the reorganization of the fullerene layers over time. Figure 4.2 shows the change in lattice structure after the sample was aged in vacuum for 10 hours.[85b] In the top panel of Figure 4.2, A and B denote areas with the *R*0° orientation, nestled next to a large domain with *R*30° structure. After 10 hours, the bottom panel of Figure 4.2, shows the entire region rearranged to the *R*30° structure. It is apparent from these images that the first monolayer

of C_{60} on Au is very mobile and can rearrange to the most favorable structure if given enough time. Tang's study indicated that all of the observed film structures were stable in UHV for prolonged time periods. It is important to point out that Tang's study only investigates the structure of films comprised of < 5 layers of C_{60} molecules. The possibility of hindering the molecules' migration/rearrangement on the surface must be considered if thicker films (> 10 nm) are deposited. The result of hindering surface migration may be a large variety of lattice packing within the film. The literature also shows that the C_{60} molecules experience significant rotation in solid films and on surfaces.[56] Free rotation of the molecules can have an impact on the collected spectroscopy data as well as their reaction with other species.

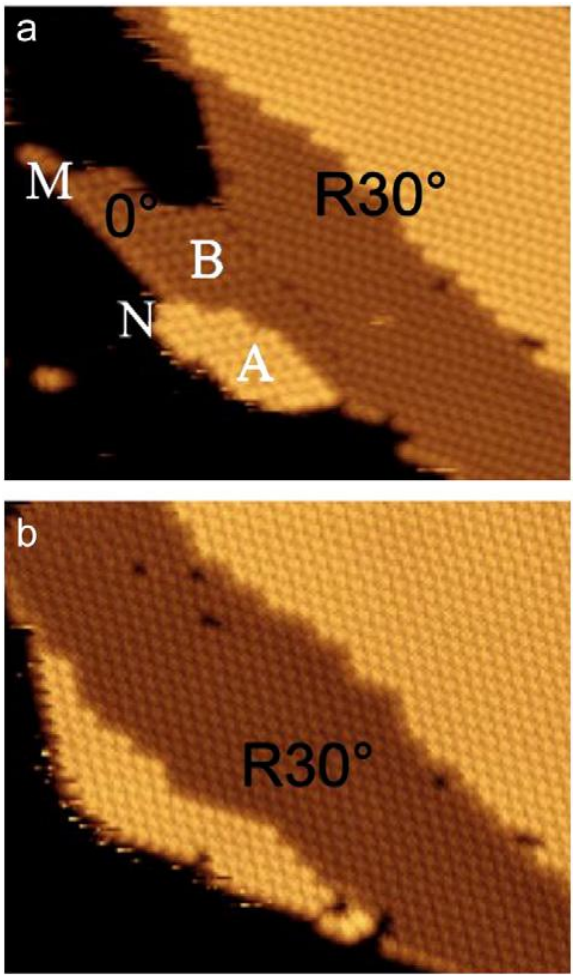

Figure 4.2: STM images from a study performed by Tang *et al.* The top panel shows two different lattice packing structures. The bottom panel is an image of the same area shown in the top panel. The bottom image was taken 10 hours after the top one. Obvious rearrangement of the film has taken place, resulting in the entire area having a *R*30° orientation.[85b] Reprinted from *Surface Science, 604,* 1310-1314, Copyright 2010, with permission from Elsevier.

4.1.3 Ozone

The other reactant in the system is the highly oxidizing pollutant, ozone. Ozone is a reactive and extremely unstable molecule. Ozone is found naturally in small concentrations in the stratosphere, the upper layer of the Earth's atmosphere, as well as in the troposphere, the lowest layer of the atmosphere. Ozone, in the troposphere, is a product of air pollution from a number of different

sources, such as automobile exhaust and industrial emissions. The molecule reacts readily with unsaturated hydrocarbons, making C_{60} a prime candidate for ozone oxidation.

4.1.3.1 Reactions of Ozone and C_{60}

The solution phase reaction of ozone and C_{60} has been studied in much detail.[11a, 11d, 11f, g, 36, 60a-d, 87] Research shows that ozone reacts with C_{60} in the same manner as other alkenes; via a 1,3 dipole addition to the double bond. In 2000, Heymann *et al.* were able to detect and isolate the primary ozonide of C_{60} ($C_{60}O_3$).[36] They were also able to determine the reaction site on the C_{60} cage was a 6,6 bond (double bond), as opposed to a 5,6 bond. Figure 4.3, structure A, shows the proposed structure of the 6,6 closed adduct $C_{60}O_3$. Based on Criegee's mechanism for the ozonolysis of alkenes, once the primary ozonide forms, it should decompose into the Criegee Intermediate, an unstable diradical species, Figure 4.3, structure B. The Criegee Intermediate can then rearrange to form a secondary ozonide or react with other species to form a wide variety of products.[88] A strong motivation for this research is the fact that neither the primary ozonide nor the Criegee Intermediate of C_{60} have been observed at the gas-surface interface.

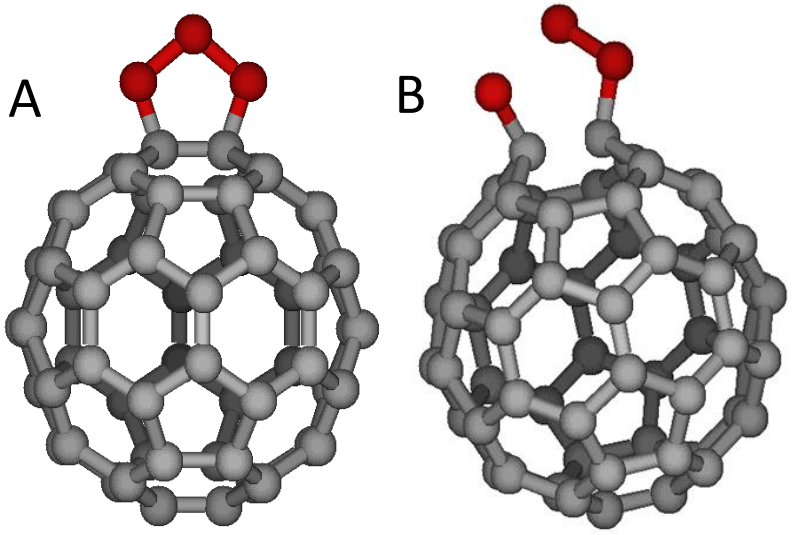

Figure 4.3: Structure A is the proposed configuration of $C_{60}O_3$. Structure B is the proposed configuration of the Criegee Intermediate of $C_{60}O_3$.

4.1.4 Objectives

The objectives of the research described herein were to develop a detailed description of the reaction mechanism between C_{60} and ozone. The intended goals were to observe any and all intermediates and products formed as a result of ozone exposure, as well as determine which pathways must be followed to lead to the observed species. From a kinetic view, the initial

reaction probability (γ) was measured. Along with the initial reaction probability, the rates of formation and decomposition for the various intermediates and products were determined. Intermediates and products were associated with one another based on similar rates. The correlation was used to propose reaction pathways and a mechanism. Finally, activation energies for various species were calculated to describe the kinetics. These objectives were met by exposing C_{60} surfaces, made in high vacuum, to high concentrations of gas-phase ozone. Since the C_{60} surfaces were made by vapor-deposition of fullerenes onto clean Au slides, RAIRS was utilized to observe the surface changes in real-time. Support for the IR assignments was provided by XPS and Electronic Structure Calculations (ESC). By obtaining a detailed understanding of this reaction, the environmental fate of fullerenes after their reaction with prominent pollutants, such as ozone, can be predicted.

4.2 Experimental Details

4.2.1 Materials

All chemicals were used as received without further purification unless otherwise noted. The C_{60} fullerene powder was obtained from BuckyUSA (BU-604, > 99.9%). Methylene Chloride (HPLC grade), NH_3 gas (> 99.9%), and silica gel (grade 03) were obtained from Sigma-Aldrich, Inc. Research grade oxygen, ultrahigh purity nitrogen, liquid nitrogen, and dry ice were purchased from Airgas Specialty Gases. Isotopically labeled oxygen ($^{18}O_2$, 97%) was obtained from Cambridge Isotope Laboratories. Polycrystalline gold substrates were received from Evaporated Metal Films. Reagent grade acetone was obtained from Pharmco-Aaper and Commercial Alcohols.

4.2.2 Ozone Synthesis and Storage

Caution: Ozone is a VERY TOXIC, DANGEROUSLY REACTIVE, OXIDIZING gas.[40]

Special precautions should be made when working with this chemical.

The full details of the synthesis and storage of ozone is described in Chapter 2. A shortened account is contained here. Ozone was produced using a commercial generator from Ozone Solutions (model: SR-32). The generator uses research grade oxygen and a corona discharge setup to create a mixture of O_2/O_3. The O_2/O_3 mixture, which only contains ~2% O_3, was flowed through a custom-made glass trap. The trap was filled with high surface area silica gel (Sigma-Aldrich, grade 03, >8 mesh), and held at a constant temperature of -79°C. Silica gel with a high concentration of ozone adsorbed to its surface takes on a violet color, see Figure 4.4. It took approximately eight hours to fill the entire trap with ozone. To warm up the ozone for use, the dry ice was removed from the Dewar. After removing the dry ice, room temperature acetone was added to the Dewar until the bath height completely covered the silica gel in the trap. While acetone was added to the Dewar, the trap was pumped on with a mechanical pump. The pump was used until the temperature of the bath reached -55°C; pumping until that temperature was

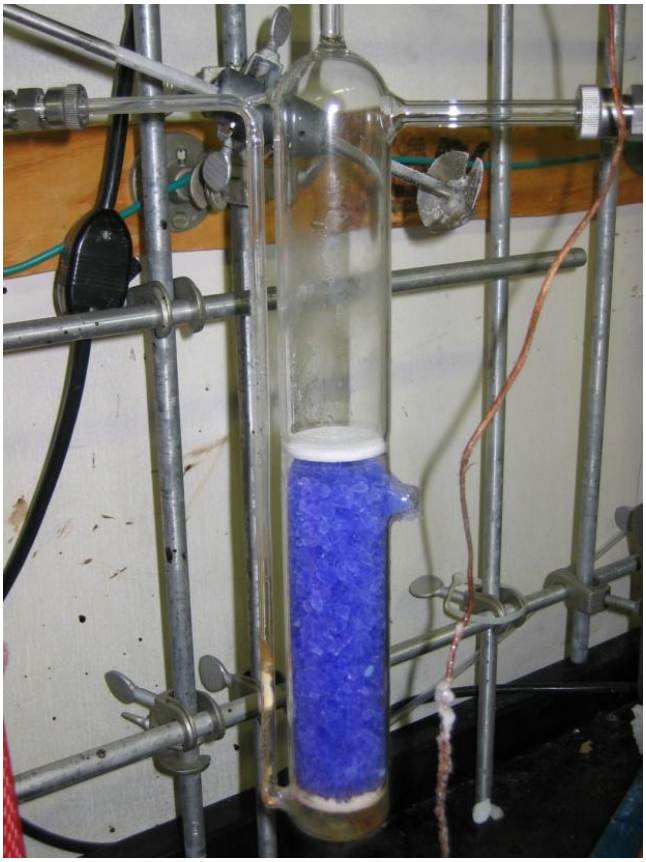

Figure 4.4: Ozone trap filled with high surface area silica gel. The silica gel is purple because it has ozone adsorbed to its surface.

reached helped to remove any O· and O_2 impurities and purify the ozone. When the acetone bath reached -55°C (the temperature at which ozone desorbs from silica gel), the valve between the trap and the mechanical pump was closed and the ozone was directed through a UV-Vis flow cell and into the capillary array doser (CAD). The UV-Vis flow cell was positioned directly behind the CAD, so the ozone concentration was monitored immediately before it entered the chamber. Typically, the acetone bath was held at -55°C, however, the temperature could be changed to alter the amount of ozone desorbing from the silica gel and therefore adjust the flux of ozone onto the surface. The average dosing pressure of ozone was ~25 Torr.

To determine the concentration of ozone, the absorbance value (measured at 254.04 nm) was recorded from the UV-Vis spectrometer (StellarNet, Inc., model: EPP2000). The ozone absorbance was used with Beer's Law, shown in equation 4.1,

$$A = \varepsilon \mathrm{b} C \tag{4.1}$$

where A is the absorbance, ε is the molar absorptivity, b is the path length, and C is the concentration.

4.2.3 Formation of C_{60} Surfaces

Fullerenes were deposited on polycrystalline gold slides. The slides were purchased from Evaporated Metal Films, Inc. They were made by first depositing a 50 Å thick layer of chromium onto a glass slide, then depositing ~1000 Å of Au. The dimensions of the slides are 1" x 1" x 0.062". The Au slides were cleaned before introduction into the UHV chamber, by submersion into a solution of 70% sulfuric acid and 30% hydrogen peroxide (30%), also known as piranha solution, for ~45 minutes. *Warning: Piranha solution is an oxidizing agent which reacts violently with organics! Extreme caution should be taken when using this solution!* Once the Au slides were removed from the piranha, they were rinsed thoroughly with deionized water

(Millipore Purification Systems, 18.2 MΩ), and then dried completely with UHP nitrogen. After drying, the slide was placed into the UHV chamber, and then cleaned with ozone for one hour. The piranha solution was used to remove the majority of the hydrocarbons that adsorb to the surface from exposure to air. When the surface was mounted in the UHV chamber, ozone was used to remove any remaining hydrocarbons. After one hour of ozone exposure, the cleaned Au slide was scanned with the IR spectrometer; this scan is called a background scan. The background is saved and the Au slide is transferred into the load lock to deposit C_{60}. Full details of the actual deposition procedure can be found in Chapter 2.

4.2.4 Surface Exposure

After the fullerenes were deposited onto the Au slide, the slide was transferred back into the main chamber. Once the slide was positioned as close as possible to the original position (IR position before C_{60} deposition), it was exposed to mid-infrared radiation (MIR). Since difference spectra were acquired, it was very beneficial to position the slide in the same location before and after deposition. Optimal positioning ensured the baseline was as flat as possible and resulted in less noise in the spectra. This practice is made easier by remembering to record the coordinates (X, Y, and rotation) on the manipulator before transferring into the load lock for deposition. Upon proper realignment of the sample, the fullerene surface was scanned to obtain a spectrum of the sample before ozone exposure. With an initial spectrum recorded, then saved as a background, the first spectrum before opening the ozone doser should be a perfectly flat line positioned exactly at 0 on the intensity scale (y-axis). The ozone was then introduced into the main chamber via the CAD.

4.2.5 Reflection-Absorption Infrared Spectroscopic Measurements

The reaction of gas-phase ozone with surface-bound C_{60} was followed in real-time with a Bruker IFS 66v/S spectrometer. The spectrometer was equipped with a SiC globar source, which produces a beam of MIR. The IR beam was focused onto the Au surface in the middle of the UHV chamber at an incident angle of ~86° relative to the surface normal. The detector used with the Bruker spectrometer was a mid-range MCT detector (750 - 4000 cm^{-1}), that required cooling with liquid nitrogen. Every spectrum shown in this dissertation was produced by the average of 100 scans acquired over 90 seconds. The resolution was set at 2 cm^{-1} and the scanner velocity was held at 20 kHz.

4.2.6 Infrared Spectral Analysis

RAIRS is a surface-sensitive technique used to observe the decomposition of original surface species and the formation of surface intermediates and final products. The characteristics of the actual RAIR peaks can also tell the researcher a great deal about the orientation of molecules on the surface. While this chapter will discuss, in detail, all of the peaks observed, a great deal of focus will be on three main peaks. The first two are well-known IR active modes for C_{60}: 1182 and 1428 cm^{-1}. The other peak is representative of an intermediate species and is easily followed because of its significant IR activity. All reactant, intermediate, and product peaks were integrated and analyzed using two programs: OPUS® software (same software used to record the IR data during ozone exposures) and Origin Software. Individual macros were written to integrate the area under the curve of each peak (both positive and negative) during the reaction. These macros allow for data analysis to be performed in a reasonable amount of time for large quantities of data.

4.2.7 X-ray Photoelectron Spectroscopic Measurements

The C_{60} surfaces were characterized before and after ozone exposure using a X-ray photoelectron spectrometer (XPS), which is described detail in Chapter 2. Since the XPS was incorporated into the chamber setup, data was collected without removing the surface from vacuum. This configuration was beneficial because some species formed during ozone exposure may not be stable in air, so scanning the surface directly after dosing made it possible to observe species that might be elusive outside of a vacuum environment. To perform XPS analysis in the main chamber, the sample was rotated into position using the 360° rotatable manipulator. The sample is positioned relative to the hemispherical analyzer (HA), to the desired angle of detection. If the sample is situated in front of the HA so that the HA is normal to the surface, the position is optimum for sampling below the surface interface; detecting photoelectrons from the deepest elements accessible to the instrument. If the surface is aligned at a 15° angle with respect to the HA, it is known as a grazing angle, which is ideal for studying molecules at the surface of the sample. Once the sample was positioned, a Mg Kα (1253.6 eV) x-ray source was used at 250 W (12.5 kV and 20 mA). The impinging x-rays produced photoelectrons, that were subsequently detected with the HA. A survey scan was collected first to get a general idea of the elemental composition of the surface. After the survey scan was inspected, high resolution scans of observed elements were taken using more selective pass energies.

4.2.8 Temperature Programmed Desorption Measurements

The Extrel mass spectrometer was used to perform temperature programmed desorption (TPD) measurements. TPD is a method for observing the controlled desorption of molecules from a surface. Once the C_{60} surface was attached to the manipulator, it was heated in order to desorb the fullerene molecules. The molecules were then detected with the Extrel mass

spectrometer. This technique can be used to determine the heat of adsorption, gather information about the coverage, and obtain kinetic information about the desorption process.

4.3 Results and Discussion

4.3.1 Ozone Exposure of Surface-Bound C_{60}

The RAIR spectra for the reaction between gas-phase ozone and surface-bound fullerenes are shown in Figure 4.5. More specifically, Figure 4.5 displays difference spectra recorded during the gas-surface reaction. Difference spectra are created by subtracting the original

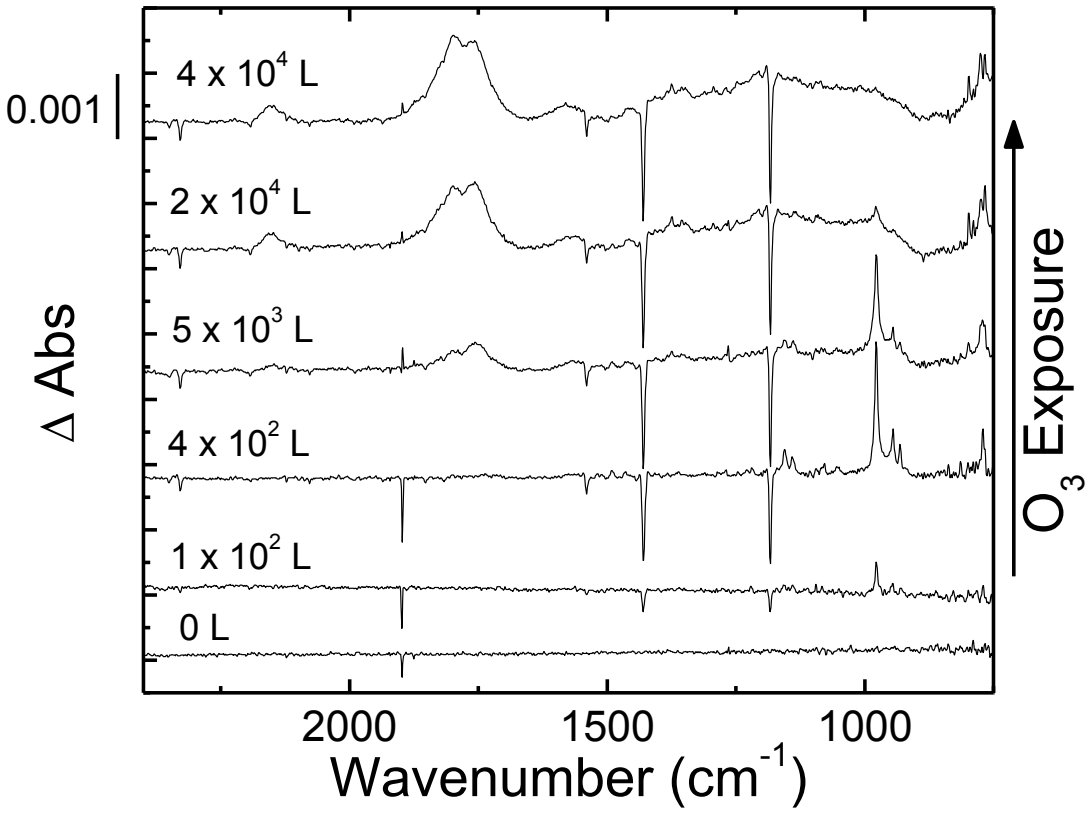

Figure 4.5: Difference spectra recorded during a 3.5 hour ozone exposure of a C_{60} surface. The amount of ozone exposure is indicated in Langmuirs (L) above the specific spectrum. In less than a minute (100 L), ozone has begun to react with the fullerenes and form new IR active species on the surface. After 90 seconds (400 L), six intermediate peaks appear. As exposure continues, the initial six peaks disappear and new peaks arise in the carbonyl region and around 2150 cm^{-1}.

spectrum from the new one. The result of this subtraction is any negative peaks that appear in a spectrum represent species on the surface that are consumed, or reacted; positive peaks

correspond to new features. In this instance, the difference spectra were created by saving the spectrum of an unoxidized C_{60} surface (Figure 3.1) as a background (or original spectrum) and then subtracting that background from each new scan.

In the first 90 seconds (~400 Langmuirs (L); L = 10^{-6} Torr·s) of ozone exposure, the IR active modes of the C_{60} molecules (1428 and 1182 cm^{-1}) decreased. The decrease was due to reaction on the fullerene molecules. The reaction altered the symmetry of the molecule, and changed the observable IR active modes, therefore resulting in a decrease in the peaks at 1428 and 1182 cm^{-1}. While the peaks due to the fullerenes decreased, there was a simultaneous growth of several new peaks. Figure 4.6 shows the six peaks that developed immediately upon ozone exposure. Based on Criegee's mechanism for ozonolysis of olefins,[88] ozone reacts with a double bond to form the primary ozonide (PO). The PO, a very unstable species, thermally decomposes to form the Criegee Intermediate (CI) and a carbonyl species.

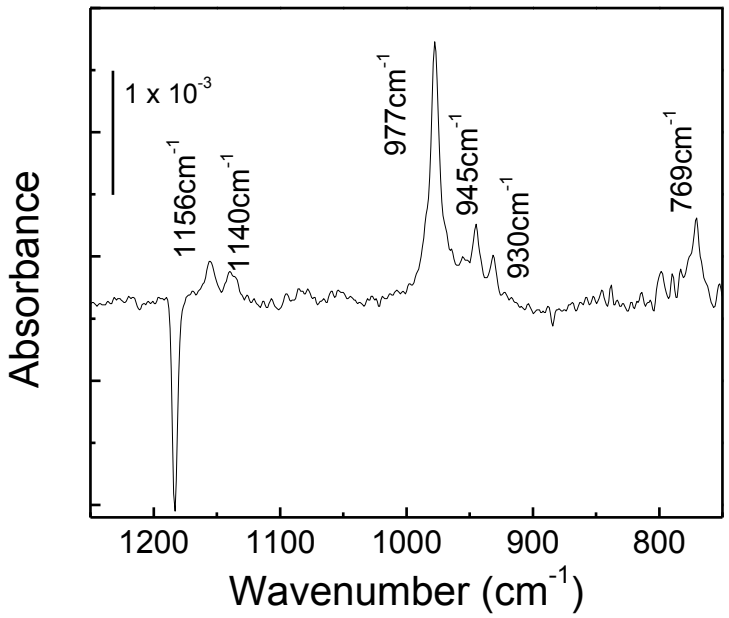

Figure 4.6: Enlarged view of a RAIR spectrum recorded after only 90 seconds of ozone exposure. The six peaks present all exhibit intermediate behavior.

Electronic structure calculations were used to help assign vibrational modes that developed during O_3 exposure. The close agreement (5 and 6 cm^{-1}) between the frequencies calculated for the unoxidized C_{60} molecule (see Chapter 3, pg. 68) and the experimentally

obtained values suggested acceptable frequencies for the oxidized fullerene would also be calculated.

The first calculations performed were a geometry optimization and frequency analysis of the proposed structure for the primary ozonide of C_{60}. Based on existing literature, the most likely reaction site on the C_{60} cage is the 6,6 (or double) bond.[37-38, 87h, 89] The 6,6 bond is defined as a border between two hexagonal rings and, of the two types of bonds in the molecule, possesses slightly more double bond character than the 5,6 bond (found between a pentagon ring and hexagon ring).[1] The structure used for modeling was setup with the ozone molecule addition across one of the 6,6 bonds. One of the resulting vibrational modes (shown in Figure 4.7) was found to correspond with the symmetric stretch of the ozonide ring. The possibility that the peak at 977 cm^{-1} represented the symmetric stretch of the ozonide was considered, however a conclusion cannot be drawn based solely on calculations.

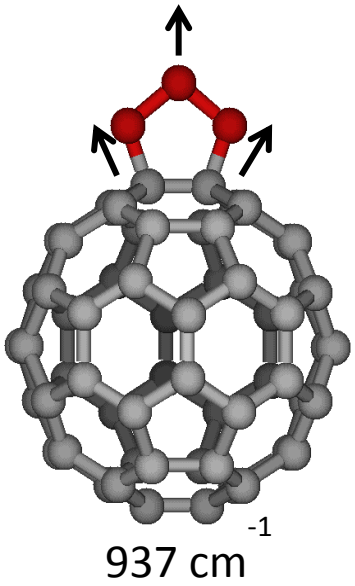

Figure 4.7: Vibrational modes of the primary ozonide of C_{60} ($C_{60}O_3$) calculated with B3LYP/3-21G*.

While this is the first UHV surface science study of the reaction between C_{60} and ozone, there have been extensive studies performed on this system in the liquid phase.[11a, 11f, g, 60a, 60c, d, 87c, d, 90] Cataldo studied C_{60} in numerous solvents,[11a, 11f] reported products formed, rates of product formation, and the observation of the PO of C_{60} in an investigation carried out with several other researchers.[36] The PO was observed in a C_{60}/toluene solution after an oxygen/ozone mixture was bubbled through at 0°C. The $C_{60}O_3$ intermediate thermally dissociated into the epoxide, $C_{60}O$, and liberated O_2.[36]

With precedence in the literature, the preliminary assignment of 977 cm^{-1} to the PO of C_{60} seems reasonable. The final set of experiments performed to confirm the assignment were exposures with isotopically-labeled ozone. The C_{60} surface was dosed with ^{18}O labeled ozone. Based on equation 4.2, Hooke's Law, the intermediate and product peaks were expected to red-shift due to the presence of $^{18}O_3$. In Hooke's Law, ν represents the natural frequency, k is the spring constant, and μ is the reduced mass of the atoms involved in the vibrational mode of interest.

$$\nu = \frac{1}{2\pi}\sqrt{\frac{k}{\mu}} \tag{4.2}$$

Figure 4.8 compares the PO peak for an $^{16}O_3$ exposure and an $^{18}O_3$ exposure. As predicted using Hooke's Law, the peak at 977 cm^{-1} has red-shifted as a result of dosing with ^{18}O labeled ozone; specifically, the peak shifts 9 cm^{-1}, to 968 cm^{-1}. To help identify the species associated with the peak at 977 cm^{-1}, additional calculations were completed. The calculations should produce frequencies that exhibit the same change in frequency, or shift, as that observed in the experimental data. However, one important aspect must be taken into

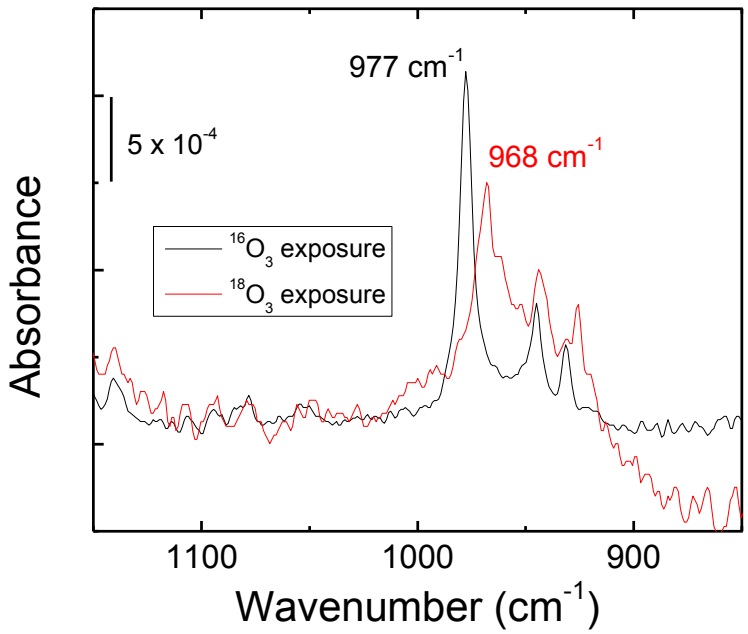

Figure 4.8: RAIR spectra from two different ozone exposures of C_{60} surfaces. The black trace is a spectrum from an experiment where a C_{60} surface was exposed to $^{16}O_3$. The red trace is from an experiment where a C_{60} surface was exposed to $^{18}O_3$.

consideration first: the likelihood of at least five different combinations of ^{18}O and ^{16}O to form ozone (e.g. ^{18}O-^{18}O-^{18}O, ^{18}O-^{18}O-^{16}O, ^{18}O-^{16}O-^{18}O, ^{18}O-^{16}O-^{16}O, ^{16}O-^{18}O-^{16}O). Each different grouping of the oxygen atoms results in an altered shift in peak position. In order to simplify the calculations required, the ozone was characterized during dosing with the mass spectrometer. Figure 4.9 shows the signal for $^{18}O_3$ and $^{16}O_3$ during the exposure. The masses for all other combinations of ^{18}O and ^{16}O ozone were also monitored. The only mass detected was that for $^{18}O_3$. With the determination that all of the ozone formed was $^{18}O_3$, a geometry optimization and IR frequency analysis were performed on $C_{60}{}^{18}O_3$.

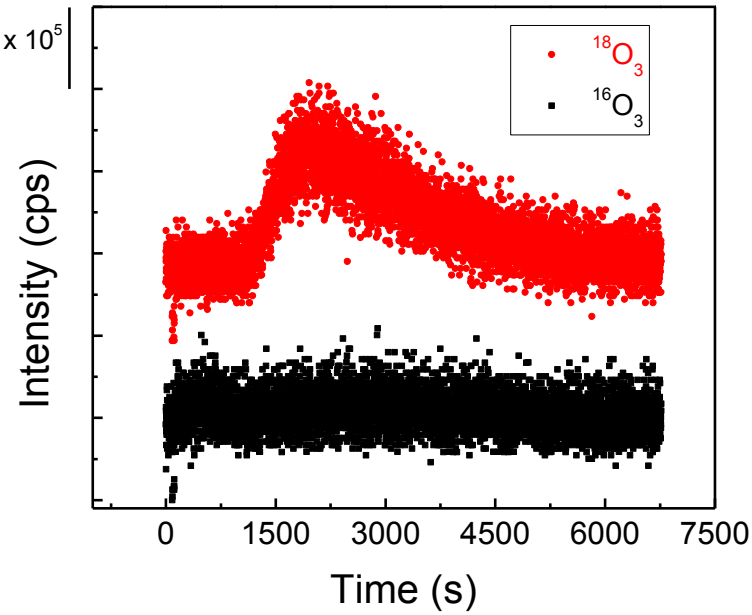

Figure 4.9: The mass spectra for $^{18}O_3$ and $^{16}O_3$ recorded during the isotopically-labeled exposure of C_{60}. The data implies that the surface was exposed to $^{18}O_3$.

Upon comparing the $^{18}O_3$ and $^{16}O_3$ calculations, the frequency due to the symmetric stretch of the ozonide ring shifts to 908 cm^{-1}. While the shift is to lower frequencies, the change in frequency is too large (difference of 29 cm^{-1}, instead of 9 cm^{-1}). Because the amount in which the peaks shifted was not the same between experiment and calculation, it is probable that the peak at 977 cm^{-1} is not due to the symmetric stretch of the primary ozonide. All other calculated frequencies were animated to determine which motion experienced a 9 cm^{-1} peak shift with inclusion of heavy ozone. The only frequency that underwent a similar shift was due to the stretching of the C-O bonds of the ozonide ring. The C-O bonds stretch in opposite directions,

shown in Figure 4.10, and with $^{16}O_3$ the calculated frequency was 924 cm^{-1}. When the calculation was performed with $^{18}O_3$, the resulting frequency was 913 cm^{-1}. The difference of 11 cm^{-1} is the only observed peak shift that is comparable to the experimental value. Based on these results, the peak at 977 cm^{-1} is assigned to the C-O stretches of the primary ozonide ring.

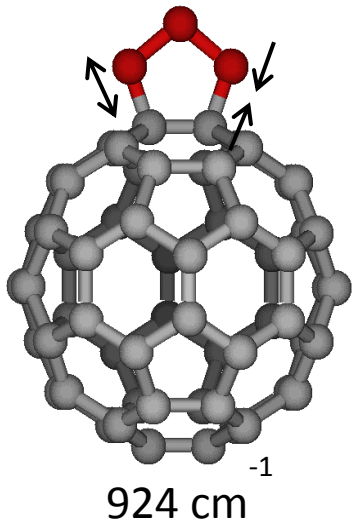

Figure 4.10: The calculated frequency for the C-O stretching of the PO.

To determine whether any of the other early peaks are due to the PO, experiments in which the flux of ozone was reduced significantly were performed in an effort to reduce the rate of the initial reaction. The goal of these experiments was to stagger the appearance of the peaks. The peaks that come in first should, in principle, be due to the PO and the peaks that appear later, representative of the Criegee Intermediate. The low flux exposures resulted in the appearance of only one peak, at 977 cm^{-1}, shown in Figure 4.11. When the peak at 977 cm^{-1} was monitored throughout the rest of the exposure, behavior indicative of transient species (i.e. intermediates) was observed, depicted in Figure 4.12. Figure 4.12 shows the integrated change in area of the peak at 977 cm^{-1} as a function of the total flux of ozone. Upon ozone exposure, a finite number of primary ozonides were formed, which resulted in a maximum intensity of the peak at 977 cm^{-1}. The primary ozonide, a short-lived species, decomposed; the PO decomposition caused the peak at 977 cm^{-1} to decay, until it completely disappeared (~3.5 hrs. after ozone exposure began). The data continued to support the hypothesis that the peak at 977 cm^{-1} represented the PO. When the other five peaks shown in Figure 4.6 were monitored, the changes in peak intensity over time were consistent with intermediate species. The other intermediate peaks could be attributed to either the PO or the CI as well.

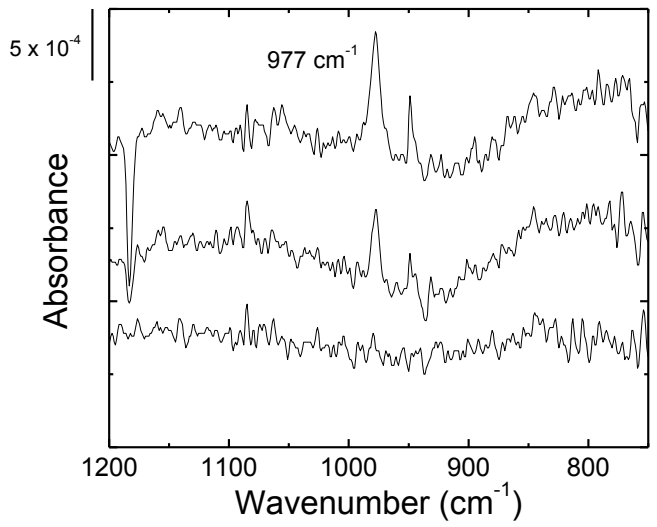

Figure 4.11: RAIR spectra from the first 30 minutes of a low flux ozone exposure. The peak at 977 cm^{-1} was the only evidence of a species exhibiting intermediate behavior during initial dosing.

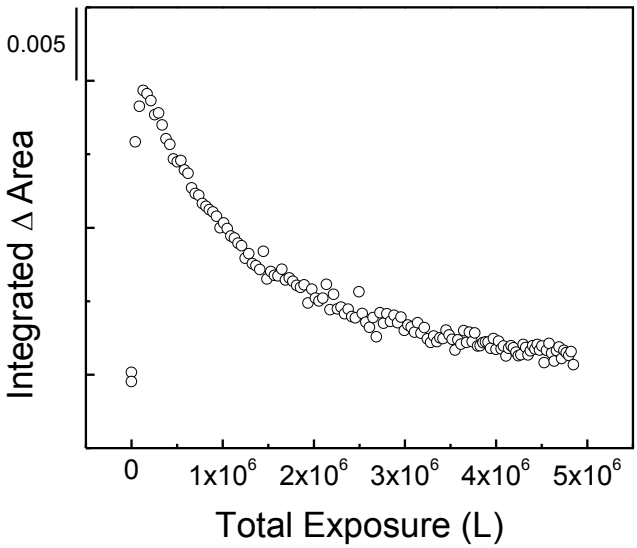

Figure 4.12: The change in integrated area of the peak at 977cm^{-1} versus the total flux of ozone. The profile suggests that the species represented by the peak at 977cm^{-1} is an intermediate.

A number of experiments were performed to further confirm the hypothesis that the peak at 977 cm^{-1} was in fact due to the primary ozonide. The first task was to determine if the peak was due to an intermediate or instead, an ozonolysis product that reacted with a second ozone molecule forming a new product. To establish whether the peak represented an intermediate or a product, the fullerene surface was exposed to ozone for a predetermined amount of time; long enough for the peak at 977 cm^{-1} to grow to maximum intensity. After dosing for the set amount of time, the ozone beam was closed and the peak was monitored for the following 4 hours. If the peak corresponded to a product that reacted with a second ozone molecule to form another product, the peak would be expected to remain once ozone was removed from the system. If the peak represented the primary ozonide, it would have started to decay regardless of the presence of ozone. The experiment showed that with and without exposure to ozone, the peak at 977 cm^{-1}

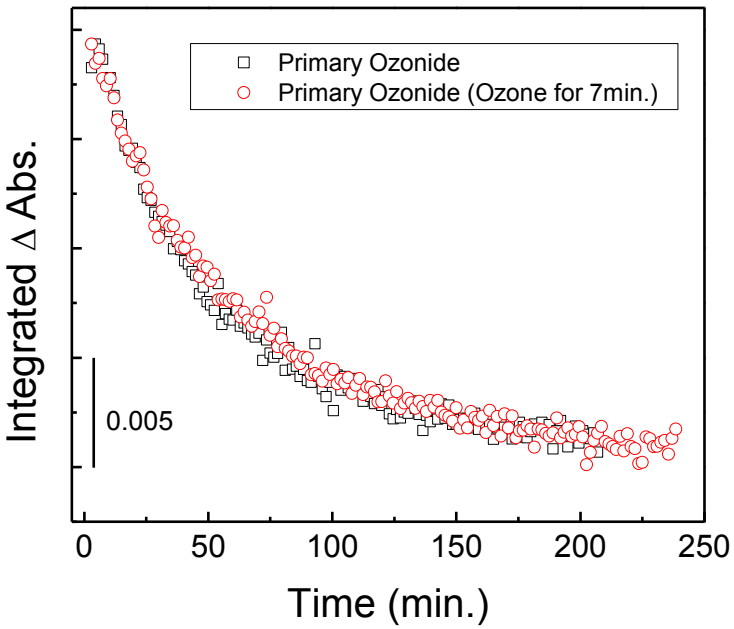

Figure 4.13: The integrated change in absorbance of 977 cm^{-1} over time with and without ozone exposure. The black squares represent data from an experiment where the C_{60} surface was continuously exposed to ozone. The red circles represent data from an experiment where the surface was only exposed to ozone for 7 min.

was not stable, even in ultra-high vacuum. Figure 4.13 displays the data from the experiment, and more importantly, it shows that the rate of decay was the same even when ozone was not present. The conclusion from the experiment is that the peak at 977 cm^{-1} is an intermediate species that thermally decomposes. The results support the hypothesis that the 977 cm^{-1} peak is due to the PO. Using the graph in Figure 4.13, a lifetime (τ) was calculated for the primary ozonide of C_{60} at the gas-surface interface. The lifetime was obtained by dividing 1 by the rate constant for PO decay ($1/k = \tau$). The lifetime of the PO in UHV was calculated as ~46.5 min. While this value may seem high, it is dwarfed in comparison to the $C_{70}O_3$ solution-phase lifetime of 650 min. reported by Heymann *et al*.[91]

Considering all the data collected during these experiments, and the overwhelming support for the assignment of the PO, there is confidence that the primary ozonide of C_{60} has been detected at room temperature, in real-time; this is the first observation of the PO of C_{60} at the gas-surface interface.

4.3.2 Intermediates

Although the peak at 977 cm^{-1} was the most intense, five other peaks were observed in the first few minutes of ozone exposure. The other peaks, shown in Figure 4.6, appear at 769, 930, 945, 1140, and 1156 cm^{-1}. In order to assign these peaks, the electronic structure calculations and isotopically-labeled data were further reviewed. After exposure to heavy ozone, the peak at 769 cm^{-1} shifted approximately 1 cm^{-1}, to 768 cm^{-1}. Comparison of the $^{18}O_3$ and $^{16}O_3$ calculations revealed only one peak in this region was seen with a shift of 1 cm^{-1}, suggesting the peak at 769 cm^{-1} is due to a breathing motion of the molecule which induces some movement of the ozonide ring, see Figure 4.14. The peak at 945 cm^{-1} shifted 2 cm^{-1} in the spectra recorded during the $^{18}O_3$ exposure. The calculations showed a frequency, with a 3 cm^{-1} shift, representative of a breathing mode that induces an asymmetric stretch of the oxygens and the carbons in the ozonide ring. With similar peak shifts, the peak at 945 cm^{-1} has been assigned to this particular breathing mode, see Figure 4.15. Unfortunately, the peak at 930 cm^{-1}, which experienced a 5 cm^{-1} shift with isotopically-labeled ozone, did not match any of the frequencies predicted with the calculations. The final two peaks, at 1140 and 1156 cm^{-1}, are preliminarily assigned to

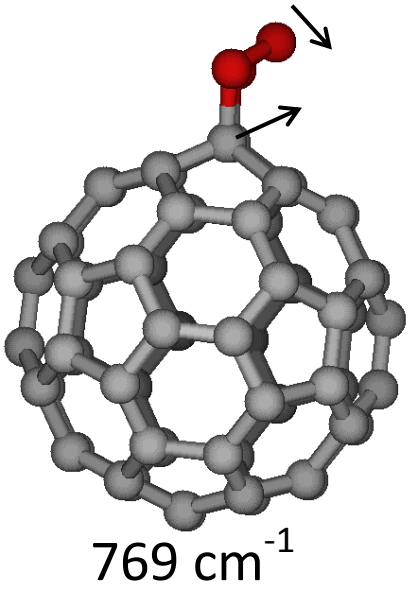

Figure 4.14: Motion of the molecules in the ozonide ring that produces a peak at 769 cm^{-1}.

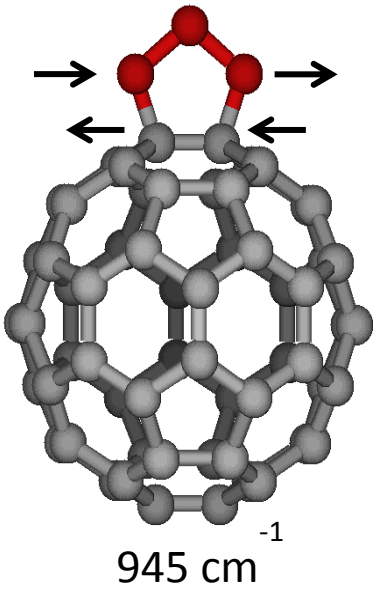

Figure 4.15: The motions that produce a peak at 945 cm^{-1}.

specific motions of the ozonide ring. Both of these peaks only shift ~ 1-2 cm^{-1}, and the calculations predicted numerous frequencies in this region which undergo similar shifts. The proposed assignment of these peaks, therefore, is also based on the fact that the predicted intensities for the motions, shown in Figure 4.16, have the highest values. More in depth isotopic studies are required to conclusively assign the species associated with 1140 and 1156 cm^{-1}.

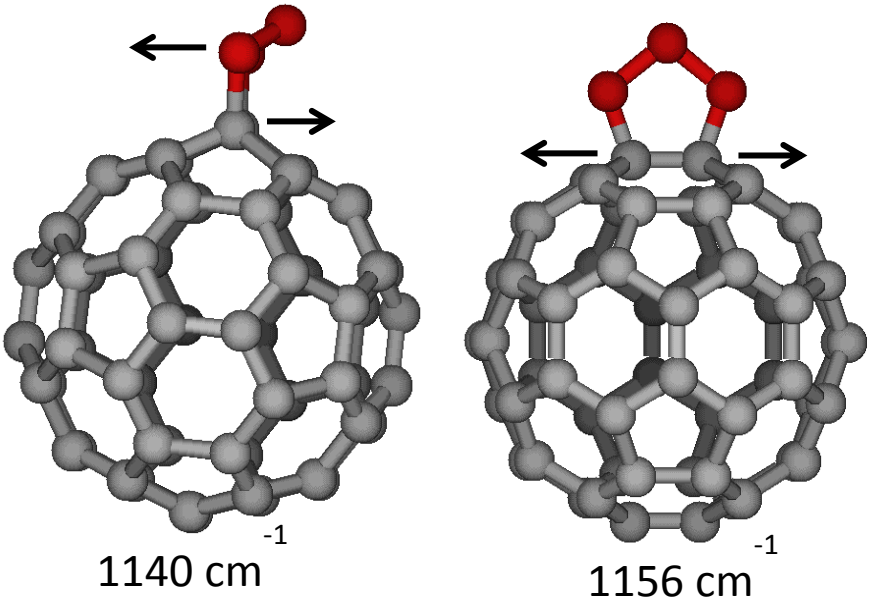

Figure 4.16: Preliminary assignments for the motions which produce peaks at 1140 and 1156 cm^{-1}.

Using the IR data, plots can be created to display the kinetics of the peaks. From the plots, the decay rates for the associated species were determined. All five species showed rate constants between (2.5 – 3.0) x 10^{-5} s^{-1}. The similar decay rates imply that all five peaks may stem from the same intermediate. This comparison of the peak profiles, support the preliminary conclusion that all five peaks represent different motions of the primary ozonide of C_{60}.

The results provided from the electronic structure calculations require one final point of discussion. Before the isotopically-labeled experiments were carried out, the peak at 977 cm^{-1} was initially assigned to the asymmetric stretch of the primary ozonide ring. The initial assignment was based on the significant intensity predicted by the calculations. Upon

recalculation using $^{18}O_3$, the calculated peak with that same intensity experienced a much larger shift than that seen in the experiments. Because the shifts did not match, a different assignment of 977 cm^{-1} was made (shown above in Figure 4.10), a motion still associated with the PO, however, the final assigned mode was much lower in intensity. It is possible that the peak at 977 cm^{-1} is due to the asymmetric stretch of the PO because the calculation methods used Hooke's Law, therefore assuming the molecule is a harmonic oscillator. C_{60} is far from a harmonic oscillator, especially after an ozone molecule is bonded to the cage. This inability to account for $C_{60}O_3$'s anharmonicity means the mode assignment of 977 cm^{-1} is still preliminary. Nevertheless, it can be said with confidence that the peak is representative of a motion of the primary ozonide, a conclusion reached by the substantial agreement between the rate of decay of C_{60} and the rate of formation of the PO.

4.3.3 Products of Ozonolysis

Ozone exposure to a C_{60} surface causes immediate reaction. This reaction is characterized in RAIRS by the appearance of negative peaks at 1182 and 1428 cm^{-1}, and the simultaneous development of six separate intermediate peaks. While these two features alone can provide significant information about this unexplored gas-surface reaction, there are several more peaks to consider. As illustrated in Figure 4.17, there are several other peaks that appear almost as quickly as the intermediates peaks. A study by Brosset *et al.* gives support to the possibility that the small peaks at 1052 and 1078 $cm^{-1}$are a result of the initial adsorption of gas-phase ozone on the fullerene surface.[92] In Brosset's study the ν_3 asymmetric stretching mode of ozone was observed at 1037 cm^{-1} and the ν_1 symmetric mode was recorded at 1108 cm^{-1}. The peaks at 1052 and 1078 cm^{-1} are just seen in the beginning of the exposure, and only intermittently. These peaks were also shifted in the isotopically labeled experiments, indicating that they were associated with ozone. Their identity was not accurately determined in these tests; therefore the assignment of physisorbed ozone is

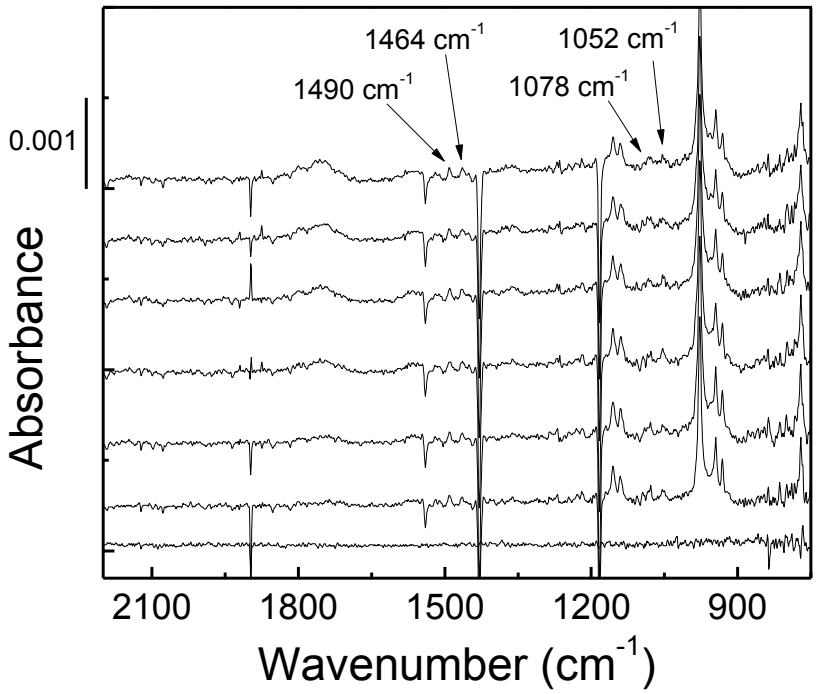

Figure 4.17: RAIR spectra collected during the first 9 minutes of ozone exposure. The peaks at 1052 and 1078 cm^{-1} are due to ozone adsorbed to the surface, and those present at 1464 and 1490 cm^{-1} represent the mono-epoxide of C_{60} ($C_{60}O$).

only a proposal and requires further exploration. The peaks at 1464 and 1490 cm^{-1} are due to the formation of the mono-epoxide of C_{60}.[93] As the exposure continues, these peaks become less prominent, and in some scans, non-existent. The reason for the change in observable signal will be discussed in detail in Section 4.3.4. A number of other product peaks also grow in, starting almost immediately after the intermediates are formed. The appearance of product peaks in the carbonyl region can be seen in both Figure 4.5 and Figure 4.17. The final peak count at the end of the experiment (3.5 hours of ozone dosing) is: 6 intermediate peaks and 14 product peaks. A peak is considered significant as long as its intensity is three times that of the peak-to-peak noise in an adjacent region. If this intensity requirement is met, the peak is above the limit of detection (LOD) and subject to evaluation. The peaks were initially assigned using existing pertinent literature. Table 4.1 lists all of the observed peaks, the description, and the assignment.

Table 4.1: List of all peaks observed during the gas-surface reaction of Ozone and C_{60}

Peak Position (cm^{-1})	Peak Description	Peak Assignment
1182	Reactant – surface species	IR-active fullerene mode
1428	Reactant – surface species	IR-active fullerene mode
769	Intermediate	PO
930	Intermediate	PO
945	Intermediate	PO
977	Intermediate	PO
1140	Intermediate	PO
1156	Intermediate	PO
774	Product	Ether
797	Product	Epoxide
1052	Reactant – adsorbed gas	Ozone
1078	Reactant – adsorbed gas	Ozone
1354	Product	Epoxide
1374	Product	Ether
1464	Product	Epoxide
1490	Product	Epoxide
1568	Product	Enhancement of aromatic –C-C– stretch due to the addition of polar groups
1760	Product	Carbonyl functionalities
1800	Product	Anhydride
1825	Product	Anhydride
1862	Product	Anhydride
2151	Product	Ketene

In an effort to assign other peaks present in the IR spectra, and better describe the mechanism for ozonolysis, the rates of formation of the product peaks were compared. Plots of the integrated change in area of the peaks as a function of ozone exposure were used to determine the rate constants. The values measured were $k_{774} = 4.9 \times 10^{-5}\ s^{-1}$, $k_{1354} = 2.8 \times 10^{-5}\ s^{-1}$, and $k_{1374} = 3.2 \times 10^{-5}\ s^{-1}$. Preliminary calculations of a single epoxide and ether functionality on the C_{60} structure suggest the peaks may represent these species. Extensive calculations are required to correctly assign the product peaks, the assigned listed herein are based on existing literature.

A broad product peak was observed at 1568 cm^{-1} after minimal ozone exposure. This peak was also seen in a number of other relevant studies and has been attributed to the enhancement of an aromatic C-C stretch of the C_{60} cages.[94] The stretch is enhanced by the addition of polar functional groups to the fullerene cage. The remaining product peaks appear in the carbonyl region (4 peaks – see Figure 4.18) and at 2151 cm^{-1}. The carbonyl region includes four separate product peaks; the first, at 1760 cm^{-1} is recognized as ketones and the remaining three are assigned to anhydride groups.[11a, 11f] Figure 4.18 shows how the individual peaks change with time, or increasing ozone exposure (underlying black curves). The rates of formation for each peak in the carbonyl region were determined by plotting the integrated change in absorbance versus total exposure, shown in Figure 4.19. The rate of

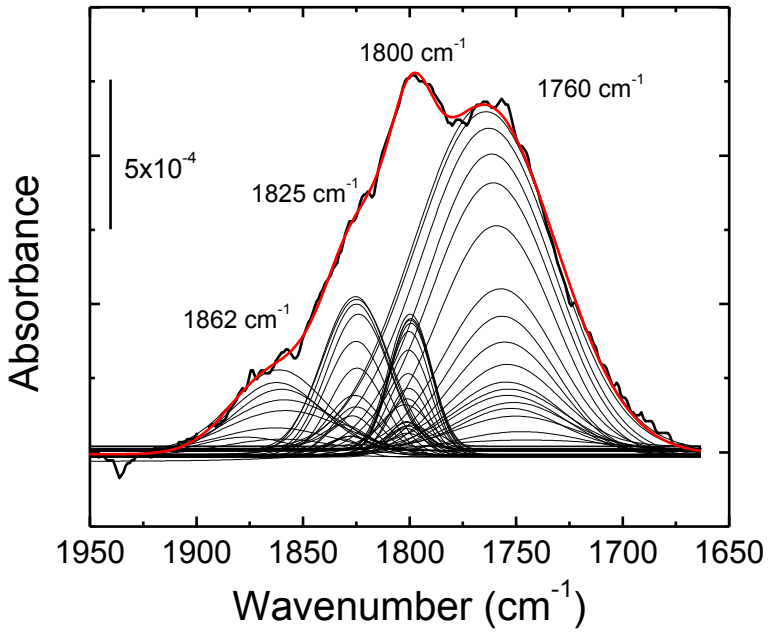

Figure 4.18: Expanded view of the carbonyl region from the final RAIR spectrum recorded after 3.5 hours of dosing a C_{60} surface with ozone.

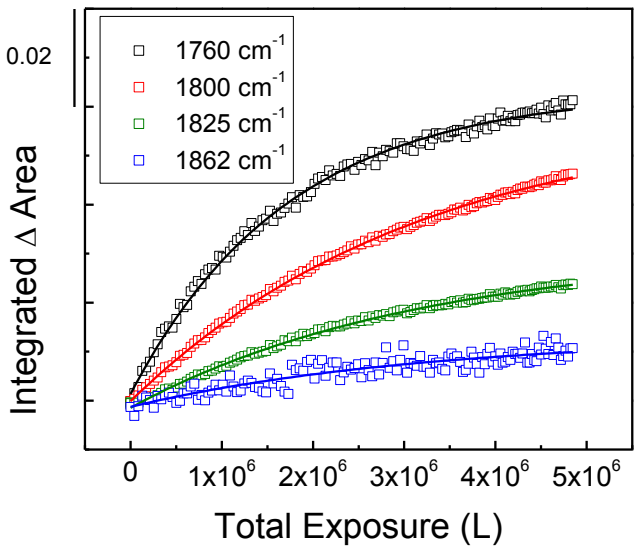

Figure 4.19: The rates of formation for the four peaks in the carbonyl region. The data indicates that the ketones form faster than the anhydrides.

formation for the ketone groups is 9.8 x 10^{-6} s^{-1} and the anhydrides all form with an approximate rate of 1.9 x 10^{-5} s^{-1}.

To help support and confirm the IR assignment of the peaks, X-ray photoelectron spectroscopy (XPS) was employed. The first figure in this section (Figure 4.20) displays the C 1s and O 1s regions with a comparison of the data before the surface was exposed to ozone and

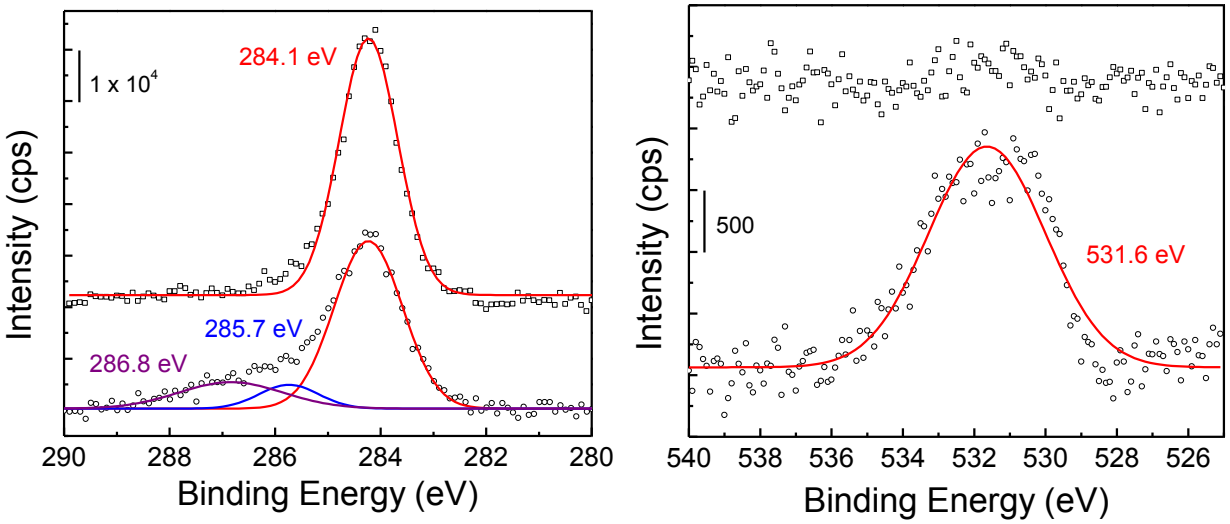

Figure 4.20: XPS data collected before and after ozone exposure. The graph on the left is of the C 1s region. The upper trace (before ozone) shows only one oxidation state of carbon, the lower trace (after ozone) shows three different bonding environments for the carbon atoms. The graph on the left shows the O 1s region and it is apparent that after ozone exposure there is a significant amount of oxygen present on the surface (lower trace).

after ozone exposure. In both graphs, the upper trace was recorded before ozone exposure and the lower trace was recorded after ozone exposure. The graph on the left shows data from the C 1s region. It is obvious from the before and after comparison of this region that the carbon atoms of the C_{60} molecules were significantly oxidized by the impinging ozone molecules. However, regardless of the extensive oxidation, the total amount of carbon on the surface remained constant. After oxidation, the main carbon peak (representing C-C, C=C bonding) was still the most prominent species, two new peaks developed during exposure. The first peak, at 285.7 eV, is attributed to C-O bonds within the surface, and the second peak, at 286.8 eV is representative

of C=O bonds. The second graph (on the right) depicts the O 1s region. The initial (upper trace) shows no discernable peaks, however, after ozone exposure, a prominent peak appeared at 531 eV. No other peaks were observed in the XPS data, indicating that the surface is only comprised of C_{60} molecules before exposure, and oxidized C_{60} molecules after exposure.

The final product peak, appearing at 2151 cm^{-1}, may represent a ketene functionality, based on peak position. The ketene functional group, having the form RR'C=C=O, is highly reactive and therefore quite short lived under atmospheric conditions. The observation of this particular functional group has not been specifically reported for any reaction between ozone and C_{60}. The peak at 2151 cm^{-1} was found to be stable in UHV for multiple days but if the surface was removed from the chamber, even for only a few seconds, then immediately replaced, the

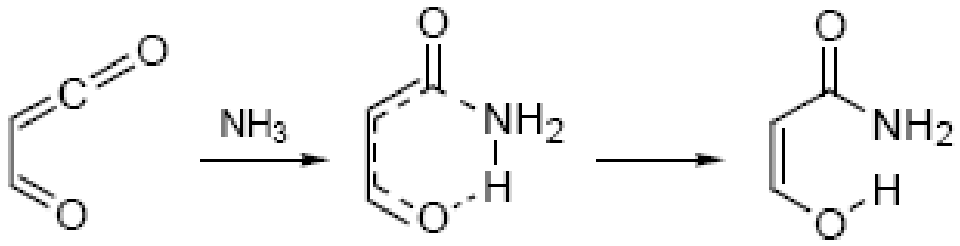

Figure 4.21: The proposed mechanism for the formation of enol amides on an oxidized C_{60} surface.

peak was no longer observable. With the proposal that this peak represented a ketene, confirmation of the assignment was obtained by dosing with gas-phase ammonia. Amines are well known to react with ketenes to form amide groups, an IR active species.[95] Therefore, an ammonia exposure was used to test for the presence of ketenes. The mechanism shown in Figure 4.21 is an example of how the enol amide might form on the highly oxidized C_{60} surface. The enol amide is most likely formed from the reaction of NH_3 with the highly oxidized fullerene surface, supported by the observed IR peaks and their assignments: 1437 cm-1: C-N stretch (~1400 cm-1), 1594 cm^{-1}: NH_2 deformation (1620 – 1590 cm^{-1}), 1709 cm^{-1} : C=O stretch (1730 –

1680 cm^{-1}), 1778 cm^{-1} : C=O stretch (1800 – 1740 cm^{-1}), 3250 cm^{-1} : N-H stretch (3357 – 3250 cm^{-1}).[96] Based on the results, shown in Figure 4.22, the observations are consistent with the hypothesis that ketene functionalities are one of the products of the ozone oxidation of C_{60} surfaces.

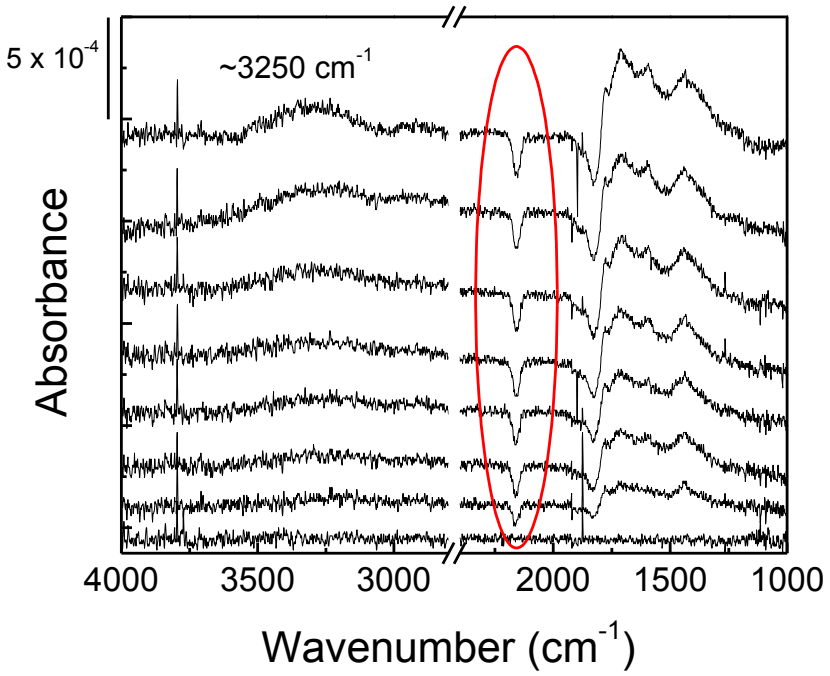

Figure 4.22: RAIR spectra from the NH_3 exposure of an oxidized C_{60} surface. The data shows a decrease of the peak attributed to the ketene and the appearance of several peaks indicative of an enol amide.

The x-ray photoelectron spectrometer was also used as a secondary confirmation for the presence of ketene groups on the surface. Evidence of nitrogen on the surface after exposure to NH_3 supported the conclusion that the ketene functionalities had converted to enol amides. Figure 4.23 shows a shallow peak in the N 1s region. The low intensity of this peak is most likely due to several factors. One, the equipment (i.e. doser) used to expose the surface to NH_3 did not introduce the gas as close to the sample as the equipment used to expose the surface to ozone. The distance between the source of gas and the surface is important because flux decreases by a factor of two over distance; therefore, the concentration of impinging NH_3 was less than the amount of ozone. Lowering the amount of NH_3 hitting the surface also lowers the reaction probability. Secondly, the amount of ketene functionalities on the surface was not as high as the number of other products which form from ozone exposure. Consequently, the number of enol amides formed upon NH_3 exposure will also be relatively low. That said the small peak detected in the N 1s region helps to corroborate our assignment of the ketene product peak.

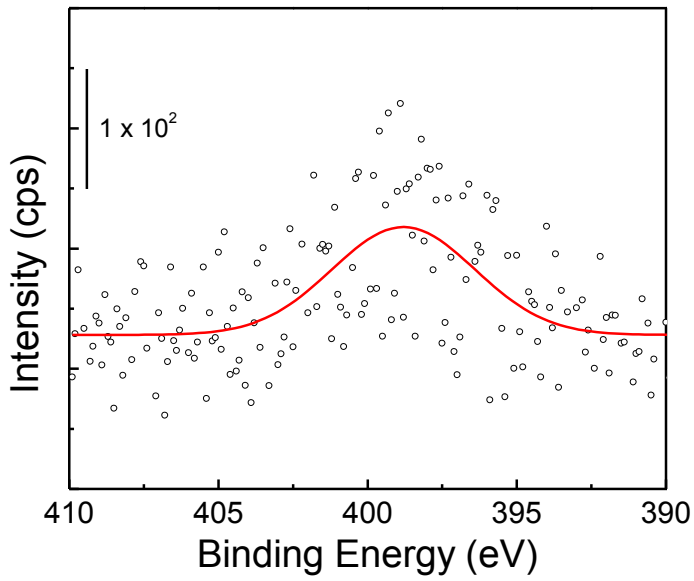

Figure 4.23: XPS data of the N 1s region. Oxidized C_{60} surface was scanned after exposure to NH_3.

4.3.4 Mechanistic Details

One of the main objectives of this research was to develop a detailed picture of the mechanism by which ozone oxidizes surface-bound fullerenes. While this problem is complex, studying how ozone reacts with a fullerene surface is significantly easier than trying to

comprehend the reaction when there are other species involved (e.g. H_2O, NO_2, $OH\cdot$). Using the RAIRS, XPS, and electronic structure calculation (ESC) data, the first few steps in the reaction have been determined. The impinging ozone molecule adds across a 6/6 bond on the C_{60} cage to form the primary ozonide; see Chapter 1, pg. 23. After the formation of the primary ozonide, the IR and ESC data suggest that the –C-C– and one of the –O-O– bonds rupture to create the Criegee Intermediate. The process clearly follows the well-known Criegee mechanism for the ozonolysis of much simpler alkenes.[88] From the data collected, a number of other final products that form on the C_{60} surface have been identified.

After the first step (i.e. the formation of the PO), there are several potential pathways available for the next step of the ozonolysis mechanism. Existing ozonolysis literature suggests two possible reaction pathways that can lead to the formation of products: 1) the primary ozonide thermally decomposes into the Criegee Intermediate, which rearranges to products, or 2) the reaction of the primary ozonide and a second ozone molecule to form other products. In order to determine which pathway was followed a set of experiments was performed to observe the

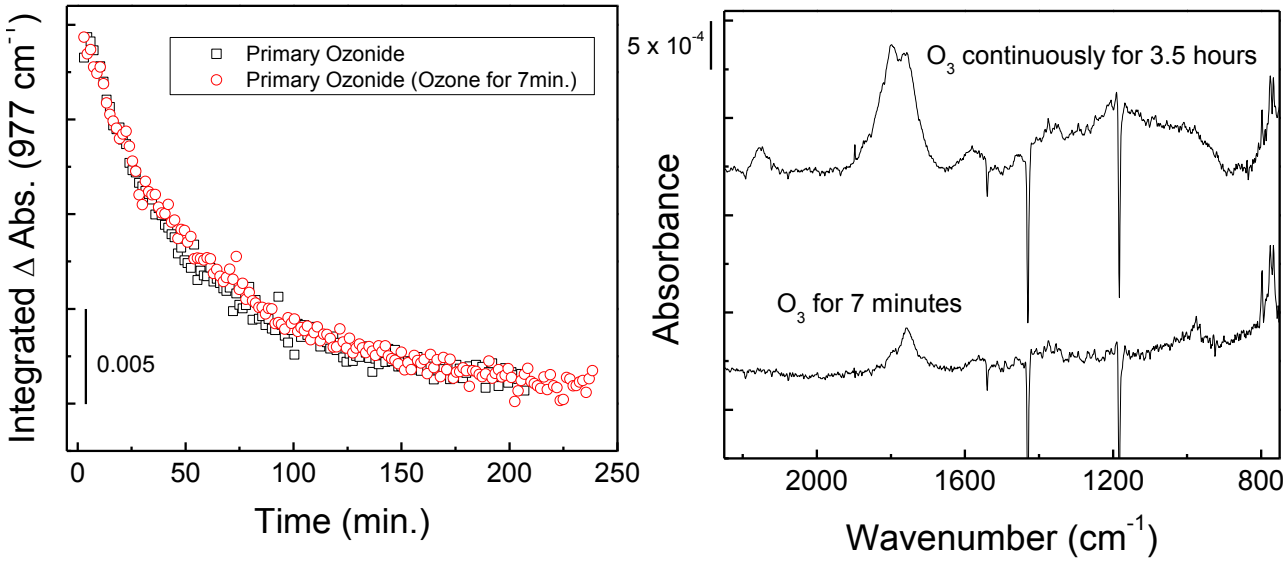

Figure 4.24: The graph on the left is a comparison of the decay rate of the primary ozonide peak at 977 cm^{-1} from an experiment with continuous ozone dosing and an experiment where ozone is only dosed for 7 minutes. The graph on the right shows the final RAIR spectrum from each of these experiments.

behavior of the PO in the presence and absence of ozone. The decay rate for the PO peak (977 cm^{-1}) was monitored in an experiment where ozone was continuously dosed for 3.5 hours. That decay rate was then compared to one where ozone was only dosed for 7 minutes (long enough to let all the POs form), then the beam was closed. The comparison of these two experiments, shown in Figure 4.24 (left graph), indicates that the PO undergoes thermal decomposition in both cases. However, the RAIR spectra, shown in Figure 4.24 (right graph), show the formation of different final products. The top trace is the final spectrum recorded after dosing with gas-phase ozone for 3.5 hours. Significant oxidation is apparent in the carbonyl region, as well as a large peak around 2151 cm^{-1}, assigned to the ketene product. The bottom spectrum is the last spectrum obtained from the experiment in which ozone was dosed for only 7 minutes. Both spectra were recorded ~3.5 hours after ozone was initially introduced to the surface. There is an obvious difference in the carbonyl regions of the two spectra and, more importantly, the 7 minute ozone dosing experiment shows no evidence of ketene formation. The data from these two experiments can not only be used to determine that the primary ozonide undergoes thermal decomposition, but also to assign specific products to particular reaction pathways. The first pathway (7 minute exposure), shown in Scheme 1, leads to product formation via rearrangement of the CI. Notice, the only products observed in the 7 minute exposure spectrum are assigned to epoxides, ethers, ketones, and a very small amount of anhydrides. The other pathway can be seen in the full 3.5 hour ozone exposure. This pathway, shown in Scheme 2, includes all the products formed in the CI rearrangement pathway plus considerably more ketones and anhydrides, and of course, the ketene. Since the only difference between these two experiments is the presence of ozone, it is proposed that the difference in products is a result of at least one additional ozone molecule reacting with the Criegee Intermediate.

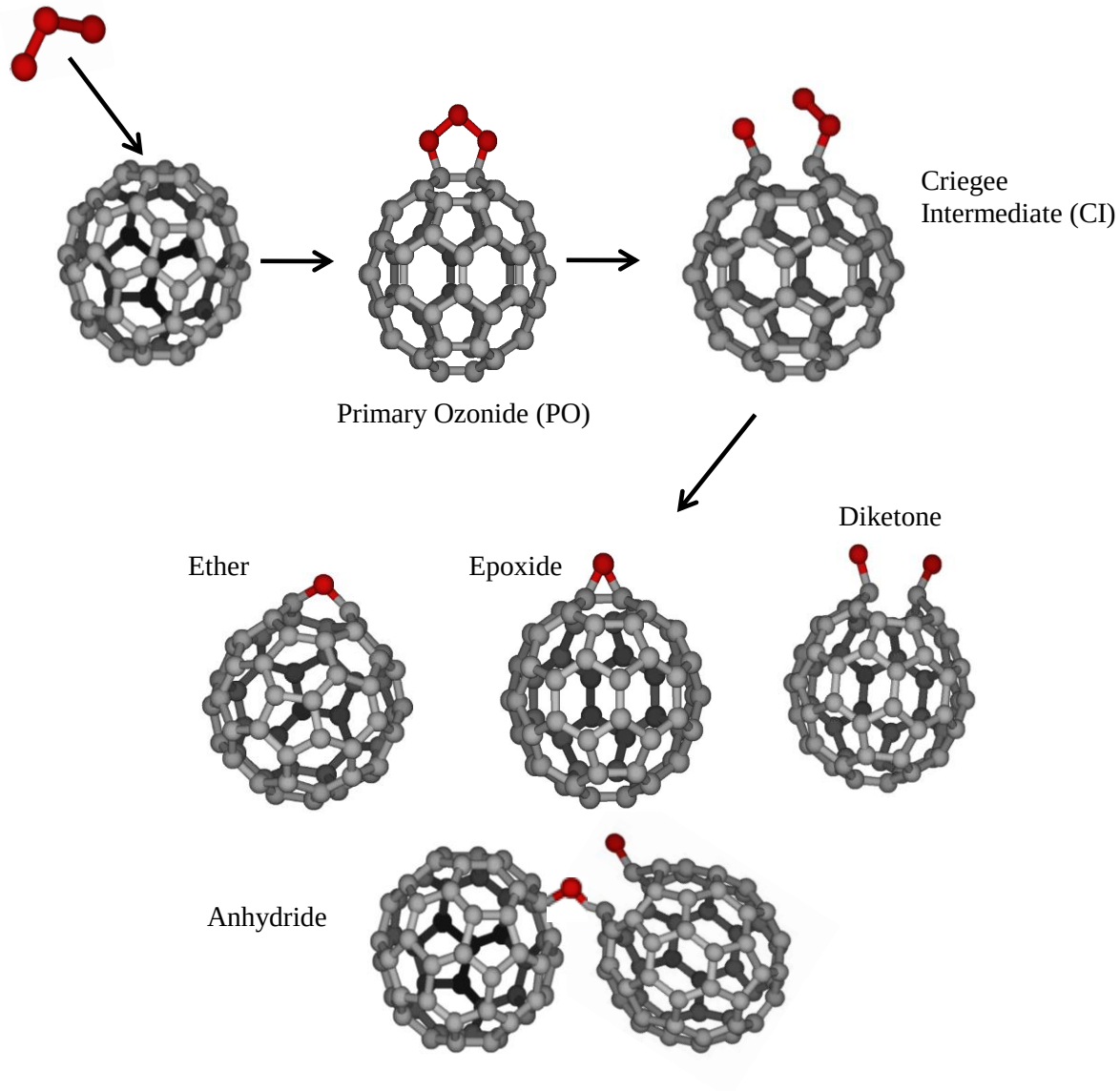

Scheme 1: One of the proposed mechanisms for the reaction of gas-phase ozone with surface-bound fullerenes. In this mechanism the products are formed through the rearrangement of the Criegee Intermediate.

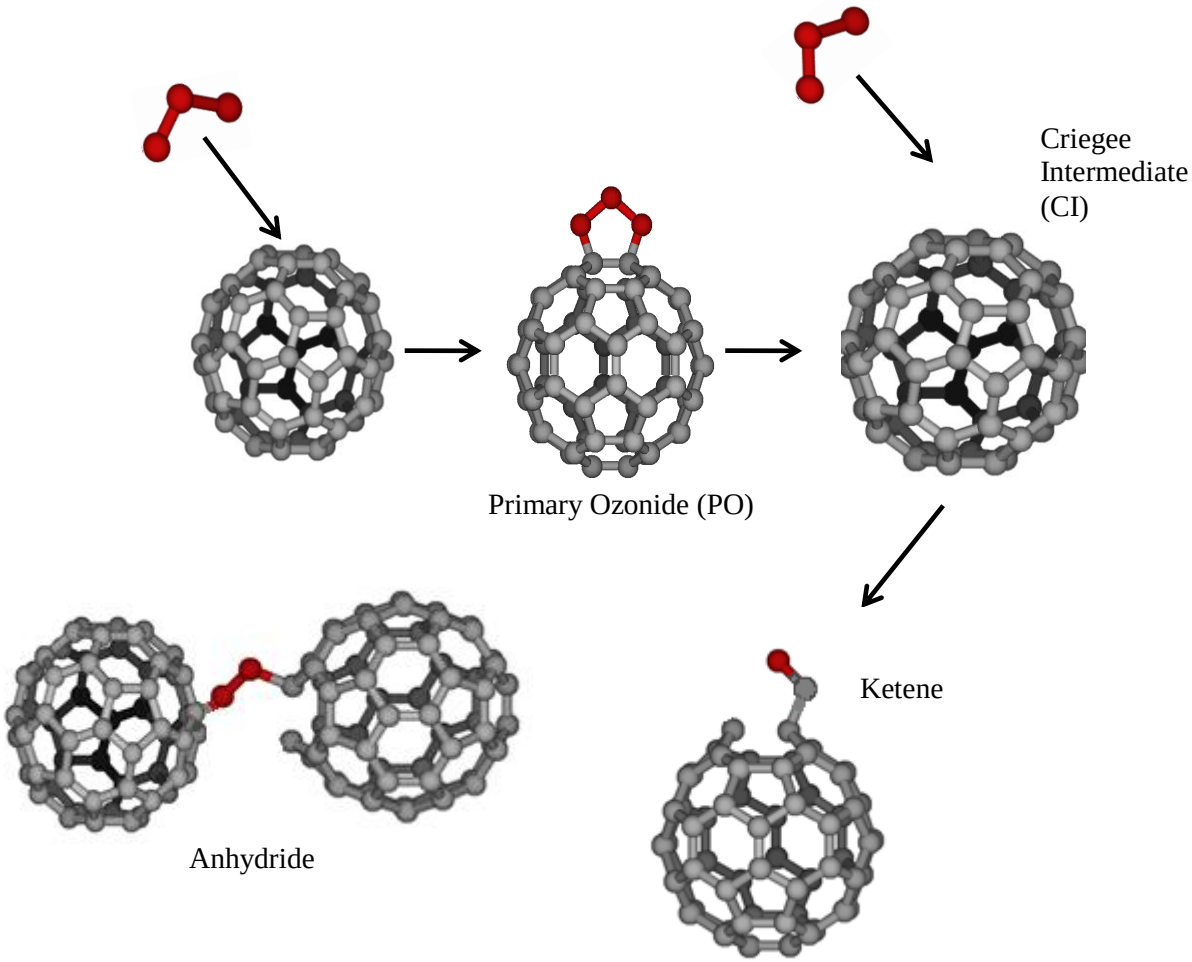

Scheme 2: One of the proposed mechanisms for the reaction of gas-phase ozone with surface-bound fullerenes. In this mechanism the products are formed through the reaction of the Criegee Intermediate with a second ozone molecule.

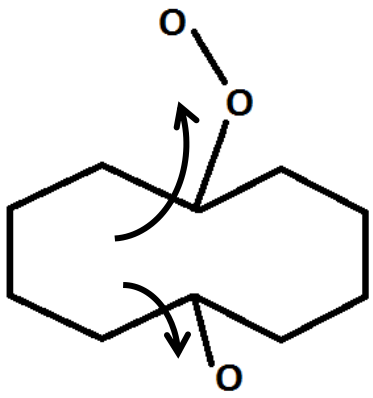

Figure 4.25: Drawing of the hole created in the fullerene cage as a result of the addition of one ozone molecule across a 6/6 bond.

The O_3 molecule/CI reaction pathway is shown in Scheme 2. In reality, the ozone molecule may react with any part of the susceptible ring which supports the CI. Figure 4.25 shows what the structure of the top of the C_{60}/CI cage might look like if the –C-C– bond ruptures with one of the –O-O– bonds during PO decomposition. The arrows in the figure indicate the most likely orientation (based on ESCs) of the carbons attached to the oxygen atoms. The "flaring out" of these carbons creates a hole in

$$C_{60} + O_3 \rightarrow C_{60}(O_3)_{\text{external cage}} \rightarrow {}^{+}\text{O-}[C_{60}] - \text{O-O}^{-}$$

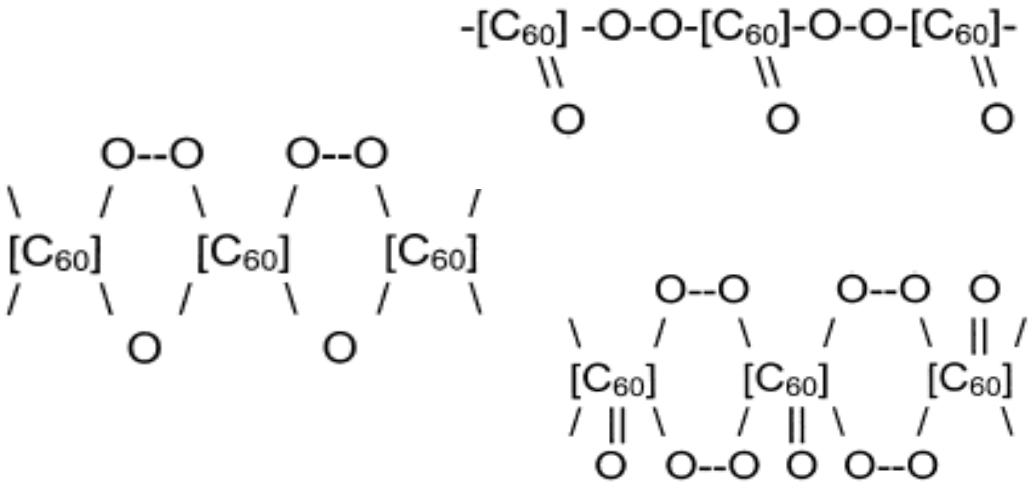

Figure 4.26: Proposed structures for the ozopolymer. Reprinted from *Polymer Degradation and Stability, 70(2)*, 237-243, Copyright 2000, with permission from Elsevier.

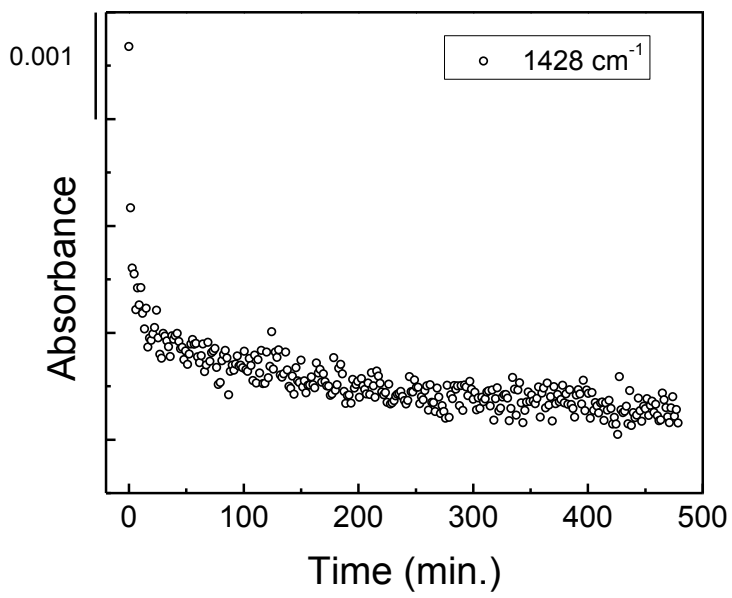

Figure 4.27: Plot of the change in integrated area of the C_{60} peak at 1428 cm^{-1} versus time exposed to ozone.

the top of the cage. An impinging ozone molecule could attack a –C-C– bond within the ten-membered ring (parameter of the hole). Several studies have shown that ozone is more likely to react with another site on the same ring that has already been oxidized.[97] It has also been shown that upon heating of the ozopolymer product, molecular oxygen is liberated and reformation of the fullerene cages is observed.[11a, 11c, d, 60d] If ozone attacks and ruptures another –C-C- bond on the same ring, the fullerene cage will continue to open, allowing the oxygen atoms to come into contact with neighboring cages (or parts of cages), and perhaps interact intermolecularly. The resulting species is known as an ozopolymer and has been observed in numerous studies of fullerenes and ozone. The ozopolymer, structures shown in Figure 4.26, is the product of extensive ozonolysis of fullerenes. It is specifically characterized by the appearance of several different anhydride peaks in the IR spectra (observable at wavenumbers > 1800 cm^{-1}). Figure 4.27 displays a plot of the integrated change in area of one of the main fullerene peaks (1428 cm^{-1}) over an 8 hour ozone exposure. It is clear from the data that after the first ~10 minutes the fullerene peaks do not decrease much further. Based on the data, it is likely that the initial observed decrease is due to the extensive oxidation of the top 20% of the C_{60} film (i.e. formation of ozopolymer). The gradual decline over the next 7.8 hours is most likely a result of the slow diffusion of ozone

through the ozopolymer layer and into the bulk of the film. When the surface is scanned post-exposure, the majority of the C_{60} peak intensity remains unperturbed, see Figure 4.28. The lack of oxidation in the bulk of the film may be a result of tightly packed C_{60} molecules within the lower layers. The subsurface C_{60} molecules may be unavailable for oxidation because of ozone's inability to traverse the layers with greater organization. Additional details, such as rate constants, kinetic models, and activation energies, can be gathered from the comparison of peak profiles and used to improve the mechanistic scheme.

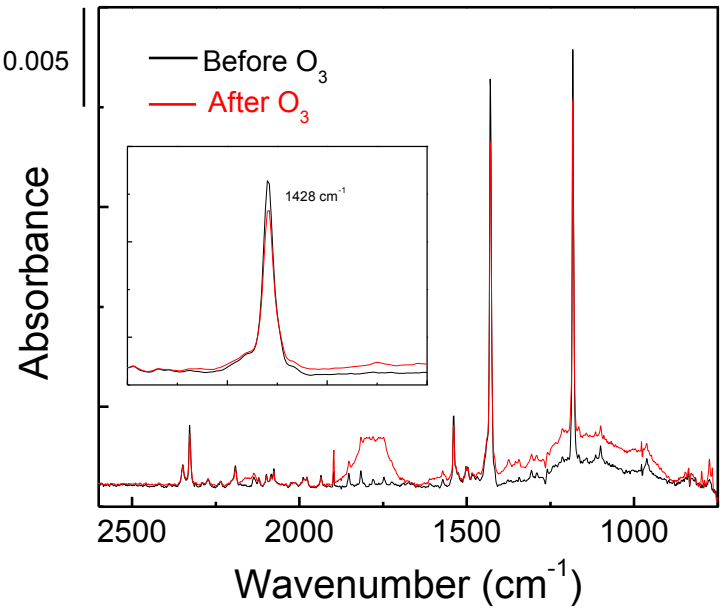

Figure 4.28: RAIR spectra of a C_{60} surface before and after ozone oxidation. The spectra show that ozone only oxidizes approximately 10-20% of the surface.

4.3.5 Kinetic Measurements

Another important objective of this research was the development of an initial kinetic understanding of the ozonolysis of surface-bound C_{60} films. If a detailed kinetic model is developed the associated rates of reaction can be incorporated into UHV models and other simulations to further predict the behavior of fullerenes in the environment. The first kinetic value measured was the initial reaction probability. The initial reaction probability is the likelihood that a reaction will occur upon the collision of two particles. The expression for the initial reaction probability (γ) is shown in equation 4.3:

$$\gamma = \frac{4\boldsymbol{k}\ \mathrm{L}}{<\mathrm{v}>[\mathrm{O}_3]} \qquad (4.3)$$

where *k* is the reaction rate, <v> is the average velocity of an ozone molecule at room temperature, $[O_3]$ is the concentration of ozone molecules to which the surface is exposed, and L represents the number of reactive sites on the surface. – for these calculations *k* was obtained from the fit of the decay curve of 1428 cm^{-1} (fullerene IR-active peak), depicted in Figure 4.29. The curve was fit with an exponential decay equation, also known as the integrated first-order rate law. The integrated first-order rate law is represented by Equation 4.4:

$$\Delta A = Be^{-kt} \qquad (4.4)$$

where A is the signal, in this case, the IR absorbance; *B* is the frequency factor; *k* is the reaction rate. For the data in Figure 4.29, it is the rate at which the species represented by 1428 cm^{-1} (C_{60}) was decomposing; and finally *t* is time. By fitting the data in Figure 4.29 with Equation 4.4, the value for *k* was obtained. Once *k* was acquired, the last variable needed for Equation 4.3 was L. To determine L, the surface coverage of the sample must be known.

The surface coverage of the sample was calculated by constructing a calibration curve of the C_{60} surfaces. A bell jar evaporator, equipped with a quartz crystal microbalance (QCM), was used to deposit C_{60} molecules onto a 1" x 1" Au slide. The QCM was calibrated for C_{60} deposition and was used to measure the amount (in nm) of C_{60} deposited onto the Au slide. After the slide was removed from the evaporator it was placed into the UHV chamber and scanned with the RAIR spectrometer. By monitoring the fullerene IR-active modes (1182 cm^{-1} and 1428 cm^{-1}), specific film thicknesses were associated with measured IR intensities. The resulting calibration curve is shown in Figure 4.30. To determine the degree of oxidation of the C_{60} film,

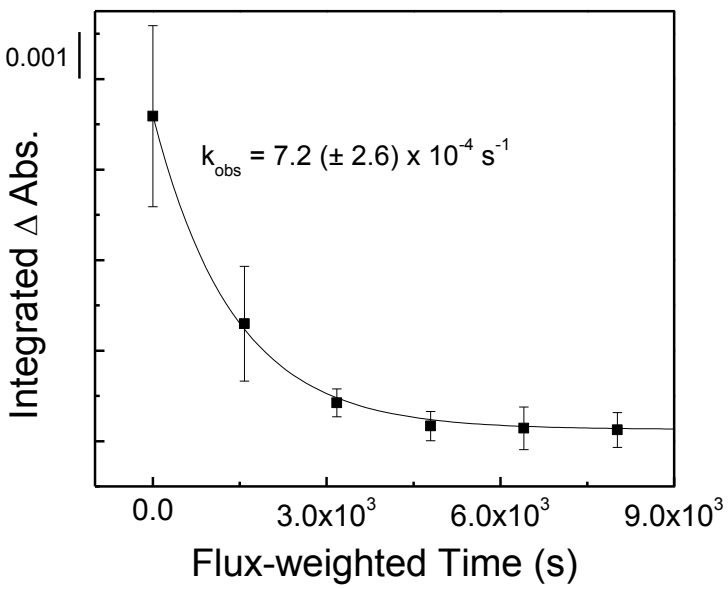

Figure 4.29: The initial decay of the fullerene peak at 1428 cm^{-1}. Fit with an exponential decay curve, k_{obs} = 7.2 x 10^{-4} s^{-1}.

the IR intensity (1182 cm^{-1}) after oxidation was plugged into the calibration curve for y and the equation was solved for film thickness, or x. For all of the C_{60} films, the use of the calibration curve showed that only 10-20% of the films were oxidized by ozone.

The final consideration in the calculation of L was the number of reaction sites per fullerene cage. The literature shows evidence of the addition of up to 29 oxygen atoms on a fullerene cage during ozonolysis.[90] If γ is calculated assuming that all thirty double bonds react with ozone, the resulting value for the initial reaction probability is 1.4 x 10^{-3}. If the initial reaction probability is calculated per molecule, γ = 4.8 x 10^{-5}. The value for γ has not been reported for the O_3/C_{60} system at the gas-surface interface, therefore the value can only be compared to a different, however still relevant system. Previous studies in the Morris group have focused on the oxidation of vinyl-terminated SAMs with gas-phase

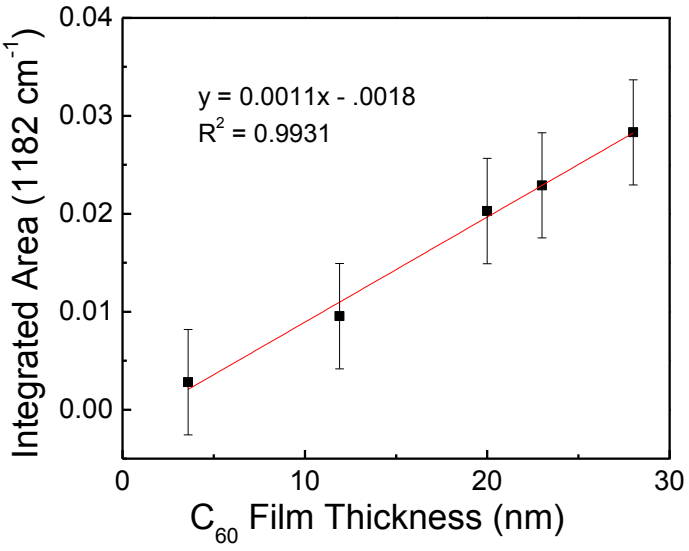

Figure 4.30: C_{60} film calibration curve. Created using a bell jar evaporator, equipped with a QCM, and a RAIR spectrometer.

ozone.[39] The reported value for the initial reaction probability of ozone with vinyl-terminated (C=C) SAMs was 1.1 x 10^{-5} s^{-1}.[31, 39] The comparison of these values indicates that the probability of ozone reacting with surface-bound C_{60} upon collision is two orders of magnitude higher than its immediate reaction with the terminal double bond of a vinyl-terminated SAM, especially if all thirty double bonds on the C_{60} molecule react with ozone. The difference is most likely due to higher reactivity of the fullerene molecule, a result of the pentagons included in the molecule's structure.

After determining the initial reaction probability, the next goal was to assess the reaction rate of the fullerenes and the rate of formation of the primary ozonide of C_{60}. In theory, if ozone adds directly to the 6/6 bond of the fullerene cage, immediately forming the primary ozonide, the growth of the PO (i.e. increase of the peak at 977 cm^{-1}) should be equivalent to the reaction of the fullerene cage (i.e. the decrease of peaks 1182 cm^{-1} and 1428 cm^{-1}). The graph in Figure 4.31 shows the fullerene peak decay and the primary ozonide formation. The equivalent rates (k_{obs}) for these processes indicate that the fullerenes are directly converted to the primary ozonide of C_{60}.

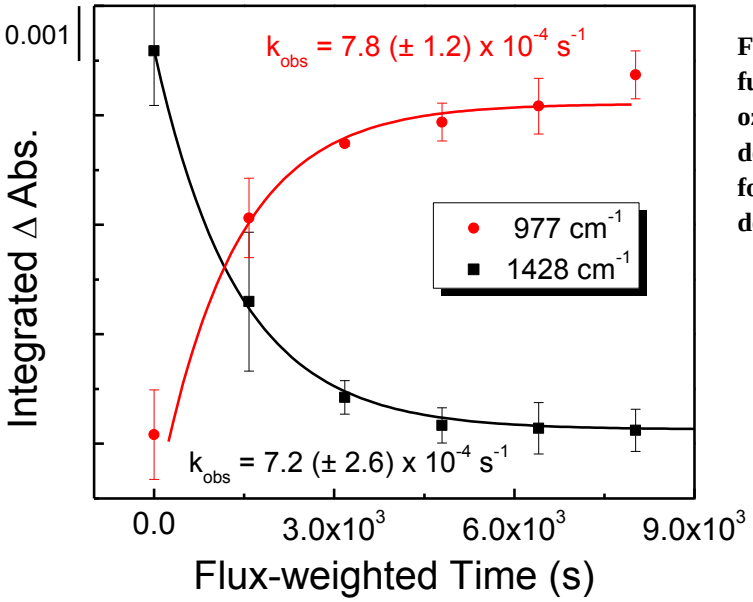

Figure 4.31: Comparison of the fullerene decay rate and the primary ozonide formation. The fullerene cages decompose at the same rate the PO forms, indicating a first-order dependency.

The final objective for the kinetic studies was to perform temperature-dependent exposures. The goal of this series of experiments was to determine the activation energies for the formation of the primary ozonide, as well as its decomposition. These are the first reported values for this species at the gas-surface interface. Ozone exposures were performed with the surface temperature held at 273, 278, 283, 288, and 298 K. The Arrhenius plot, seen in Figure 4.32, shows the data collected for the formation of the primary ozonide on a C_{60} cage. An activation energy (E_a) was not calculated because of the significant spread observed within the data. The large degree of scattered exhibited by the data indicates the possibility of a low barrier to PO formation. A low barrier to PO formation is also well-supported by the IR data, which demonstrates the immediate appearance of the PO upon exposure to ozone, even at lower temperatures. Several theoretical studies in the literature have hypothesized about a negligibly small or non-existent barrier to form the PO of C_{60}.[98] A solution phase study performed by Anachkov *et al.* reported an activation energy of 2.4 kcal mol^{-1} (10.0 kJ/mol) for C_{60} ozonolysis.[60a] Based on the data collected in these studies, as well as comparison to existing literature values, the barrier for the formation of the primary ozonide is relatively low and easily overcome by gas-phase ozone from an effusive beam source at all of the surface temperatures applied in these studies.

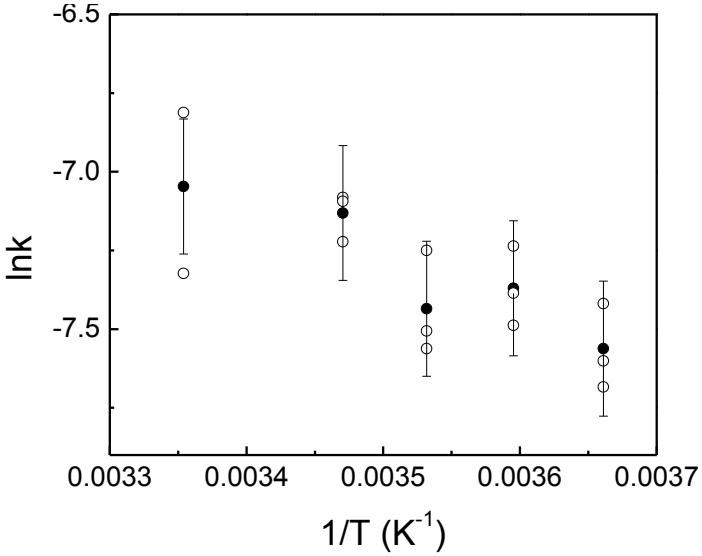

Figure 4.32: An Arrhenius plot for the formation of the PO of C_{60} ($C_{60}O_3$). Data was collected over a temperature range of 273-298 K.

The decomposition of the primary ozonide was also studied. The data collected for this species, shown in Figure 4.33, was very scattered; suggesting the rate of decomposition of the PO was unaffected throughout this temperature range. It is probable that the energy barrier for the decomposition is too small to accurately determine at these temperatures. Due to experimental limitations, quantitative values for the activation energy were not recorded. These values can be explored with future studies in the Morris group.

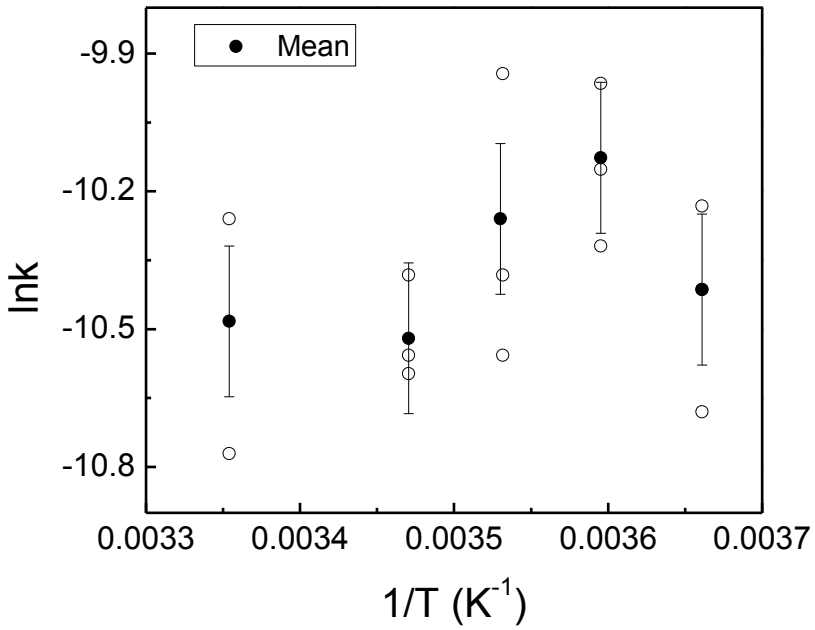

Figure 4.33: An Arrhenius plot for the decomposition of the PO of C_{60} ($C_{60}O_3$). Data was collected over a temperature range of 273-298 K.

4.4 Summary

The reactions of gas-phase ozone and surface-bound fullerenes were studied in depth in a UHV chamber equipped with RAIRS, XPS, MS, and UV-Vis. Electronic structure calculations with the Gaussian code were also performed on specific species formed throughout the reaction. Well-ordered, characterized C_{60} films were formed in HV, with virtually no contamination. After characterization of the fullerene films, they were exposed to gas-phase ozone and monitored in real-time. When the reaction was complete, the surface was scanned with an XPS. The

combination of RAIRS and XPS enabled the elucidation of a mechanism for ozonolysis. Using RAIRS, the formation and subsequent decomposition of the primary ozonide of C_{60} was detected and identified. Upon decomposition the Criegee Intermediate is formed, which can either rearrange to form epoxide, ether, or ketone functionalities, or it can react with another impinging ozone molecule and form anhydrides and ketenes. The ketene formation was confirmed by dosing NH_3 and observing predicted products. Extensive oxidation of the fullerene surface leads to the formation of an ozopolymer of the top ~10-20% of the overall film. The ozopolymer appears to protect the underlying film from further oxidation. Some slow penetration of ozone into the bulk of the film is seen with continuous ozone exposure but this happens over hours (~5-10 hours), as opposed to seconds. XPS showed three different oxidation states of carbon, one attributed to the C-C bonds of the fullerene cages, the second a result of the C-O bonds, and the third, representing C=O bonds. Isotopically-labeled ozone dosing and electronic structure calculations were extremely helpful in assigning the primary ozonide.

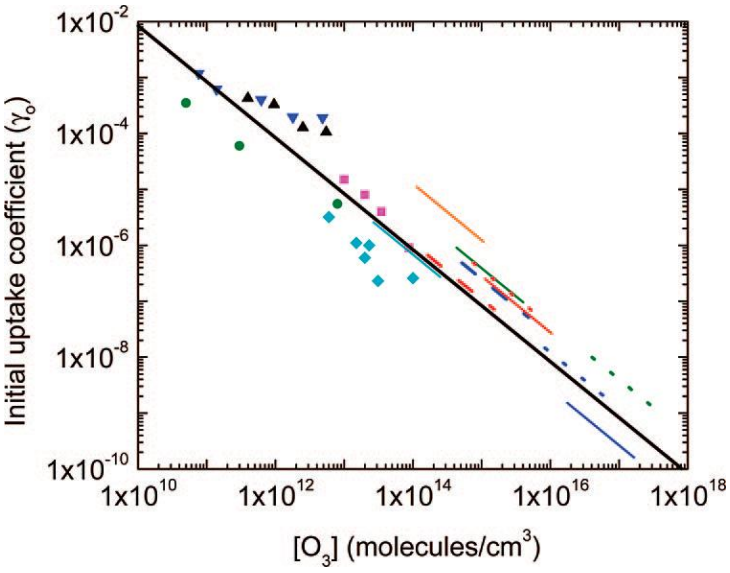

Figure 4.34: The initital uptake coefficient (γo) as a function of [O_3]. The solid black line is a prediction of the Langmuir-Hinshelwood model for ozone-saturated surfaces.[99] Reprinted with permission from McCabe *et al. JPC C* 2010, *113(6)*, 2020-2127. Copyright 2010 American Chemical Society.

The kinetic analysis revealed an initial reaction probability of 1.4 x 10^{-3}, if all 30 double bonds of the C_{60} cage are consumed, or 4.8 x 10^{-5}, if only one site is consumed per cage. In 2009, McCabe and Abbatt published a study of the heterogeneous loss of gas-phase ozone on soot.[99] They calculated values for the initial uptake

coefficient (γ_o), analogous to the initial reaction probability. Their reported γ_o was (8-100) x 10^{-5}, depending on the specific surface area of the soot sample. McCabe and Abbatt plotted their values for γ as a function of the concentration of ozone, along with γ values for a number of different studies, shown in Figure 4.34. The studies were performed on a variety of surfaces; from other types of soot, to surfaces containing metal oxide active sites. The solid black line represents the predicted behavior for the Langmuir-Hinshelwood model for an ozone-saturated surface. The data collected in these studies falls slightly above the L-H model (γ = 1.4 x 10^{-3}, $[O_3]$ = 5.8 x 10^{12} molecules cm^{-3}); suggesting that C_{60} is more reactive with ozone than typical alkenes. This result is not surprising when the increased reactivity of the molecule, along with the number of potential reaction sites (~ 30 double bonds) is taken into consideration. There is also an important difference in experimental method that can have an impact on the measured reaction probability. The experiments described herein were all performed in UHV. The UHV environment allows a surface to be exposed that possesses minimal adsorbed contamination; meaning the reactive sites are more easily available to ozone than if the same sample were studied under ambient conditions. The exposure of a fullerene surface at atmospheric pressures might result in a greater value for the initial reaction probability, indicating that reaction with ozone is less likely, only because the reactive sites may be unavailable. The issue with reporting an initial reaction probability from atmospheric studies is ozone can potentially react with other species present, not solely C_{60}. To eliminate the possibility of these additional reactions, and ensure the reaction sites are readily accessible to ozone, these experiments were performed in UHV, adding confidence to the measurements reported. Based on the plot in Figure 4.34, McCabe and Abbatt suggest a common pathway for the uptake of ozone onto a surface must exist, and the rate determining step involves only the ozone molecule, as opposed to features

inherent in the surface. The UHV data for C_{60} ozonolysis at the gas-surface interface supports their hypothesis, but it is important to point out that the data also implies C_{60} is likely a more reactive molecule than a typical alkene.

The assignment of peak 977 cm^{-1} to the primary ozonide was further supported by evaluating the rate of fullerene cage decomposition versus the rate of appearance of 977 cm^{-1}. Precisely as the cages were reacted, the peak at 977 cm^{-1} was appearing in the spectrum. This correlation indicates that these species have a first-order dependency upon one another, as would be expected for an alkene and primary ozonide species. Finally, temperature-dependent studies to calculate activation energies for the formation and decomposition of the primary ozonide were carried out. The activation energy for the formation of the primary ozonide of C_{60} was not quantitatively determined. The scattered in the data suggests a small barrier for the formation of the PO. The data for the decomposition of the PO implies a small barrier. Further studies are required over a broader temperature range to obtain a quantitative value. These results are an important addition, not only to the study of fullerene chemistry, but to the understanding of ozone reactivity as well.

Chapter 5

The Ozone Oxidation of Larger Surface-Bound Fullerenes: C_{70}, C_{76}, C_{78}, C_{84}

5.1 Introduction

As fullerenes increase in size, their structures change, and so too do their physical and chemical properties. The field of fullerene chemistry has grown into a vast area of research of, not only the characteristics of these unique molecules, but their use in many different scientific applications.[100] While C_{60} is the most common, there are scores of other fullerenes, each with its own cage structure and distinctive properties. Just as Chapter 4 focused on the ozonolysis of C_{60} for environmental and health concerns, the oxidation studies of larger fullerenes are motivated by many of the same reasons. A number of gas-phase computational studies suggest that as the number of carbons incorporated into the cage increases, so does the overall stability of the molecule.[101] The first experimental evidence of this hypothesis was presented in 2007 by Rojas *et al.*[102] Rojas *et al.* found that as the number of carbon atoms per cage increased the degree of strain on the individual carbon atoms decreased. While this conclusion is an important confirmation of the above hypothesis, it is not surprising. A significant portion of C_{60}'s reactivity is attributed to the high degree of curvature, and therefore strain, imposed by the inclusion of pentagonal rings within the cage structure. As the fullerenes grow in size, the number of hexagonal rings increases (e.g. C_{60} has 20 hexagons, C_{70} has 25), but the number of pentagons stays the same (e.g. both C_{60} and C_{70} have 12 pentagons). Thus, with fewer pentagons, sections of the cage structure begin to resemble a graphene sheet, or a single-walled carbon nanotube, as opposed to a sphere. The research presented in this chapter is the result of an investigation focused on the ozone oxidation of larger surface-bound fullerenes. If the physical and chemical

properties differ for the larger molecules, it is possible that their reactivity with ozone may also change.

The reactivity of ozone and unsaturated sites is well-established. In fact, the study of fullerene oxidation via ozone has been the focus of numerous studies; originally because the ozonolysis of larger fullerenes was found to be a useful technique for fullerene modification. The details of larger fullerene ozonolysis are however, not fully understood. In 1993, Heymann and Chibante performed the simultaneous ozonation of a mixture of C_{60}, C_{70}, C_{76}, C_{78}, and C_{84} in toluene.[60c] They concluded that C_{70} was oxidized more slowly than any of the other fullerenes and that the rate of oxidation increased in the order C_{60}, C_{76}, C_{78}, and C_{84}, with C_{84} oxidizing at the fastest rate. Heymann and Chibante also assume that the rate of transformation of the molozonide (referred to as the primary ozonide in this document) to product is faster than the rate of formation of the molozonide. Their data and the data included later in this chapter are the only two studies that compare the rates of ozone reaction for this group of fullerenes. Several years later, Anachkov *et al.* studied the effect of temperature on the rate of ozonolysis of C_{60} and C_{70}.[60a] These researchers reported that C_{70} reacts more quickly with ozone than the smaller C_{60} molecule. Anachkov's conclusions are well supported by a number of other studies,[60f] however, many researchers in the field turned to theory to better understand the differences in fullerene reactivity.

Theoretical calculations have been employed for the last few years to investigate the initial interaction between ozone and fullerenes, as well as predict the reactivity of larger fullerenes. Sabirov's 2008 DFT study of ozone's addition to C_{60} and C_{70} revealed and confirmed many experimental hypotheses. Similar to alkene primary ozonides, the species forms first as a pre-reactionary complex that later converts to a primary ozonide. Sabirov *et al.* were also able to

determine the most likely bonding sites for an incoming ozone molecule on both the C_{60} and C_{70} fullerenes. For both molecules, the theoretical predictions correlate well with predictions based on experimental data.[36, 91] With experiment and theory able to complement each other for the study of this system, researchers can analyze the reaction from beginning to end: reactants, intermediates, and of course, products. The goal of these studies was to determine 1) if the rates of reaction at the gas-surface interface are similar to those observed in solution phase, 2) if ozone reacts with the larger fullerenes (C_{76}, C_{78}, and C_{84}) via the same initial step (i.e. formation of the primary ozonide), and 3) if the products of ozonolysis of larger fullerenes are comparable to those observed for C_{60} and C_{70}. The chemistry at the gas-surface interface is very different than that seen in other phases (e.g. gas, solution, solid) because effects such as solvation, are no longer present. Therefore, the reaction of gas-phase ozone and surface-bound fullerenes should be treated as an unstudied system and explored fully to gain a complete understanding of the reaction.

Perhaps one of the most interesting abilities of fullerene molecules is their propensity for coalescence reactions. Any study that focuses on the extensive ozonolysis of fullerenes reports the observation of large carbon clusters or polymeric material.[11a, 11f, 103] While the appearance of such a material is intriguing, the dramatic alteration of its chemical properties is even more so. The polymeric material, often referred to as ozopolymer, is hydrophilic and readily soluble in water, methanol, and other polar solvents; behavior dissimilar to unoxidized fullerenes. Based on the observation of this material, is seems reasonable that ozone may be capable of more than just fullerene functionalization.

Research into the ozone oxidation of larger fullerenes is scarce. The bulk of the studies have been performed on C_{60} and C_{70}. The work has shown that C_{70} oxidizes in much the same

way as C_{60}, with similar products formed and an end result of ozopolymer formation.[1] The work included in this chapter focuses on the ozonolysis of C_{70}, C_{76}, C_{78}, and C_{84}. This research compares the rates of reaction as well as the mechanistic differences which occur as a result of the distinct cage structures. Understanding how each fullerene reacts individually will provide more information about fullerenes and further expand the community's knowledge of this interesting family of molecules. The ultimate desire is the utilization of the results to aid in the prediction of the environmental fate of these carbonaceous nanomaterials.

5.2 Experimental Details

5.2.1 Materials

All chemicals were used as received without further purification unless otherwise noted. Fullerenes (C_{70}, C_{76}, C_{78}, and C_{84}) were purchased from Bucky USA. Research grade oxygen, ultrahigh purity nitrogen, liquid nitrogen, and dry ice were purchased from Airgas Specialty Gases. Polycrystalline gold substrates were received from Evaporated Metal Films. Reagent grade acetone was obtained from Pharmco-Aaper and Commercial Alcohols. The details of ozone synthesis and storage are covered in Chapter 2 and Chapter 4.

5.2.2 Formation of C_n Films

Fullerenes were deposited on polycrystalline gold surfaces, which provide a highly reflective support for the fullerenes thereby enabling the use of reflection-absorption IR in the study of their reactivity. The Au substrates were purchased from Evaporated Metal Films, Inc. They are made by first depositing a 50 Å thick layer of chromium (used as an adhesive layer) onto a glass slide, then depositing ~1000 Å of Au. The dimensions of the slides were 1" x 1" x 0.062". To clean an Au slide before introduction into the UHV chamber, it was submersed in a

solution of 70% sulfuric acid and 30% hydrogen peroxide (30%), also known as piranha solution, for ~45 minutes. *Warning: Piranha solution is an oxidizing agent which reacts violently with organics! Extreme caution should be taken when using this solution!* The piranha solution was used to remove the majority of the hydrocarbons which adsorb to the surface from exposure to air. Once the Au slide was removed from the piranha, it was rinsed thoroughly with deionized water (Millipore Purification Systems, 18.2 MΩ), and then dried completely with UHP nitrogen. After drying, the slide was placed into the UHV chamber. Immediately after the Au slide was placed into the load lock chamber, the crucible evaporator was detached from the load lock, any remaining fullerene from the previous experiment was taken out, the crucible was cleaned, and then new fullerene powder was placed in the crucible. After transferring into the UHV main chamber, the Au slide was then cleaned with ozone for one hour. Ozone was used to remove any remaining hydrocarbons from the surface before fullerene deposition. Two advantages of cleaning the surface with gas-phase ozone in UHV were: 1) the actual removal of the hydrocarbons was monitored using RAIRS and 2) the surface remained clean until deposition since the fullerenes were deposited in vacuum. After one hour of ozone cleaning, a spectrum of the freshly cleaned Au slide was recorded with the IR. The spectrum was saved to be used later as a background. The Au slide was transferred into the load lock to deposit the fullerene of choice. As stated in Chapter 2, the voltage and current required to deposited fullerenes on the Au slide varied depending upon the fullerene. For C_{70}, total time for film deposition was 35 minutes, with the maximum voltage and current of 4.5 V and 4.5 A. The maximum temperature during C_{70} deposition was 772 K. C_{76} deposition, which proved the most difficult, required 5 V and 5 A, resulting in a maximum deposition temperature of 984 K. C_{78} and C_{84} deposition lasted 45 minutes, was achieved with 7 V and 7 A, and reached a maximum temperature of 1299 K.

5.2.3 Surface Exposure

After the fullerenes were deposited onto the Au slide, the slide was transferred back into the main chamber. Once the slide was positioned as close as possible to the position occupied when the background was recorded, it was scanned with the IR. Utilization of difference spectra requires the position of the slide to be the same before and after deposition, to help ensure the baseline is as flat as possible in the resulting spectra. In practice, this is achieved by recording the coordinates (X, Y, and rotation) on the manipulator before transferring into the load lock for deposition. Upon proper realignment of the sample, the fullerene surface is scanned to obtain a spectrum of the sample before ozone exposure. With an initial spectrum recorded, then saved as a background, the first spectrum before opening the ozone doser should be positioned exactly at 0 on the intensity scale (y-axis). The ozone is then introduced into the main chamber via the capillary array doser (CAD).

5.2.4 RAIRS Data Acquisition

The reaction of gas-phase ozone with surface-bound fullerenes is followed in real time with a Bruker IFS 66v/S spectrometer. The spectrometer is equipped with a SiC globar source, which produces an IR beam. The IR beam is focused onto the Au surface in the middle of the UHV chamber at an incident angle of ~86° relative to the surface normal. The detector used with the Bruker spectrometer is a mid-range MCT detector (750 - 4000 cm^{-1}), that requires cooling with liquid nitrogen. Every spectrum shown in this dissertation is produced by the co-addition of 100 scans acquired over 90 seconds. The resolution was set at 2 cm^{-1} and the scanner velocity was held at 20 kHz.

5.2.5 XPS Measurements

The fullerene surfaces were characterized before and after ozone exposure using two different X-ray photoelectron spectrometers (XPS), which are described detail in Chapter 2. One of the spectrometers is incorporated into the chamber setup, allowing for the collection of data without removing the surface from vacuum. This configuration is beneficial because some species formed during ozone exposure may not be stable in atmosphere, so scanning the surface directly after dosing permits observation of species that might unstable in atmospheric studies. To perform XPS analysis in the main chamber, the sample is rotated into position using the 360° rotatable manipulator. The sample is positioned relative to the hemispherical analyzer (HA), depending upon the desired angle of detection. If the sample is situated in front of the HA so that the HA is normal to the surface, the position is optimum for sampling elements below the surface. If the surface is aligned at a 15° angle with respect to the HA, it is known as a grazing angle, which is ideal for studying the surface of the sample. Once the sample is positioned, a Mg Kα (1253.6 eV) x-ray source is used at 250 W (12.5 kV and 20 mA). The impinging x-rays produce photoelectrons, which are subsequently detected with the HA. A survey scan is collected first to obtain an overall representation of the elemental composition of the surface. After the survey scan is inspected, individual regions (or elements) are focused on with more selective pass energy. The second XPS is located in the Surface Analysis Lab at Virginia Tech. This instrument was utilized when the *in situ* XPS was in need of repair.

5.2.6 Electronic Structure Calculations

Electronic structure calculations were performed on each fullerene molecule in the primary ozonide form (e.g. $C_{70}O_3$, $C_{76}O_3$, $C_{78}O_3$, and $C_{84}O_3$). The calculations are an important addition to the experimental data because ozone oxidation of these molecules has yet to be

studied. If comparable frequencies can be calculated, it will provide support for peak assignments and general mechanisms proposed. The modeling method used was density functional theory (DFT). Specifically, the exchange-correlation hybrid functional B3LYP with a small 3-21G* basis. This particular method has been employed by other researchers and found to predict the geometry and electronic structure of fullerenes with reasonable certainty.[55]

5.3 Ozone Exposure

5.3.1 Ozone Oxidation of Surface-Bound C_{70}

The RAIR spectra for the reaction between gas-phase ozone and surface-bound C_{70} are shown in Figure 5.1. After the surface has been exposed to 350 L of ozone (1L = 10^{-6} Torr·s), the IR primary active mode of the C_{70} molecule (1431 cm^{-1}) begins to decrease, indicating a reaction on the C_{70} cages. The disappearance of the C_{70} modes coincides with the appearance of a peak centered around 970 cm^{-1} (967 and 975 cm^{-1}), see Figure 5.2. The C_{70} structure has three likely reaction sites for the ozone molecule: *a,b*, *c,c*, and *d,e*, shown in Figure 5.3. These three bonds are the most likely sites for reaction because they possess the most double bond character, a function of the neighboring pentagon rings. Calculations have shown that two of the three sites (*a,b* and *c,c*) are

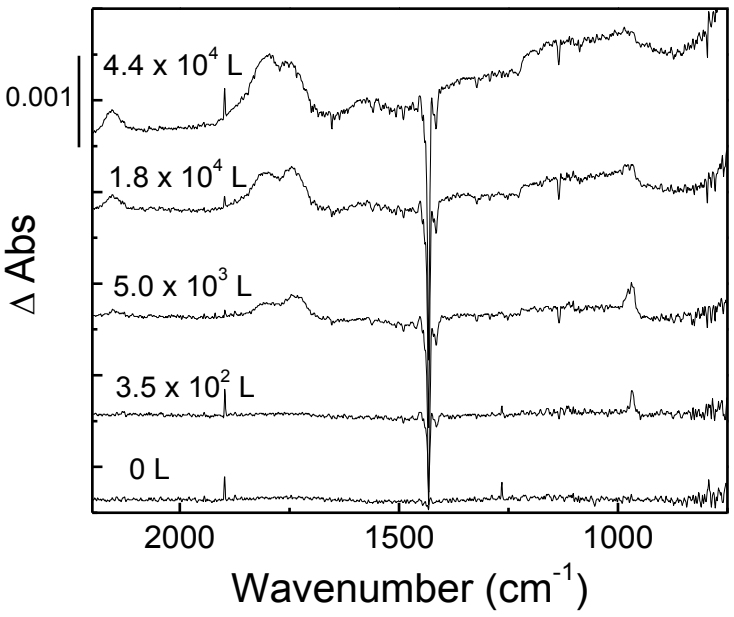

Figure 5.1: RAIR difference spectra of the ozone exposure of a C_{70} film deposited on Au in high vacuum. A peak centered at 970 cm^{-1} exhibits intermediate behavior.

more favorable and upon reaction with an ozone molecule, result in the formation of $C_{70}O_3$.[89a] The peak observed in this data not only exhibits behavior indicative of an intermediate species (see Figure 5.4), similar to that demonstrated in the peak corresponding to the primary ozonide of C_{60} (977 cm^{-1}), but also appears to potentially include more than one peak, shown in of Figure 5.2. The appearance of two intermediate peaks, or two primary ozonide peaks, is expected based on existing experimental and computational studies.[38, 91] Heymann *et al.* were able to identify two different ozonide species on the C_{70} molecule after exposure to ozone. In the study, ozone was bubbled through solutions of C_{70} in toluene, after which aliquots were removed and run through an HPLC. Immediately after ozonation, two prominent peaks appeared in the chromatogram that were later assigned to the *a,b*-$C_{70}O_3$ ozonide adduct and the *c,c*-$C_{70}O_3$ ozonide adduct. The spectrum shown in figure 5.2, suggests that the C_{70} molecules within the film may have formed two isomers of $C_{70}O_3$.

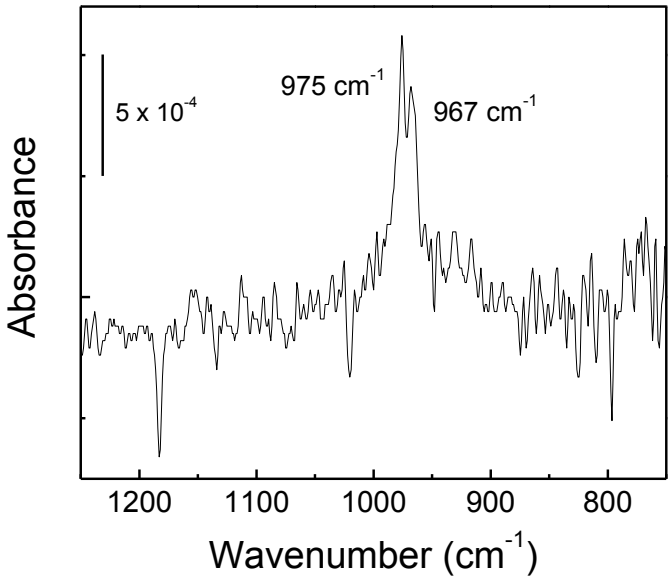

Figure 5.2: Peak that appears when the C_{70} film is exposed to gas-phase ozone. The literature suggests that this could potentially be two peaks, both possessing behavior suggestive of an intermediate.

Analogous to the results of C_{60}, when the primary ozonide peak decreases, product peaks appear in the spectra, see Figure 5.1. C_{70} appears to have a similar variety of ozonolysis products as its smaller counterpart, C_{60}. Figure 5.5 shows a direct comparison of the C_{60} and C_{70} spectra following ozone exposure. The product peaks at 1582, 1754, 1795, and 2151 cm^{-1} are assigned to the C=C bond enhancement, carbonyl functionalities, anhydrides, and ketenes, respectively.[11a, 11f]

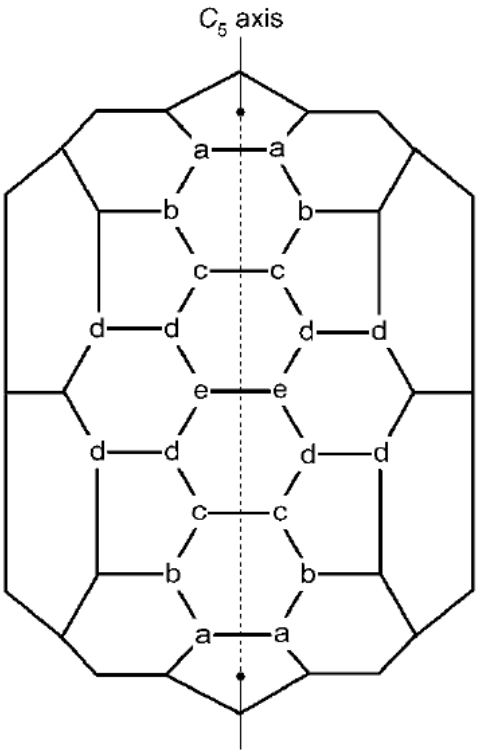

Figure 5.3: Depiction of a section of the C_{70} cage. Within this section, it is possible to observe the five different types of carbon sites present in the C_{70} molecule, as well as the eight types of bonds.

X-ray photoelectron spectroscopy (XPS) was employed to support assignment of the peaks observed with RAIRS. The product peaks seen during the ozonolysis of C_{70} were very similar to those detected during oxidation of C_{60}. It follows that the C_{70} data obtained with XPS should be analogous to that collected for C_{60}. The C 1s region for C_{70}, shown in Figure 5.6, indicates that over 70% of the carbon atoms within the C_{70} film are unoxidized (i.e. bonded to other carbon atoms). The underivatized carbon is represented by the intense peak at 284.6 eV. The peak at 286.5 eV is due to a variety of C-O bonds (e.g. esters, ethers, epoxides, anhydrides) and the data suggests that there are more C-O functionalities than C=O (peak at 289.4 eV), another observation of the IR data. The data recorded in the O 1s region for oxidized C_{70} tells the same story (Figure 5.7). The peak at 533.4 eV belongs to C-O moieties, while the one at 531.7 eV is due to C=O functionalities.

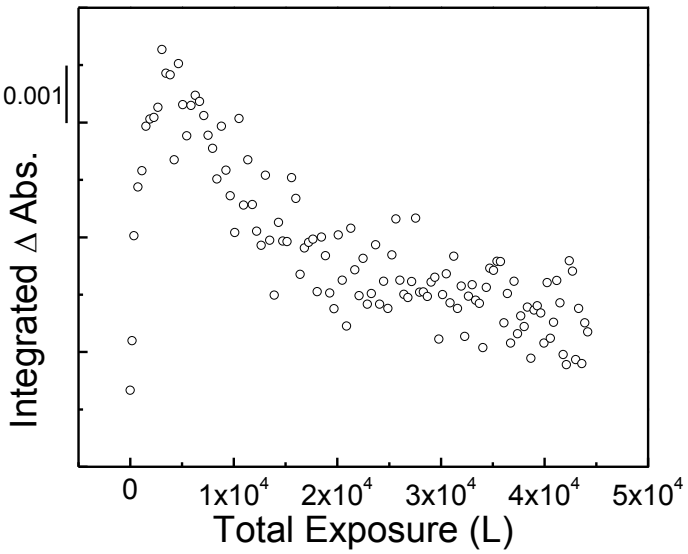

Figure 5.4: The peak profile for the peak shown in Figure 5.2. The profile indicates the species responsible for the peak is an intermediate, perhaps primary ozonide of C_{70}.

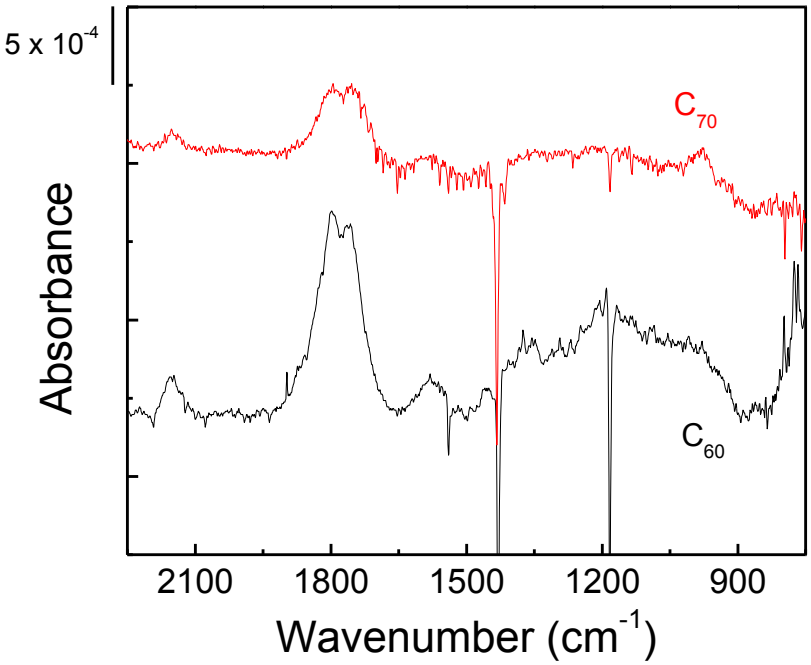

Figure 5.5: A direct comparison of the final spectra of C_{60} and C_{70} after exposure to gas-phase ozone. C_{60} appears to undergo more extensive oxidation and form a larger variety of products.

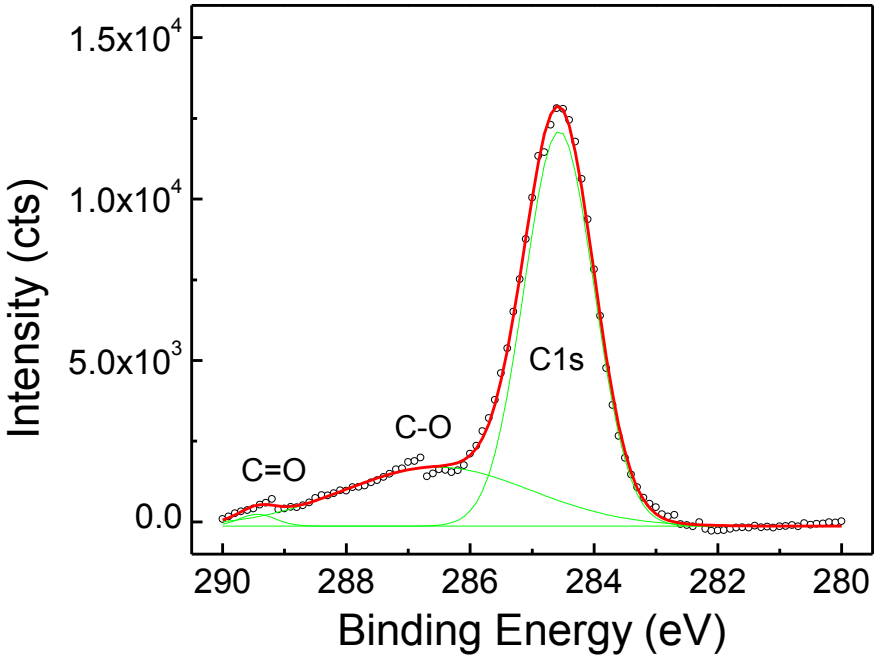

Figure 5.6: C 1s region collected for the oxidized C_{70} surface. The data implies that the majority of the carbon is unoxidized, with some C-O and C=O bonding present within the surface.

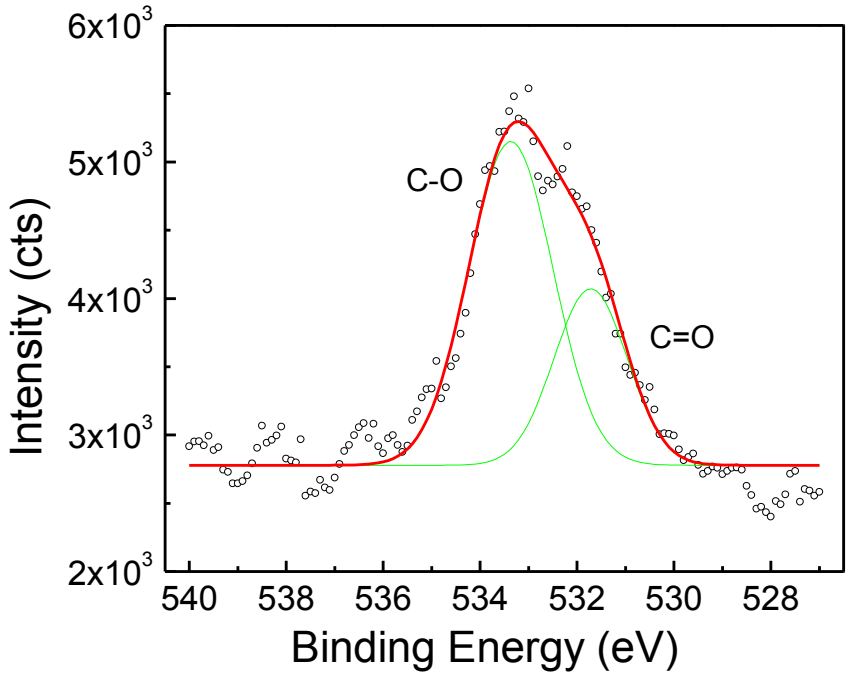

Figure 5.7: O 1s region for the C_{70} surface after exposure to ozone. The peak contains two components, the one at higher binding energies is attributed to C-O groups in the film, while the lower component is due to C=O species.

The DFT, specifically B3LYP/3-21G*, was used to model two different primary ozonides of C_{70}. The ozone molecule was added across the *a,b* bond on one and a *c,c* bond in the other. The structures used are shown in Figure 5.8. In the IR spectrum of C_{70}, if two peaks are

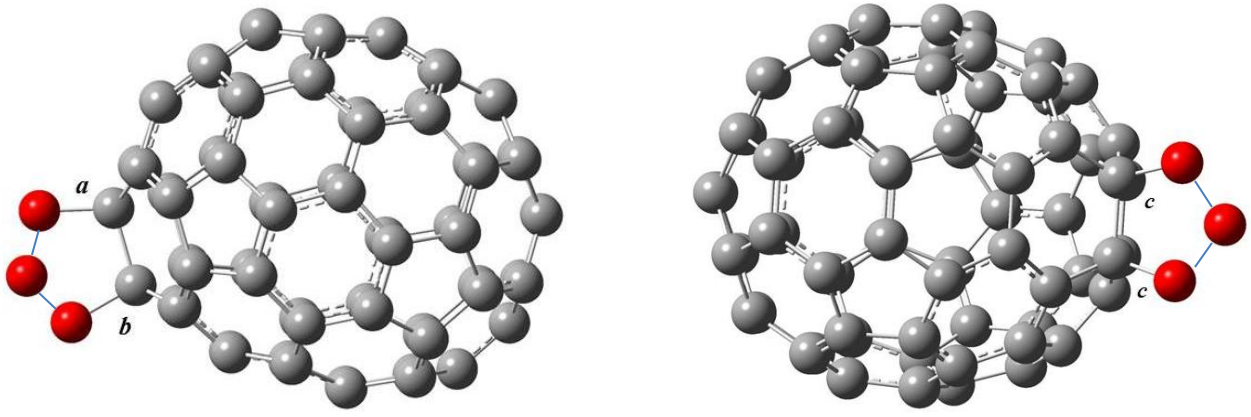

Figure 5.8: The two C_{70} structures studied with B3LYP/3-21G*. The structure on the left is a result of the ozone addition across a *a,b* bond, while the structure on the right is formed when ozone addition occurs on a *c,c* bond.

considered, the intermediate peaks appear at 967 and 975 cm^{-1}, as shown in Figure 5.2. Based on the literature, it is likely that there were two intermediate peaks because ozone addition occurred across both types of bonds within the C_{70} film. An IR frequency analysis was performed on both of the structures shown in Figure 5.8. The calculations predicted that the primary ozonide of C_{70}, when ozone adds across the *a,b* bond, will produce an IR active peak at 947 cm^{-1}. For the ozone addition across the *c,c* bond, the symmetric stretch of the primary ozonide was calculated at a frequency of 950 cm^{-1}. Both computed values are off by approximately 15 cm^{-1}, a minor difference when using this low level of theory. With the supporting electronic structure calculations, it is reasonable to suggest the peaks exhibiting intermediate behavior in the C_{70} spectra are, in fact, a result of two different primary ozonides of the ellipsoidal fullerene molecule. To further test this hypothesis, additional studies, perhaps using isotopically-labeled $^{18}O_3$, are required. By performing added experiments more concrete verification of peak assignments will be obtained. These experiments will likely be pursued by a future member of the Morris Research Group.

5.3.2 Ozone Oxidation of Surface-Bound C_{76}

The RAIR spectra for the reaction between gas-phase ozone and surface-bound C_{76} are shown in Figure 5.9. After the surface has been exposed to only 350 L of ozone, the primary IR active mode of the C_{76} molecule (1440 cm^{-1}) begins to decrease, indicating a reaction on the C_{76} cage. Unfortunately, any possible intermediate peaks formed during ozonolysis were unobservable via RAIRS. Regardless, reactions on the cage structures and subsequent products formed as a result of the ozone oxidation were detected. If the ozone oxidized the C_{76} cage via the same pathway as that observed for C_{60}, the most favorable sites for reaction are the α and β sites near the "poles" of the molecule, shown in Figure 5.10.[89b] It is important to note that, also

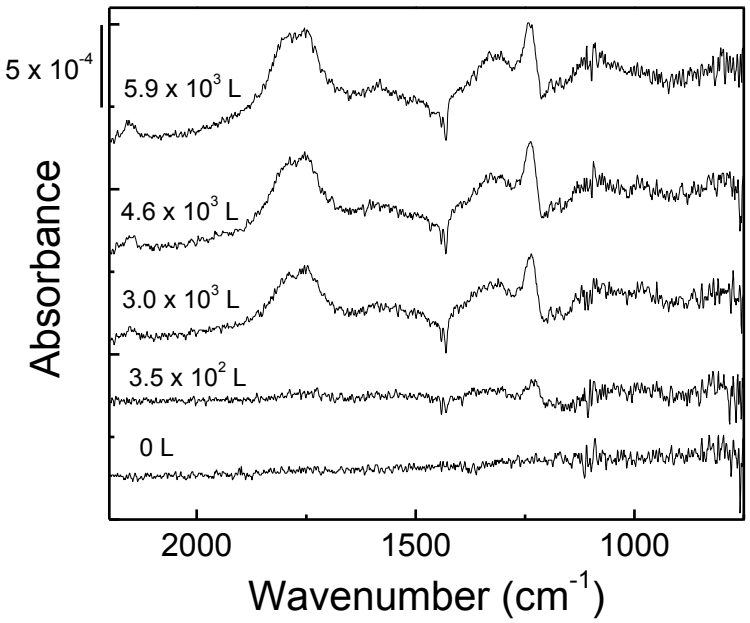

Figure 5.9: RAIR spectra recorded during the ozone exposure of a C_{76} film created in high vacuum.

similar to C_{60}, the reactive sites for C_{76} are 6/6 bonds. While the bond itself does not belong to a pentagon, each carbon in the 6/6 bond is incorporated into a pentagonal ring. The pentagons induce strain on the cage structure, therefore providing a more reactive site for ozone to attack. Another similarity between the ozonolysis of C_{76} and that of C_{60} and C_{70}, is the resulting products. As observed in the ozonolysis of C_{60} and C_{70}, the IR spectra of oxidized C_{76} indicates an enhancement of the C=C bond, carbonyl functionalities, anhydrides, and ketenes. However, there appears to be a new product present in the spectra as well. Based on existing literature, the large peak, centered at 1237 cm^{-1}, is representative of a C-O bond. Several studies of the ozone ox idation of carbon nanotubes have observed peaks located in a similar

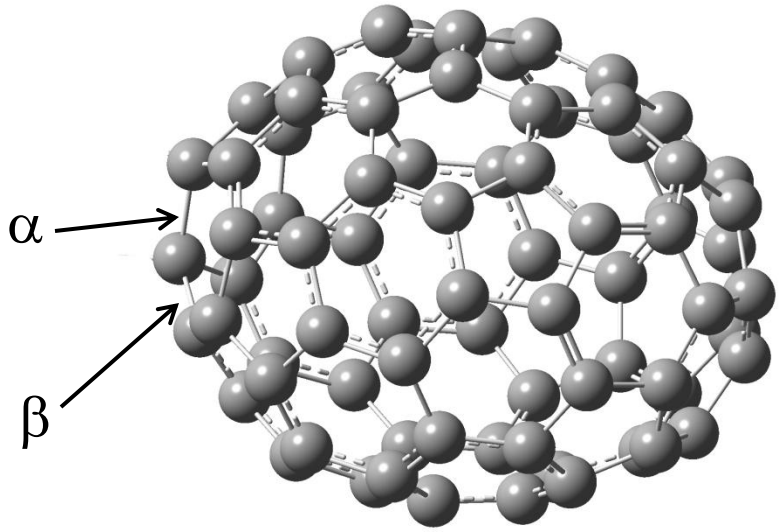

Figure 5.10: The cage structure of a C_{76} molecule. The most favorable sites for ozone reaction are positioned at the "poles" of the molecule; they are denoted as α sites and β sites.

position.[104] Studies report the assignment of this peak to an ester functionality.

The detection of a different product with RAIRS is supported by the intense C-O peak at 286.5 eV in the C 1s region, Figure 5.11. The XPS data indicates that a significant portion of the oxidation species possess C-O moieties (e.g. ester, ethers, epoxides, anhydrides). However, the presence of C=O functional groups is also detected (peak at 288.4 eV). Figure 5.12, displays the results of the O1s region, and helps corroborate the above statement, with peaks at 532.8 eV (C-O) and 531.2 eV (C=O).

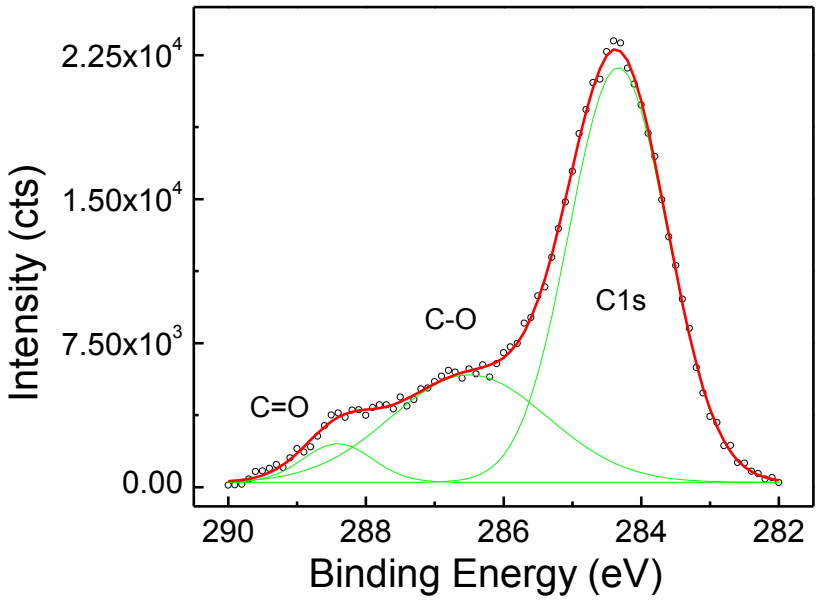

Figure 5.11 (above): The fitted C 1s region of an oxidized C_{76} surface.

Figure 5.12 (below): The fitted O 1s region of an oxidized C_{76} surface.

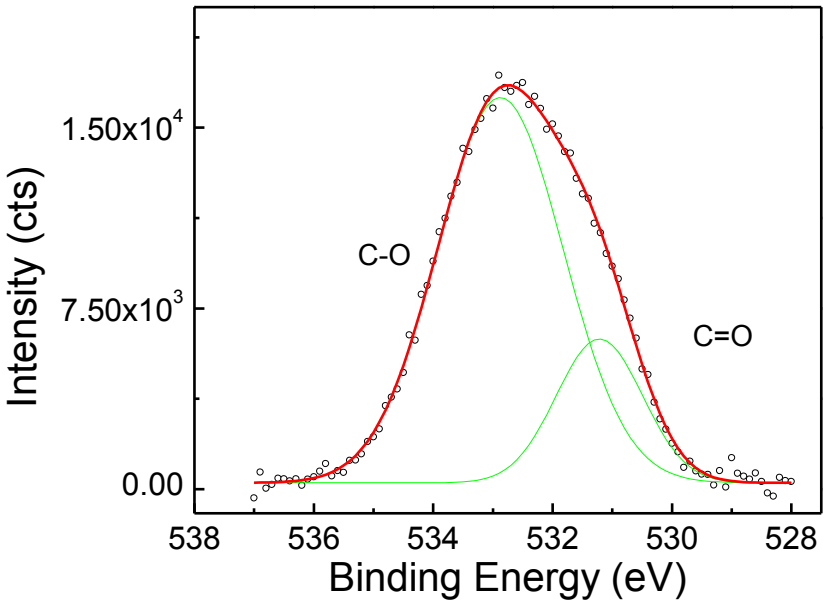

Unfortunately, any peaks displaying intermediate behavior were not observed in the C_{76}/O_3 data. However, a computational geometry optimization and IR frequency analysis were performed on the possible primary ozonide structures of C_{76}. Because the previous calculations have produced values that agree very well with experiment, these calculations can be compared to more resolved experimental data collected in the future.

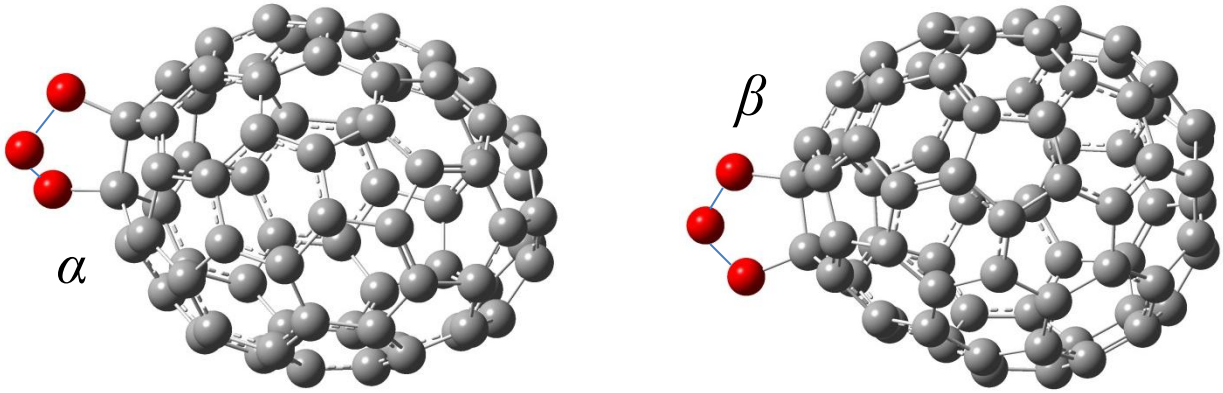

Figure 5.13: The two C_{76} structures studied with B3LYP/3-21G*. The structure on the left is a result of the ozone addition across an α bond, while the structure on the right is formed when ozone addition occurs on a β bond.

The reactive sites for the C_{76} molecule are denoted α and β sites, and are located on the poles of the cage structure. The calculations of each of the above structures, Figure 5.13, found several IR active modes for the primary ozonide of C_{76}. A few of the modes are listed in Table 5.1, along with their assignment.

Table 5.1: Calculated IR frequencies for the primary ozonide of C76 and the corresponding assignments.

Reaction Site	Frequency (cm^{-1})	Assignment
$C_{76}O_3$ (α)	796	Asymmetric ozonide stretch
	872	Symmetric stretch for C-C bond within the ozonide ring
	901	Symmetric ozonide stretch
$C_{76}O_3$ (β)	880	Symmetric stretch for C-C bond within the ozonide ring
	898	Symmetric ozonide stretch
	945	C-O stretch within ozonide ring

5.3.3 Ozone Oxidation of Surface-Bound C_{78}

The RAIR spectra for the reaction between gas-phase ozone and surface-bound C_{78} are shown in Figure 5.14. After the surface has been exposed to only 560 L of ozone, the IR active modes of the C_{78} molecules begin to decrease, indicating a reaction on the C_{78} cages. As the C_{78} modes decrease, a broad peak in the low wavenumber region (780 – 880 cm^{-1}), displaying intermediate characteristics (shown in Figure 5.16), begins to appear, shown in Figure 5.15. The peak, which is most likely associated with the primary ozonide of C_{78}, is extremely broad, presumably a result of primary ozonides formed on several different reactive sites on the C_{78} cage. As the peak decreases, numerous product peaks begin to appear. The peak positions along with their assignments are listed in Table 5.2. Unlike the ozonolysis of C_{60}, the oxidation products of C_{78} do not include anhydrides, evidenced by the lack of peaks in the 1700-1800 cm^{-1} region. The reason for the absence of this product will be discussed in a later section.

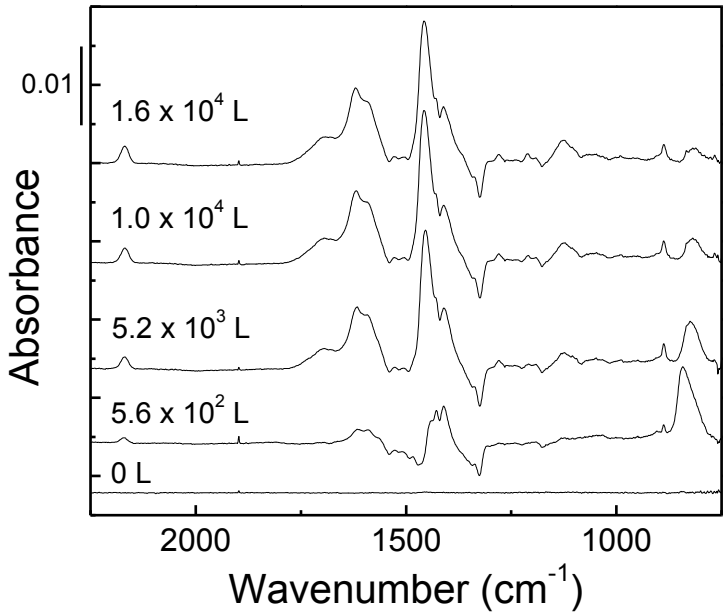

Figure 5.14: RAIR difference spectra from the ozone exposure of a C_{78} film created in high vacuum. The broad peak in the low wavenumber region (780-880 cm^{-1}) exhibits behavior indicative of an intermediate species.

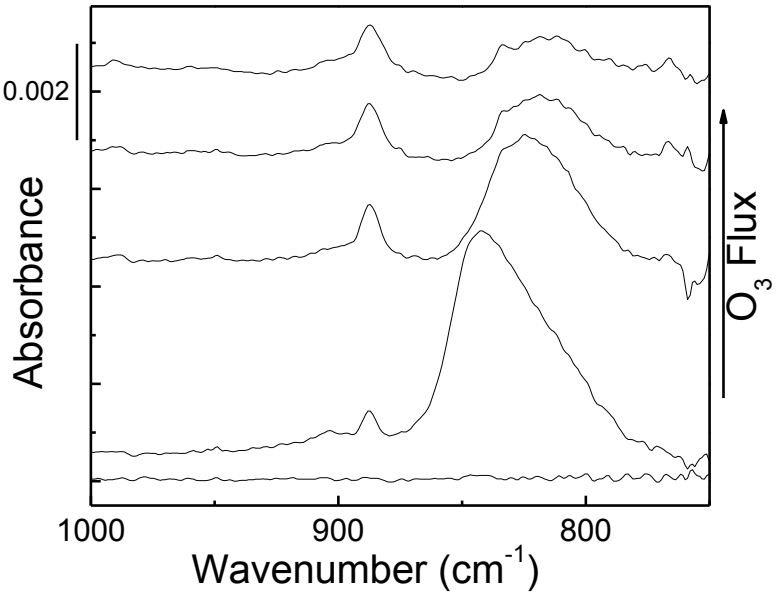

Figure 5.15: RAIR spectra of a peak with intermediate behavior which appears during the ozone oxidation of C_{78}. As ozone exposure continues, the peak decreases. By the end of the ozone exposure, the peak has completely disappeared.

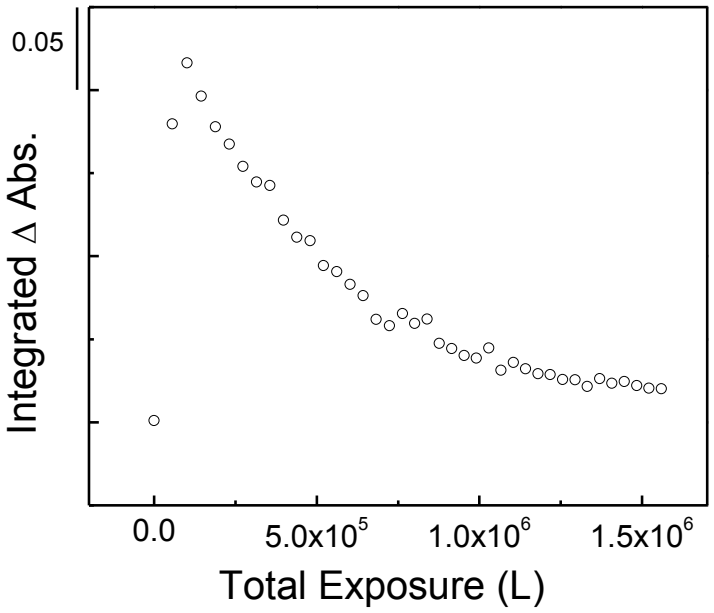

Figure 5.16: The peak profile for the peak with intermediate behavior, shown in Figure 5.15. This behavior suggests that the species associated with the peak may be the PO of C_{78} ($C_{78}O_3$).

Table 5.2: Observed peaks during the ozone oxidation of surface-bound C_{78}. The peaks have been assigned to likely functional groups and compared with existing literature values.

Peak Position (cm^{-1})	Assignment	Literature Peak Position (cm^{-1})
887	Epoxide deformation mode	876[105]
1125	Ester asymmetric stretch	1127[105]
1211	Epoxide breathing mode	1211[105]
1279	Ester (C=O) stretch	1283[105]
1410	Fullerene modes	---
1428	Fullerene modes	---
1454	Fullerene modes	---
1589	Enhancement of C=C bonds	1581[104a]
1620	Carbonyls	1617[105]
1680	Carbonyls	1677[105]
2168	Ketenes	---

The XPS data, much like the RAIR data, changed drastically as the largest fullerenes were studied, beginning with C_{78}. The basic profile of the C 1s region, shown in Figure 5.17, is much more complex than previously observed, and contains five peaks, likely associated with carbon species. The first peak, centered around 285 eV, includes signal from the sp^2 hybridized carbon within the film, and the sp^3 hybridized carbon. The carbon atoms within the fullerene cage structure are classified as sp^2 hybridized atoms, but as ozone oxidizes the structure, the carbons involved in reactive sites end up with sp^3 character. As with smaller fullerenes, the majority of the film is unoxidized and so the bulk of the carbon maintains its sp^2 character, shown by the peak at 284.9 eV. Approximately 5% of the carbon signal displays sp^3 hybridization after ozonolysis (peak at 285.4 eV). The data from thorough experiments with C_{60} and O_3, indicates that only the top 10-20% of the fullerene film was oxidized during ozone exposures. With that fact in mind, it is likely that roughly the same percentage of the larger fullerene films was oxidized. However, only about 5-10% oxidation was observed in the C 1s region, compared to the smaller fullerene cages. The second peak shown in the C 1s region was a result of extensive oxidation of the "poles" of the C_{78} molecules. As the fullerene cages get

larger, they contain more hexagon rings, while the number of pentagons stays constant. The consequence of this structural feature is a decrease in the number of reactive sites for ozone addition. This decrease in the number of available reactive sites could explain the observation of only ~ 5% sp^3 carbons, as opposed to 10%. Consistently throughout the oxidation of fullerenes, the reactive sites are most often observed as 6/6 bonds between two pentagonal rings. With larger fullerene cages, the pentagons are spaced farther apart, the cage becomes reactive in specific regions. For C_{78}, the reactive regions are the caps of the molecule, or "poles", where a larger degree of curvature exists (i.e. more pentagon rings in closer proximity to one another). Because only part of the molecule is reactive, a transition in the type of ozonolysis products, specifically, a lack of anhydrides and more extensive oxidation in smaller regions was observed. The more extensive oxidation causes oxide species that are heavily conjugated with C=C or C=O bonds; in most cases, combinations of both bond types were noted. These conjugated products are represented by the peak centered at 289 eV.

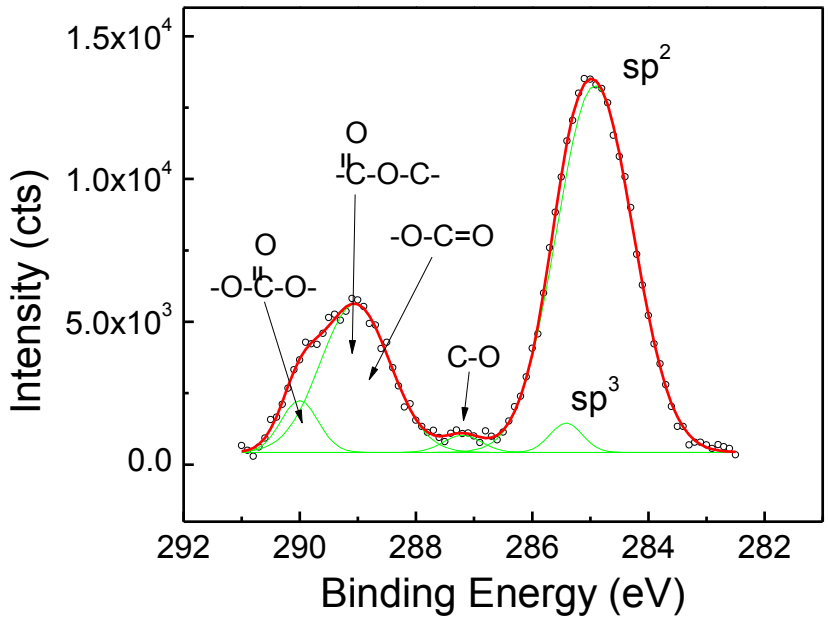

Figure 5.17: The C 1s region of a C_{78} film after exposure to ozone. The peak at lower binding energies contains contributions from the two types of hybridized carbon atoms within the film. The peak at higher binding energies is a result of extensive oxidation of the poles of the C_{78} molecules.

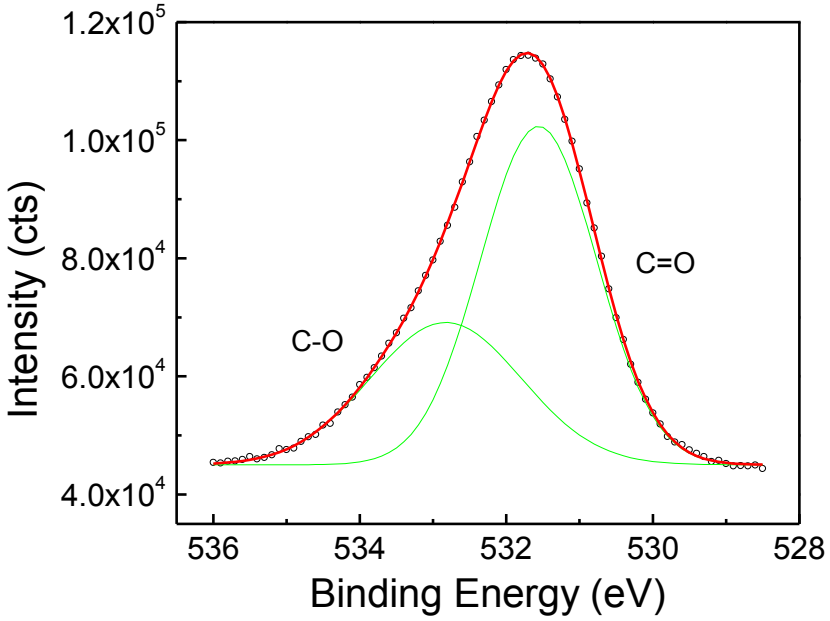

Figure 5.18: The O 1s region of a C_{78} film after exposure to ozone. The C_{78} molecules experience a higher degree of oxidation, but in more localized regions upon the cage structure.

The lower energy peak, at 289.0 eV, is due to ester functionalities, and the higher energy peak, at 289.9 eV corresponds to carbonate species. The final peak in the C 1s region lies at 287.2 eV, and is assigned to epoxide and ether functionalities.

The O 1s region, shown in Figure 5.18, also depicts the trend observed in the C 1s region and the IR spectra. A larger amount of C=O moieties is confirmed by the peak at 531.6 eV, while the number C-O bonds appears less intense, shown by the peak at 532.8 eV.

As the fullerene molecules increase in size, the number possible structures also increases. C_{78} has five different structural isomers. To perform the IR frequency analysis on this larger fullerene, the most stable structure with D_3 symmetry was chosen for the calculations. The molecular structure analyzed is shown in Figure 5.19. Two frequencies determined to be associated with the primary ozonide of C_{78} were at 866 and 898 cm^{-1}. These frequencies fall within the broad peak observed in the RAIR spectra recorded during the ozonolysis of C_{78}. As C_{78} has four other isomers, each with over 20 distinct atoms, there are a number of different reactive sites on each individual cage structure. The each combination of a particular isomer and reactive site to comprise the $C_{78}O_3$ molecule will have its own unique IR spectrum. The broad

peaks observed in the IR data suggest that not only were different isomers present within the film but also ozone reacted at various sites upon the cages. When studying larger fullerenes, a more thorough and detailed set of calculations is required to best explain all the features within the IR data.

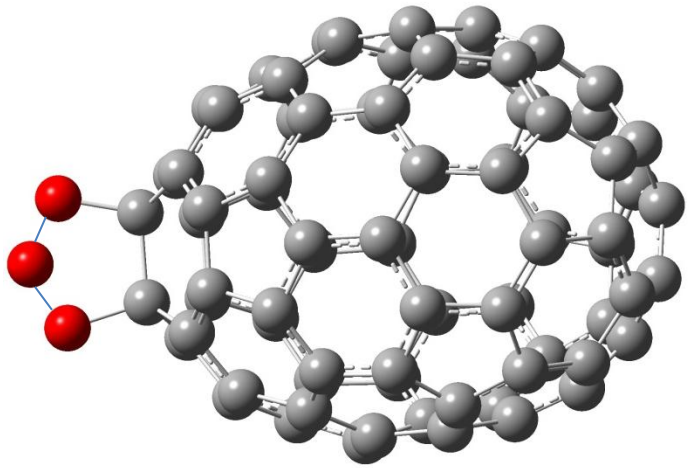

Figure 5.19: The structure of $C_{78}O_3$ used for electronic structure calculations. The C_{78} molecule possesses D_3 symmetry.

5.3.4 Ozone Oxidation of Surface-Bound C_{84}

The RAIR spectra for the reaction between gas-phase ozone and surface-bound C_{84} are shown in Figure 5.20. After the surface has been exposed to only 130 L of ozone, the IR active modes of the C_{84} molecules begin to decrease, indicating a reaction on the C_{84} cages. As with C_{78}, the spectra have the appearance of new oxidation products and a broad peak (780 – 880 cm^{-1}) exhibiting intermediate behavior. The peak, shown in Figure 5.21, is in all likelihood associated with the primary ozonide(s) of C_{84}. The decomposition of the primary ozonide, shown in Figure 5.22, was accompanied by the formation of a variety of oxidation products; the peak

positions are listed in Table 5.3. Again, no anhydrides appear to be present as a result of oxidizing C_{84} with ozone.

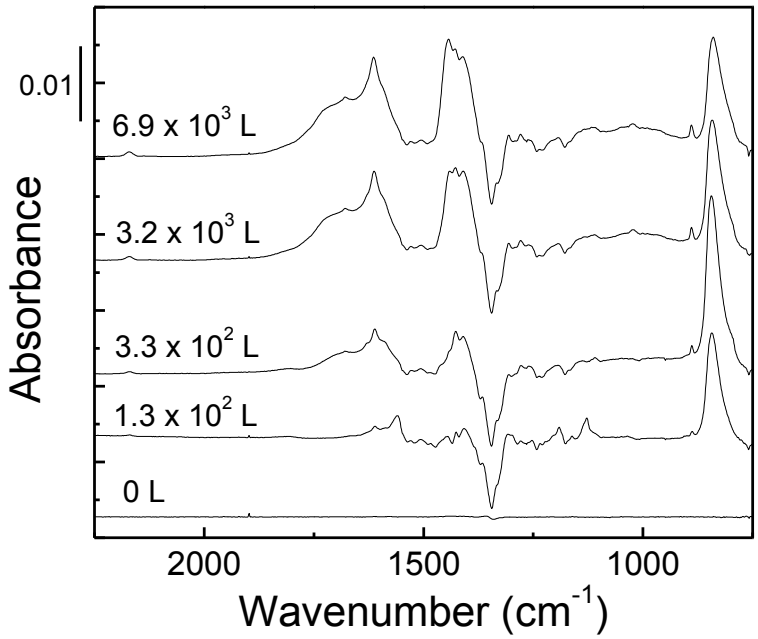

Figure 5.20: RAIR difference spectra of the ozonolysis of a C_{84} film. As ozone exposure continues, a larger peak, displaying intermediate behavior appears in the low wavenumber region.

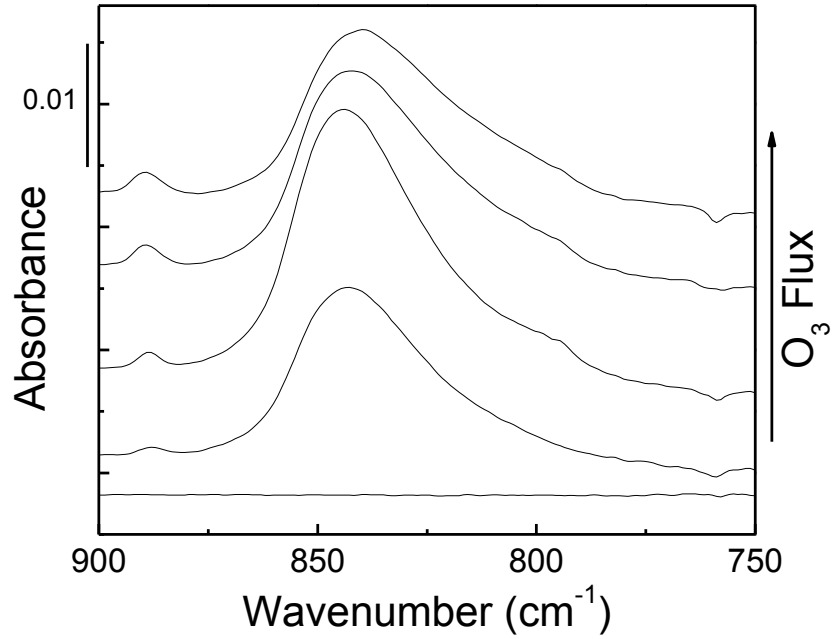

Figure 5.21: RAIR spectra from the ozone exposure of C_{84}. Graph shows the peak with intermediate behavior and how it changes with increasing exposure to ozone.

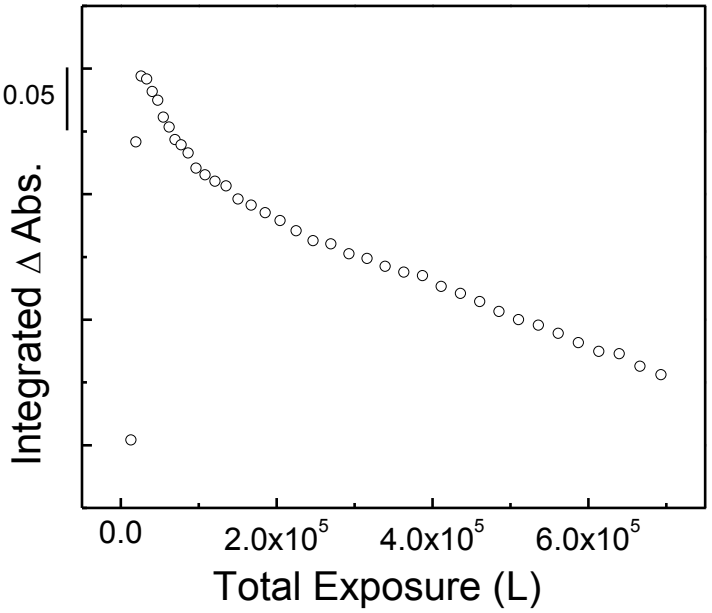

Figure 5.22: The profile for the peak shown in Figure 5.21. The profile shows how the peak changes as a function of ozone exposure. This behavior suggests the peak may represent the primary ozonide of C_{84} ($C_{84}O_3$).

Table 5.3: Observed peaks during the ozone oxidation of surface-bound C_{84}. The peaks have been assigned to likely functional groups and compared with existing literature values.

Peak Position (cm^{-1})	Assignment	Literature Peak Position (cm^{-1})
887	Epoxide deformation mode	876[105]
1022	Epoxide breathing mode	1013[105]
1128	Ester asymmetric stretch	1127[105]
1189	Ester symmetric stretch	1186[105]
1279	Ester (C=O) stretch	1283[105]
1407	Fullerene modes	---
1427	Fullerene modes	---
1442	Fullerene modes	---
1559	Enhancement of C=C bonds	1581[104a]
1589	Enhancement of C=C bonds	1581[104a]
1612	Carbonyls conjugated with C=C	1617[105]
1678	Carbonyls conjugated with C=C	1677[105]
1726	C=O (ketones, esters, lactones)	---
2168	Ketenes	---

The XPS data for the oxidized C_{84} film was very similar to that collected for C_{78}. As with C_{78}, the profile differs significantly from that seen for C_{60}, C_{70}, and C_{76}. Again, this change in the C 1s and O 1s regions, is a result of the substantial difference in cage structure of these larger fullerenes. For the C 1s region, shown in Figure 5.23, of the oxidized C_{84} film, the majority of the fullerene film remains unoxidized and is represented by the peak at 284.7 eV. It was not

possible to differentiate between the sp^2 and sp^3 carbons in the C_{84} data. As with C_{78}, the number of available oxidation sites decreases with respect to the overall size of the fullerene cage, suggesting that less of the carbon atoms lose their sp^2 character. There is a peak at 286.4 eV, assigned to epoxides and ethers, and two peaks at 288.2 and 289.5 eV, due to highly conjugated oxide species. The O 1s region confirms the formation of more carbonyl species within the oxidized C_{84} film. Figure 5.24 shows the large O 1s peak, that has been fitted to display both components at 532.5 and 531.3 eV, due to the C-O and C=O bonding environments, respectively.

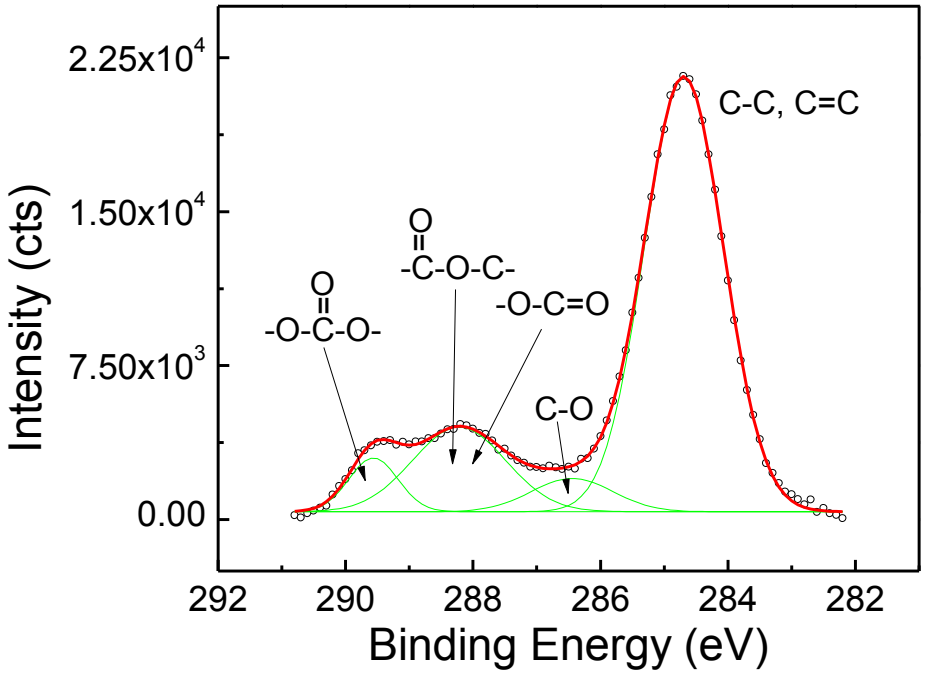

Figure 5.23: The C 1s region for a C_{84} film after exposure to ozone. The data supports the extensive oxidation of the C_{84} cages.

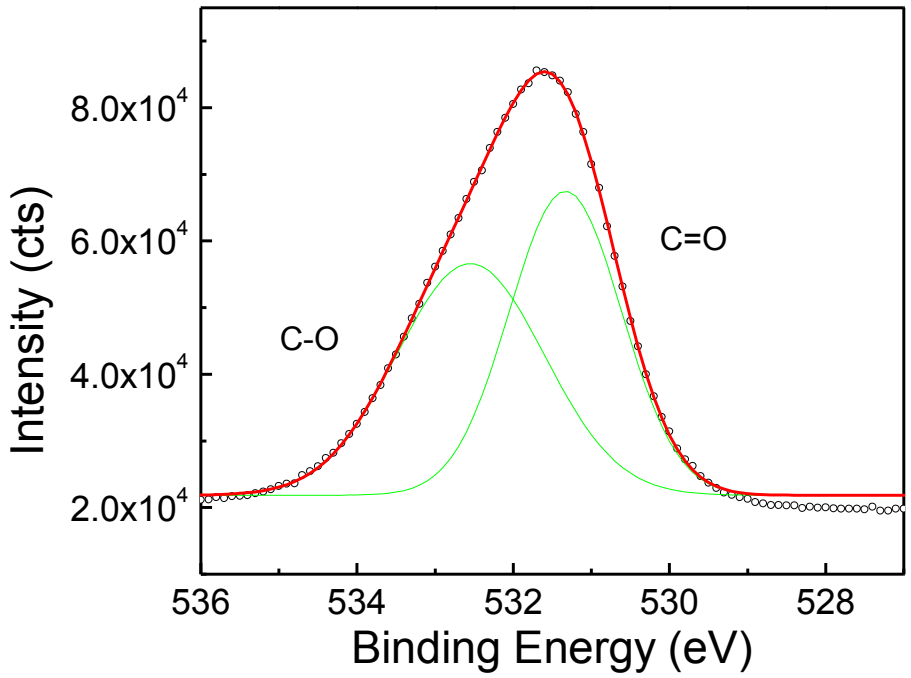

Figure 5.24: The O 1s region for an oxidized C_{84} film. The peak fitting depicts the contributions from C-O and C=O bonds.

The structure of C_{84} resembles an egg, with an oval-like shape, and large groupings of hexagons, uninterrupted by pentagons. With IR data very comparable to C_{78}, similar results were expected from the electronic structure calculations of C_{84}. The two structures analyzed are shown in Figure 5.25. The $C_{84}O_3$ structure on the left includes a C_{84} cage with D_2 symmetry, while the one on the right possesses D_{2d} symmetry. The number of structural isomers increases significantly for C_{84}; this cage molecule has 24 possible isomers, making it even more likely that the IR data includes signal from many different cage structure/reaction site combinations. The calculations yielded primary ozonide frequencies at 858, 866, and 891 cm^{-1} for $C_{84}O_3$ (D_2), and 851 and 858 cm^{-1} for $C_{84}O_3$ (D_{2d}). It is promising that the calculated PO frequencies fall within

the observed experimental peak, but additional calculations should be performed on more combinations of isomers and reactions sites.

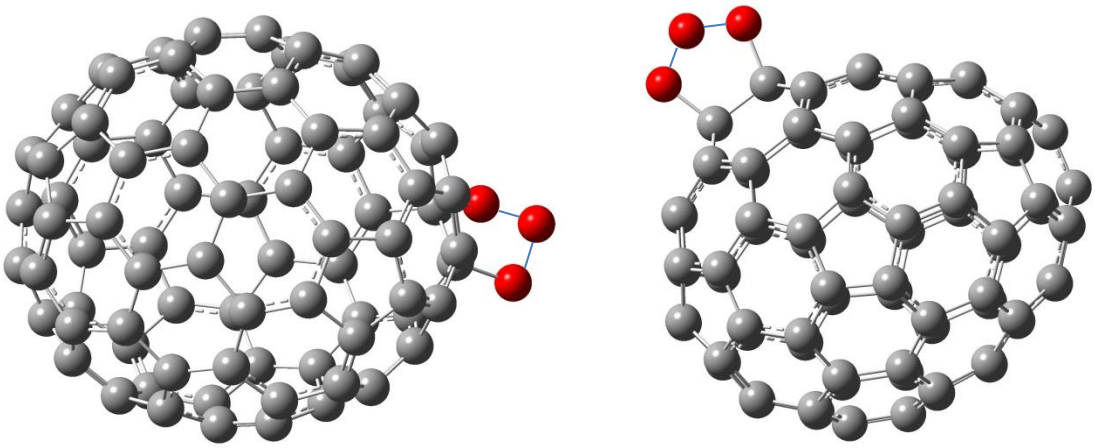

Figure 5.25: The two $C_{84}O_3$ structures analyzed with B3LYP/3-21G*. The structure on the left includes a cage with D_2 symmetry, while the one on the right uses a D_{2d} cage.

5.4 Discussion

5.4.1 Mechanism for the Ozone Exposure of Surface-Bound C_{70}

The mechanism for the oxidation of a C_{70} surface via ozone exposure is similar to that observed for the ozonolysis of C_{60}. The reaction proceeds via the addition of an ozone molecule across a reactive bond within the C_{70} cage. The two reactive bond sites on the C_{70} cage are known as *a,b* and *c,c* bonds.[38] The addition of an ozone molecule across one of these reactive sites leads to the formation of the primary ozonide. Once the primary ozonide decomposes (a feature that has been observed with RAIRS), the formation of products begins. The ozone exposure of C_{70} leads to such products as carbonyls (ketone, diketones, and esters), anhydrides,[11a, 11d, 11f, 60a, b] and ketenes. The ozonolysis of C_{70} also leads to the formation of the "ozopolymer", a product of extensive oxidation, characterized by anhydride linkages. The

anhydride linkages occur after exposure to significant amounts of ozone, which causes the fullerene cages to open and cross-link intermolecularly.

5.4.2 Kinetics for the Ozone Exposure of Surface-Bound C_{70}

Using the IR data and the values calculated for flux of ozone, rates for the oxidation of C_{70} were calculated, as well as the rate of decomposition of the peak associated with the primary ozonide. Figure 5.26 shows the decrease of the peak at 1431 cm^{-1} as a function of the total exposure of ozone. The decay is best fit by two separate exponentials. The first exponential has an observed rate constant (k) of 1.8 x 10^{-4} (± 2.5 x 10^{-5}) s^{-1}, and the second possesses a slower rate of 1.5 x 10^{-5} (± 1.5 x 10^{-6}) s^{-1}. There are two likely explanations for two rates: 1) The faster rate is due to the oxidation of the fullerenes at the gas-surface interface. The second rate explains the reaction of molecules below the gas-surface interface. The sub-surface reactions are a result of ozone diffusion into the bulk of the C_{70} film. Because the packing density most likely increases below the gas-surface interface, it is logical that more time would be required to form the ozopolymer (i.e. see the tail of the blue curve in Figure 5.26). It is also probable, based on the fact that C_{70} has fewer reaction sites, that

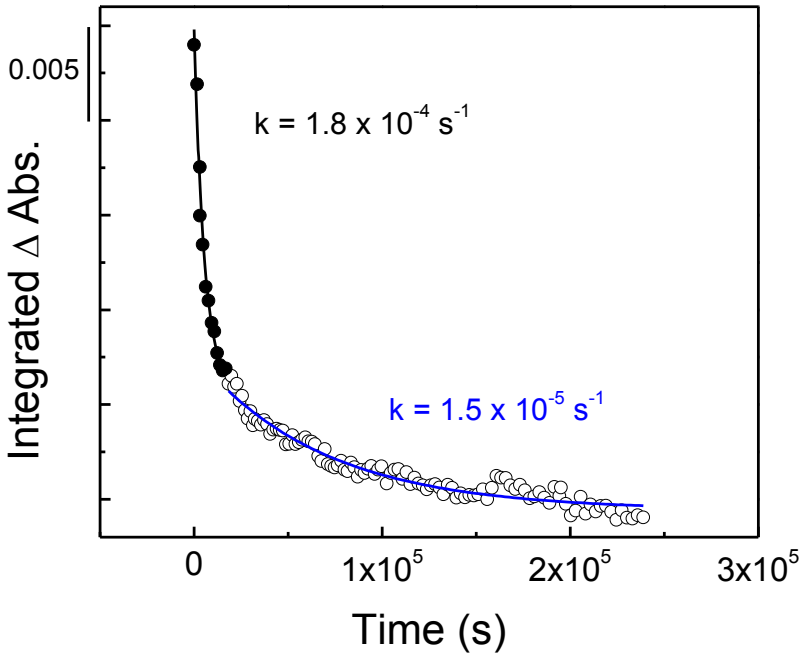

Figure 5.26: A graph of the change in C_{70} IR modes as a function of time. The curve fitting implies that there are two reaction processes occurring.

diffusion has a larger impact on this system. With less reaction sites to encounter, an ozone molecule may migrate through the bulk for a longer amount of time before it comes across a reactive bond. 2) Because there are two possible reaction sites on the C_{70} molecule, one site may be more reactive than the other, therefore the ozone would react at that particular site at a faster rate; once those sites are consumed, ozone begins to react at the other reaction site, at a different rate.

The rate of decomposition of the peak associated with the primary ozonide was also analyzed. Figure 5.27, shows the full peak profile for the pair of peaks centered at 970 cm^{-1}. The decay rate for the peak is 2.5 x 10^{-5} (± 2.6 x 10^{-6}) s^{-1}.

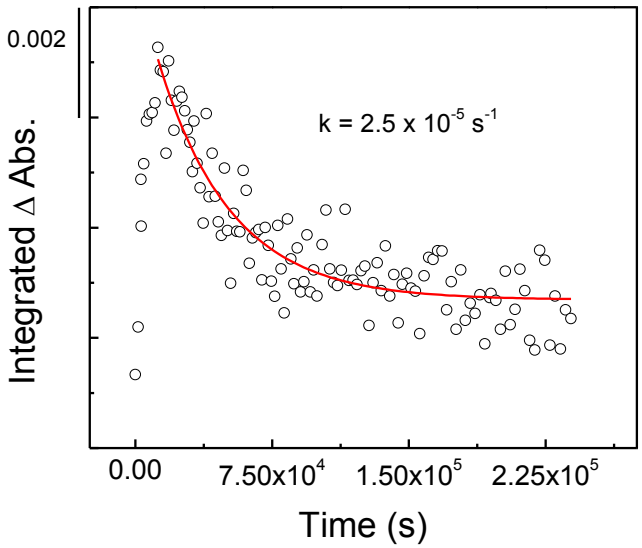

Figure 5.27: The profile of the peak associated with the primary ozonide of C_{70}. The red line shows the fit of the decay curve, providing a k of 2.5 x 10^{-5} s^{-1}.

Finally, the initial decay rate of the C_{70} molecules and the initial formation rate of the peak at 970 cm^{-1} were compared. The comparison of these rates, shown in Figure 5.28, implies that the formation of the primary ozonide is first-order with respect to the decomposition of the C_{70} molecules. The close agreement between these two rates, k_{C70} = 1.8 x 10^{-4} (± 2.5 x 10^{-5}) s^{-1}

and k_{PO} = 2.2 x 10^{-4} (± 5.7 x 10^{-5}) s^{-1}, is a reasonable confirmation that the ozonation of the C_{70} film occurs via the formation of the primary ozonide, just like C_{60}.

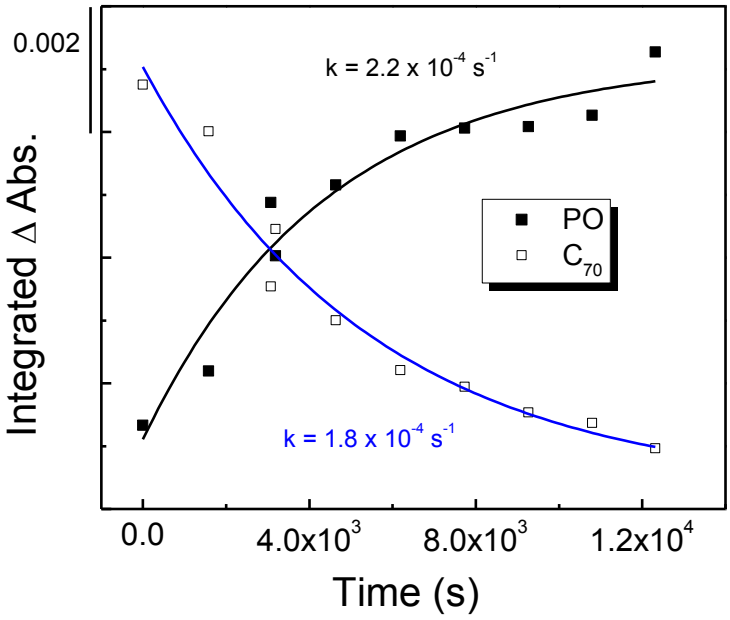

Figure 5.28: A comparison of the decay rate of the C_{70} molecules and the formation of the intermediate peak assigned to the primary ozonide. The equivalent rates imply that the two species have a first-order relationship.

5.4.3 Mechanism for the Ozone exposure of Surface-Bound C_{76}

Because the basic structure of all fullerene molecules (i.e. pentagons and hexagons) is the same, it is likely that ozone interacts with C_{76} via the same initial steps as with all the other fullerenes included in this study. The reaction proceeds with the addition of an ozone molecule across either an α or a β site on the pole of the C_{76} cage. Once the primary ozonide forms, it undergoes immediate decomposition to form various products. The products observed for the ozonolysis of C_{76} are carbonyls (specifically esters), anhydrides, and ketenes.

5.4.4 Kinetics for the Ozone exposure of Surface-Bound C_{76}

Unfortunately, the peak associated with the primary ozonide of C_{76} was not observed in these experiments, therefore no rates were determined for the intermediate. However, a decay rate for the C_{76} molecules upon exposure to ozone was calculated. Figure 5.29 shows the decay curve for the C_{76} molecules. The observed rate constant is 1.3×10^{-4} ($\pm 1.5 \times 10^{-5}$) s^{-1}.

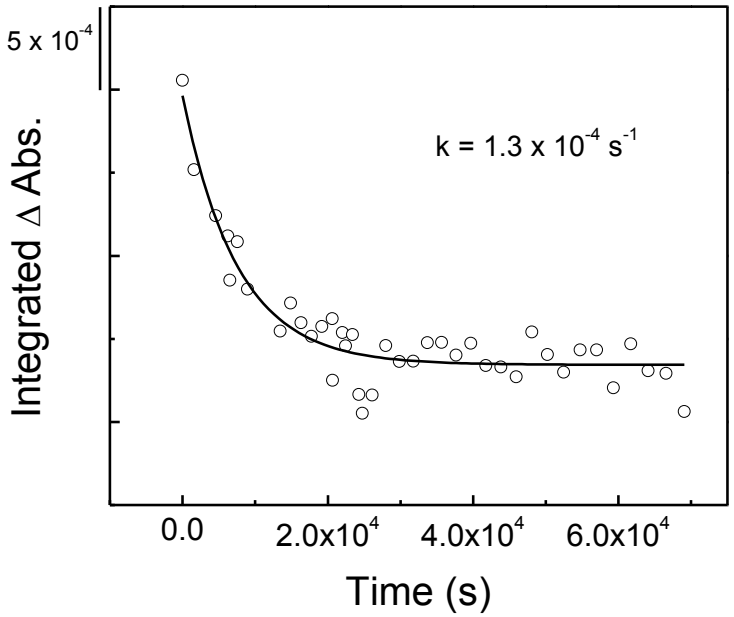

Figure 5.29: The integrated change in absorbance of 1440 cm^{-1} (C_{76} peak) as a function of ozone exposure.

5.4.5 Mechanism for the Ozone exposure of Surface-Bound C_{78}

The IR data indicates that when a C_{78} film is exposed to gas-phase ozone, a complex reaction takes place. The reaction begins with the formation of the primary ozonide of C_{78}. The existence of short-lived intermediates was determined based on the immediate decrease in the C_{78} modes, as well as the simultaneous appearance of a broad peak, which possessed intermediate behavior, at low wavenumbers (~800 cm^{-1}). Similar to C_{60}, C_{70}, and C_{76}, the

mechanism for ozone oxidation begins with the primary ozonide. After that step though, the similarities start to decrease. In analyzing the IR spectra and trying to assign products to the observed peaks, it was more beneficial to compare the data to literature data on the ozonolysis of carbon nanotubes.[11e, 104-106] The product peaks present in the oxidation of C_{78} are all comparable to product peaks detected in the carbon nanotube studies. This change in experimental products and the comparability to CNT data can be explained simply by considering the increasing size of the fullerene cage. The C_{78} cage has large portions of its surface that strongly resemble a carbon nanotube surface. The D_3 isomer of C_{78} has an equilateral belt comprised entirely of hexagons rings. These "unreactive" sections of the fullerene cages are likened to the walls of a carbon nanotube. In the CNT/O_3 studies, reports showed that the reactive portions of the carbon nanotubes were the end caps. The CNT end caps underwent extensive oxidation, leaving the walls of the tube virtually intact. The oxidation of larger fullerenes can be thought of in much the same way. The "poles" of the fullerene cages, where a larger number of pentagons are located, and therefore reactive sites, are the location for oxidation. Because the oxidation takes place in more localized regions of the cage, this may explain the lack of anhydride products (i.e. less chance of intermolecular bonding). The anhydrides are a result of the fullerene cage opening up and allowing reactive sites to be brought within close proximity of one another. Since the molecules do not rupture completely, the overall structure is maintained and consequently, cross-linking (i.e. anhydride formation) is kept to a minimum. Instead, a significant amount of carbonyl products are observed, C=O and C-O functionalities that are heavily conjugated with C=C and other C=O bonds, and ketenes.

5.4.6 Kinetics for the Ozone exposure of Surface-Bound C_{78}

The rate at which the C_{78} molecules react was determined by plotting the change in fullerene peak signal as a function of ozone exposure. The curve, shown in Figure 5.30, was fit with an exponential decay producing an observed rate constant of 6.0 x 10^{-4} (± 3.0 x 10^{-5}) s^{-1}. The decay curve for the C_{78} molecules does not seem to imply that diffusion is a considerable part of this interaction. The peak associated with the primary ozonide of C_{78} was analyzed as well. Initial observation of the peak profile, Figure 5.31, supports the conclusion that the peak centered at 800 cm^{-1} is related to the PO. The peak decomposes with an observed rate constant of 5.2 x 10^{-5} (± 2.1 x 10^{-6}) s^{-1}.

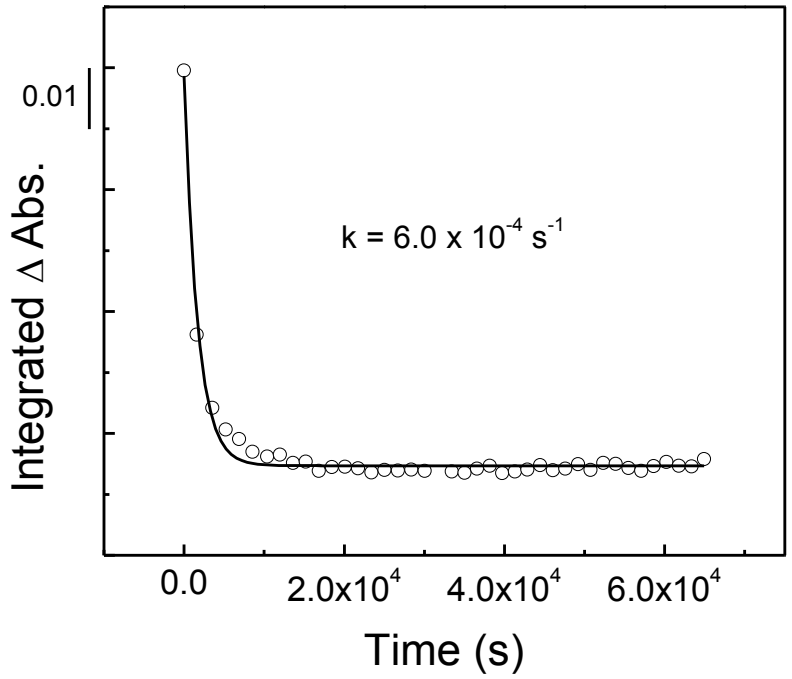

Figure 5.30: The change in C_{78} signal as a function of flux-weighted time. The ozone exposure has been converted to time in order to calculate reaction rates.

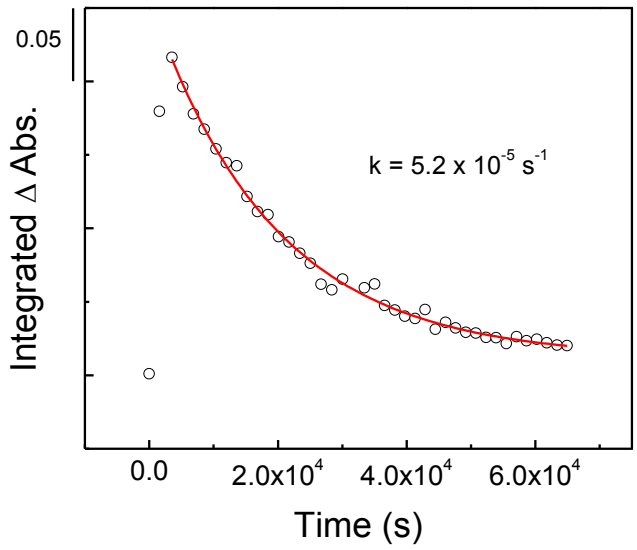

Figure 5.31: The peak profile for the species associated with the primary ozonide of C_{78} ($C_{78}O_3$). The rate constant for the decay of the PO of C_{78}.

The rate of C_{78} consumption was compared with the rate of intermediate formation. As seen with the other fullerene studies, the rates are dependent upon one another with a first-order characteristic. The observance of comparable rates indicates that the depletion of fullerene modes is a result of oxidation via ozone; a process that starts with the creation of the PO.

5.4.7 Mechanism for the Ozone exposure of Surface-Bound C_{84}

The mechanism for the ozone oxidation of C_{84} films is very similar to that observed for C_{78}. The first step in both mechanisms is the formation of the primary ozonide, which then decomposes to form highly conjugated oxidation products. The C_{84} data is also comparable to the existing carbon nanotube data. The poles of the C_{84} spheres are oxidized, while the equatorial belt stays mostly intact.

5.4.8 Kinetics for the Ozone exposure of Surface-Bound C_{84}

The rate of C_{84} fullerene decomposition was measured and the observed rate constant was determined to be 1.0 x 10^{-4} (± 7.0 x 10^{-6}) s^{-1}, as shown in Figure 5.32. The data produces an ozonolysis rate constant similar to those observed for the other fullerenes included in this study. Further supporting the hypothesis that the ozone molecule limits the rate of reaction, instead of features within the exposed surface.

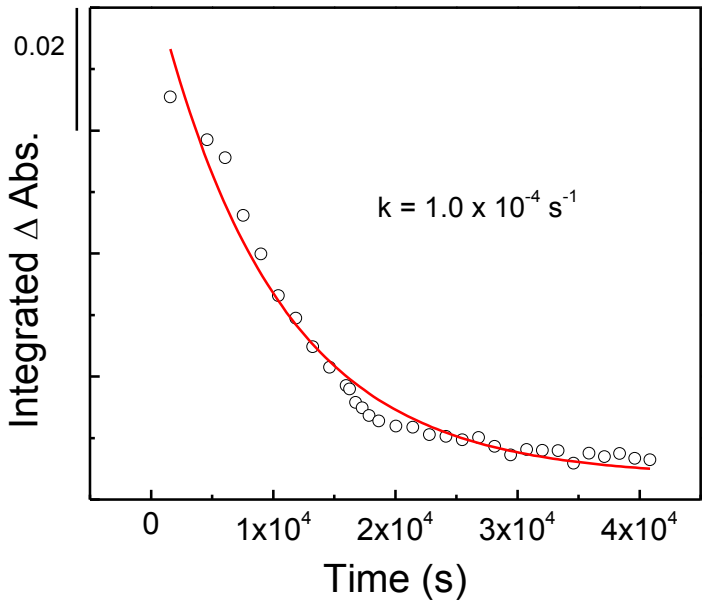

Figure 5.32: The decay curve for the C_{84} fullerene film. The curve indicates a reaction on the fullerene cages. The ozone exposure has been converted to time in order to calculate reaction rates.

To determine the rate constant for the decomposition of the primary ozonide, the change in peak area versus the total exposure of ozone was plotted, shown in Figure 5.33. The decay curve is best fit by the exponential decay equation. The rate constant for the ozonolysis of C_{84} is k = 2.4 x10^{-5} (± 4.1 x 10^{-6}) s^{-1}. This value indicates the rate at which C_{84} is oxidized by ozone is

slightly faster than that observed for the smaller fullerenes. However, the results shown for C_{78} and C_{84} are strictly preliminary, until further experiments are performed. Only one ozone exposure was performed on these two surfaces because of limited availability of the C_{78} and C_{84} material.

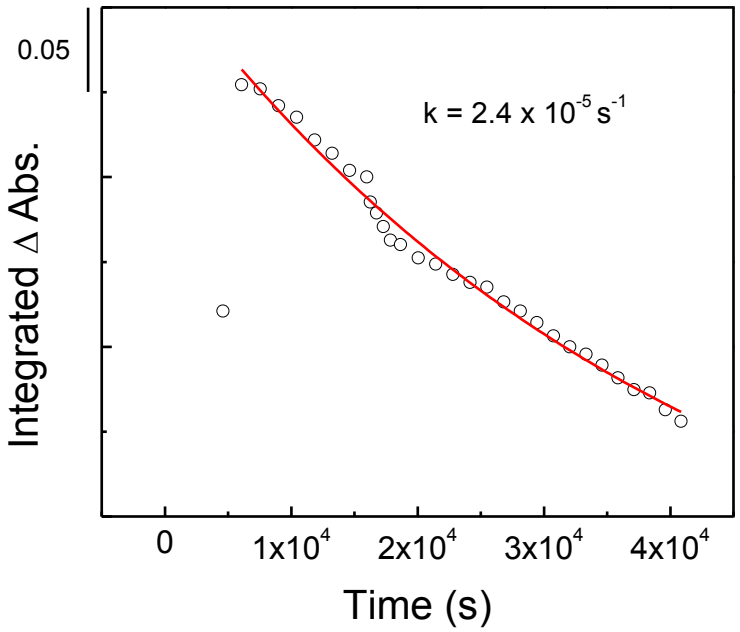

Figure 5.33: The decay curve for the decomposition of the primary ozonide of C_{84}.

Also, the rates of fullerene decomposition and PO formation were compared, giving similar values, but not as alike as the values obtained for the other fullerenes studied. While the rates do not match exactly, the rates are similar enough to suggest that the ozone interacts with C_{84} via the formation of the primary ozonide species. The observance of an intermediate peak in the expected IR region provides reasonable support for this belief.

5.5 Rates of Decomposition for C_{60}, C_{70}, C_{76}, C_{78}, C_{84}

One of the main objectives of this study was to understand how the rate of ozonolysis is affected by the size of the fullerene molecule. By comparing the rate at which C_{60} is oxidized to the rates for all other molecules involved in this investigation, the existence of a trend due to the size of the cage can be evaluated. Figure 5.34 shows the rates at which fullerene molecules decompose upon exposure to ozone. It is clear from the graph that the fullerenes studied in these experiments oxidize at very comparable rates, all having *k* values within an order of magnitude. Interestingly, many other alkenes have been observed to oxidize at similar rates upon exposure to ozone; see Chapter 4 for discussion.[99] This data suggests that the structure of the fullerene is irrelevant with respect to the rate of the initial reaction with ozone.

Figure 5.34: A plot showing the ozone oxidation rate of fullerenes as a function of the cage size.

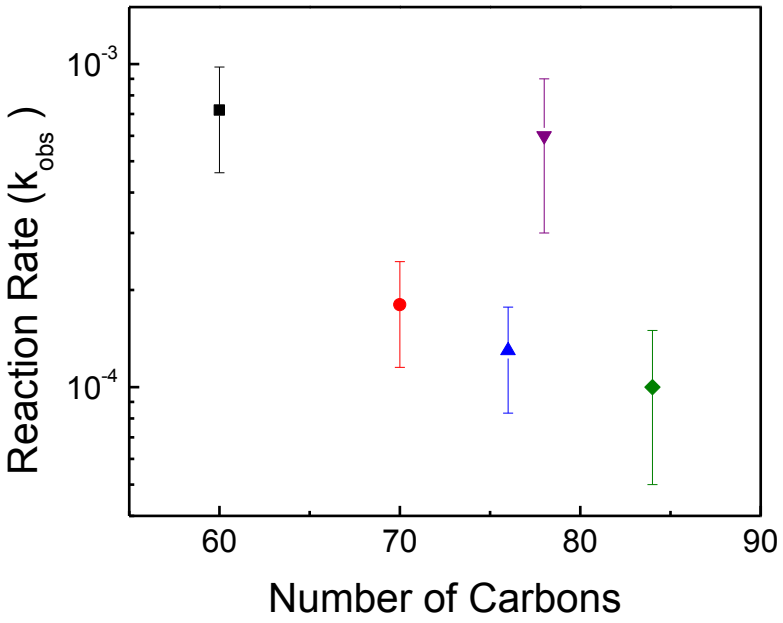

5.6 Summary

Chapter 5 covered the study of the larger fullerene molecules, C_{70}, C_{76}, C_{78}, and C_{84}, and their reaction with gas-phase ozone. The study found that the ozone oxidation of surface-bound C_{70} occurred in a similar manner as the ozonolysis of C_{60}. A peak exhibiting intermediate behavior was observed, most likely due to the primary ozonide of C_{70}. The peak slowly decreased throughout the exposure, indicating the species decomposed. With the decrease in this peak, product peaks appeared in the spectra. The peaks suggested the formation of ketones, anhydrides, and ketenes. The C_{76} surface reacted readily with ozone as well; the RAIRS spectra for this reaction was also consistent with ketone, anhydride, and ketene products. However, when C_{76} was oxidized, a new product peak appeared in the spectra, tentatively assigned to ester functionalities. Finally, the ozonolysis of C_{78} and C_{84} was more comparable to the ozonolysis of carbon nanotubes than that of the smaller fullerenes (C_{60}, C_{70}, C_{76}). No anhydrides were detected, presumably because the larger molecules have reactive sites spaced farther apart and they are not freely rotating within the film like the smaller fullerenes.

The oxidation rates were calculated for each fullerene and the data indicates that fullerenes are oxidized at similar rates to other alkenes upon exposure to gas-phase ozone. The conclusion that fullerene structure has no impact on the rate of ozonolysis is important in further understanding the reactivity of this pollutant.

Chapter 6

Reactions of the Surface-Bound Terbium Endohedrals and Gas-Phase Ozone

6.1 Introduction

The study of functionalized fullerenes began shortly after the initial discovery of the unique cage molecules. As with any new molecule, researchers were just as interested in how they could modify and alter the chemical properties, as they were in studying the underivatized version. The first endofunctionalized fullerene (i.e. functionalization through addition of atoms or molecules inside the fullerene cage), La@C_{60}, was synthesized in 1985 by Heath *et al*. Since that time, scientists have been exploring the many possible atoms and molecules which can be inserted into different size cages and the resulting chemical properties, which are unique to each individual combination.

In particular, fullerenes containing the lanthanide elements, a group including both Lanthanum and Terbium, have many uses: contrast agents for MRIs, glass catalysts, phosphors, magnets, and optoelectronics, to name a few.[107] Terbium metallofullerenes are among those with unique electronic and physical properties and are produced with significantly higher yields than many of the other lanthanide endohedrals. Terbium, itself, is an interesting element. Never found as a free element in nature, its most abundant species is the oxide, Tb_2O_3. In fact, the only way single Tb atoms have been isolated is by placement into fullerene molecules.[108] Terbium endohedrals are used as optical materials, with prodigious optical properties, including luminescence. While the positives of endohedral research and application seem to outweigh the negatives, the reality is the potential negative consequences have not yet been considered. From the research previously discussed in this document, it has been stated that the ozonolysis of fullerenes results in the rupturing of the cage structure, as well as extensive oxidation of the

molecule. Terbium is known to readily oxidize, the reason why it is only observed in its oxide forms in the environment. Also, the toxicity of Tb and its oxides is not well known, or even investigated in detail. Therefore, the objective of the research discussed in this Chapter is to determine what happens to the Tb endohedrals structure upon exposure to ozone. Specifically, the goals were to determine 1) whether or not the endohedrals were oxidized by ozone, 2) if ozone oxidation exposed the Tb, 3) once exposed, if Tb was oxidized by ozone, and finally 4) if the newly oxidized Tb desorbed into the gas phase. If the oxidation and subsequent desorption of Tb from the ozonolysis of these endohedrals is observed, this research will identify a potential source for the release of toxic heavy metals into the environment.

6.2 Experimental Details

6.2.1 Materials

All chemicals were used as received without further purification unless otherwise noted. The Terbium endohedrals were purchased from Bucky USA. Research grade oxygen, ultrahigh purity nitrogen, liquid nitrogen, and dry ice were purchased from Airgas Specialty Gases. Polycrystalline gold substrates were received from Evaporated Metal Films. Reagent grade acetone was obtained from Pharmco-Aaper and Commercial Alcohols. The details of ozone synthesis and storage are covered in Chapter 2 and Chapter 4.

6.2.2 Formation of Terbium Endohedral Surfaces

Fullerenes were deposited onto polycrystalline gold slides. The slides were purchased from Evaporated Metal Films, Inc. They were made by first depositing a 50 Å thick layer of chromium onto a glass slide, then depositing ~1000 Å of Au. The dimensions of the slides are 1” x 1” x 0.062”. To clean the Au slides before introduction into the UHV chamber, they were submersed in a solution of 70% sulfuric acid and 30% hydrogen peroxide (30%), also known as

piranha solution, for ~45 minutes. *Warning: Piranha solution is an oxidizing agent which reacts violently with organics! Extreme caution should be taken when using this solution!* Once the Au slides were removed from the piranha, they were rinsed thoroughly with deionized water (Millipore Purification Systems, 18.2 MΩ), and then dried completely with UHP nitrogen. After drying, the slide was placed into the rapid-transfer load lock of the UHV chamber. After transferring into the UHV main chamber, the Au slide was then cleaned with ozone for one hour. The piranha solution was used to remove the majority of the hydrocarbons which adsorb to the surface from exposure to air. However, once the slide was removed from the solution and re-exposed to atmosphere, new hydrocarbons adsorbed to the surface of the Au slide. Ozone is a very efficient way to remove the hydrocarbons from the surface before fullerene deposition. After one hour of ozone cleaning, a background was taken using the freshly cleaned Au slide. The background was saved and the Au slide was transferred into the load lock to deposit the fullerene of choice. Because the deposition of larger fullerenes required such high temperatures ($\geq$ 1000°C), it was necessary to make the endohedral films via the drop-casted technique.[109] To form a drop-casted film, the Tb endohedral powder was dissolved in methylene chloride. The resulting solution was brown in color. After the Au background was cleaned with ozone and then transferred back into the load lock, the load lock was vented with UHP N_2(g). Once the load lock was vented, the sample holder, with Au slide still attached, was removed from the end of the transfer arm and placed face up in the load lock. Then several drops of the Tb endohedral/methylene chloride solution were placed onto the Au slide. The solvent was allowed to evaporate, and then the sample holder was placed back on the end of the transfer arm. The sample was transferred into the main chamber, attached to the mount and realigned for IR and dosing.

6.2.3 Surface Exposure

After the fullerenes were deposited onto the Au slide, the slide is transferred back into the main chamber. Once the slide is positioned as close as possible to the position it occupied when the background was recorded, it is scanned with the IR. Because difference spectra was utilized, it is very beneficial to position the slide in the same location before and after deposition, this will ensure the baseline is as flat as possible and produce less noise in the resulting spectra. Upon proper realignment of the sample, the fullerene surface is scanned to obtain a spectrum of the sample before ozone exposure. With an initial spectrum recorded, then saved as a background, the first spectrum before opening the ozone doser should be a perfectly flat line positioned exactly at 0 on the intensity scale (y-axis). The gas-phase ozone is then introduced into the main chamber via the CAD.

6.2.4 RAIRS Data Acquistion

The reaction of gas-phase ozone with surface-bound Terbium endohedrals is followed in real-time with a Bruker IFS 66v/S spectrometer. The spectrometer is equipped with a SiC globar source, which produces an IR beam. The IR beam is focused onto the Au surface in the middle of the UHV chamber at an incident angle of ~86° relative to the surface normal. The detector used with the Bruker spectrometer is a mid-range MCT detector (750 - 4000 cm^{-1}), that requires cooling with liquid nitrogen. Every spectrum shown in this dissertation is produced by the co-addition of 100 scans acquired over 90 seconds. The resolution was set at 2 cm^{-1} and the scanner velocity was held at 20 kHz.

6.2.5 XPS Measurements

With X-ray Photoelectron Spectroscopy's ability to detect less than a monolayer (~ 0.01 monolayer), it was an invaluable technique for this study. The Tb endohedral surfaces were analyzed with and without exposure to ozone. The XPS analysis was performed with the instrument located in the Surface Science lab at Virginia Tech, in the Department of Chemistry. The instrument is described in detail in Chapter 2 of this document. All samples were characterized at a grazing angle of 15° relative to the surface normal. The Mg Kα anode (1253.6 eV) was used for all samples studied. The impinging x-rays produce photoelectrons, which are subsequently detected with the HA. A survey scan is collected first to get a general idea of the elemental composition of the surface. After the survey scan is inspected, individual regions (or elements) are focused on with more selective pass energy.

6.3 Results

6.3.1 Surface Characterization

6.3.1.1 RAIRS

The Tb endohedral films were characterized as soon as possible after deposition. Since the films were formed via the drop-casting method,[109] the load lock had to be pumped down into the 10^{-7} Torr range before the sample could be transferred into the main chamber. The pump down took ~20 minutes. Once in the main chamber the sample was scanned with the RAIR spectrometer. The spectrum in Figure 6.1 was collected for a drop-casted Tb endohedrals film on an Au slide. The spectrum is very similar to the one obtained for surface-bound C_{60}. As there is no existing IR data for surface-bound Tb endohedrals, it is difficult to determine whether or not these peaks are representative of the Tb endohedrals (Tb@C_{82}) or some C_{60} contamination. A peak at 796 cm^{-1} appears in the IR spectrum that is not present in the spectra for C_{60}. Without further experiments (e.g. NMR to confirm purity of Tb endohedral powder used, electronic structure calculations to

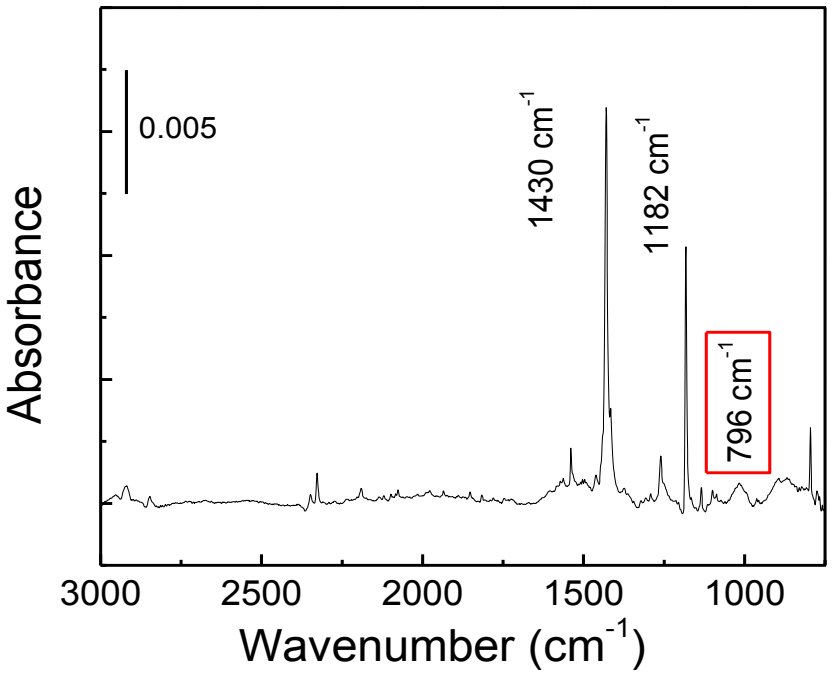

Figure 6.1: The RAIR spectrum of a drop-casted Tb endohedral film on an Au slide.

support experimentally observed frequencies), assignment of the peak at 796 cm^{-1} to the Tb endohedral is only preliminary.

6.3.1.2 XPS

X-ray photoelectron spectroscopy (XPS) was used to confirm the presence of Tb endohedrals on the Au surface. Because XPS is a quantitative spectroscopic technique capable of detecting as little as 0.1 at% (atomic percent) of an element, it is an ideal method to verify the presence of Tb endohedrals on the Au slide. XPS was also especially important in this set of experiments because the chamber in which exposures were performed and the chamber in which XPS was collected were not the same. Characterizing the endohedral surfaces before and after ozone exposure ensured the only oxidation observed was due to interactions with ozone. The binding energy values of each observed data region were calibrated using the Au 4f 5/2 peak (83.8 eV).

The first spectrum, shown in Figure 6.2, depicting the C 1s region, was collected from a $Tb@C_{82}$ film without any ozone oxidation. The spectrum shows a single peak centered at 284.5

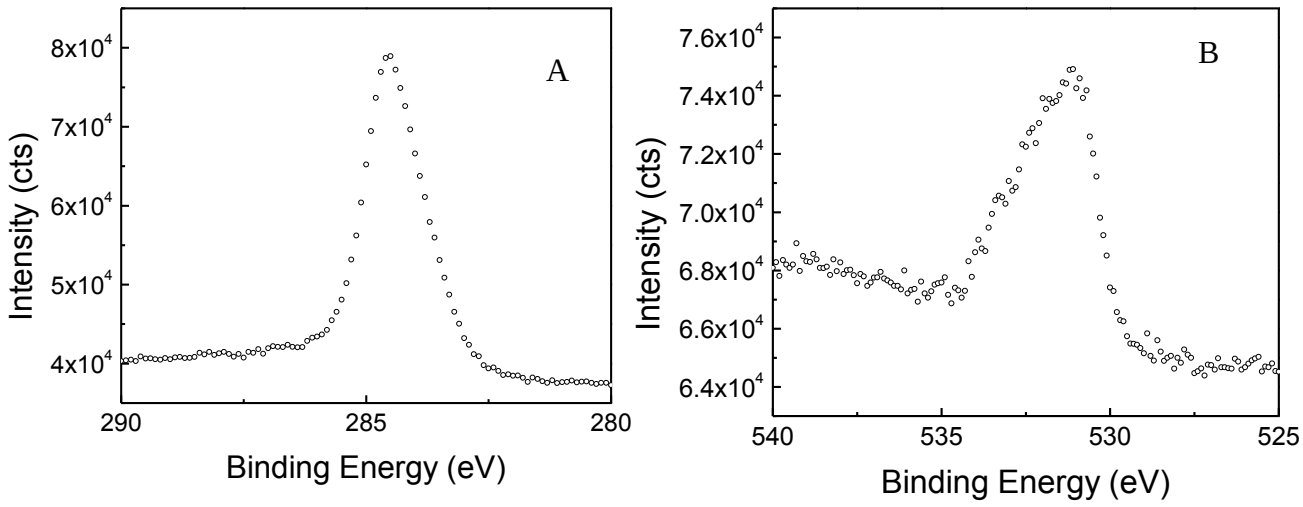

Figure 6.2: XPS data recorded for an unoxidized Tb endohedral surface. The spectrum A is the C 1s region and spectrum B shows data from the O 1s region.

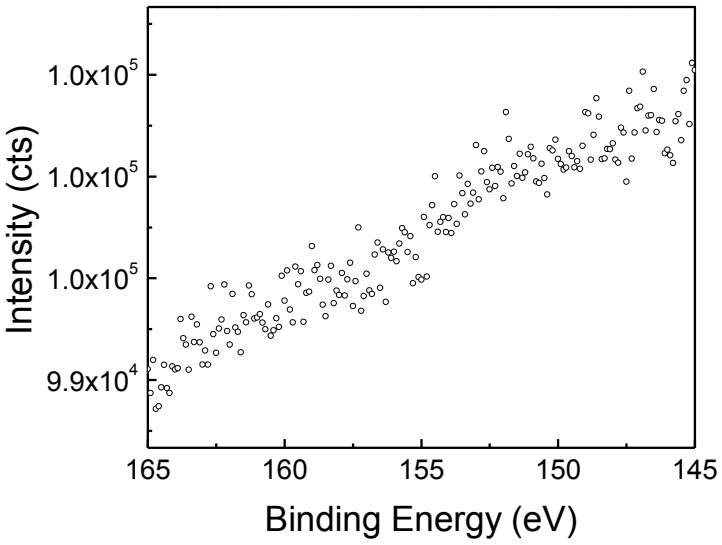

Figure 6.3: XPS data showing the Tb 4d region; no significant signal from Tb.

eV. The single peak is indicative of unoxidized fullerene cages present on the surface. However, when the O 1s region is explored, a significant peak appears at approximately 531 eV. The peak observed in the O 1s region is most likely due to some Au oxide present after cleaning the surface with ozone. The peak in the C 1s region implies the presence of only unoxidized carbon, therefore the Au oxide is a reasonable explanation for the existence of the oxygen peak. Regardless of the fact that there is a peak in the O 1s region before ozone exposure, the most important fact is that the carbon remains unoxidized. The last region scanned before ozonolysis was the Tb 4d region. In Figure 6.3, the Tb 4d region surprisingly does not appear to possess any signal from the Tb enclosed within the fullerene cages. Future studies investigating this system could perform TPD to confirm the presence of Tb inside the fullerene cages prior to ozonolysis.

6.3.2 Ozone Exposure

6.3.2.1 RAIRS

The RAIR spectra for the reaction between gas-phase ozone and surface-bound Tb endohedral fullerenes are shown in Figure 6.4. More specifically, Figure 6.4 displays difference spectra for this gas-surface reaction. As the surface is exposed to continuous ozone, the modes

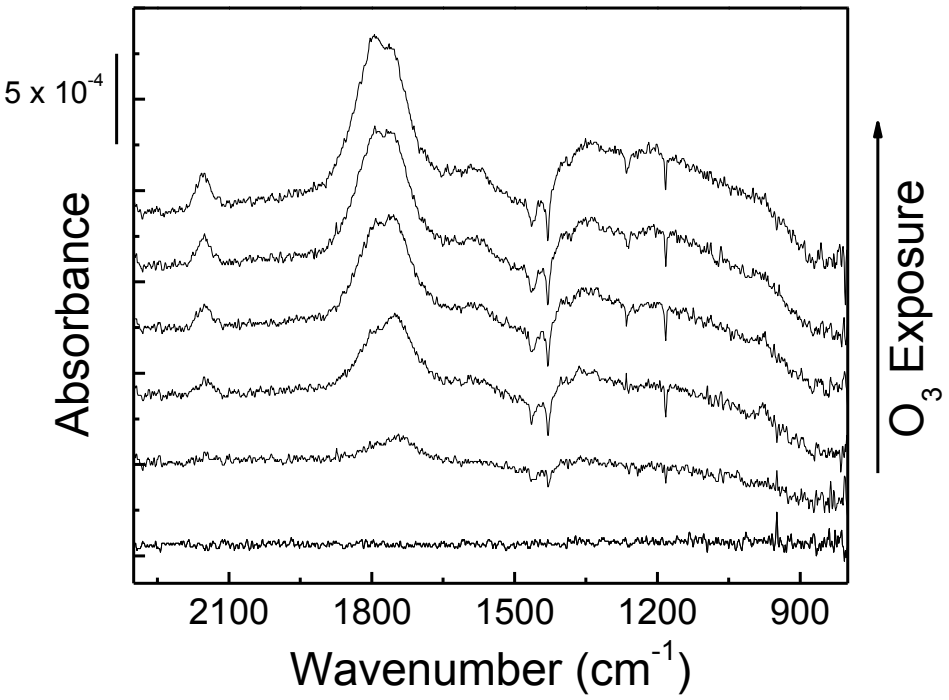

Figure 6.4: RAIR spectra for the ozone oxidation of surface-bound Tb endohedrals.

associated with the fullerene cages appear as negative features, indicating reactions on the cage structure. There also appears to be a weak feature at ~ 975 cm^{-1}. The peak at lower wavenumbers is attributed to a primary ozonide. Product peaks grow in as well; carbonyls, ketenes, and some anhydrides. The presence of anhydride peaks, based on the mechanism proposed for C_{60} ozonolysis, are a result of significant oxidation and cage cross-linkage. Since the IR data indicates that the endohedral cages have been opened as a result of ozone oxidation, it is important to determine whether or not there is evidence of Tb oxidation. Overall, the IR spectra following the ozone exposure of Tb@C_{82} were very similar to the same experiment performed with C_{60}. The presence of Tb does not appear to affect the reactivity of the external cage or product formation. However, this data does not provide insight into possible oxidation of the Tb following cage rupture.

6.3.2.2 XPS

The RAIRS data was able to confirm that the surface was significantly oxidized as a result of exposure to gas-phase ozone. However, it did not conclusively show whether or not the Tb atoms inside the fullerene cages were also oxidized. To determine the oxidation state of the Tb atoms, XPS was employed. The Perkin-Elmer XPS (model: 5300), located in the Surface Analysis Lab at Virginia Tech, was used to analyze the drop-casted Tb endohedral surfaces. Samples were analyzed before ozone exposure and after 7, 15, 30, and 60 minutes of exposure. For all samples, the C 1s, O 1s, and Tb 4d regions were scanned. All regions are shown in Figure 6.5, on the following page. The XPS data provides a great deal of information about this ozonolysis experiment. First, the Tb endohedrals can be characterized solely dependent upon the XPS signal. The interaction between the C_{82} cage and the Tb atom inside is electronic charge transferring.[110] A peak at 152 eV is typically indicative of this charge transfer between the rare earth metal and the coordinator. Observance of this peak position suggests the Tb signal detected initially is due to the atoms present inside the fullerene molecules. As the XPS is collected over time, the overall signal in each region decreases as a function of time (i.e. longer exposure to ozone). The possibility that some of the oxidation products continuously desorbed into the gas-phase during exposure must be considered, because significant product signal was not seen in the mass spectrometer. The C 1s region (left column), shows as ozone exposure continues, the carbon present in the film (fullerene cages) undergoes extensive oxidation. The oxidation is characterized by the appearance of a shoulder at higher wavenumbers (286-290 eV).[90] The O 1s peak shape remains relatively unchanged, and mainly appears to decrease in intensity, similar to all other peaks observed. Finally, the Tb 4d region possesses the most interesting, and telling, information. As shown in Figure 6.3 before ozone exposure, there is no obvious peak due to Tb.

After only 7 minutes of dosing with ozone, a significant Tb peak appears at 152.5 eV. The immediate appearance of the Tb 4d peak is most likely a result of the oxidation of the fullerene cages (i.e. formation and subsequent decomposition of primary ozonides). At 15 minutes of ozone exposure, the peak at 152.5 eV decreases in intensity, and there appears to be some small increase in signal at 161 eV. It is only after 30 minutes of ozone dosing that a definite peak at 161 eV has grown in, representing oxidation of the Tb atoms inside the fullerenes. The last data collected, after dosing for one hour, implies that the Tb oxides have desorbed into the gas-phase and the small amount of signal remaining at 152.5 eV is due to unoxidized Tb still existing within the fullerenes.

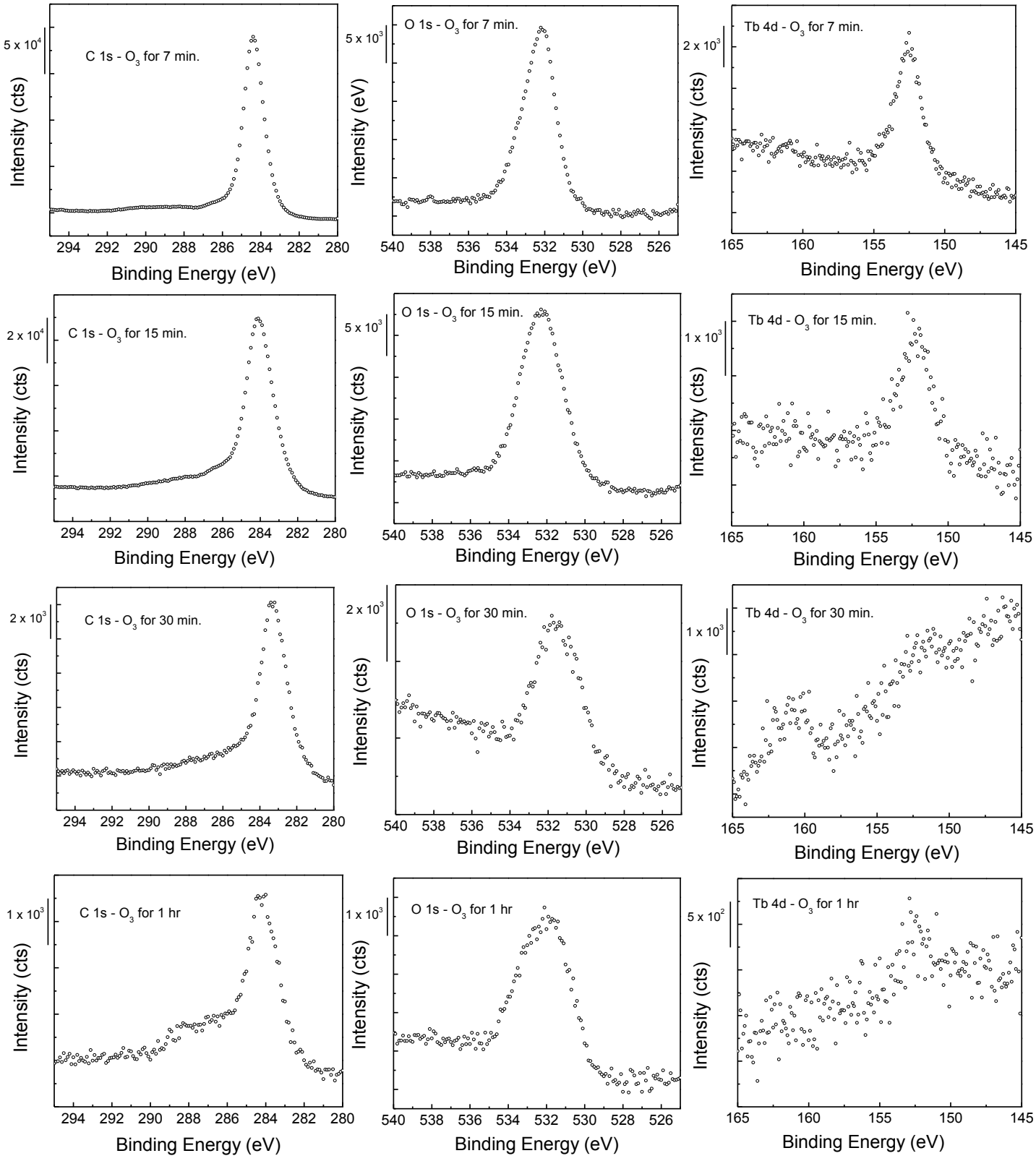

Figure 6.5: The time-resolved XPS study for the ozone oxidation of surface-bound Tb endohedrals. The C 1s region is shown on the left, O 1s region in the middle, and Tb 4d on the right. Each spectrum indicates how long the sample was exposed to gas-phase ozone before elemental analysis was performed.

6.4 Summary

The exposure of Tb endohedral surfaces to gas-phase ozone indicates that the reaction begins via the formation of primary ozonides on the endohedral cages. The POs immediately decompose forming, first, small holes in the fullerene cage structure, but upon further oxidation, larger holes. These larger holes are wide enough for ozone to enter the interior of the fullerene cage and oxidize the contained Tb atoms. Extensive ozonolysis even appears to promote Tb oxide desorption into the gas-phase. The XPS data shows that the reaction occurs in very distinct steps: 1) Primary ozonide formation and decomposition (i.e. small hole formation), 2) further oxidation at the small hole defects, allowing them to open into larger holes, 3) ozone entrance into the core of the cage, resulting in Tb oxidation, and 4) Tb oxide desorption. To further probe the oxidized Tb endohedral surface, TPD could be performed to determine in what state the Tb oxides are present in the surface. One possibility is the aggregation of individual Tb oxides to form more stable complexes, such as Tb_4O_7. However, without knowing more about the mobility of Tb oxides over oxidized carbonaceous materials, this is only a hypothesis. Perhaps the larger oxides are formed as the fullerenes are extensively oxidized, i.e. the formation of the ozopolymer allows Tb oxides to form Tb_4O_7. The final suggested explanation for the oxidized Tb species is the formation of Tb carbonyls. Similar to tungsten hexacarbonyl, which possesses a high vapor pressure, perhaps Tb carbonyls are formed and desorb into the gas-phase. The concern with this potential product is the harmful nature of such complexes.

The data discussed in Chapter 6 raises concerns as to the environmental fate of endohedrals. These results demonstrate the need for further studies involving prominent pollutants and endohedrals containing heavy metals and other potentially harmful atoms/molecules. While the contained species may not be dangerous in their pure form, it is

important to know what damage the products of these environmentally relevant reactions may cause.

Chapter 7

Summary and Conclusions

7.1 Summary

The main goal of this research was to develop a fundamental understanding of the mechanism and kinetics of the gas-surface reaction between gas-phase ozone and surface-bound fullerenes. Fullerenes are frequently studied and employed in numerous areas of research and industry. Their recurrent utilization requires large-scale manufacturing, which will result in a larger abundance of the molecules in the troposphere. Therefore, the reaction of fullerenes with molecules common to the troposphere, such as pollutants, requires some attention. Understanding the gas-surface reactions between oxidizing gases, such as ozone, and fullerenes is crucial to predicting their influence and impact on the environment.

In order to investigate this system, fullerene surfaces were formed in a high vacuum environment. The load lock chamber was modified with a crucible evaporator and an additional transfer arm allowing *in vacu* cleaning of the Au surface, followed by fullerene deposition, subsequent exposure to ozone, and finally analysis. Fullerene film formation in vacuum helped to minimize contamination of the system. The surfaces were exposed to gas-phase ozone and simultaneously monitored with reflection absorption infrared spectroscopy and mass spectrometry. Post-analysis was performed with x-ray photoelectron spectroscopy.

Five separate fullerene surfaces, C_{60}, C_{70}, C_{76}, C_{78}, and C_{84}, were studied in these experiments. The vibrational spectra of each fullerene were characterized with RAIRS and density functional theory calculations. The IR spectra for C_{60} and C_{70} agreed well with current reports and the calculations produced frequencies and intensities similar to those observed during experimentation. The close agreement between collected IR data and the calculated frequencies suggests that C_{60} and C_{70} exist as freely-rotating molecules within the fullerene films, exhibiting

vibrational characteristics of gas-phase molecules. The rotating behavior has been observed in a number of other studies, and is well documented in the literature.[56a,b] The three larger fullerenes, while there are some similarities between the experimental and computational data, and existing studies, require more research to definitively assign the IR spectra. It is possible that some of the difficulty associated with the characterization of the higher fullerenes was due to the temperatures required for vapor deposition. Larger fullerenes are particularly susceptible to the Stone-Wales Transformation, a stabilization mechanism of fullerenes, especially above 700 °C.[70-71, 111] Because the films were characterized immediately after deposition, it is possible that these structural rearrangements were still active, adding complexity to the IR spectra. Development of a better deposition procedure is suggested.

After IR characterization, the fullerenes films were exposed to gas-phase ozone. A great detail of focus was given to C_{60} and ozone. Using RAIRS, the formation and subsequent decomposition of the primary ozonide of C_{60} was detected and identified. A prominent peak, exhibiting intermediate behavior, was observed at 977 cm^{-1}. It was hypothesized that the peak was representative of the primary ozonide. In order to confirm the assignment, isotopically-labeled experiments were carried out, using $^{18}O_3$. Exposure of the C_{60} film to $^{18}O_3$ resulted in a red shift of the observed peaks. The shift was assessed with electronic structure calculations, also performed with $^{18}O_3$. While the calculations did support the hypothesis that 977 cm^{-1} was due to the primary ozonide, more conclusive evidence was provided by comparing the rate of formation of the peak at 977 cm^{-1} to the rate of decay of C_{60} (decrease of the peak at 1428 cm^{-1}). Therefore, with significant confidence, the peak at 977 cm-1 is assigned to the primary ozonide of C_{60} ($C_{60}O_3$). Upon decomposition of the PO, the Criegee Intermediate is formed, which can rearrange to form epoxide, ether, or ketone functionalities, or it can react with another impinging

ozone molecule and form anhydrides and ketenes. The ketene formation was confirmed by dosing NH_3 and observing predicted products. Extensive oxidation of the fullerene surface leads to the formation of an ozopolymer of the top ~10-20% of the overall film. The ozopolymer appears to protect the underlying film from further oxidation, a behavior also seen by Cataldo while studying the oxidation of solid C_{60} via ozone.[11d] Some slow penetration of ozone into the bulk of the film is seen with continuous ozone exposure but this happens over hours (~5-10 hours), as opposed to seconds. XPS showed three different oxidation states of carbon, one attributed to the C-C bonds of the fullerene cages, the second a result of the C-O bonds, and the third, representing C=O bonds.

The kinetic analysis revealed an initial reaction probability of 1.4×10^{-3}, if all 30 double bonds of the C_{60} cage are consumed, or 4.8×10^{-5}, if only one site is consumed per cage. The assignment of peak 977 cm^{-1} to the primary ozonide was further supported by evaluating the rate of fullerene cage decomposition versus the rate of appearance of 977 cm^{-1}. Precisely as the cages were reacted, the peak at 977 cm^{-1} was appearing in the spectrum. This correlation indicates that these species have a first-order dependency upon one another, as would be expected for an alkene and primary ozonide species. Finally, temperature-dependent studies to calculate activation energies for the formation and decomposition of the primary ozonide were carried out. The data implies small barriers to the formation and decomposition of the PO. These results add important information to the existing studies of C_{60} and ozone. Specifically, they confirm the hypothesis that ozone reacts with fullerenes in the same manner as with other alkenes; via the formation of the primary ozonide. They also provide kinetics for this initial reaction and allow for an assessment of the reactivity of C_{60} and ozone versus other unsaturated organics.

Perhaps the most interesting implications of this work are yet to come. The data reported herein was also compared with data collected from the Marr Research Group in the Environmental Engineering Department at Virginia Tech. The Marr Group prepared C_{60} aerosols and exposed them to atmospheric concentrations of ozone. The oxidized aerosols were then deposited onto Au slides and analyzed in the UHV chamber using RAIRS. Intriguingly, similar products, specifically, the monoepoxide ($C_{60}O$), were observed in both samples. Assessment of the UHV and environmental studies in parallel provides a great deal of insight into the environmental fate of C_{60}, especially in the atmosphere. The next research effort for this system should evaluate the ozonolysis products in regards to health implications.

The ozonolysis of larger fullerenes found that the oxidation of surface-bound C_{70} was very similar to the results collected for the ozonolysis of C_{60}. A peak exhibiting intermediate behavior was observed, most likely due to the primary ozonide of C_{70}. The peak slowly decreased throughout the exposure, indicating the species decomposed. With the decrease in this peak, product peaks appeared in the spectra. The peaks suggested the formation of ketones, anhydrides, and ketenes. The C_{76} surface reacted readily with ozone as well; the RAIRS spectra for this reaction was also consistent with ketone, anhydride, and ketene products. However, when C_{76} was oxidized, a new product peak appeared in the spectra, preliminarily assigned to ester functionalities. Finally, the RAIRS data suggested the ozonolysis of C_{78} and C_{84} were more comparable to the ozonolysis of carbon nanotubes. No anhydrides were detected, presumably because the larger molecules have reactive sites spaced farther apart and they are not freely rotating within the film like the smaller fullerenes.

Lastly, the ozone oxidation of Terbium endohedrals was studied. This study was motivated by the hypothesis that upon exposure to ozone, surface-bound endohedrals would

oxidize, resulting in a rupture of the fullerene cage. Once the cage was ruptured the ozone could oxidize the Tb inside. The XPS data suggests that this hypothesis is correct. The fullerenes were oxidized as a result of exposure to ozone, followed by the oxidation of Tb. The final observation in this study was the disappearance of the Tb signal in the XPS data. It is possible that, once oxidized, the Tb desorbs into the gas-phase.

7.2 Environmental Impacts

The data presented in this document indicates that the ozone oxidation of fullerenes at the gas-surface interface occurs readily. The fullerenes experience extensive oxidation, similar to that which has been observed in the solution phase.[11a, 11f] The eventual product of the oxidation is a water-soluble material known as the ozopolymer. The conversion of fullerenes from a hydrophobic species to a hydrophilic species is of serious concern, especially since the impacts of oxidized fullerenes have not been thoroughly investigated. It is interesting to note that comparable products were formed between solution phase experiments and the exposures performed in ultrahigh vacuum. This data demonstrates ozone's affinity for unsaturated sites.

One other product observed was the ketene. The ketene is known to be unstable in atmosphere, so its formation in the ozonolysis of fullerenes is an important discovery. When the reaction occurs at atmosphere, the ketene product can be considered an additional reactive site for other numerous species.

7.3 Future Studies

Future studies of these systems will help to develop the story included in this document and confirm the proposed assignments and mechanisms. The intermediates of C_{60} and O_3 can be conclusively identified with further isotopic studies, including all combinations of ^{18}O and ^{16}O

ozone. The isotopic studies should be supported with detailed calculations. It would be interesting to repeat the temperature-dependent studies over a larger temperature range and quantitatively determine the activation energies for the formation and decomposition of the primary ozonide. If the larger fullerenes are studied further, the surface coverage for each fullerene should be determined, so as to calculate an initial reaction probability with ozone. Finally, temperature programmed desorption should be carried out on the oxidized Tb endohedrals in order to detect any remaining Tb oxides on the surface; a supporting argument for the conclusions made in Chapter 6.

7.4 Conclusions

Ultrahigh vacuum studies of the ozone oxidation of surface-bound fullerenes have revealed information, not only about this gas-surface reaction, but also the general mechanism for ozone's reaction with fullerenes. These experiments conclude that ozone reacts with fullerenes via a cycloaddition reaction in which ozone adds across a double bond on the fullerene structure. This data helps further the knowledge of ozone's reactivity with carbonaceous nanomaterials.

Appendix

8.1 IR Assignments for Unoxidized C_{60} Film

Identification	Lit. Calc. Value[29] (cm^{-1})	Lit. Expt. Value[29] (cm^{-1})	Expt. Value (cm^{-1})
$H_g(2) + H_u(1)$	775	774.7	774.3
$H_u(1) + G_g(2)$	963.5	961.7	961.9
$G_u(2) + H_g(1)$	1033	1036.9	1038.0
$H_g(5)$ – isotopically-induced	1101.0	1099.6	1100.4
$F_{2u}(2) + H_g(2)$	1112.5	1114.0	1114.9
$H_g(4) + H_u(1)$	1117.5	1114.0	1117.6
$A_u(1)$ – isotopically-induced	1143.0	1141.0	1142.2
$F_{2u}(2) + G_g(1)$	1166	1164.1	1164.6
$F_{1u}(3)$ – IR active mode	1182.9	1182.9	1183.0
$G_u(3) + H_g(1)$	1197	1196.9	1197.7
$G_g(3) + G_u(1)$	1205.5	1203.7	1204.5
$F_{2g}(2) + H_u(1)$	1207.5	1213.3	1213.8
$H_g(2) + H_u(4)$	1233.5	1234.5	1234.9
$G_u(4) + H_g(1)$	1243	1242.2	1241.7
$F_{2g}(3) + H_u(1)$	1256.5	1258.6	1259.1
$G_g(1) + H_u(4)$	1287	1289.4	1291.5
$F_{1g}(1) + H_u(4)$	1303	1306.8	1306.8
$F_{2g}(1) + G_u(2)$	1326.5	1329.9	1329.1
$H_g(4) + H_u(2)$	1338	1342.5	1343.2
$F_{1u}(4)$ – IR active mode	1429.2	1429.2	1429.4
$F_{2u}(3) + H_g(2)$	1458.5	1462.0	1462.9
$A_g(2)$ – isotopically-induced	1470.0	1468.7	1468.9
$F_{2g}(3) + H_u(2)$	1477	1479.3	1479.2
$F_{2u}(2) + G_g(3)$	1486	1483.2	1484.4
$G_u(1) + H_g(5)$	1500.5	1495.7	1497.1
$F_{1g}(2) + F_{1u}(4)$	1502	1501.5	1502.7
$G_g(6)$ – isotopically-induced	1524.5	1523.7	1525.4
$G_u(2) + H_g(4)$	1535	1531.4	1533.2
$F_{1g}(2) + H_u(2)$	1538.5	1538.1	1538.9
$G_g(2) + G_u(3)$	1545	1545.8	1545.8
$H_g(4) + H_u(4)$	1576	1570.9	1572.0
$G_g(3) + H_u(4)$	1607	1607.5	1609.8
$3F_{1u}(2)$	1727.4	-	1724.2
$G_u(4) + H_g(4)$	1745	1746.3	1746.8
$F_{2u}(2) + H_g(5)$	1781	1779.1	1779.3

Identification	Lit. Calc. Value[29] (cm^{-1})	Lit. Expt. Value[29] (cm^{-1})	Expt. Value (cm^{-1})
$F_{2g}(2) + G_u(3)$	1789	1789.7	1790.6
$F_{2u}(3) + H_g(4)$	1801	1806.1	1807.5
$H_g(2) + H_u(6)$	1817.5	1815.7	1816.7
$F_{1u}(2) + H_g(6)$	1826.8	1824.4	1828.0
$F_{2g}(3) + G_u(3)$	1838	1841.8	1842.1
$F_{2u}(2) + H_g(1)$	1849.5	1851.4	1852.7
$H_g(4) + H_u(5)$	1892	1890.9	1897.9
$F_{1g}(3) + F_{1u}(2)$	1933.3	1934.3	1935.6
$F_{1u}(3) + H_g(4)$	1957.9	1957.4	1956.5
$G_u(1) + H_g(8)$	1977	1976.7	1977.1
$H_g(7) + H_u(2)$	1989.5	1988.3	1989.5
$A_g(2) + F_{1u}(1)$	1996.5	1994.1	1995.3
$F_{2g}(1) + G_u(6)$	2012.5	2016.2	2013.1
$G_u(5) + H_g(3)$	2021	2023.9	2018.2
$G_u(3) + H_g(5)$	2025	2023.9	2024.8
$G_u(4) + H_g(5)$	2071	2075.0	2076.9
$G_u(5) + H_g(4)$	2085	2083.7	2084.8
$H_g(3) + H_u(6)$	2096	2097.2	2098.9
$F_{2g}(4) + G_u(2)$	2120	2120.3	2121.2
$F_{1u}(4) + H_g(3)$	2140.2	2134.8	2136.9
$F_{2g}(4) + H_u(4)$	2161	2163.7	2164.9
$G_u(3) + H_g(6)$	2175	2174.3	2176.3
$G_g(3) + H_u(6)$	2191	2189.7	2191.4
$F_{1u}(4) + H_g(4)$	2204.2	2202.2	2204.3
$H_g(7) + H_u(4)$	2227.5	2234.1	2225.9
$H_g(8) + H_u(3)$	2273.5	2271.7	2273.3
$F_{2u}(5) + H_g(3)$	2287.5	2290.0	2290.8
$G_g(5) + G_u(4)$	2326	2326.6	2328.4
$G_u(3) + H_g(7)$	2350.5	2346.8	2349.0
$G_g(4) + G_u(5)$	2385.5	2388.3	2389.6
$F_{2u}(5) + H_g(5)$	2677.5	2675.5	2677.0
$G_u(5) + H_g(7)$	2736.5	2735.3	2736.6
$G_g(6) + H_u(6)$	2909.5	2908.8	2910.1

References

1. Hoffmann, T.; Odum, J. R.; Bowman, F.; Collins, D.; Klockow, D.; Flagan, R. C.; Sienfeld, J. H., Formation of Organic Aerosols from the Oxidation of Biogenic Hydrocarbons. *Journal of Atmospheric Chemistry* **1997,** *26*, 189-222.
2. (a) Atkinson, R.; Aschmann, S. M.; Winer, A. M.; Pitts, J. N., Jr., Gas Phase Reaction of NO_2 with Alkenes and Dialkenes. *International Journal of Chemical Kinetics* **1984,** *16*, 697-706; (b) Niki, H.; Maker, P. D.; Savage, C. M.; Breitenbach, L. P.; Hurley, M. D., An FTIR Spectroscopic Study of the Kinetics and Mechanism for the NO_2-Initiated Oxidation of Tetramethyl Ethylene at 298K. *International Journal of Chemical Kinetics* **1986,** *18*, 1235-1247; (c) Pryor, W. A.; Lightsey, J. W., Mechanisms of Nitrogen Dioxide Reactions: Initiation of Lipid Peroxidation and the Production of Nitrous Acid. *Science* **1981,** *214*, 435-437; (d) Pryor, W. A.; Lightsey, J. W.; Church, D. F., Reaction of Nitrogen Dioxide with Alkenes and Polyunsaturated Fatty Acids: Addition and Hydrogen Abstraction Mechanisms. *J. Am. Chem. Soc.* **1982,** *104*, 6685-6692; (e) Sprung, J. L.; Akimoto, H.; Pitts, J. N., Jr., Nitrogen Dioxide Catalyzed Geometric Isomerization of Olefins. Isomerization Kinetics of the 2-Butenes and the 2-Pentenes. *J. Am. Chem. Soc.* **1974,** *96* (21), 6549-6554.
3. (a) Li, J. J. G., C. Z.; Wang, Q.; Xu, P.; Wang, Z. L.; Xu, Z.; Bai, X. D., Field emission from high aspect ratio tubular carbon cones grown on gold wire. *Applied Physics Letters* **2005,** *87* (14), 143107-143109; (b) Hahn, J. J., Sung Mi; Jung, Hyun Young; Heo, Soo Bong; Shin, Ji Hye; Suh, Jung Sang, Fabrication of clean carbon nanotube field emitters. *Applied Physics Letters* **2006,** *88* (11), 113101-113103; (c) Seelaboyina, R. H., Jun; Choi, Won Bong, Enhanced field emission of thin multiwall carbon nanotubes by electron multiplication from microchannel plate. *Applied Physics Letters* **2006,** *88* (19), 194104-19104-3.
4. Consales, M. C., A.; Penza, M.; Aversa, P.; Cassano, G.; Giordano, M.; Cusano, A., Carbon Nanotubes Coated Acoustic and Optical VOCs Sensors: Towards the Tailoring of the Sensing Performances. *Nanotechnology, IEEE Transactions* **2007,** *6* (6), 601-612.
5. (a) Qian, X.-M. N., S. M., Single-molecule and single-nanoparticle SERS: from fundamental mechanisms to biomedical applications. *Chemical Society Reviews* **2008,** *37*, 912-920; (b) Son, S. J. B., Xia; Lee, Sang Bok, Inorganic hollow nanoparticles and nanotubes in nanomedicine: Part 1. Drug/gene delivery applications *Drug Discovery Today* **2007,** *12* (15-16), 650-656; (c) Sinha, N. Y., J. T.-W., Carbon Nanotubes for biomedical applications. *NanoBioscience, IEEE Transactions* **2005,** *4* (2), 180-195.
6. Nesper, R. I., A.; Krumeich, F., Synthesis and Characterization of Carbon-Based Nanoparticles and Highly Magnetic Nanoparticles with Carbon Coatings. *Advanced Functional Materials* **2006,** *16* (2), 296-305.
7. Colvin, V. L., The potential environmental impact of engineered nanomaterials. *Nature Biotechnology* **2003,** *21* (10), 1166-1170.
8. (a) Poland, C. A. D., Rodger; Kinloch, Ian; Maynard, Andrew; Wallace, William A. H.; Seaton, Anthony; Stone, Vicki; Brown, Simon; MacNee, William; Donaldson, Ken, Carbon nanotubes introduced into the abdominal cavity of mice show asbestos like pathogenicity in a pilot study. *Nature - Nanotechnology Letters* **2008,** *3*, 423-428; (b) Kane, A. B. H., Robert H., The asbestos analogy revisited. *Nature - Nanotechnology Letters* **2008,** *3*, 378-388.
9. Takagi, A. H., A.; Nishimura, T.; Fukumori, N.; Ogata, A.; Ohashi, N.; Kitajima, S.; Kanno, J., Induction of mesothelioma in p53+/- mouse by intraperitoneal application of multi-wall carbon nanotube. *J. Toxicol. Sci.* **2008,** *33* (1), 105-116.

10. Park, J.; Gomez, A. L.; Walser, M. L.; Lin, A.; Nizkorodov, S. A., Ozonolysis and photolysis of alkene-terminated self-assembled monolayers on quartz nanoparticles: implications for photochemical aging of organic aerosol particles. *Physical Chemistry Chemical Physics* **2006,** *8* (21), 2506-2512.
11. (a) Cataldo, F., Polymeric fullerene oxide (fullerene ozopolymers) produced by prolonged ozonation of C60 and C70 fullerenes. *Carbon* **2002,** *40* (9), 1457-1467; (b) Cataldo, F., Encapsulation of C60 fullerene in g-cyclodextrin: a new concept in the protection of organic substrates and polymers from ozone attack Kinetic aspects on the reactivity between C60 and O3. *Polymer Degradation and Stability* **2002,** *77* (1), 111-120; (c) Cataldo, F., Ozone reaction with carbon nanostructures 2: the reaction of ozone with milled graphite and different carbon black grades. *Journal of Nanoscience and Nanotechnology* **2007,** *7* (4/5), 1446-1454; (d) Cataldo, F., Ozone reaction with carbon nanostructures 1: reaction between solid C60 and C70 fullerenes and ozone. *Journal of Nanoscience and Nanotechnology* **2007,** *7* (4/5), 1439-1445; (e) Cataldo, F., A Study on the Action of Ozone on Multiwall Carbon Nanotubes. *Fuller Nanotub Car N* **2008,** *16*, 1-17; (f) Cataldo, F.; Heymann, D., A study of polymeric products formed by C60 and C70 fullerene ozonation. *Polymer Degradation and Stability* **2000,** *70* (2), 237-243; (g) Cataldo, F.; Ori, O., Ozone reaction with C60 fullerene. A study on the antiozonant activity of C60 fullerene in dienic rubber. *Polymer Degradation and Stability* **1995,** *48* (2), 291-6; (h) Cataldo, F.; Ursini, O., The role of carbon nanostructures in the ozonization of different carbon black grades, together with graphite and rubber crumb in an IR gas cell. *Fullerenes, Nanotubes, and Carbon Nanostructures* **2007,** *15* (1), 1-20.
12. Pacioli, L., *De Divina Proportione*. Milan, 1497.
13. Dresselhaus, M. S. D., G.; Eklund, P.C., *Science of Fullerenes and Carbon Nanotubes*. Academic Press: San Diego, 1996.
14. Kroto, H. W.; Heath, J. R.; Obrien, S. C.; Curl, R. F.; Smalley, R. E., C-60 - Buckminsterfullerene. *Nature* **1985,** *318* (6042), 162-163.
15. Kroto, H. W. A., A. W.; Balm, S. P., C_{60}: Buckminsterfullerene. *Chem. Rev.* **1991,** *91*, 1213-1235.
16. Taylor, R. W., David R. M., The chemistry of fullerenes. *Nature* **1993,** *363*, 685-693.
17. Rubin, M. B., The History of Ozone. The Schonbein Period, 1839-1868. *Bull. Hist. Chem.* **2001,** *26* (1), 40-57.
18. Soret, J.-L., Studies on the density of ozone. *Annuals of Physics* **1867,** *208* (9), 165-174.
19. (a) Hughes, R. H., Structure of Ozone from the Microwave Spectrum between 9000 and 45 000 Mc *The Journal of Chemical Physics* **1956,** *24* (1), 131-138; (b) Trambarulo, R. G., S. N.; Burrus, J. C. A.; Gordy, W., The Molecular Structure, Dipole Moment, and g Factor of Ozone from Its Microwave Spectrum *The Journal of Chemical Physics* **1953,** *21* (5), 851-855.
20. Horvath, M. B., L.; Huettner, J., *Ozone*. Elsevier: New York, 1985.
21. Bailey, P. S., *Ozonation in Organic Chemistry, Volume I, Olefinic Compounds*. Academic Press: New York, 1978; Vol. 1, p 272.
22. Pryor, W. A.; Das, B.; Church, D. F., The Ozonation of Unsaturated Fatty Acids: Aldehydes and Hydrogen Peroxide as Products and Possible Mediators of Ozone Toxicity. *Chem. Res. Toxicol.* **1991,** *4*, 341-348.
23. (a) Ewing, J. W.; Cosgrove, J. P.; Giamalva, D. H.; Church, D. F.; Pryor, W. A., Autoxidation of methyl linoleate initiated by the ozonide of allylbenzene. *Lipids* **1989,** *24*, 609-615; (b) Pryor, W. A., Can vitamin E protect us against the pathological effects of ozone in smog? *Am. J. Clin. Nutr.* **1991,** *53*, 702-722.

24. Wadt, W. R.; Goddard, W. A., III, The Electronic Structure of the Criegee Intermediate. Ramifications for the Mechanism of Ozonolysis. *J. Am. Chem. Soc.* **1975,** *97* (11), 3004-3021.
25. Davis, G. M. Interfacial Reaction of an Olefin-Terminated Self-Assembled Monolayer Exposed of Nitrogen Dioxide: An Investigation Into the Recation Rate and Mechanism. Virginia Polytechnic Institute and State University, Blacksburg, 2003.
26. Schonbein, C. F., *J. Prakt. Chem.* **1868,** *105* (1), 232.
27. Wadia, Y.; Tobias, D. J.; Stafford, R.; Finlayson-Pitts, B. J., Real-Time Monitoring of the Kinetics and Gas-Phase Products of the Reactions of Ozone with an Unsaturated Phospholipid at the Air-Water Interface. *Langmuir* **2000,** *16*, 9321-9330.
28. Warneck, P., *Chemistry of the Natural Atmosphere, Second Edition*. 2 ed.; Academic Press: San Diego, 2000; p 927.
29. Atkinson, R.; Tuazon, E. C.; Aschmann, S. M., Products of the Gas-Phase Reactions of O_3 with Alkenes. *Environmental Science & Technology* **1995,** *29*, 1860-1866.
30. Feltham, E. J.; Almond, M. J.; Marston, G.; Ly, V. P.; Wiltshire, K. S., Reactions of alkenes with ozone in the gas phase: a matrix-isolation study of secondary ozonides and carbonyl-containing products. *Spectrochimica Acta Part A* **2000,** *56*, 2605-2616.
31. Fiegland, L. R.; McCorn Saint Fleur, M.; Morris, J. R., Reactions of C=C-Terminated Self-Assembled Monolayers with Gas-Phase Ozone. *Langmuir* **2005,** *21*, 2660-2661.
32. Yan, L.; Marzolin, C.; Terfort, A.; Whitesides, G. M., Formation and Reaction of Interchain Carboxylic Anhydride Groups on Self-Assembled Monolayers on Gold. *Langmuir* **1997,** *13* (25), 6704-6712.
33. McIntire, T. M.; Lea, A. S.; Gaspar, D. J.; Jaitly, N.; Dubowski, Y.; Li, Q.; Finlayson-Pitts, B. J., Unusual aggregates from the oxidation of alkene self-assembled monolayers: a previously unrecognized mechanism for SAM ozonolysis? *Physcial Chemistry Chemical Physics* **2005,** *7* (20), 3605-3609.
34. Finlayson-Pitts, B. J.; Pitts, J. N., *Chemistry of the Upper and Lower Atmosphere - Theory, Experiments, and Applications*. Academic Press: San Diego, 2000.
35. (a) Bertram, A. K.; Ivanov, A. V.; Hunter, M.; Molina, L. T.; Molina, M. J., The Reaction Probability of OH on Organic Surfaces of Tropospheric Interest. *J. Phys. Chem. A* **2001,** *105* (41), 9415-9421; (b) Katrib, Y.; Martin, S. T.; Rudich, Y.; Davidovits, P.; Jayne, J. T.; Worsnop, D. R., Density changes of aerosol particles as a result of chemical reaction. *Atmos. Chem. Phys.* **2005,** *5* (1), 275-291; (c) Moise, T.; Rudich, Y., *J. Geophys. Res.* **2000,** *105*, 14667.
36. Heymann, D.; Bachilo, S. M.; Weisman, R. B.; Cataldo, F.; Fokkens, R. H.; Nibbering, N. M. M.; Vis, R. D.; Chibante, L. P. F., C60O3, a Fullerene Ozonide: Synthesis and Dissociation to C60O and O2. *Journal of the American Chemical Society* **2000,** *122* (46), 11473-11479.
37. Shang, Z.; Pan, Y.; Cai, Z.; Zhao, X.; Tang, A., An AM1 Study of the Reaction of Ozone with C60. *Journal of Physical Chemistry A* **2000,** *104* (9), 1915-1919.
38. Sabirov, D. S.; Khursan, S. L.; Bulgakov, R. G., Ozone addition to C-60 and C-70 fullerenes: A DFT study. *Journal of Molecular Graphics & Modelling* **2008,** *27* (2), 124-130.
39. Fiegland, L. R. Ultrahigh vacuum studies of the reaction mechanisms of ozone with saturated and unsaturated self-assembled monolayers. VPI & SU, Blacksburg, 2008.
40. Koike, K. N., M.; Izumi, K.; Nakamura, S.; Fujiwara, S.; Horiguchi, S., *Journal of chemical Engineering of Japan* **1999,** *32*, 295-299.
41. Yates, J. T., Jr., *Experimental Innovations in Surface Science*. 1 ed.; AIP/Springer-Verlag: New York, 1998; p 920.

42. Cohen, M., *Organic Syntheses*. 1988; Vol. 6.
43. (a) Greenler, R. G., Infrared Study of Adsorbed Molecules on Metal Surfaces by Reflection Techniques. *The Journal of Chemical Physics* **1966,** *44* (1), 310-315; (b) Trenary, M., Reflection Absorption Infrafred Spectroscopy and the Structure of Molecular Adsorbates on Metal Surfaces. *Annual Review of Physical Chemistry* **2000,** *51*, 381-403.
44. Zhukov, V. P., I.; Yates, J. T., Jr., Delivery of pure ozone in ultrahigh vacuum. *Journal of Vacuum Science & Technology A* **2000,** *18* (3).
45. Siegbahn, K. In *Electron Spectroscopy for Atoms, Molecules, and Condensed Matter*, Nobel Lecture, 1981.
46. Rybicki, G. B. L., A. P., *Radiative Processes in Astrophysics* Wiley-VCH: 1985.
47. Guo, S. F., Daniel P.; Nagel, Phillip M.; Kandel, S. Alex, Thermal Diffusion of C_{60} Molecules and Clusters on Au(111). *J. Phys. Chem. B* **2004,** *108*, 14074-14081.
48. Skrzypek, M. D., Z.; Brol, P.; Gburski, Z., Cluster and layers of fullerene molecules between graphite planes. *Journal of Molecular Structure* **2004,** *704* (1-3), 287-290.
49. Wang, K. A. R., A. M.; Eklund, P. C.; Dresselhaus, M. S.; Dresselhaus, G., Observation of Higher-Order Infrared Modes in Solid C_{60} Films. *Physical Review B* **1993,** *48* (15), 11375-11380.
50. Lyon, J. T.; Andrews, L., Infrared spectrum of the Au-C60 complex. *ChemPhysChem* **2005,** *6* (2), 229-232.
51. (a) Bethune, D. S. M., G.; Tang, W. C.; Rosen, H. J.; Golden, W. G.; Seki, H.; Brown, C. A.; Derries, M. S., Vibrational Raman and infrared spectra of chromatographically separated C60 and C70 fullerene clusters. *Chemical Physics Letters* **1991,** *179*, 181; (b) Jishi, R. A. D., M. S.; Dresselhaus, G.; Wang, Kai-An; Zhou, Ping; Rao, A. M.; Eklund, P. C., Vibrational mode frequencies in C_{70}. *Chemical Physics Letters* **1993,** *206* (1,2,3,4), 187-192; (c) Procacci, P. C., Gianni; Salvi, Pier Remigio; Schettino, Vincenzo, Vibrational frequencies of C_{70}. *Chemical Physics Letters* **1992,** *195* (4), 347-351; (d) Xia, H. J., Qing; Tian, Decheng, Vibrational spectrum of C_{70}. *Chemical Physics Letters* **1992,** *198* (1,2), 109-112.
52. Etti, R. C., Ito; Diederich, Francois; Whetten, Robert L., Isolation of C_{76}, a chiral (D_2) allotrope of carbon. *Nature* **1991,** *353*, 149-153.
53. Benz, M. F., Marianna; Fowler, Patrick W.; Fuchs, Dirk; Kappes, Manfred M.; Lehner, Carolin; Michel, Rudi H.; Orlandi, Giorgio; Zerbetto, Francesco, Experimental and Theoretical Study of the Infrared, Raman, and Electronic Spectra of Two Isomers of C_{78} of C_{2u} Symmetry. *Journal of Physical Chemistry* **1996,** *100*, 13399-13407.

54. Avent, A. G. D., Dominique; Penicaud, Alain; Taylor, Roger, The minor isomers and IR spectrum of [84]fullerene. *Journal of the Chemical Society, Perkin Trans.* **1997,** *2*, 1907-1910.
55. Zandler, M. E. D. S., F., The remarkable ability of B3LYP/3-21G(*) calculations to describe geometry, spectral and electrochemical properties of molecular and supramolecular porphyrin–fullerene conjugates. *C. R. Chimie* **2006,** *9*, 960-981.
56. (a) Johnson, R. D. Y., Costantino S.; de Vriest, Mattanjah S.; Dorn, Harry C.; Salem, Jesse R.; Bethune, Donald S., C_{60} solid state rotational dynamics and production and EPR spectroscopy of fullerenes containing metal atoms. *Nanotechnology* **1992,** *3*, 164-166; (b) Johnson, R. D. Y., Costantino S.; de Vriest, Mattanjah S.; Dorn, Harry C.; Salem, Jesse R.; Bethune, Donald S., C_{60} Rotation in the Solid State: Dynamics of a Faceted Spherical Top. *Science* **1992,** *255* (5049), 1235-1238.
57. Chase, B. H., N.; Holler, E., Vibrational Spectroscopy of C_{60} and C_{70} Temperature-Dependent Studies. *J. Phys. Chem.* **1992,** *96*, 4262-4266.

58. Krozer, A. R., M., X-ray photoemission spectroscopy study of UV/ozone oxidation of Au under ultrahigh vacuum conditions. *J. Vac. Sci. Technol. A* **1997,** *15* (3), 1704-1710.
59. Frisch, M. J. T., G. W.; Schlegel, H. B.; Scuseria, G. E.; Robb, M. A.; Cheeseman, J. R.; Scalmani, G.; Barone, V.; Mennucci, B.; Petersson, G. A.; Nakatsuji, H.; Caricato, M.; Li, X.; Hratchian, H. P.; Izmaylov, A. F.; Bloino, J.; Zheng, G.; Sonnenberg, J. L.; Hada, M.; Ehara, M.; Toyota, K.; Fukuda, R.; Hasegawa, J.; Ishida, M.; Nakajima, T.; Honda, Y.; Kitao, O.; Nakai, H.; Vreven, T.; Montgomery, Jr., J. A.; Peralta, J. E.; Ogliaro, F.; Bearpark, M.; Heyd, J. J.; Brothers, E.; Kudin, K. N.; Staroverov, V. N.; Kobayashi, R.; Normand, J.; Raghavachari, K.; Rendell, A.; Burant, J. C.; Iyengar, S. S.; Tomasi, J.; Cossi, M.; Rega, N.; Millam, N. J.; Klene, M.; Knox, J. E.; Cross, J. B.; Bakken, V.; Adamo, C.; Jaramillo, J.; Gomperts, R.; Stratmann, R. E.; Yazyev, O.; Austin, A. J.; Cammi, R.; Pomelli, C.; Ochterski, J. W.; Martin, R. L.; Morokuma, K.; Zakrzewski, V. G.; Voth, G. A.; Salvador, P.; Dannenberg, J. J.; Dapprich, S.; Daniels, A. D.; Farkas, Ö.; Foresman, J. B.; Ortiz, J. V.; Cioslowski, J.; Fox, D. J. *Gaussian 09, Revision A.1,* Gaussian, Inc.: Wallingford CT, 2009.
60. (a) Anachkov, M. P.; Cataldo, F.; Rakovsky, S. K., Ozone Reaction with C70 and C60 Fullerenes: The Effect of Temperature on the Reaction Kinetics. *Fullerenes, Nanotubes, and Carbon Nanostructures* **2004,** *12* (4), 745-752; (b) Davydov, V. Y.; Filatova, G. N.; Knipovich, O. M., Oxidation of C60 and C70 fullerenes by ozone. *Molecular Crystals and Liquid Crystals Science and Technology, Section C: Molecular Materials* **1998,** *10* (1-4), 221-224; (c) Heymann, D.; Chibante, L. P. F., Reaction of C60, C70, C76, C78, and C84 with ozone at 23.5 DegC. *Recueil des Travaux Chimiques des Pays-Bas* **1993,** *112* (12), 639-42; (d) Heymann, D.; Chibante, L. P. F., Reaction of fullerenes C60 and C70 with ozone at different temperatures. *Recueil des Travaux Chimiques des Pays-Bas* **1993,** *112* (10), 531-4; (e) Li, W.; Hao, C.; Wu, S.; Teng, Q.; Zhao, X.; Tang, A.; feng, J., Oxidation of C70 by ozone and the spectrum of C70O. *Huaxue Yanjiu Yu Yingyong* **1997,** *9* (6), 608-610; (f) Razumovskii, S. D.; Bulgakov, P. G.; Ponomareva, Y. G.; Budtov, V. P., Kinetics and stoichiometry of the reaction between ozone and C70 fullerene in CCl4. *Kinetics and Catalysis* **2006,** *47* (3), 347-350; (g) Xia, S.-W.; Liang, Y.-H.; Chen, L.; Pan, Y.-M.; Zhao, X.-Z.; Tang, A.-C., Theoretical studies on the mechanism of the reaction of C70 with ozone. *Huaxue Xuebao* **2003,** *61* (6), 824-834.
61. von Czarnowski, A. M.-B., K. H., Infrared-active vibrational modes in C 7O fullerene. *Chemical Physics Letters* **1995,** *246*, 321-324.
62. (a) Cheng, A. K., Michael L., Solid C_{70}: A molecular-dynamics study of the structure and orientational ordering. *Physical Review B* **1992,** *46* (8), 4958-4962; (b) Firiej, L. B., Z.; Bernier, P.; Zahab, A.; Ribet, M.; Coustel, N.; Aznar, R., Molecular Motion in Solid C_{70} by ^{13}C High Resolution NMR. *Solid State Communications* **1993,** *87* (8), 669-673.
63. Fischer, J. E. H., P. A., *J. Phys. Chem. Solids* **1993,** *54*, 1725.
64. Shinohara, Y. S., R.; Kimura, T.; Dresselhaus, G.; Dresselhaus, M. S., Infrared-active modes of C_{70}. *Chemical Physics Letters* **1994,** *227*, 365-370.
65. Hare, J. P. D., T. John; Kroto, Harold W.; Taylor, Roger; Allaf, A. Wahab; Balm, Simon; Walton, David R. M., The IR Spectra of Fullerene-60 and -70. *Journal of the Chemical Society, Chemical Communications* **1991**, 412-413.
66. Michel, R. H. S., H.; Gierden, R.; Hennrich, F.; Rockenberger, J.; Beck, R. D.; Kappes, M. M.; Lehner, C.; Adelmann, P.; Armbruster, J. F., Vibrational Spectroscopy of Purified C_{76}. *Ber. Bunsenges. Phys. Chem.* **1994,** *98* (7), 975-978.
67. Fowler, P. W. B., R. C.; Manolopoulos, D. E., The Higher Fullerenes: A Candidate for the Structure of C_{78}. *Journal of the Chemical Society, Faraday Trans.* **1991,** *87* (18), 3103-3104.

68. (a) Uemura, S. T., I.; Sakata, M.; Kunitake, M., Electrochemical STM investigation of C_{70}, C_{60}/C_{70} mixed fullerene and hydrogenated fullerene adlayers on Au(111) prepared using the electrochemical replacement method. *Journal of Electroanalytical Chemistry* **2008,** *623*, 1-7; (b) Aiyer, H. N. G., A.; Rao, C. N. R., Scanning tunneling microscopy and spectroscopy of C_{70} thin films. *Bull. Mater. Sci.* **1994,** *17* (6), 563-575.
69. Li, Y. Z. P., J. C.; Chander, M.; Weaver, J. H., Overlayer growth and molecular structures of C_{84} and other large fullerenes:

A scanning-tunneling-microscopy study. *Physical Review B* **1993,** *47* (16), 10867-10872.
70. Zhao, Y. L., Y.; Yakobon, B. I., Fullerene shape transformations via Stone-Wales bond rotations. *Physical Review B* **2003,** *68*, 233403-1 - 233403-4.
71. Hawkins, J. M. N., M.; Meyer, A., Resolution and Configurational Stability of the Chiral Fullerenes C_{76}, C_{78}, and C_{84}: A Limit for the Activation Energy of the Stone-Wales Transformation. *Journal of the American Chemical Society* **1994,** *116*, 7642-7645.
72. (a) Sawamura, M.; Kuninobu, Y.; Toganoh, M.; Matsuo, Y.; Yamanaka, M.; Nakamura, E., Hybrid of ferrocene and fullerene. *Journal of the American Chemical Society* **2002,** *124* (32), 9354-9355; (b) Toganoh, M.; Matsuo, Y.; Nakamura, E., Synthesis of ferrocene/hydrofullerene hybrid and functionalized bucky ferrocenes. *Journal of the American Chemical Society* **2003,** *125* (46), 13974-13975.
73. (a) Paci, P.; Cappelluti, E.; Grimaldi, C.; Pietronero, L.; Strassler, S., Nonadiabatic high-T-c superconductivity in hole-doped fullerenes. *Physical Review B* **2004,** *69* (2), -; (b) Varshney, D., Pairing mechanism and superconductivity of Rb3C60 fullerides. *Journal of Superconductivity* **2000,** *13* (1), 171-179.
74. (a) Huang, S. T.; Liao, J. S.; Fang, H. W.; Lin, C. M., Synthesis and anti-inflammation evaluation of new C-60 fulleropyrrolidines bearing biologically active xanthine. *Bioorganic & Medicinal Chemistry Letters* **2008,** *18* (1), 99-103; (b) Ryan, J. J.; Bateman, H. R.; Stover, A.; Gomez, G.; Norton, S. K.; Zhao, W.; Schwartz, L. B.; Lenk, R.; Kepley, C. L., Fullerene nanomaterials inhibit the allergic response. *Journal of Immunology* **2007,** *179* (1), 665-672; (c) Yamakoshi, Y.; Umezawa, N.; Ryu, A.; Arakane, K.; Miyata, N.; Goda, Y.; Masumizu, T.; Nagano, T., Active oxygen species generated from photoexcited fullerene (C-60) as potential medicines: O-2(-center dot) versus O-1(2). *Journal of the American Chemical Society* **2003,** *125* (42), 12803-12809.
75. (a) Satterley, C. J. P., Luis M. A.; Saywell, Alex; Magnano, Graziano; Rienzo, Anna; Mayor, Louise C.; Dhanak, Vinod R.; Beton, Peter H.; O'Shea, James N., Electrospray deposition of fullerenes in ultra-high vacuum: in situ scanning tunneling microscopy and photoemission spectroscopy. *Nanotechnology* **2007,** *18* (45), 455304/1-455304/5; (b) Swami, N. S., Surface science studies of fullerene and fulleride thin films: electronic, vibrational and electrical characterization **1998**, 166.
76. (a) Ball, J. M. B., Ricardo K. M.; Kooistra, Floris B.; Frost, Jarvist M.; Qi, Yabing; Domingo, Ester Buchaca; Smith, Jeremy; de Leeuw, Dago M.; Hummelen, Jan C.; Nelson, Jenny; et al, Soluble fullerene derivatives. The effect of electronic structure on transistor performance and air stability. *Journal of Applied Physics* **2011,** *110* (1), 014506/1-014506/9; (b) Nagai, T. T., Yoshito; Aso, Yoshio; Ie, Hirotaka; Nozawa, Takahiro, Fullerene derivatives, semiconductor materials and thin films containing them, and semiconductor elements, field effect transistors, and organic thin-film solar cells. *Jpn. Kokai Tokkyo Koho* **2011**; (c) Li, Y. K., Toshiro; Hatakeyama, Rikizo, Photoresponse of fullerene and azafullerene peapod field effect transistors *IEEE Conference on Nanotechnology* **2009**, 86-89.

77. (a) Murata, S. K., Keisuke, Secondary lithium batteries with battery-to-battery uniformity. *Jpn. Kokai Tokkyo Koho* **2005**; (b) Soga, I., Electrochemical devices with fullerene-containing layers electric double layer capacitors, and batteries *Jpn. Kokai Tokkyo Koho* **2005**; (c) Kiritani, H., Electrochemical devices for electric double layer capacitors and batteries *Jpn. Kokai Tokkyo Koho* **2005**.
78. (a) Matsuo, Y., Fullerenes and organic thin film solar cells *Kagaku to Kyoiku* **2011,** *59* (5), 242-245; (b) Matsuo, Y. Z., Ying; Soga, Iwao; Sato, Yoshiharu; Nakamura, Eiichi, Synthesis of 1,4-diaryl[60]fullerenes by bis-hydroarylation of C60 and their use in solution-processable, thin-film organic photovoltaic cells *Tetrahedron Letters* **2011,** *52* (17), 2240-2242; (c) Uetani, Y. F., Jun, Photoelectric fullerene derivatives *Jpn. Kokai Tokkyo Koho* **2011**.
79. (a) Jakubov, T. S. M., David E. , Interaction between C60 fullerene and alkali metals demonstrating superconductivity. *Procedia Chemistry* **2009,** *1* (2), 1584-1589; (b) Dutton, G. Q., Daniel P.; Lindstrom, C. D.; Zhu, X.-Y. , Exciton dynamics at molecule-metal interfaces: C60/Au(111). *Physical Review B: Condensed Matter and Materials Physics* **2005,** *72* (4), 045441/1-045441/11; (c) Hou, J. G., C60 and metals: interfacial interaction and epitaxy orientation *Dianzi Xianwei Xuebao* **1997,** *16* (4), 481-484; (d) Hunt, M. R. C. R., Petra; Modesti, Silvio, Localization of substrate-induced modification in the electronic structure of C60 at fullerene-metal interfaces *Physical Review B: Condensed Matter* **1997,** *55* (12), 7882-7888; (e) Maxwell, A. J. B., P. A.; Arvanitis, D.; Hasselstroem, J.; Martensson, N. , C 1s ionization potential and energy referencing for solid C60 films on metal surfaces *Chemical Physics Letters* **1996,** *260* (1,2), 71-77; (f) Fartash, A., Temperature dependent orientational epitaxy of C60 films on noble metal (111) surfaces: Au, Ag and Cu *Materials Research Society Symposium Proceedings* **1995,** *359*, 393-8.
80. Wilson, R. J. M., G.; Bethune, D. S.; Johnson, R. D.; Chambliss, D. D.; de Vries, M. S.; Hunziker, H. E.; Wendt, H. R., Imaging C60 clusters on a surface using a scanning tunnelling microscope. *Nature* **1990,** *348*, 621-622.
81. Singh, T. B. S., N. S.; Yang, H.; Yang, L.; Plochberger, B.; Sitter, H., Correlation of crystalline and structural properties of C60 thin films grown at various temperature with charge carrier mobility. *Applied Physics Letters* **2007,** *90*, 213512-1 - 213512-3.
82. Ren, S. Y., Shengrong; Zhao, Yapu, Preparation and Tribiological Studies of C60 Thin Film Chemisorbed on a Functional Polymer Surface. *Langmuir* **2004,** *20*, 3601-3605.
83. (a) Hoen, S. C., N. G.; Xiang, X. D.; Mostovoy, R.; Hou, Jianguo; Vareka, W. Q.; Zettle, A. , Elastic properties of a van der Waals solid: fullerene (C_{60}) *Physical Review B: Condensed Matter and Materials Physics* **1992,** *46* (19), 12737-9; (b) Li, Y. Z. C., M.; Patrin, J. C.; Weaver, J. H.; Chibante, L. P. F.; Smalley, R. E., Order and disorder in C_{60} and K_xC_{60} multilayers: direct imaging with scanning tunneling microscopy *Science* **1991,** *253* (5018), 429-433.
84. Ohno, T. R. C., Y.; Harvey, S. E.; Kroll, G. H.; Weaver, J. H.; Haufler, R. E.; Smalley, R. E., Fullerene (C_{60}) bonding and energy-level alignment on metal and semiconductor surfaces. *Physical Review B: Condensed Matter and Materials Physics* **1991,** *44* (24), 13747-13755.
85. (a) Altman, E. I. C., R. J., Determination of the orientation of C60 adsorbed on Au(111) and Ag(111). *Physical Review B* **1993,** *48* (24), 18244-18249; (b) Tang, L. Z., Xin; Guo, Quanmin, Organizing C60 molecules on a nanostructured Au(111) surface *Surface Science* **2010,** *604*, 1310-1314; (c) Akers, K. F., K.; Zhang, P.; Moskovits, M., Order-Disorder Transition in Polycrystalline C_{60} Films. *Science* **1991,** *259*, 1152-1155.
86. (a) Zhang, Y. G., Xiaoping; Weaver, Michael J., Scanning Tunnelling Microscopy of C60 and C70 on Ordered Au(111) and Au(110): Molecular Structure and Electron Transmission.

J. Phys. Chem. **1992,** *96*, 510-513; (b) Gardener, J. A. B., G. A. D.; Castell, M. R., Scanning tunnelling microscopy studies of C60 monolayers on Au(111). *Physical Review B* **2009,** *80*, 235434-235442.
87. (a) Anachkov, M. P.; Cataldo, F.; Rakovsky, S. K., Reaction kinetics of C60 fullerene ozonation. *Fullerenes, Nanotubes, and Carbon Nanostructures* **2003,** *11* (2), 95-103; (b) Bulgakov, R. G.; Akhmadieva, R. G.; Musavirova, A. S.; Abdrakhmanov, A. M.; Ushakova, Z. I.; Sharifullina, F. M., The first example of chemiluminescence of fullerenes - oxidation of C60 by ozone in solution. *Russian Chemical Bulletin (Translation of Izvestiya Akademii Nauk, Seriya Khimicheskaya)* **1999,** *48* (6), 1190; (c) Bulgakov, R. G.; Musavirova, A. S.; Abdrakhmanov, A. M.; Nevyadovskii, E. Y.; Khursan, S. L.; Razumovskii, S. D., Chemiluminescence in Ozonolysis of Solutions of Fullerene C60. *Journal of Applied Spectroscopy (Translation of Zhurnal Prikladnoi Spektroskopii)* **2002,** *69* (2), 220-225; (d) Bulgakov, R. G.; Nevyadovskii, E. Y.; Belyaeva, A. S.; Golikova, M. T.; Ushakova, Z. I.; Ponomareva, Y. G.; Dzhemilev, U. M.; Razumovskii, S. D.; Valyamova, F. G., Water-soluble polyketones and esters as the main stable products of ozonolysis of fullerene C60 solutions. *Russian Chemical Bulletin (Translation of Izvestiya Akademii Nauk, Seriya Khimicheskaya)* **2004,** *53* (1), 148-159; (e) Davydov, V. Y.; Filatova, G. N.; Knipovich, O. M.; Lunin, V. V., Study of the kinetics of fullerenes ozonolysis. *Proceedings - Electrochemical Society* **1996,** *96-10* (Recent Advances in the Chemistry and Physics of Fullerenes and Related Materials, Vol. 3), 1295-1306; (f) Deng, J.-P.; Mou, C.-Y.; Han, C.-C., Oxidation of fullerenes by ozone. *Fullerene Science and Technology* **1997,** *5* (7), 1325-1336; (g) Heymann, D.; Chibante, L. P. F., Photo-transformations of fullerenes (C60, C70) and fullerene oxides (C60O, C60O2). *Chemical Physics Letters* **1993,** *207* (4-6), 339-42; (h) Li, X.; Cai, R.-f.; Kong, Q.-y.; Zhao, L.; Li, Y.-f.; Yu, H.-k.; Hou, J.; Hou, H.-q., Studies on oxidation of C60. *Gaodeng Xuexiao Huaxue Xuebao* **2001,** *22* (4), 515-519; (i) Malhotra, R.; Kumar, S.; Satyam, A., Ozonolysis of [60]fullerene. *Journal of the Chemical Society, Chemical Communications* **1994,** (11), 1339-40; (j) Razumovskii, S. D.; Bulgakov, R. G.; Nevyadovskii, E. Y., Kinetics and Stoichiometry of the Reaction of Ozone with Fullerene C60 in a CCl4 Solution. *Kinetics and Catalysis (Translation of Kinetika i Kataliz)* **2003,** *44* (2), 229-232; (k) Van Cleempoel, A.; Gijbels, R.; Claeys, M.; Van den Heuvel, H., Characterization of ozonated C60 and C70 by high performance liquid chromatography and low- and high-energy collision-induced dissociation tandem mass spectrometry. *Rapid Communications in Mass Spectrometry* **1996,** *10* (13), 1579-1584.
88. (a) Criegee, R.; Schroder, G., *Chem. Ber.* **1960,** *93*, 689; (b) Criegee, R.; Werner, G., *Justus Liebigs Ann. Chem.* **1949,** *9*.
89. (a) Sabirov, D. S. B., R. G.; Khursan, S. L.; Dzhemilev, U. M., A New Approach to the Estimation of the Fullerene Reactivity in 1,3-Dipolar Addition Based on Polarizability Indices. *Doklady Physcial Chemistry* **2009,** *425* (1), 54-56; (b) Sabirov, D. S. K., S. L.; Bulgakov, R. G., 1,3Dipolar addition reactions to fullerenes: the role of the local curvature of carbon surface. *Russian Chemical Bulletin, International Edition* **2008,** *57* (12), 2520-2525.
90. Fortner, J. D.; Kim, D. I.; Boyd, A. M.; Falkner, J. C.; Moran, S.; Colvin, V. L.; Hughes, J. B.; Kim, J. H., Reaction of Water-Stable C-60 aggregates with ozone. *Environmental Science & Technology* **2007,** *41* (21), 7497-7502.
91. Heymann, D. B., S. M.; Weisman, R. B., Ozonides, Epoxides, and Oxidoannulenes of C_{70}. *Journal of the American Chemical Society* **2002,** *124*, 6317-6323.
92. Brosset, P. D., R.; Gauthier-Roy, B.; Abouaf-Marguin, L., *Chem. Phys.* **1993,** *172*, 315.

93. (a) Heymann, D. W., R. Bruce, Fullerene oxides and ozonides. *C. R. Chimie* **2006,** *9*, 1107-1116; (b) Krause, M. D., L.; Seifert, G.; Fowler, P. W.; Gromov, A.; Kratschmer, W.; Gutierez, R.; Porezag, D.; Frauenheim, T., Vibrational signatures o fullerene oxides. *J. Chem. Soc., Faraday Trans.* **1998,** *94* (16), 2287-2294.
94. Vassallo, A. M.; Pang, L. S. K.; Coleclarke, P. A.; Wilson, M. A., Emission Ftir Study of C60 Thermal-Stability and Oxidation. *Journal of the American Chemical Society* **1991,** *113* (20), 7820-7821.
95. (a) de Lucas, N. C. N.-F., J. C.; Andraos, J.; Lusztyk, J.; Wagner, B. D.; Scaiano, J. C., Reactivity of Fluorenylideneketene towards Amines. A Laster Photolysis Study with Ultraviolet and Infrared Detection. *Tetrahedron Letters* **1997,** *38* (29), 5147-5150; (b) Qiao, G. G. H.; Andraos, J.; Wentrup, C., Reactivity of ketenes in matrices. Direct observation of ketene-pyridine ylides. *Journal of the American Chemical Society* **1996,** *118* (24), 5634-5638; (c) Visser, P. Z., Ralf; Wong, Ming Wah; Wentrup, Curt, Reactivity of Carbenes and Ketenes in Low-Temperature Matrices. Carbene CO Trapping, Wolff Rearrangement, and Ketene-Pyridine Ylide (Zwitterion) Observation. *Journal of the American Chemical Society* **1996,** *118*, 12598-12602; (d) Wagner, B. D.; Arnold, B. R.; Brown, G. S.; Lusztyk, J., Spectroscopy and absolute reactivity of ketenes in acetonitrile studied by laser flash photolysis with time-resolved infrared detection. *Journal of the American Chemical Society* **1998,** *120* (8), 1827-1834.
96. (a) Basheer, A.; Rappoport, Z., Oxa-ene reaction of enols of amides with 4-phenyl-1,2,4-triazoline-3,5-dione. *Journal of Organic Chemistry* **2008,** *73* (1), 184-190; (b) Sung, K. S.; Tidwell, T. T., Amination of ketene: A theoretical study. *Journal of the American Chemical Society* **1998,** *120* (13), 3043-3048.
97. Kepert, D. L.; Clare, B. W., Hatch opening and closing on oxygenation and deoxygenation of C-60 bathysphere. *Inorganica Chimica Acta* **2002,** *327*, 41-53.
98. Sabirov, D. S. K., S. L.; Bulgakov, R. G., Ozone addition to C60 and C70 fullerenes: A DFT study. *Journal of Molecular Graphics and Modelling* **2008,** *27*, 124-130.
99. McCabe, J. A., J. P. D., Heterogeneous Loss of Gas-Phase Ozone on n-Hexane Soot Surfaces: Similar Kinetics to Loss on Other Chemically Unsaturated Solid Surfaces. *J. Phys. Chem. C* **2009,** *113*, 2120-2127.
100. (a) Bakry, R. V., Rainer M.; Najam-ul-Haq, Muhammad; Rainer, Matthias; Szabo, Zoltan; Huck, Christian W.; Bonn, Gunther K., Medicinal applications of fullerenes. *Int. J. Nanomedicine* **2007,** *2* (4), 639-649; (b) Conway, B. E., *Electrochemical Supercapacitors: Scientific Fundamentals and Technological Applications*. first ed.; Springer: 1999; (c) Sherigara, B. S.; Kutner, W.; D'Souza, F., Electrocatalytic Properties and Sensor Applications of Fullerenes and Carbon Nanotubes. *Electroanalysis* **2003,** *15* (9), 753-772; (d) Tagmatarchis, N. S., H., *Fullerenes in Medicinal Chemistry and their Biological Applications*. Bentham Science Publishers: 2001; Vol. 1.
101. (a) Cioslowski, J. R., N.; Moncrieff, D. J., *Journal of the American Chemical Society* **2000,** *122*; (b) Tseng, S. P. S., M. Y.; Yu, C. H., *Theor. Chim. Acta* **1995,** *92*; (c) Tseng, S. P. Y., C. H., *Chemical Physics Letters* **1994,** *231*; (d) Cioslowski, J., *Chemical Physics Letters* **1993,** *216*.
102. Rojas, A. M., Melchor; Amador, Patricia; Torres, Luis Alfonso, Increasing Stability of the Fullerenes with the Number of Carbon Atoms: The Experimental Evidence. *Journal of Physical Chemistry B* **2007,** *111*, 9031-9035.

103. McElvany, S. W.; Callahan, J. H.; Ross, M. M.; Lamb, L. D.; Huffman, D. R., Large odd-numbered carbon clusters from fullerene-ozone reactions. *Science (Washington, DC, United States)* **1993,** *260* (5114), 1632-4.
104. (a) Mawhinney, D. B. N., Viktor; Kuznetsova, Anya; Yates, John T, Jr.; Liu, J.; Smalley, R. E., Infrared Spectral Evidence for the Etching of Carbon Nanotubes: Ozone Oxidation at 298 K. *Journal of the American Chemical Society* **2000,** *122*, 2383-2384; (b) Peng, K. L., L.-Q.; Li, H.; Meyer, H.; Zhang, Z., Room temperature functionalization of carbon nanotubes using an ozone/water vapor mixture. *Carbon* **2011,** *49*, 70-76.
105. Yim, W.-L. J., J. Karl, Ozone Oxidation of Single Walled Carbon Nanotubes from Density Functional Theory. *Journal of Physical Chemistry C* **2009,** *113*, 17636-17642.
106. Simmons, J. M. N., B. M.; Baker, S. E.; Marcus, Matthew S.; Castellini, O. M.; Lee, C.-S.; Hamers, R. J.; Eriksson, M. A., The effect of ozone oxidation on single-walled carbon nanotubes. University of Wisconsin - Madison: Madison, pp 1-28.
107. Bolskar, R. D. A., J. Michael Derivatization and solubilization of fullerenes for use in therapeutic and diagnostic applications. 2003.
108. Feng, L. S., Baoyun; He, Xiaoran; Gu, Zhennan, ISOLATION AND SPECTROSCOPIC STUDY OF A SERIES OF MONOTERBIUM ENDOHEDRAL METALLOFULLERENES. *Fuller Nanotub Car N* **2002,** *10* (4), 353-361.

109. Guo, S. N., Phillip M.; Deering, Amanda L.; Van Lue, Staci M.; Kandel, S. Alex, Scanning tunneling microscopy of surface-adsorbed fullerenes: C60, C70, and C84. *Surface Science* **2007,** *601*, 994-1000.
110. Dayong, S. Z., Liu; Xinghua, Guo; Wenguo, Xu; Shuying, Liu, Electronic structure and fluorescent property of endohedral terbium f ullerenes. *Chinese Science Bulletin* **1997,** *42* (21), 1798-1802.
111. Balaban, A. S., Thomas G.; Zhu, Hongyao; Klein, Douglas J., Generalizations of the Stone-Wales rearrangement for cage compounds, including fuflerenes. *Journal of Molecular Structure (Theochem)* **1996,** *363*, 291-301.